

<https://doi.org/10.35662/unine-thesis-2836>

**Metrological and stability studies
in high-performance rubidium vapor-cell atomic clocks**

Laboratoire Temps-Fréquence (LTF)

**Thèse présentée à la Faculté des sciences
de l'Université de Neuchâtel**

**pour l'obtention du grade de
DOCTEUR ÈS SCIENCES**

par :

NIL ALMAT

MSc en Microtechnique de l'École Polytechnique Fédérale de Lausanne (EPFL)

Acceptée le 5 juin 2020 sur proposition du jury :

Prof. Dr. Gaetano MILETI, Université de Neuchâtel, Neuchâtel, Directeur de thèse

Prof. Dr. Erling RIIS, University of Strathclyde, Glasgow, United Kingdom, Rapporteur

Dr. Sébastien BIZE, Observatoire de Paris (LNE-SYRTE), Paris, France, Rapporteur

Dr. Christoph AFFOLDERBACH, Université de Neuchâtel, Neuchâtel, Rapporteur

Université de Neuchâtel, juillet 2020

IMPRIMATUR POUR THESE DE DOCTORAT

La Faculté des sciences de l'Université de Neuchâtel
autorise l'impression de la présente thèse soutenue par

Madame Nil ALMAT

Titre:

**“Metrological and stability studies in
high-performance rubidium
vapor-cell atomic clocks”**

sur le rapport des membres du jury composé comme suit:

- Prof. titulaire Gaetano Mileti, directeur de thèse, Université de Neuchâtel, Suisse
- Prof. Erling Riis, University of Strathclyde, United Kingdom
- Dr Sébastien Bize, Observatoire de Paris (LNE-SYRTE), France
- Dr Christoph Affolderbach, Université de Neuchâtel

Neuchâtel, le 13 juillet 2020

Le Doyen, Prof. P. Felber



Abstract

This thesis presents the metrological and stability studies in compact and high-performance atomic clocks based on a rubidium (Rb) vapor cell and double-resonance (DR) spectroscopy¹. We address the limitations of the clock frequency stability on short (at 1 s) and medium-to-long (up to 1 day) timescales using two separate Rb vapor-cell clocks. First, the experimental studies on the physical effects that perturb the clock frequency and degrade the long-term stability are performed for a pulsed optically pumped DR (POP-DR) Rb clock based on a laser diode (LD) emitting at 780 nm. Secondly, a Rb clock operated in a continuous-wave DR (CW-DR) scheme is used to assess the application potential of frequency-doubled telecom lasers initially emitting at 1560 nm. Various applications, such as satellite-based navigation systems, industrial or fundamental metrology, telecommunications, that require a compact frequency reference widely exploit the vapor-cell clocks. In particular for satellite navigation systems, a compact size with a volume of few liters and a high-frequency stability performance at the level of $1 \cdot 10^{-14}$ at 1 day (equivalent to 1 ns/day) are essential.

On long-term timescales, the fluctuations of the experimental and environmental parameters impact the clock frequency stability via various physical processes. The individual impacts of these processes are characterized by a coefficient quantifying the clock frequency sensitivity to the fluctuating parameter and the fluctuations of the sensitive parameter. Using our POP-DR clock, we measured a frequency instability below $2 \cdot 10^{-14}$ up to 1 day of averaging time. The clock frequency stability is optimized for long-term timescales. The impact of the second-order Zeeman effect limiting the clock stability is reduced to and that of the temperature fluctuations is consolidated at the level of few 10^{-15} at 1 day. The established long-term instability budget presented in this thesis indicates that the dominant contribution arises from light-induced effects.

The short-term frequency stability of laser-pumped vapor-cell clocks is limited by several noise contributions, among which the laser (intensity and/or frequency) noise is most often the dominant factor. To reduce the impact of the laser noise, we evaluate an optical source based on a low-noise telecom LD emitting at 1560 nm. The emission frequency of the telecom LD is doubled to 780 nm

¹This thesis work was done in the Laboratoire Temps-Fréquence of the University of Neuchâtel. This work was supported by the Swiss National Science Foundation (SNF): “Precision double resonance spectroscopy and metrology with stabilised lasers and atomic vapours: applications for atomic clocks and magnetometers,” n° 156621. This work also received funding from the European Union’s Horizon 2020 research and innovation programme under grant agreement no. 820393 (Quantum Technology Flagship, project macQsimal).

Abstract

and stabilized using a Rb vapor cell. The lower intensity noise and particularly the lower frequency noise of this laser system present significant advantages for Rb vapor-cell clocks and many other high-resolution applications that manipulate Rb atoms at 780 nm.

In order to improve the short-term clock frequency stability, we implemented the optimized laser system based on the low-noise telecom laser diode in a Rb vapor-cell clock operating in a CW-DR scheme. We present a short-term clock frequency instability of $2.5 \cdot 10^{-13}$ at 1 s, at the level of the state-of-the-art and established the exhaustive noise budget including the contributions from the laser and the microwave source noise. The low-frequency noise of the telecom laser allows for relaxed requirements regarding the clock operation conditions, particularly regarding the optical-pump frequency and the vapor-cell temperature that affect the laser frequency noise conversion to intensity noise. Nevertheless, the optical power fluctuations at the 780-nm output of the laser system become an important instability source at 10 s, degrading the clock stability via the intensity light-shift effect.

The results of this thesis serve to expose the limits of the frequency stability of the studied clock prototypes and to instigate new approaches to overcome these limitations. We also demonstrate that the optical frequency references based on a frequency-doubled telecom laser that benefits from the stability of Rb atomic transition frequencies present a high implementation potential in Rb vapor-cell clock applications, as well as for other applications at both wavelengths (1560 nm and 780 nm). These outcomes are beneficial for the development of the next generation of compact Rb vapor-cell clocks using a laser source and ensuring a frequency stability performance at the level of $1 \cdot 10^{-14}$ at 1 day.

Keywords: Atomic frequency standard, Rubidium vapor cell, Double resonance, Pulsed optical pumping, Spectroscopy, Frequency instability, Metrology

Résumé

Cette thèse présente les études métrologiques et de stabilité des horloges atomiques compactes de haute performance basées sur une cellule à vapeur de rubidium (Rb) et la spectroscopie à double résonance (DR)². Nous abordons les limites de la stabilité de fréquence d'horloge à court (à 1 s) et moyen-long (jusqu'à 1 jour) termes en utilisant deux différentes horloges à cellule à vapeur de Rb. Les études expérimentales des effets physiques qui perturbent la fréquence d'horloge et dégradent la stabilité à long terme sont réalisées pour une première horloge Rb à double résonance à pompage optique pulsée (POP-DR) au moyen d'une diode laser (LD) émettant à 780 nm. Une seconde horloge Rb exploitant un schéma DR à onde continue (CW-DR) est utilisée pour évaluer le potentiel d'application des lasers de télécommunications émettant à 1560 nm doublés en fréquence. Diverses applications, tel que les systèmes de navigation par satellite, la métrologie industrielle ou fondamentale, les télécommunications, qui nécessitent une référence de fréquence compacte exploitent les horloges à cellule à vapeur. En particuliers pour les systèmes de navigation par satellite, une taille compacte d'un volume de quelques litres et une haute performance de stabilité de fréquence autour de $1 \cdot 10^{-14}$ à 1 jour (équivalent à 1 ns/jour) sont essentiels.

À long terme, les fluctuations des paramètres expérimentaux et environnementaux affectent la stabilité de fréquence des horloges par le biais de différents processus physiques. Les impacts individuels de ces processus sont caractérisés par un coefficient quantifiant la sensibilité de la fréquence d'horloge à un paramètre donné et par les fluctuations de ce dernier. Pour notre horloge POP-DR, nous avons mesuré une instabilité de fréquence plus basse que $2 \cdot 10^{-14}$ jusqu'à 1 jour de temps d'intégration. La stabilité de la fréquence d'horloge est optimisée pour les échelles de temps à long terme. L'impact de l'effet Zeeman du second ordre limitant la stabilité d'horloge est réduit et celui des fluctuations de température est consolidé, aux niveaux de quelques 10^{-15} à 1 jour. Le bilan établi des sources d'instabilité à long terme présenté dans cette thèse indique que la contribution dominante provient des effets induits par la lumière.

La stabilité de fréquence à court terme des horloges à cellule à vapeur à pompage optique par un laser, est limitée par diverses contributions de bruit, parmi lesquelles le bruit du laser (intensité

²Ce travail de thèse a été réalisé au sein du Laboratoire Temps-Fréquence of the University of Neuchâtel. Ce travail a été soutenu par le Fonds National Suisse de la recherche scientifique (SNF) : "Precision double resonance spectroscopy and metrology with stabilised lasers and atomic vapours : applications for atomic clocks and magnetometers", n° 156621. Ce travail a également été financé par le programme de recherche et d'innovation Horizon 2020 de l'Union Européenne, dans le cadre de la convention de subvention n° 820393 (Quantum Technology Flagship, projet macQsimal).

et/ou fréquence) est le plus souvent le facteur dominant. Pour réduire l'impact du bruit du laser, nous évaluons une source optique basée sur une LD de télécommunication à faible bruit émettant à 1560 nm. La fréquence d'émission de la LD de télécommunication est doublée à 780 nm et stabilisée en utilisant une cellule à vapeur de Rb. Le faible bruit d'intensité et surtout de fréquence de ce système laser présente des avantages significatifs pour les horloges à cellule de vapeur de Rb et de nombreuses autres applications de haute résolution qui manipulent des atomes Rb à 780 nm.

Afin d'améliorer la stabilité de fréquence d'horloge à court terme, nous avons implémenté le système laser optimisé basé sur la diode laser de télécommunication à faible bruit dans une horloge à cellule à vapeur de Rb exploitant un schéma d'interrogation CW-DR. Nous présentons une instabilité de la fréquence d'horloge à court terme de $2.5 \cdot 10^{-13}$ à 1 s comparable aux meilleures horloges actuelles et établissons le bilan de bruit exhaustif en tenant compte des contributions du bruit du laser et de la source micro-onde. Le faible bruit de fréquence du laser de télécommunication permet d'assouplir les exigences relatives aux conditions de fonctionnement de l'horloge, notamment en ce qui concerne la fréquence du pompage optique et la température de la cellule à vapeur qui influencent la conversion du bruit de fréquence du laser en bruit d'intensité. Néanmoins, les fluctuations de la puissance optique à la sortie de 780 nm du système laser deviennent une source d'instabilité importante à 10 s, dégradant la stabilité d'horloge par l'effet de décalage de fréquence dû à l'intensité de la lumière.

Les résultats de cette thèse permettent d'exposer les limites de la stabilité de fréquence des prototypes d'horloges étudiés et de proposer de nouvelles approches pour les surmonter. Nous démontrons également que les références de fréquence optique basées sur un laser de télécommunication et doublage en fréquence bénéficiant de la stabilité de la fréquence des transitions atomiques Rb présentent un fort potentiel d'implémentation dans les applications d'horloges à cellules à vapeur de Rb et d'autres applications aux deux longueurs d'onde (1560 nm et 780 nm). Ces résultats sont bénéfiques pour le développement de la prochaine génération d'horloges compactes à cellule de vapeur de Rb utilisant une source laser et garantissant un niveau de stabilité de fréquence de $1 \cdot 10^{-14}$ à 1 jour.

Mots clefs : Étalon de fréquence atomique, Cellule à vapeur de Rubidium, Double résonance, Pompage optique pulsé, Spectroscopie, Instabilité de fréquence, Métrologie

Acknowledgment

I would like to express my gratitude to all the people who have helped and supported me on my path to the accomplishment of this thesis.

First, I would like to thank my supervisor, Prof. Gaetano Mileti, for giving me the opportunity to be part of his team and introducing me to the time and frequency community. I am truly grateful for the trust he showed in me, the guidance he provided, and the advice he shared all along the last four years. Setting the perfect example in diplomacy and project management, he helped me to learn how to conduct high-quality research and to value and effectively present my work.

Secondly, I would like to thank Dr. Christoph Affolderbach who followed my work carefully and showed the way towards perfection. The insights and expertise he shared were extremely valuable to improve my skills in the laboratory and in technical writing. I truly appreciate the time he took, even when it was scarce, to answer all my questions and discuss about the physics or career options.

Thirdly, I would like to thank Dr. Matthieu Pellaton who accompanied my work on the realization of the CW-DR clock using the telecom lasers. His challenging questions and critical remarks were a source of encouragement and consistently motivated me to go further.

I also would like to thank all the jury members, Prof. Erling Riis and Dr. Sébastien Bize, for their careful reading and evaluation of this manuscript. Their valuable comments contributed to the improvement of this manuscript.

I would like to express my great appreciation to Prof. Thomas Südmeyer who impressed me with his passion for physics and teaching. I also would like to thank Dr. Stéphane Schilt for his help in reviewing scientific articles and Dr. Renaud Matthey for his support. I would like to thank Dr. Vladimir Dolgovskiy who shared his expertise in the development and management of a research project. He also showed me the possibility of existence and maintenance of an organized desk.

My special thanks go to my colleagues with whom I shared the office and the pursuit of the PhD: Dr. Reza Gharavipour, Dr. William Moreno, and Etienne Batori. Your encouragement at any point of my thesis and our discussions within the struggle to find solutions to our physics problems were very valuable to move forward in my work. The fun you brought in our office was an essential point to lighten our days. Another special thank-you goes to Florian Gruet who supported me in the laboratory. Your serenity and endless patience were exemplary.

Acknowledgment

A particular thank-you goes to Patrick Scherler who was always available to help me on the technical aspects of the atomic clocks, by working meticulously long hours or simply with an aluminum sheet. I also would like to thank Marc Dürrenberger for sharing his knowledge and tricks on the electronics. I also would like to thank Daniel Varidel and Dominique Schenker for their support. I would like to extend my particular thanks to Séverine and Patricia for their support and continuous smile. I am also very thankful to the previous LTF secretariat, Joëlle and Natacha (rest in peace) for all their help.

I want to thank my past and present colleagues on the physics floor. Nayara, Kutan, Sargis, Loïc, thank you for the cheerful moments and the escapades at the lake side, in the mountains, or on the virtual worlds. I would also like to thank my colleagues for contributing to the fun atmosphere on our floor: Pierre, Norbert, Jakub, Olga, François, Maxime, Valentin, Clément, Atif, Julian, Marin, and Kenichi.

I would like to thank our external colleagues from INRIM; Dr. Claudio Calosso for building and providing us the LO to operate our POP Rb clock and Dr. Salvatore Micalizio for his encouragement on my work on the POP Rb clock. I also would like to thank Dr. James Camparo and Dr. Eric Burt for their support and sharing their valuable teaching approaches. Their challenging questions on my work and the following discussions were very valuable to enhance my understanding of the physics of atomic clocks. I am grateful to Prof. Antoine Weis for accepting me in his lectures and introducing me to the fun of the atomic physics. I also thank him for his support to my work and the insightful discussions at the conference in Belgrade.

I would like to address my heartfelt appreciation to my family and my friends for their support, affection, understanding, and being always there for me at any circumstances, even in my –physical or mental– absence. Without their love and encouragement, I could have not reached this point. I want to express my profound gratitude to my parents, Füsün and Töre, my brother, Murat, and my beloved one and my best "distraction", Joe, for the endless support and love they fueled me with.

Contents

Abstract	i
Résumé	iii
Acknowledgment	v
Contents	vii
List of Figures	xi
List of Tables	xv
List of publications	xvii
Acronyms	xxi
Physical constants	xxiii
Notations	xxv
Introduction	1
I.1. Compact vapor-cell clocks	3
I.2. Thesis outline	5
1 Basic principles of DR vapor-cell clocks based on laser optical pumping	7
1.1 Rb atomic structure	8
1.1.1 Three-level model	9
1.2 Optical absorption in vapor cells	11
1.2.1 Doppler broadening	11
1.2.2 Doppler-free absorption spectroscopy	12
1.2.3 Buffer-gas line broadening	13
1.3 Double-resonance interaction in buffer-gas cells	13
1.3.1 Optical and microwave interactions	14
1.3.2 Continuous wave scheme	17
1.3.2.1 CW-DR signal	17

Contents

1.3.3	Pulsed-optimally pumped scheme	19
1.3.3.1	Bloch vector representation	20
1.3.3.2	Ramsey signal	21
1.4	Ground-state life time and line broadening	22
1.5	Clock frequency perturbations	22
1.5.1	Second-order Zeeman shift	23
1.5.2	Buffer-gas density shift	23
1.5.3	Barometric effect	25
1.5.4	Spin-exchange shift	25
1.5.5	Light-induced shifts	29
1.5.6	Microwave-power shift	30
1.5.7	Cavity-pulling shift	31
1.5.8	Summary of clock frequency shifts	33
1.6	Atomic clock frequency instability	34
1.6.1	Overlapping Allan deviation	35
1.6.2	Short-term clock frequency instability	36
1.6.2.1	Optical detection noises	36
1.6.2.2	Light shift effects	37
1.6.2.3	Microwave phase noise	38
1.6.2.4	Short-term clock instability budget	38
1.6.3	Medium-to-long term clock instability	39
1.7	Conclusion	40
2	Experimental setups	43
2.1	Laser systems	44
2.1.1	Laser heads based on 780-nm laser diodes	44
2.1.1.1	Laser spectral characterization	46
2.1.2	Frequency-doubled laser systems	47
2.2	Physics packages	49
2.2.1	Buffer-gas cell	50
2.2.2	Magnetron-type cavity	50
2.2.3	C-field coils and magnetic shielding	52
2.2.4	Temperature control	52
2.3	CW-DR Rb vapor-cell clock	54
2.3.1	Optical sources (FD-ECL, FD-DFB, LH-CW)	54
2.3.2	Physics package (PP-CW)	54
2.3.3	Local oscillator (LO-CW)	56
2.4	POP-DR Rb vapor-cell clock	58
2.4.1	Optical source (LH-POP)	58
2.4.2	Physics package (PP-POP)	60
2.4.3	Local oscillator (LO-POP)	62
2.4.4	Hermetic chamber	63
2.5	Frequency instability characterization methods	65

2.5.1	Microwave frequency standards	65
2.5.2	Optical frequency standards	65
2.6	Conclusion	66
3	Evaluation of long-term instabilities in a POP-DR Rb cell clock	67
3.1	Ramsey signal	68
3.2	Trade-off between short- and long-term clock stability	69
3.3	Analysis of long-term clock instability sources	70
3.3.1	Second-order Zeeman shift	70
3.3.2	Buffer-gas density shift	71
3.3.2.1	Cell and stem temperature coefficients	72
3.3.2.2	Temperature fluctuations	73
3.3.3	Barometric effect	74
3.3.4	Spin-exchange shift	76
3.3.5	Light-induced shifts	77
3.3.6	Microwave-power shift	79
3.3.7	Cavity-pulling shift	81
3.3.8	Other shifts	82
3.4	Long-term clock instability budget	83
3.5	Measured long-term clock instability	85
3.6	Conclusion	90
4	Optical sources for Rb clocks based on frequency-doubled telecom lasers	91
4.1	Telecom lasers in atomic physics	92
4.2	Spectral characterization of FD laser systems	93
4.2.1	Basic spectral properties of FD laser systems	93
4.2.2	Relative intensity noise of FD laser systems	95
4.2.3	Frequency noise of FD laser systems	96
4.2.4	Laser linewidth measurements	97
4.3	Frequency instability measurements at two wavelengths	98
4.4	Evaluation of the optical power fluctuations	102
4.5	Application to Rb vapor-cell clocks	103
4.5.1	Impact on short-term clock stability	103
4.5.2	Impact on long-term clock stability	104
4.6	Conclusion	106
5	CW-DR Rb vapor-cell clock realization using telecom lasers	109
5.1	FM-to-AM noise conversion via the atomic vapor cell	110
5.2	Double-resonance clock signal optimization	111
5.3	Noise contributions to the short-term clock instability	115
5.3.1	Signal-to-noise limit	115
5.3.2	Light shift effects	118
5.3.3	Microwave phase noise contribution	118
5.3.4	Total short-term instability budget	120

Contents

5.4 Measured short-term clock instability	121
5.5 Discussion on the medium-long term clock instability	122
5.6 Conclusion	123
Conclusions and perspectives	125
C.1. High-performance POP-DR Rb clock	125
C.2. Optical frequency reference at two wavelengths (1560 and 780 nm)	126
C.3. CW-DR Rb clock using a telecom laser	128
C.4. Perspectives	129
Appendix A – Optical detection noise	133
Appendix B – Error signal optimization for the clock	137
Bibliography	141
Curriculum Vitae	153

List of Figures

11	<i>Basic operation principle of a passive atomic clock</i>	2
12	<i>Clock frequency instability as a function of SWaP</i>	3
13	<i>State-of-the-art frequency instability of laboratory and industrial clocks</i>	5
1.1	<i>Schematics of a vapor-cell atomic clock based on the DR interrogation principle</i>	8
1.2	<i>Energy levels of the D_1 and D_2 lines in ^{87}Rb</i>	10
1.3	<i>Three-level model approximation including the hyperfine ground states and one excited state</i>	10
1.4	<i>CW-DR scheme: simultaneously applied fields in the time domain and interactions illustrated on the three-level model</i>	15
1.5	<i>POP-DR scheme: timing sequence and interactions illustrated on the three-level model</i>	15
1.6	<i>CW-DR signal</i>	18
1.7	<i>Bloch spheres</i>	21
1.8	<i>Ground-state population inversion during Ramsey time</i>	26
1.9	<i>Spin-exchange shift as a function of the microwave pulse area estimated for various free-decay phase durations (Ramsey times)</i>	27
1.10	<i>Cavity-pulling shift as a function of the microwave pulse area estimated for the two cases of optical-pump frequency on the D_2 line</i>	32
1.11	<i>Laser frequency-modulation conversion to amplitude-modulation via an atomic frequency discriminator</i>	37
2.1	<i>Photography of the continuous-wave optical source: LH-CW</i>	45
2.2	<i>Photography of the pulsed optical source: LH-POP</i>	45
2.3	<i>Schematic of the FD laser system stabilized on Rb frequency reference</i>	48
2.4	<i>Photography of the frequency reference unit: FRU</i>	48
2.5	<i>PPLN output optical power as a function of the input power for different PPLN temperature</i>	49
2.6	<i>Photography of the vapor cells (a) and (b) and the magnetron-type microwave cavity (c) and (d)</i>	50
2.7	<i>Photography and drawings of the microwave cavity with additional monitoring NTCs</i>	53
2.8	<i>Temperature fluctuations measured in simultaneous in the laboratory and on the microwave cavity</i>	53

List of Figures

2.9	<i>Schematic of the CW-DR clock setup employing the frequency-doubled laser system, PP-CW, and LO-CW</i>	55
2.10	<i>Transmission signals of the LH-CW reference cell and the CW-DR clock cell</i>	56
2.11	<i>Zeeman spectrum measured using the PP-CW and the FD-ECL</i>	57
2.12	<i>Phase noise measured at the 6.835 GHz output of the LO-CW</i>	58
2.13	<i>Schematic of the POP-DR clock setup employing the LH-POP, PP-POP, and LO-POP</i>	59
2.14	<i>Microwave cavity resonance under optimized clock operating conditions</i>	61
2.15	<i>Pulsed interrogation pattern of the POP-DR clock</i>	62
2.16	<i>Temperature and pressure fluctuations measured inside and outside the hermetic chamber</i>	64
2.17	<i>Chamber internal pressure fluctuations as a function of chamber internal temperature fluctuations</i>	64
2.18	<i>Schematics of beat-note measurement setups</i>	66
3.1	<i>Ramsey spectra measured for microwave pulses of $\theta = \pi/2$ and $\theta = 0.56\pi$</i>	68
3.2	<i>Clock frequency shift as a function of the applied C-field, the second-order Zeeman shift $\Delta\nu_{Ze}$</i>	71
3.3	<i>Magnetic field fluctuations and clock stability limit via second-order Zeeman shift effect</i>	71
3.4	<i>Clock frequency shift as a function of the clock cell temperature, the buffer-gas density shift $\Delta\nu_{BG}$</i>	72
3.5	<i>Clock frequency shift as a function of the stem temperature</i>	73
3.6	<i>Temperature fluctuations measured on the cell and stem of the PP-POP (placed in the hermetic chamber) and on the microwave cavity of the PP-CW (placed outside the chamber)</i>	74
3.7	<i>Chamber internal and external pressure and temperature fluctuations</i>	75
3.8	<i>Relative clock frequency fluctuations and chamber pressure variations</i>	76
3.9	<i>Relative clock frequency shift versus chamber pressure recorded simultaneously</i>	76
3.10	<i>Clock frequency shift as a function of the optical pump and detection powers for laser frequencies tuned to the $5^2S_{1/2}, F = 2\rangle$ ground-state transitions.</i>	77
3.11	<i>Clock frequency shift as a function of laser frequency on the $5^2S_{1/2}, F = 2\rangle$ ground-state transitions</i>	78
3.12	<i>Relative optical power fluctuations measured at the clock cell input in the pulsed operation mode and estimated clock frequency stability limit via the intensity LS effect</i>	79
3.13	<i>Clock frequency shift as a function of the applied microwave pulse area</i>	80
3.14	<i>Microwave power fluctuations and clock stability limit via MPS effect</i>	81
3.15	<i>Measured long-term clock frequency instability</i>	86
3.16	<i>Simultaneously measured clock frequency, chamber pressure, LH-POP reference signal, and cell, stem, and laboratory temperature fluctuations</i>	88
3.17	<i>Estimated clock frequency fluctuations induced by the temperature, barometric, and light intensity sensitivities</i>	89
3.18	<i>LH-POP Doppler-free absorption and environmental parameters fluctuations.</i>	89
4.1	<i>Optical power at the 1560 and 780-nm of the FD-ECL versus the drive current for different LD temperatures</i>	94

4.2	<i>Frequency tuning with laser drive current and temperature</i>	94
4.3	<i>Relative intensity noise spectrum for the three laser systems</i>	96
4.4	<i>FM noise spectra measured at the 780-nm outputs of the three laser systems</i>	97
4.5	<i>Frequency instability of the beat-note signals between three laser systems</i>	99
4.6	<i>Beat 2 and Beat 3 frequencies, reference Rb cell input and output signals of the FD-DFB laser system, and laboratory temperature</i>	100
4.7	<i>Beat 1 frequency, reference Rb cell output signals of the two lasers systems forming the beat (FD-ECL and LH-CW), and laboratory temperature</i>	101
4.8	<i>Relative optical power fluctuations measured at the reference Rb cell input of the three laser systems</i>	102
4.9	<i>Relative optical power fluctuations measured at different stages of the FD-ECL laser system</i>	103
4.10	<i>Laser frequency instability and requirements for high-performance Rb-cell clock applications at 780 nm and for CO₂ detection at 1572 nm</i>	107
5.1	<i>Absorption signals of the reference Rb cell of LH-CW and of the clock Rb cell of PP-CW</i>	110
5.2	<i>CW-DR clock signal parameters as a function of the optical power at the PP-CW input</i>	112
5.3	<i>CW-DR clock signal parameters as a function of the microwave power</i>	113
5.4	<i>CW-DR clock signals measured using the three laser systems for the two optical-pump frequencies</i>	114
5.5	<i>Error signals measured using the three laser systems for the two optical-pump frequencies</i>	115
5.6	<i>Clock detection noise PSDs measured using the three laser systems for the two optical-pump frequencies</i>	116
5.7	<i>Intensity light-shift measurements using the three laser systems for all the four optical-pump frequencies</i>	119
5.8	<i>Short-term clock instabilities measured using the three laser systems for the two optical-pump frequencies</i>	122
5.9	<i>Optical power fluctuations measured at the clock PP-CW input for lasers stabilized to CO10-11 and F12</i>	123
C1	<i>Fractional frequency fluctuations of the optical frequency for the frequency-doubled telecom laser and typical instability requirements for applications around 780 nm and 1560 nm</i>	128
C2	<i>State-of-the-art clock stability for laboratory and industrial clocks, including the results of this work</i>	130
C3	<i>Clock instability as a function of clock SWaP for industrial clocks and including the results of this work</i>	131
A.1	<i>Typical transmission signal of the clock Rb vapor cell as function of the laser frequency</i>	134
A.2	<i>CW-DR clock detection noise PSD as function of the optical and microwave powers</i>	135
B.1	<i>Discriminator slope of the error signal as function of microwave frequency modulation parameters</i>	139

List of Tables

1.1	<i>Buffer-gas shift coefficients for ^{87}Rb using Ar and N_2 gases</i>	24
1.2	<i>Spin-exchange coefficients for $\theta = \pi/2$ or 0.56π, optical pumping from $2\rangle$, and cell at 62.16°C</i>	28
1.3	<i>Cavity-pulling shift coefficients for $\theta = \pi/2$ and $\theta = 0.56\pi$, optical pumping from $2\rangle$, and cell temperature of 62.16°C at atmospheric pressure</i>	32
1.4	<i>Estimated clock frequency shift of the POP-DR clock</i>	33
1.5	<i>Short-term instability budget at $\tau = 1$ s for the state-of-the-art CW-DR Rb clock</i>	39
1.6	<i>Preliminary long-term instability budget at $\tau = 10^4$ s for the POP-DR clock</i>	41
2.1	<i>Spectral characteristics of the LH-CW and LH-POP</i>	47
2.2	<i>Key parameters of the simulated microwave performance of the magnetron cavity</i>	51
2.3	<i>Environmental sensitivity coefficients of the resonance frequency of the magnetron-type cavity implemented in PP-POP</i>	61
3.1	<i>Key parameters of the central Ramsey fringes measured for $\theta = \pi/2$ and $\theta = 0.56\pi$ pulses</i>	68
3.2	<i>Discriminator slope of the FM-to-AM noise conversion via the clock Rb cell for laser frequency tuned to one of the $5^2S_{1/2}, F = 2\rangle$ ground-state transitions</i>	69
3.3	<i>Light –intensity and frequency– induced clock frequency sensitivity coefficients</i>	78
3.4	<i>Cavity-pulling shift coefficients and estimated clock stability limits for the experimental parameter fluctuations</i>	82
3.5	<i>Long-term instability budget at $\tau = 10^4$ to 10^5 s for the POP-DR clock</i>	84
3.6	<i>Clock experimental parameters in view of optimized long-term stability performance</i>	85
4.1	<i>Spectral properties of the three laser systems</i>	95
4.2	<i>Linewidth of the three laser systems measured at 780-nm output</i>	98
4.3	<i>Three beat notes between the three laser systems</i>	99
4.4	<i>Measured Beat 1 frequency sensitivity coefficients due to variations of FD-ECL experimental parameters and estimated stability limitations at $\tau = 10^4$ s</i>	101
4.5	<i>Estimated SNR limit of short-term clock stability for the f stabilized laser intensity and frequency noise of the three laser systems</i>	104
4.6	<i>Estimated limitations of long-term clock stability from intensity and frequency fluctuations of the three laser systems via intensity LS (ILS) and frequency LS (FLS) effects, respectively</i>	105

List of Tables

5.1	<i>Reference transition labels, frequency detunings from F12, and the corresponding frequency discriminators obtained via the clock Rb cell</i>	111
5.2	<i>Optimized CW-DR signal parameters measured using the three laser systems for two optical-pump frequencies</i>	114
5.3	<i>Estimated SNR limit of the clock stability and the independent contributions of the laser AM noise and the FM-to-AM noise conversion via the clock Rb cell to the measured clock detection noise for three laser systems and two optical-pump frequencies tuned to CO10-11 and F12</i>	117
5.4	<i>Intensity light-shift coefficients measured using the three laser systems for the optical-pump frequencies tuned to the four reference transitions</i>	119
5.5	<i>Frequency light-shift coefficients measured using the three laser systems for the laser frequency tuned to the reference transitions of the hyperfine components F=1 and F=2</i>	119
5.6	<i>Total short-term clock instability budget for the three laser systems and the two optical-pump frequencies</i>	120
C1	<i>Performance of the frequency-doubled telecom laser compared to the laser heads based on a LD emitting at 780 nm</i>	127

List of publications

Parts of this thesis are published in the following journal papers and conference proceedings. Some contents are originally copied with permission from the corresponding publisher. The copyright of the original publications are held by the respective copyright holders.

Articles in peer-reviewed journals

1. E. Batori, **N. Almat**, C. Affolderbach, G. Mileti, "GNSS-grade space atomic frequency standards: current status and ongoing developments," *Advances in Space Research*, 2020, to be published.
2. **N. Almat**, M. Gharavipour, W. Moreno, F. Gruet, C. Affolderbach, G. Mileti, "Long-term analysis towards $< 10^{-14}$ level for POP Rb cell atomic clock," *IEEE Transactions on Ultrasonics, Ferroelectrics, and Frequency Control*, vol. 67, no. 1, pp. 207–216, 2020.
3. W. Moreno, M. Pellaton, C. Affolderbach, **N. Almat**, M. Gharavipour, F. Gruet, G. Mileti, "Impact of microwave-field inhomogeneity in double-resonance vapor cell Ramsey spectroscopy," *Quantum Electronics*, vol. 49, no. 3, pp. 293–297, 2019.
4. **N. Almat**, M. Pellaton, W. Moreno, F. Gruet, C. Affolderbach, G. Mileti, "Rb vapor-cell clock demonstration with a frequency-doubled telecom laser," *Applied Optics*, vol. 57, no. 16, pp. 4707–4713, 2018.
5. **N. Almat**, W. Moreno, M. Pellaton, F. Gruet, C. Affolderbach, G. Mileti, "Characterization of frequency-doubled $1.5 - \mu\text{m}$ lasers for high performance Rb clocks," *IEEE Transactions on Ultrasonics, Ferroelectrics, and Frequency Control*, vol. 65 no. 1, pp. 919–926, 2018.

International conferences with proceedings

1. **N. Almat**, M. Gharavipour, W. Moreno, C. Affolderbach, G. Mileti, "Long-term analysis towards $< 10^{-14}$ level for POP Rb cell atomic clock," in *Proceedings Joint conference of the IEEE International Frequency Control Symposium and European Frequency and Time Forum*, Orlando, Florida, USA, April 14 – 18, 2019 (oral presentation and poster presentation as the best student paper award finalist by N. Almat).

List of publications

2. W. Moreno, M. Pellaton, **N. Almat**, M. Gharavipour, C. Affolderbach, G. Mileti, "Investigations on microwave power shift in compact vapor-cell atomic clock," in *Proceedings Joint conference of the IEEE International Frequency Control Symposium and European Frequency and Time Forum*, Orlando, Florida, USA, April 14 – 18, 2019 (poster presentation by C. Affolderbach).
3. C. Affolderbach, **N. Almat**, M. Gharavipour, F. Gruet, W. Moreno, M. Pellaton, G. Mileti, "Selected studies on high performance laser-pumped Rubidium atomic clocks," in *Proceedings International Frequency Control Symposium*, Squaw Creek, Olympic Valley, California, USA, May 22 – 24, 2018 (oral presentation by G. Mileti).
4. **N. Almat**, W. Moreno, M. Pellaton, M. Gharavipour, F. Gruet, C. Affolderbach, G. Mileti, "Cell-Based Stabilized Laser Sources and Light-Shifts in Pulsed Rb Atomic Clocks," in *Proceedings Joint conference of European Frequency and Time Forum and International Frequency Control Symposium*, Besançon, France, July 9 – 13, 2017 (oral presentation by W. Moreno, poster presentation as the best student paper award finalist by N. Almat).
5. F. Gruet, R. Matthey, C. Affolderbach, **N. Almat**, G. Mileti, "Methods and Setup for Spectral Characterization of Laser Diodes for Atomic Clocks," in *Proceedings International Conference on Space Optics*, Biarritz, France, October 18 – 21, 2016 (poster presentation by F. Gruet).

International conferences without proceedings

1. **N. Almat**, W. Moreno, F. Gruet, C. Affolderbach, G. Mileti, "Long-term stability analysis at 10^{-14} level of a highly compact vapour-cell atomic clock for GNSS applications," *7th international colloquium on scientific and fundamental aspects of GNSS*, Zurich, Switzerland, September 4 – 6, 2019 (oral presentation by C. Affolderbach).
2. **N. Almat**, W. Moreno, F. Gruet, C. Affolderbach, G. Mileti, "Long-term stability analysis of a compact Ramsey-scheme vapor-cell atomic clock at 10^{-14} level," *Joint Annual Meeting of the Swiss Physical Society and Austrian Physical Society*, Zurich, Switzerland, August 26 – 30, 2019 (oral presentation by N. Almat).
3. C. Affolderbach, **N. Almat**, M. Gharavipour, F. Gruet, W. Moreno, M. Pellaton, G. Mileti, "Ramsey spectroscopy in vapour-cells for compact high-performance atomic clocks," *8th International Symposium and School Modern Problems of Laser Physics*, Novosibirsk, Russia, August 27 – September 1, 2018 (invited oral presentation by G. Mileti).
4. C. Affolderbach, **N. Almat**, M. Gharavipour, F. Gruet, R. Matthey, W. Moreno, G. Mileti, "High performance and miniature laser-pumped vapour-cell frequency standards," *3rd URSI Regional Conference on Radio Science*, Tirupati, India, March 1 – 3, 2017 (invited plenary talk by G. Mileti).
5. **N. Almat**, W. Moreno, M. Pellaton, F. Gruet, C. Affolderbach, G. Mileti, "Frequency-doubled laser sources stabilized to Rb-cell references," *Photonica*, Belgrade, Serbia, August 28 – September 1, 2017 (poster presentation by N. Almat).

6. C. Affolderbach, **N. Almat**, M. Gharavipour, F. Gruet, W. Moreno, M. Pellaton, G. Mileti, "Laser-pumped high performance vapor-cell atomic clocks," *Annual Meeting of the Swiss Physical Society*, Geneva, Switzerland, 21 – 25 August 2017 (oral presentation by C. Affolderbach).
7. F. Gruet, C. Affolderbach, **N. Almat**, R. Matthey, P. Berthoud, G. Mileti, "Spectral characterization of 894 nm DFB laser diodes and development of a Cs atomic clock," *CTI Micro-Nano Event 2016*, Basel, Switzerland, June 30, 2016 (poster presentation by G. Mileti).

Acronyms

AHM	Active Hydrogen Maser
AM	Amplitude Modulation
AOM	Acousto-Optic Modulator
BG	Buffer Gas
CP	Cavity Pulling
CPT	Coherent Population Trapping
CSAC	Chip Scale Atomic Clock
CW	Continuous Wave
DFB	Distributed Feedback
DR	Double Resonance
ECL	External Cavity Laser
EDFA	Erbium-Doped Fiber Amplifier
EM	ElectroMagnetic
EPFL	École Polytechnique Fédérale de Lausanne
ESA	European Space Agency
FD	Frequency Doubled
FEMTO-ST	Franche-Comté Electronique Mécanique Thermique et Optique – Sciences et Technologies
FM	Frequency Modulation
FoF	Field Orientation Factor
FRU	Frequency Reference Unit
FWHM	Full Width at Half Maximum
GLONASS	Global Navigation Satellite System
GNSS	Global Navigation Satellite System
GPS	Global Positioning System
INRIM	Instituto Nazionale di Ricerca Metrologica
LD	Laser Diode
LH	Laser Head
LNE-SYRTE	Laboratoire National de Métrologie et d’Essais - Systèmes de Référence Temps-Espace
LO	Local Oscillator

Acronyms

LS	L ight S hift
LTF	L aboratoire T emps- F réquence
LW	L inewidth
MPS	M icrowave P ower S hift
NTC	N egative T emperature C oefficient
OCXO	O ven- C ontrolled C rystal O scillator
PD	P hoto D etector
PHM	P assive H ydrogen M aser
PM	P olarization M aintaining
POP	P ulsed O ptically P umped
PP	P hysics P ackage
PPLN	P eriodically P oled L ithium N iobate
RAFS	R ubidium A tomic F requency S tandard
RF	R adio F requency
RIN	R elative I ntensity N oise
SE	S pin E xchange
SHG	S econd H armonic G eneration
SIOM	S hanghai I nstitute of O ptics and F ine M echanics
SM	S ingle M ode
SMSR	S ide M ode S uppression R atio
SNF	S wiss N ational S cience F oundation
SNR	S ignal-to- N oise R atio
TC	T emperature C oefficient
UNINE	U niversit� de N euch�tel

Physical constants

Speed of light [1]	c	$299\,792\,458\text{ m s}^{-1}$
Planck constant $\frac{h}{2\pi}$ [1]	\hbar	$1.054\,571\,817 \cdot 10^{-34}\text{ J s}$
Elementary charge [1]	e	$1.602\,176\,634 \cdot 10^{-19}\text{ C}$
Boltzmann constant [1]	k_B	$1.380\,649 \cdot 10^{-23}\text{ J K}^{-1}$
Magnetic permeability [1]	μ_0	$4\pi \cdot 10^{-7}\text{ N A}^{-2}$
Electric permittivity [1]	ϵ_0	$8.854\,187\,8128(13) \cdot 10^{-12}\text{ F m}^{-1}$
Bohr magneton $\frac{e\hbar}{2m_e}$ [1]	μ_B	$9.274\,010\,0783(28) \cdot 10^{-24}\text{ J T}^{-1}$
Electron mass [1]	m_e	$9.109\,383\,7015(28) \cdot 10^{-31}\text{ kg}$
Free electron's Landé g-factor [1]	g_S	$2.002\,319\,304\,362\,56(35)$
Bound electron's Landé g-factor ($5^2S_{1/2}$) [2]	g_J	$2.002\,331\,13(20)$
^{87}Rb nucleus' Landé g-factor [2]	g_I	$-0.000\,995\,141\,4(10)$
^{87}Rb atomic mass [2]	m_e	$1.443\,160\,648(72) \cdot 10^{-25}\text{ kg}$

Notations

Symbol	Denotation	Unit
ω, Ω	Angular frequencies	$\text{rad}\cdot\text{s}^{-1}$
Γ, γ	Linewidths or rates in the angular frequency domain	$\text{rad}\cdot\text{s}^{-1}$ or s^{-1}
ν	Frequencies	Hz
W	Linewidths (full width at half maximum) in the frequency domain	Hz
$\Delta\nu$	Frequency shifts	Hz

Introduction

Time and timekeeping have long been crucial components in human history. The periodic motion of the Earth around the sun and itself, and of the moon around the Earth, creates cyclical natural consequences for life on earth, including days, years, seasons, and tides. These periodic phenomena have allowed humankind to keep track of time and inspired early efforts to measure time. However, the measurable time interval of such early efforts was limited to hours or days, and the period was not stable in time. In the pursuit of improving the precision of the measurement of time, reducing the smallest measurable time interval (i.e., the oscillation period T), oscillating mechanical and electrical systems that imitate a periodic movement were developed [3]. A stable oscillator combined with a system to deliver the information constitutes a clock, which provides a periodic signal that is useful for timekeeping. In atomic clocks, the oscillating system is formed by a single atom or an ensemble of atoms driven by electromagnetic (EM) radiation(s). The oscillation frequency f ($f = 1/T$) corresponds to the Bohr frequency of the transition between two specific quantum states of the atom(s) and therefore benefits from the stability of the atomic quantum states and their energy differences.

Beyond the measurement of time, the effective communication of time between entities requires a universal definition of a time unit. The unit of time in the international system of units (SI) is the second and is defined as "the duration of 9 192 631 770 periods of the radiation corresponding to the transition between the two hyperfine levels of the ground state of the cesium 133 atom at rest and at a temperature of 0 K" [4]. The SI second is realized using the primary clocks, such as thermal cesium (Cs) beam [5] and cold Cs fountain clocks [6], within which the Ramsey spectroscopy [7] is applied to traveling atoms. Cesium fountain clocks, with a relative precision on the order of $10^{-15} - 10^{-16}$, are used as primary frequency references in several national metrology institutes [8–10]. The use of a higher atomic transition frequency, such as in the optical region (THz range), presents a fundamental advantage in improving precision by about three orders of magnitude compared to clocks based on microwave transitions (GHz range). Optical atomic clocks push the precision levels towards the 10^{-18} [11–13], provoking discussions on the redefinition of the SI second [14, 15].

Atomic clocks based on atoms other than Cs (e.g. hydrogen or rubidium), whose transition frequencies differ from the definition of the SI second, are used as secondary frequency references [13]. This thesis concerns compact rubidium (Rb) vapor-cell clocks [16], for which we address the frequency

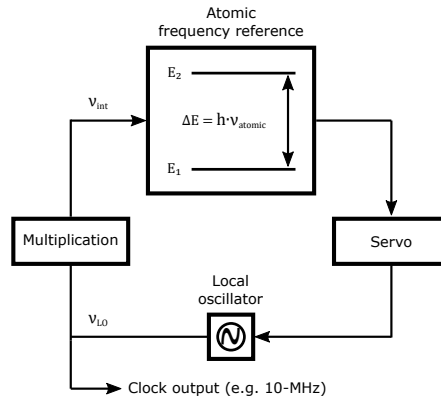


Figure 11 – Basic operation principle of a passive atomic clock.

stability limitations on short and long timescales. We evaluate the impacts of different frequency perturbation sources in view of improving the clock stability. Rb vapor-cell clocks are passive³ frequency standards. In passive atomic clocks, the frequency of an external local oscillator (LO) is stabilized to the Bohr frequency of an atomic transition ν_{atomic} , as illustrated in Figure 11. A group of atoms are interrogated with an oscillating field near ν_{atomic} . The interrogation field at frequency ν_{int} is obtained from the LO at frequency ν_{LO} (typically 5 or 10 MHz) which is multiplied to reach the atomic transition frequency. The atomic transition frequency is detected and a correction signal is applied to the LO in order to maintain the interrogation field frequency at $\nu_{\text{int}} \approx \nu_{\text{atomic}}$. The LO provides the useful output of the atomic clocks as an (e.g. 5 or 10 MHz) electrical signal whose frequency is properly related to the atomic transition frequency. The clock frequency corresponding to an atomic transition frequency can be perturbed in the presence of other atoms or external fields. The performance of an atomic clock is evaluated with two criteria: *accuracy* (or *inaccuracy*), indicating the deviation of the clock frequency from the target frequency (SI definition), and *stability* (or *instability*) representing the dispersion of the clock frequency in time [17]. However, for a meaningful comparison between different clock types, it is more appropriate to introduce these quantities relative to the frequency at which they are evaluated: *relative accuracy* and *relative stability*. Following the definition of the SI second, the evaluation of the accuracy of an atomic clock is particularly useful for Cs beam or fountain clocks. The frequency instability of an atomic clock can be characterized in comparison to a frequency reference (i.e., another oscillator with a known and better stability). The clock frequency instability is characterized using the Allan deviation in three timescale regions: short term (rapid fluctuations over seconds), medium term (fluctuations over minutes to hours), and long term (slow fluctuations over up to one day) (cf. section 1.6).

Today, primary and secondary atomic clocks are at the heart of numerous applications that require a high-precision timekeeping solution [18], such as synchronization in telecommunication networks, power grids, and transportation; time-stamping in big data and financial services; satellite-based navigation systems; undersea exploration; industrial metrology; and fundamental research. The best-suited clock therefore varies depending on the requirements of the specific application. In addition to their metrological properties, atomic clocks are often categorized by their SWaP: size,

³In active frequency standards, the radiation emitted by excited atoms is detected.

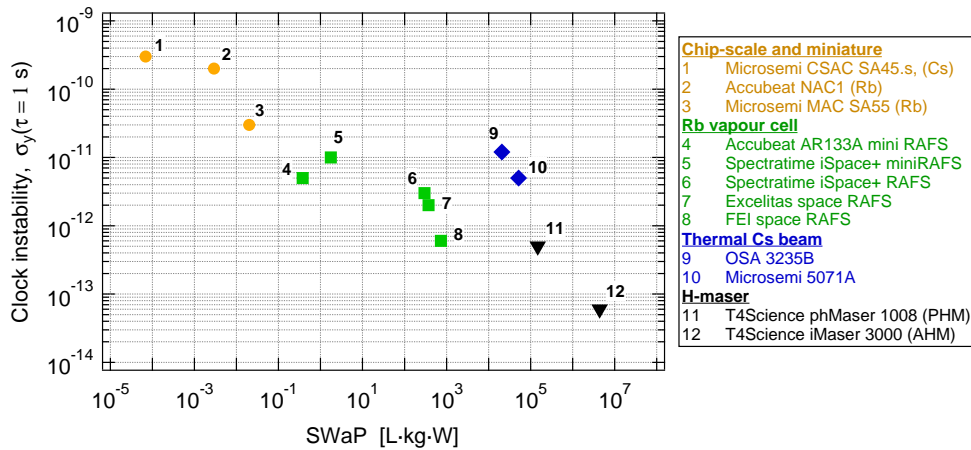


Figure I2 – Clock frequency instability as a function of SWaP. Data are extracted from: 1: [29]. 2: [30]. 3: [31]. 4: [32]. 5: [33]. 6: [34]. 7: [35]. 8: [36]. 9: [37]. 10: [38]. 11: [39]. 12: [40].

weight, and power consumption. Figure I2⁴ illustrates the short-term clock frequency instability of various industrial clocks as a function of their SWaP, which is expressed in this thesis by the single number of the product of the three parameters in L·kg·W. Clock performance and the SWaP are usually subject to a trade-off concerning the intended application, as depicted in Figure I2. Chip-scale and miniature clocks (e.g. [19]) (SWaP < 0.1) are the smallest atomic clocks, well suited for applications that do not require a high-stability performance, but easily transportable and low-power-consuming timing references. Meanwhile, thermal Cs beam clocks (e.g. [20]) have relatively large SWaP and moderate stability; nevertheless, they can deliver accuracy and are primarily used in synchronization applications. Active or passive hydrogen (H) masers (e.g. [21]) demonstrate the best short-term stability performance among frequency standards, but their SWaPs remain large, which makes them poorly suited for various applications. Furthermore, Rb vapor-cell clocks (e.g. [22]) exhibit a medium-range SWaP (between 0.1 and 10⁴) and good stability performance. These clocks combining compact size and low power consumption with good stability performance play a crucial role in Global Navigation Satellite Systems (GNSS) [23], synchronization in telecommunications [24] and power grids [25]. GNSS applications in particular require not only a good short-term stability (few 10⁻¹³ at 1 s) but also an excellent long-term stability at the level of 10⁻¹⁴ (≈ 1 ns) over one day [26] and widely exploit the Rb vapor-cell clocks as on-board secondary frequency standards [22, 27, 28].

I.1. Compact vapor-cell clocks

Compact atomic clocks are based on alkali atoms (e.g. Cs, Rb) confined in a cm-scale glass cell and exploit various approaches to interrogate the atoms, such as double-resonance (DR) spectroscopy or coherent-population trapping (CPT) in continuous-wave (CW) or pulsed operational modes. In Rb vapor-cell clocks based on double-resonance spectroscopy two EM fields are applied to interrogate the ground state hyperfine transition at a frequency of 6'834'682'610.904309 (8) Hz [41]). One

⁴In Figure I2 only commercially-available industrial clocks are presented while in terms of long-term stability the fountain clocks exhibit the best performance, which are currently maintained in metrology laboratories.

of the fields in the optical region optically pumps [42] the atoms to one of the ground states, and the other field drives the ground-state hyperfine transition in the microwave range. The optical field also usually serves to detect the atomic population as a result of the microwave interrogation. Either a discharge lamp or a laser light is used as the optical source, and the microwave field is applied using a resonator cavity. Compared to lamp-pumped Rb clocks, the use of the laser diodes for optical pumping and detection improves the signal-to-noise ratio (SNR) of the detection signal [43]. Nevertheless, most industrial Rb vapor-cell clocks with high-stability performance currently make use of a Rb discharge lamp. Lamp-pumped Rb clocks exhibit a short-term instability at the level of few 10^{-12} and long-term instability at the level of 10^{-14} .

Most laboratory Rb clocks exploit the laser diodes for optical pumping and detection [44–46]. The short-term frequency stability of these clocks $< 5 \cdot 10^{-13}$ is primarily limited by the SNR of the detection signal, toward which the laser noise, in both intensity and frequency, is the most important contribution. On long-term timescales, the fluctuations of the experimental or environmental parameters perturb the clock frequency stability via various physical effects [47]. DR Rb vapor-cell clocks can be operated using two different schemes: in the continuous-wave DR (CW-DR) scheme, the optical and microwave fields are applied simultaneously [45]; meanwhile, in the pulsed optically pumped (POP-DR) scheme, the optical and microwave interactions are separated in time [44, 48]. The POP-DR scheme consists in applying the Ramsey interrogation scheme [7] to the atoms confined in a buffer-gas cell [49]. In this case, first an intense light pulse optically pumps the atoms. A Ramsey interrogation scheme is then realized, in the absence of light, by two microwave pulses that are separated in time by an interval during which both radiations are off. Finally, a weak light pulse is used to probe the atoms and detect the atomic transition frequency. The absence of light during the microwave interrogation of the POP-DR scheme reduces the perturbations on the atomic energy levels during this period that are caused by the light due to the AC Stark shift, often called light shift. The detected atomic transition frequency is in this case less sensitive to variations of the light intensity and frequency in time through the light-shift effect by one order of magnitude [50] with respect to the CW-DR scheme. Thus, the impact of the light-shift effect on the long-term clock stability, which is one of the principal instability sources in the CW-DR scheme [16], can be decreased by one order of magnitude in the POP-DR scheme.

The alternative approach for enabling compact vapor-cell clock development exploits the coherent population trapping phenomenon [54]. In this case, two optical fields, whose frequency difference coincides with the atomic transition frequency, are used to interrogate the atoms. The state-of-the-art frequency stability reported for CPT clocks approaches the best DR clock performances in the short term [53, 55]. A medium-term clock stability reaching the 10^{-14} -level has recently been demonstrated [55], which shows the potential of such clocks for high performance on long timescales. The state-of-the-art frequency stability performance reported for compact vapor-cell clock types is depicted in Figure I3 in terms of Allan deviation [56]. Two additional clock types are also included in this plot to better situate the performance of compact and laser-pumped vapor-cell clocks in the broader picture of high-performance frequency standards. One of these two clock types is the active and passive H-maser [39, 40], which is primarily used as a frequency reference in industrial and fundamental metrology applications. The other clock type is the industrial Cs primary clock, [37, 38] which is widely employed in synchronization applications.

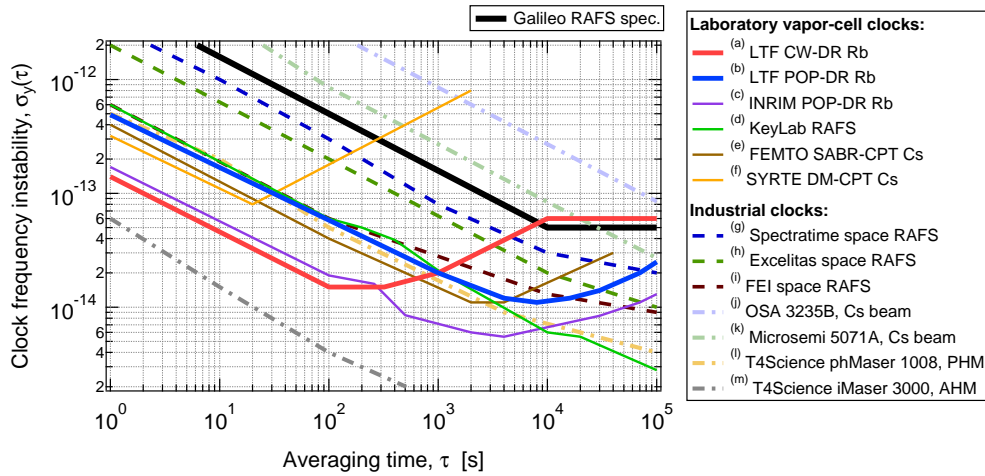


Figure I3 – State-of-the-art frequency instability of laboratory and industrial clocks. Galileo RAFS specification is extracted from [26]. Laboratory clock data are extracted from: (a) [45], (b) [51], (c) [44], (d) [28], (e) [52], (f) [53]. Industrial clock data are extracted from: (g) [34], (h) [35], (i) [36], (j) [37], (k) [38], (l) [39], (m) [40].

This thesis builds upon previous work on compact Rb vapor-cell clocks at the Laboratoire Temps-Fréquence (LTF). The Rb vapor-cell clock was developed based on a magnetron-type cavity [57] and a compact, frequency-stabilized laser head that serves as an optical source [58]. The laser head is based on a laser diode emitting at 780 nm, which corresponds to the Rb optical transition used for optical pumping and detection. Using the CW-DR approach, a short-term frequency instability of $1.4 \cdot 10^{-13} \cdot \tau^{-1/2}$ results, which is limited by the laser noise contribution [45]. The long-term instability at the level of 10^{-13} is largely limited by the light shift effects and the temperature sensitivity of the cell stem, as well as the barometric effect. The stability limit of the light shift effect is reduced by one order of magnitude through adopting the POP-DR approach, and the sensitivity of the cell stem is reduced through using a cell with a smaller stem [50]. In this way, the long-term clock stability is improved to $< 5 \cdot 10^{-14}$. The dominant contributions to clock instability of the microwave power fluctuations [59] and the barometric effect [60] are studied and optimized leading to a preliminary long-term clock stability $< 2.5 \cdot 10^{-14}$ at 10^4 s [51]. Finally, the preliminary medium-to-long-term clock instability budget identified the dominant contributions: the second-order Zeeman effect and the cell and stem temperature sensitivity. In this work, we study and optimize these effects and establish the long-term clock instability budget at 1 day through the evaluation of all the relevant contributions.

I.2. Thesis outline

In this work, we first study the impact of the dominant instability contributions and consolidate the long-term clock instability budget of the POP-DR clock (cf. chapter 3). Secondly, in order to improve the short-term clock stability, a laser system is built based on a low-noise laser diode emitting at 1560 nm, which is frequency doubled and stabilized using a Rb vapor cell cf. chapter 4). This laser system is then evaluated in a CW-DR clock cf. chapter 5). The remainder of this manuscript is structured as follows.

Chapter 1

This chapter outlines the basics of double-resonance vapor-cell clocks based on laser optical pumping. Firstly, the double-resonance principle is described in two cases: continuous wave and pulsed-optically pumped schemes, as used in chapters 5 and 3, respectively. Secondly, the clock frequency perturbation sources are reviewed. Finally, the chapter addresses clock frequency instability characterization tools and instability sources.

Chapter 2

This chapter presents the key components of the experimental setups employed in this thesis: different laser systems (based on 780 and 1560-nm laser diodes); the clock setups including an optical source; the physics package; and the local oscillator. In addition, the chapter describes the frequency stability measurement systems.

Chapter 3

This chapter presents the metrological evaluation of the long-term frequency instability of our POP Rb vapor-cell clock based on a 780-nm laser diode and magnetron-type cavity. We analyze various physical effects that perturb the clock frequency stability and are characterized by the clock sensitivity coefficients. Furthermore, it examines the stability limitations arising from the fluctuations of experimental (e.g. applied field strengths, cell and stem temperatures) and environmental (e.g. atmospheric pressure and humidity) parameters impacting the clock frequency. Finally, the chapter presents the complete long-term clock instability budget along with the measurement.

Chapter 4

This chapter reports on Rb-stabilized telecom (1560 nm) lasers' spectral characterization in view of their implementation in high-performance atomic clocks. We evaluate the spectral properties and their fluctuations on short and long timescales in order to estimate their impact on the clock performance. The application of such frequency-doubled and Rb-stabilized laser systems in other potential high-precision applications is also discussed.

Chapter 5

In this chapter, we demonstrate the realization of the Rb vapor-cell clock operated in the CW-DR scheme using frequency-doubled telecom lasers (1560 nm). We analyze the short-term clock instability budget in comparison to the use of a laser diode emitting directly at 780 nm for optical pumping and detection. Furthermore, the long-term clock stability limits due to the light-shift effects are analyzed.

1 Basic principles of DR vapor-cell clocks based on laser optical pumping

Atomic clocks are based on alkali atoms for their hydrogen-like structure with one unpaired electron in the outermost shell and for their ground-state hyperfine splitting frequency in the microwave region. Vapor-cell clocks based on double-resonance spectroscopy involve two EM radiations interacting with the atomic vapor on different energy levels. Figure 1.1 depicts the schematic of the basic operation principle for double-resonance vapor-cell clocks in CW and pulsed-optical pumping schemes. The atoms are confined in a cylindrical glass cell filled with buffer gases. The optical field coupling of one of the hyperfine ground states to the excited state is obtained from a laser diode, and the second field (6.835 GHz) coupling the two hyperfine ground states in the microwave region is contained in a resonator cavity. In the CW operation scheme, the atoms are irradiated with both fields simultaneously, while in the POP scheme, the two radiations are separated in time. The laser light tuned to the optical transition frequency from one of the hyperfine ground states is used to optically pump the other ground state via the excited state. It also serves to probe the atoms that have undergone the microwave interrogation. The resonator cavity is fed by the microwave field produced by the LO at a frequency near the hyperfine splitting frequency, and it confines the microwave field across the cell volume. External parameters acting on the atoms that perturb the energy levels lead to shifts in the ground-state hyperfine transition frequency with respect to the unperturbed case. The fluctuations of the external parameters are transferred to clock frequency fluctuations via various effects. The thorough control of an atomic frequency standard requires comprehensive knowledge of the experimental parameters, their fluctuations, and their relation with the atomic transition frequency leading to clock inaccuracy and instability contributions.

This chapter reviews the physics of the DR vapor-cell clocks that use a LD for optical pumping and detection and a resonator cavity for microwave interrogation. The following sections first present the Rb atomic structure, secondly consider the optical absorption schemes. Then, the principle of the DR (optical-microwave) interaction, treated in the semi-classical picture using density matrix formalism, is presented, followed by an overview of the relaxation processes leading to line broadening and the perturbations yielding a shift in the atomic transition frequency. Finally, the clock instability sources in the short and medium-to-long terms are introduced.

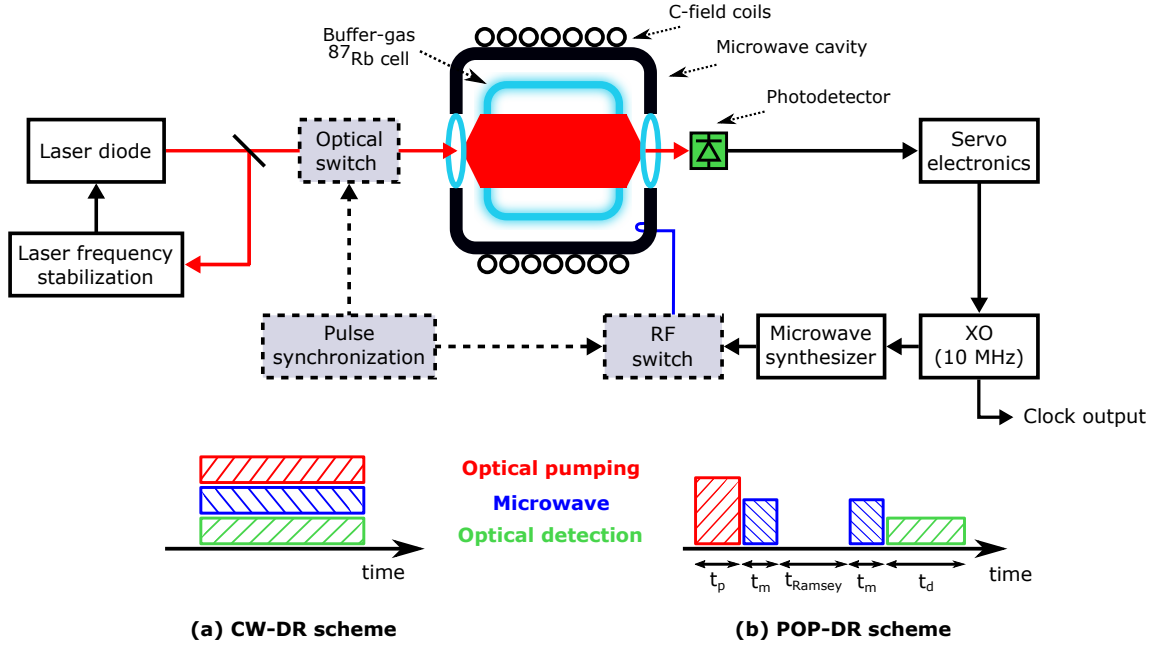


Figure 1.1 – Schematics of a vapor-cell atomic clock based on the DR interrogation principle. In the CW-DR case, the optical and microwave switches are not used and both radiations apply simultaneously. In the POP-DR case, the switches serve to apply the optical and microwave radiations following the pulsed sequence.

1.1 Rb atomic structure

Due to their single unpaired electron present in the outermost shell, alkali atoms are of great interest in many atomic physics experiments and applications. The nucleus and the filled shells may be treated together, forming a positive charge, and the valence electron of the atom at rest is in an S-state with no orbital angular momentum ($L = 0$). Only its spin angular momentum, $\mathbf{S} = 1/2$ in the case of an electron, contributes to the total electronic angular momentum $\mathbf{J} = \mathbf{L} + \mathbf{S}$. The coupling between the electron's spin and orbital angular momenta, described by the Hamiltonian $\hat{H}_{fs} = \alpha_0 \mathbf{L} \cdot \mathbf{S}$, partly lifts the degeneracy of the energy levels, which gives rise to the fine structure. The spin-orbit coupling does not affect an S-state (i.e., $L = 0$), but the levels for $L \neq 0$. In the case of $L = 1$, the level is split into two levels with total electronic angular momenta of $J = 1/2$ and $J = 3/2$. In the fine structure, the energy levels are represented in the form of $|n^{2S+1}L_J\rangle$, where n is the principal quantum number and the value for L is usually replaced by a letter such as $L = 0 \leftrightarrow S$, $L = 1 \leftrightarrow P$, $L = 2 \leftrightarrow D$, ... For ^{87}Rb , the ground state in which the single electron is under unperturbed conditions is notated as $|5^2S_{1/2}\rangle$. The optical transition between this ground state and the excited state $|5^2P_{1/2}\rangle$ is referred to as D₁ line and the optical transition between $|5^2S_{1/2}\rangle$ and $|5^2P_{3/2}\rangle$ is referred to as D₂ line. Furthermore, the interaction between the nucleus' spin, $I = 3/2$ in the case of ^{87}Rb , and the total electronic angular momentum, given by the Hamiltonian $\hat{H}_{hfs} = \beta_0 \mathbf{I} \cdot \mathbf{J}$, induces the hyperfine splitting of the atomic structure. The total angular momentum is given by $\mathbf{F} = \mathbf{I} + \mathbf{J}$. In the hyperfine structure, the energy levels are represented by $|n^{2S+1}L_J, F\rangle$, with F in the interval of $|J - I| < F < J + I$. The atomic structure of the ^{87}Rb under the above-described effects is illustrated in Figure 1.2 in the absence of an external field and in the case of an applied weak static magnetic field, as discussed in the following. For the weak magnetic field considered and due to

collisional broadening by the buffer gas, the excited state Zeeman sublevels are not resolved by laser spectroscopy, thus the excited state hyperfine levels are treated as degenerate.

If a static directional magnetic field is applied to the atoms, the hyperfine structure splits into the Zeeman sublevels under the magnetic field interaction. The energy levels of the Zeeman sublevels of the ^{87}Rb hyperfine ground states $|5^2S_{1/2}, F=1, m_F\rangle$ and $|5^2S_{1/2}, F=2, m_F\rangle$ are given by the Breit-Rabi formula [61]

$$E(F, m_F) = -\frac{E_{hfs}}{8} - g_I \mu_B B_z m_F \pm \frac{E_{hfs}}{2} (1 + m_F x + x^2)^{1/2}, \quad (1.1)$$

where

$$x = \frac{(g_I + g_J)\mu_B B_z}{E_{hfs}}, \quad (1.2)$$

and E_{hfs} is the unperturbed ground-state hyperfine splitting energy difference, g_I is the nucleus' Landé-g factor, μ_B is the Bohr magneton, $B_z = |\mathbf{B}|$ is the applied magnetic field, and the magnetic quantum number is $-F < m_F < F$. Under weak magnetic fields, the ^{87}Rb ground-state hyperfine splitting frequency can be approximated with

$$\begin{aligned} \nu_{hfs} &= \frac{E(F=2, m_F) - E(F=1, m_F)}{h} \\ &= \nu_{hfs} + (m_F^{F=1} + m_F^{F=2}) \frac{g_J \mu_B}{4h} B_z + \frac{(g_J \mu_B)^2}{2h E_{hfs}} B_z^2, \end{aligned} \quad (1.3)$$

where the coefficient linear in B_z is given by $(m_F^{F=1} + m_F^{F=2}) \frac{g_J \mu_B}{4h} = (m_F^{F=1} + m_F^{F=2}) 7 \cdot 10^3 \text{ MHz/T}$ and depends on the magnetic quantum numbers of the Zeeman sublevels involved in the transition, and the quadratic coefficient is given by $\frac{(g_J \mu_B)^2}{2h E_{hfs}} = 575.14 \cdot 10^2 \text{ MHz/T}^2$. The linear coefficient in equation (1.3) vanishes in the case of $m_F^{F=1} = m_F^{F=2} = 0$ and the transition frequency between these two levels remains sensitive to the magnetic field in the second order only. Rb vapor-cell clocks benefit from the first-order magnetic insensitivity of the transition frequency between the $m_F = 0$ Zeeman sublevels of the hyperfine ground state. The transition $|5^2S_{1/2}, F=1, m_F=0\rangle \rightarrow |5^2S_{1/2}, F=2, m_F=0\rangle$ is commonly called the *clock transition*, and its resonance frequency is the ground-state hyperfine splitting frequency $\nu_{Rb} = 6'834'682'610.904\ 309\ (8) \text{ Hz}$ [41].

1.1.1 Three-level model

The three-level approximation is based on reducing the Rb atomic structure to the two ground states $|F=1, m_F=0\rangle$ and $|F=2, m_F=0\rangle$ of the clock transition and one excited state. In buffer-gas cells, the hyperfine levels of the excited state are broadened due to collisions and overlap, which justifies the three-level model considering only one excited state. This model, given the appropriate assumptions, is often sufficient to qualitatively describe the processes in the clock operation. However, it may be insufficient to perform quantitative comparisons with the experimental results, in which case a multi-level approach – such as that presented in [62] – should be considered. In

Chapter 1. Basic principles of DR vapor-cell clocks based on laser optical pumping

the three-level system illustrated in Figure 1.3, the three states are represented by $|1\rangle$, $|2\rangle$, and $|3\rangle$, whose energy levels are associated with angular frequencies ω_i for $i = 1, 2, 3$. Γ^* is the excited state decay rate, while γ_1 and γ_2 are the ground-state population and coherence relaxation rates. Given that an optical field is applied from a laser with angular frequency ω_L tuned near the $|2\rangle \rightarrow |3\rangle$ transition frequency, the laser detuning is given by $\Omega_{L2} = \omega_L - (\omega_3 - \omega_2) = \omega_L - \omega_{32}$. For an applied microwave field with angular frequency ω_M , the microwave detuning from the ground-state hyperfine splitting frequency ($\omega_{21} = 2\pi \nu_{Rb}$) is given by $\Omega_M = \omega_M - (\omega_2 - \omega_1) = \omega_M - \omega_{21}$.

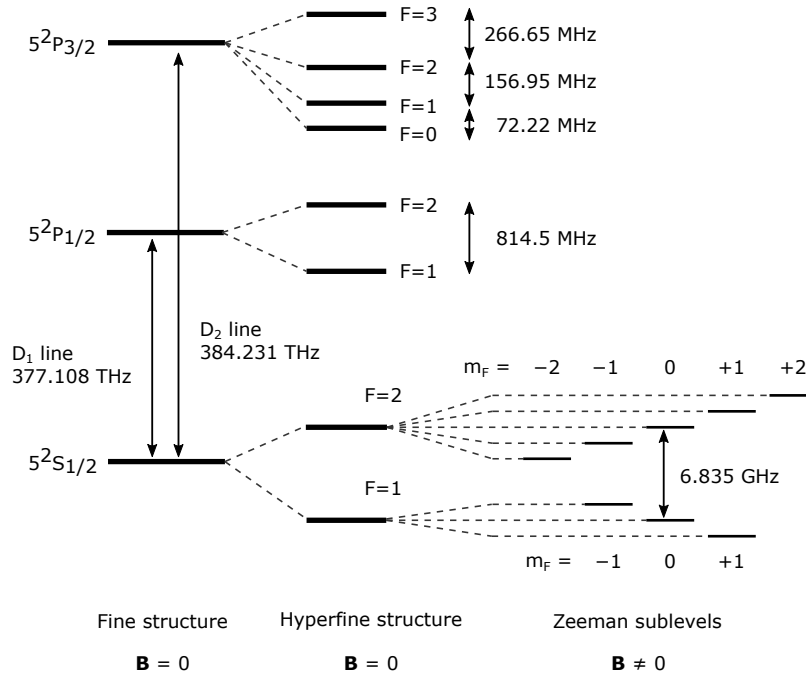


Figure 1.2 – Energy levels of the D_1 and D_2 lines in ^{87}Rb . Fine and hyperfine structures are presented under unperturbed conditions and the splitting of the hyperfine ground states under a weak static magnetic field, B , is shown where the clock transition is identified between $|F = 1, m_F = 0\rangle$ and $|F = 2, m_F = 0\rangle$ Zeeman levels.

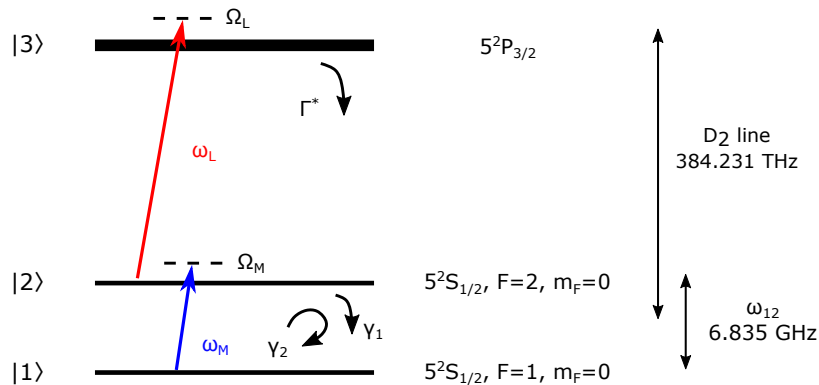


Figure 1.3 – Three-level model approximation including the hyperfine ground states and one excited state. The laser frequency tuned near the resonance $|2\rangle \rightarrow |3\rangle$. The microwave field at frequency ω_M drives the clock transition of the hyperfine ground state. Ω_L and Ω_M are the laser and microwave frequency detunings. Γ^* , γ_1 , γ_2 are the excited state and the ground-state population and coherence relaxation rates, respectively.

1.2 Optical absorption in vapor cells

Laser spectroscopy is a powerful method to detect the resonance frequency(ies) of a medium in order to assess its composition or to benefit from it as a frequency reference, as in the case of a frequency standard. In a simple scheme, the laser light propagating through an atomic medium and whose frequency ω_L is tuned across the optical transition frequency is absorbed near the resonance. The transmitted intensity $I(z)$ of the light propagating along the z-axis through this absorptive medium (e.g. the Rb vapor cell) follows the Beer-Lambert law

$$I(z) = I_0 e^{-\alpha(\omega_L) z} = I_0 e^{-\sigma(\omega_L) \Delta N z}, \quad (1.4)$$

where $\alpha(\omega_L)$ is the absorption coefficient, $\sigma(\omega_L)$ is the absorption cross section and ΔN is the population density difference between the two levels in resonance with the laser light. The absorption cross section is given by

$$\sigma(\omega_L) = \sigma_0 \frac{1}{1 + \frac{4(\omega_L - \omega_0)^2}{\Gamma_N}}, \quad (1.5)$$

where $(\omega_L - \omega_0)$ is the laser angular frequency detuning from the resonant transition frequency ω_0 and σ_0 is the peak absorption cross section (i.e., at zero detuning) given by $\sigma_0 = \sigma(\omega_L = \omega_0) = \frac{\lambda_0^2}{2\pi}$ where $\lambda_0 = \frac{2\pi c}{\omega_0}$ is the resonant transition wavelength. The absorption profile described by $\sigma(\omega_L)$ exhibits a Lorentzian line shape with a full width at half maximum (FWHM) of $\Gamma_N = 1/\tau_N$, which corresponds to the natural linewidth associated to the limited lifetime (τ_N) of the excited state. In the case of the ^{87}Rb D_2 line, the natural linewidth is $\Gamma_N/(2\pi) = 5.9$ MHz [63].

1.2.1 Doppler broadening

The atomic vapor typically is at a temperature around 60°C and the atoms exhibit a Maxwellian velocity distribution. The atoms with a velocity component $\pm v_z$ parallel (or antiparallel) to the light propagation (along the z-axis) observe the laser frequency shifted by $\mp \frac{\omega_L v_z}{c}$ due to the Doppler effect. Only the atoms in the velocity class that do not have a component along the light propagation direction will absorb the light at a frequency resonant with the atomic transition angular frequency (ω_0). In the laboratory reference, if the atoms in a velocity class are moving parallel to the light propagation ($+v_z$), they will be in resonance at a blue-shifted frequency with respect to ω_0 , and if moving in the antiparallel direction ($-v_z$), they will be in resonance at a red-shifted frequency; the Doppler shift is given by $\Delta\omega_D = \pm\omega_0 \frac{v_z}{c}$ for c speed of light. For the atomic vapor in the cell, the atoms of mass M at temperature T have a Maxwellian velocity distribution with the most probable velocity $v = \sqrt{2 k_B T/M}$, where k_B is the Boltzmann constant. The spectral lineshape of the Doppler-broadened absorption through an atomic vapor of a laser light whose frequency is scanned across ω_0 is given by

$$g_D(\omega_L) = \frac{c}{v \omega_0 \sqrt{\pi}} \exp \left\{ -\frac{c^2}{v^2} \left(\frac{\omega_L - \omega_0}{\omega_0} \right)^2 \right\}, \quad (1.6)$$

which has the Gaussian form and the FWHM is $\Gamma_D = \omega_0 \sqrt{\frac{8 \ln 2 k_B T}{M c^2}}$. ^{87}Rb -filled reference cells are used in this work for laser frequency stabilization (cf. section 2.1) and are kept at a temperature of 40°C. The corresponding Doppler broadened linewidth of the optical absorption profile is $\Gamma_D/(2\pi) = 524$ MHz, which is two orders of magnitude larger than the natural linewidth of the D_2 line. In the case of buffer-gas cells used in clock prototypes at 62.16°C, the Doppler broadening is 542 MHz. The optical absorption signal detected through the reference Rb cells results from the intrinsic excited-state lifetime and the Doppler-broadened linewidth. In the case of buffer-gas cells used for clock interrogation, the optical absorption line is further broadened by the collisional broadening (cf. section 1.2.3). The Doppler-broadened absorption of different hyperfine excited states overlap with each other in the spectral region and may hide the optical frequency references within its form. To improve the resolution in order to detect narrow atomic transition absorption peaks close to the natural linewidth, various spectroscopic techniques can be applied. In this thesis, we apply the Doppler-free absorption spectroscopy and use optical transition frequencies to stabilize the frequency of a laser diode.

1.2.2 Doppler-free absorption spectroscopy

Doppler-free absorption spectroscopy is achieved in this thesis using two counter-propagating laser lights across the atomic vapor. The laser light is split into two parts and the parts travel the vapor cell in opposite directions, overlapping with each other across the atomic vapor [64]. The first part, which is used as the pump beam, has a higher light intensity than the second part, which is used as the probe beam and has a low intensity. The latter beam can be detected using a sensitive photodetector (PD).

Pump and probe beams interact with atoms in different velocity classes due to the Doppler effect. If atoms are in the velocity class for which the longitudinal velocity is zero ($v_z = 0$), both pump and probe beams interact with the same group of atoms. In a two-level system, the intense pump beam depopulates the ground state of the group of atoms. As a result, the probe beam absorption decreases, which manifests in the absorption profile of the probe beam in the form of dips, called *Lamb dip* [65]. Meanwhile, the atoms of other velocity classes can be in resonance with pump and probe beams. In this case, we consider a three-level system with two optical transitions with angular frequencies ω_i and ω_k that share a common ground state. The atoms in the velocity class $\pm v_z$ with respect to the pump beam ($\mp v_z$ for the probe beam), such that the shifted pump beam $\omega_i = \omega_L(1 \mp v_z/c)$ is resonant with one transition and the (reverse) shifted probe beam at $\omega_k = \omega_L(1 \pm v_z/c)$ is resonant with the other transition, absorb the pump and probe beams at the same laser frequency $\omega_L = (\omega_i + \omega_k)/2$. The resulting Doppler-free absorption line presents dips associated with the velocity class ($v_z = 0$) at the optical frequency references corresponding to the six direct optical transitions between the two hyperfine ground states and four excited states of the ^{87}Rb D_2 line (cf. Figure 1.2). The Doppler-free absorption line also presents dips associated with the velocity classes that absorb the laser frequency $\omega_L = (\omega_i + \omega_k)/2$, which are called the *cross-over dips* and are denoted by *CO* followed by the F quantum numbers of the transition states (cf. Figure 2.10).

1.2.3 Buffer-gas line broadening

The Rb clocks studied in this thesis are based on a Rb vapor cell that is additionally filled with buffer gases (cf. chapter 2). The buffer gases are used to decrease the mean free path of Rb atoms and reduce wall collisions. However, buffer-gas collisions increase the de-excitation rate of the excited state $\Gamma^* = \frac{1}{\tau_e}$, reducing the lifetime τ_e (few ns), which leads to a homogeneous broadening of the optical absorption profile. The Rb clocks studied in this thesis make use of a buffer-gas mixture of Ar ($\approx 60\%$) and N₂ ($\approx 40\%$). The buffer-gas pressure-dependent broadening [63] for the mixture in the cells has a sensitivity of 14.92 MHz/hPa. For a buffer-gas pressure of 32.54 hPa the linewidth of the homogeneous broadening is $\Gamma^*/(2\pi) = 485.5$ MHz ($\tau_e \approx 0.3$ ns). In addition to the excited state lifetime, the buffer-gas pressure in the cell also impacts the ground-state relaxation rates (γ_1 and γ_2 in Figure 1.3) [66] and is a dominant source of the hyperfine splitting frequency shift [61]. These phenomena are discussed in sections 1.4 and 1.5.2, respectively.

1.3 Double-resonance interaction in buffer-gas cells

Double-resonance spectroscopy comprises two EM fields interacting with Rb atoms at two frequency ranges: optical and microwave. The optical field can typically be applied to the atoms using a Rb discharge lamp or laser diode, while the microwave field is applied using a resonator cavity [16]. A static magnetic field (C-field) is also applied along the cell's symmetry axis to lift the degeneracy of the hyperfine ground states (cf. section 1.1) and to define the quantization axis. The scheme of a DR vapor-cell atomic clock based on a laser diode is illustrated in Figure 1.1. The energy levels involved in the DR interaction are based on the three-level model introduced in section 1.1.1.

The optical field creates a population inversion in the hyperfine ground states through optical pumping [42]; the interaction of the atoms with a light resonant with one of the hyperfine ground state transitions depopulates the latter state via the excited states and pumps the atoms in the other ground state. Laser diodes ensure an efficient population inversion thanks to their monochromatic emission that can be tuned near the resonance frequency of an optical transition ($\omega_L \approx \omega_3 - \omega_i$ for $i = 1, 2$, cf. Figure 1.3) with a linewidth (2 – 5 MHz) well below ⁸⁷Rb ground-state hyperfine splitting (6.835 GHz). The laser light in DR vapor-cell clock studies is linearly polarized and should present a uniform intensity distribution across the beam radius, which covers a large part of the cell volume. In this work, the laser frequency is tuned to ⁸⁷Rb D₂ line (384.231 THz or 780.24 nm).

The microwave field is used to interrogate the atoms by repopulating the hyperfine ground state that was previously depopulated by the optical pumping. The frequency of the microwave field coincides with the ground-state hyperfine splitting frequency (i.e., clock transition frequency). The laser light, which is resonant with the ground state repopulated by the microwave field, can be used to probe the ground-state population difference Δ . When the microwave and optical fields are applied simultaneously on an atomic vapor [67], the transmitted light intensity as a function of the microwave frequency presents a drop in the form of a Lorentzian around the microwave resonance frequency $\omega_M = \omega_2 - \omega_1$. The alternative approach is based on separating the two radiations in time [49]. Similarly to the Ramsey spectroscopy [7], which is applied on a traveling atomic beam, the pulsed-optically pumped DR (POP-DR) scheme applies the fields consecutively in time while the atomic vapor is confined in a glass cell [44]. Figures 1.4 and 1.5 depict the respective time sequence

using the three-level model for the CW-DR and POP-DR interrogation schemes.

The following sections outline the basic principles of the double-resonance interrogation in the cases of CW and POP schemes. The relaxation processes that lead to line broadening and the effects that perturb the hyperfine splitting frequency are subsequently presented.

1.3.1 Optical and microwave interactions

Double-resonance interrogation is treated in the semi-classical picture, whereby the interaction fields are represented in a classical plane wave form and the atomic ensemble is represented by the density matrix operator. The optical electric field propagating along the z-axis with polarization vector \mathbf{e}_λ and wave vector \mathbf{k} is written as

$$\mathbf{E}(r, t) = \mathbf{e}_\lambda E_0 \frac{1}{2} e^{i(\omega_L t - \mathbf{k} \cdot \mathbf{r})}, \quad (1.7)$$

characterized by its amplitude E_0 and angular frequency ω_L . The microwave magnetic field is similarly written as

$$\mathbf{B}(r, t) = B_0 \frac{1}{2} e^{i\omega_M t}, \quad (1.8)$$

with amplitude B_0 and angular frequency ω_M . Under dipole approximation, the Rabi frequencies associated with the optical and microwave interactions can be written, respectively, as

$$\Omega_{Ri} = \frac{E_0}{\hbar} d_{3i}, \quad (1.9)$$

$$b_R = \frac{B_0}{\hbar} \mu_{12}, \quad (1.10)$$

where d_{3i} for $i = 1, 2$ is the electric dipole density matrix elements of the optical transition between one of the ground states $|i\rangle$ and the excited state $|3\rangle$; and μ_{12} is the magnetic moment matrix element of the microwave transition in the ground-state hyperfine levels.

In the semi-classical approach, the interactions with applied fields are governed by the perturbation Hamiltonian \hat{H}_I . The total Hamiltonian of the interaction is given by $\hat{H} = \hat{H}_0 + \hat{H}_I$, where \hat{H}_0 is the unperturbed atom's Hamiltonian with the eigenstates $|i\rangle$ for $i = 1, 2, 3$, represented by the three-level model (cf. Figure 1.3). The time evolution of the density matrix, ρ , is described by the Liouville equation

$$\frac{\partial \hat{\rho}}{\partial t} + \hat{\Gamma}_{rel}(t) = -\frac{i}{\hbar} [\hat{H}, \hat{\rho}] + \hat{\Gamma}_{exc}(t), \quad (1.11)$$

where the relaxation and excitation processes not associated with the applied fields are denoted by $\hat{\Gamma}_{rel}$ and $\hat{\Gamma}_{exc}$, respectively.

1.3. Double-resonance interaction in buffer-gas cells

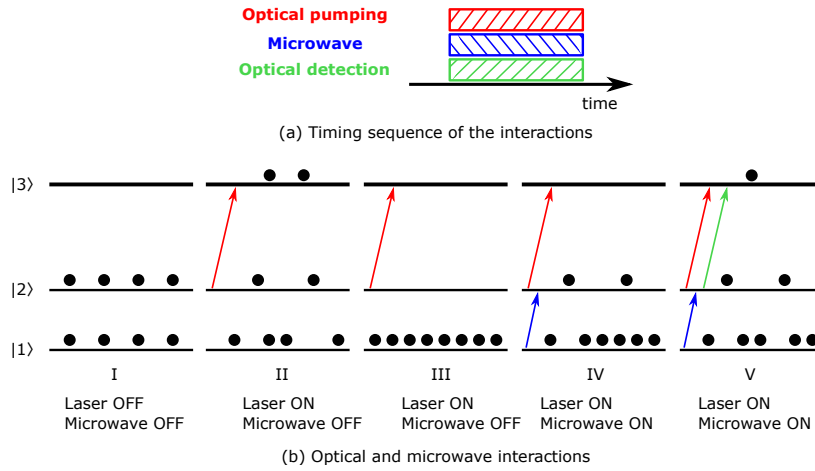


Figure 1.4 – CW-DR scheme: simultaneously applied fields in the time domain and interactions illustrated on the three-level model. (a) Sequence in time for the simultaneously applied optical and microwave fields. (b) CW-DR interactions in the three-level model: optical-pump frequency tuned to $|2\rangle \rightarrow |3\rangle$, microwave frequency tuned to $|1\rangle \rightarrow |2\rangle$. I: Laser is switched ON. Atoms in the resonant state absorb, atoms in the excited state decay in one of the ground states. II: Only laser is ON. A population inversion ($\Delta = \rho_{22} - \rho_{11}$) is created by optical pumping, the atomic vapor is transparent to laser light. III: Laser and microwave are ON. Resonant microwave field drives the atoms back to the state which is resonant with laser light. The detected light intensity as a function of the microwave field frequency reveals the population inversion demolished by the microwave interaction.

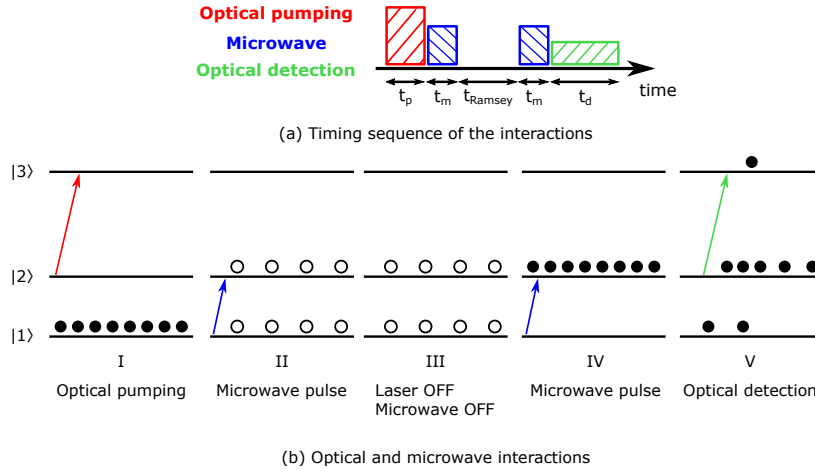


Figure 1.5 – POP-DR scheme: timing sequence and interactions illustrated on the three-level model. (a) Sequence in time for the successively applied optical and microwave fields. (b) POP-DR interactions in the three-level model: optical-pump frequency tuned to $|2\rangle \rightarrow |3\rangle$, microwave frequency tuned to $|1\rangle \rightarrow |2\rangle$. I: Laser is ON. A population inversion ($\Delta = \rho_{22} - \rho_{11}$) is created by the optical pumping, the atomic vapor is transparent to laser light at $t = t_p$. II: First microwave pulse is applied. Resonant microwave field drives the atoms to the coherent superposition state in the ground state at $t = t_p + t_m$ for t_m corresponding to the pulse area $\theta = \pi/2$. III: Both fields are OFF. Atoms evolve freely during t_R . IV: Second microwave pulse is applied. Resonant microwave field drives the atoms to state $|2\rangle$ at $t = t_p + t_m + t_R + t_m$. V: Laser is ON. The detected light intensity as a function of the microwave field frequency reveals the population inversion that have undergone the Ramsey interaction in time. The evolution in II, III, and IV are better explained by Bloch vector representations in section 1.3.3.1.

The density matrix elements ρ_{ij} for $i, j = 1, 2, 3$ represent the populations – by diagonal elements when $i = j$ – and the coherences – by off-diagonal elements when $i \neq j$ – of the states $|i\rangle$. The density matrix elements that describe the atomic response under the double-resonance interaction conditions are written as [61, 68]

$$\begin{aligned}
 \dot{\rho}_{11} + \frac{\gamma_1}{2} (\rho_{11} - \rho_{22}) &= b_R \operatorname{Im}(\delta_{12}) + \Omega_{R_1} \operatorname{Im}(\delta_{13}) + \frac{\Gamma^*}{2} \rho_{33}, \\
 \dot{\rho}_{22} + \frac{\gamma_1}{2} (\rho_{22} - \rho_{11}) &= -b_R \operatorname{Im}(\delta_{12}) + \Omega_{R_2} \operatorname{Im}(\delta_{23}) + \frac{\Gamma^*}{2} \rho_{33}, \\
 \dot{\rho}_{33} + \Gamma^* \rho_{33} &= -\Omega_{R_1} \operatorname{Im}(\delta_{13}) - \Omega_{R_2} \operatorname{Im}(\delta_{23}), \\
 \dot{\delta}_{12} + i(\Omega_M - i\gamma_2) \delta_{12} &= i \frac{b_R}{2} (\rho_{22} - \rho_{11}) + i \frac{\Omega_{R_1}}{2} \delta_{23} - i \frac{\Omega_{R_2}}{2} \delta_{13}, \\
 \dot{\delta}_{13} + i(\Omega_L + \frac{\Omega_M}{2} - i \frac{\Gamma^*}{2}) \delta_{13} &= i \frac{b_R}{2} \delta_{23} - i \frac{\Omega_{R_1}}{2} (\rho_{11} - \rho_{33}) - i \frac{\Omega_{R_2}}{2} \delta_{12}, \\
 \dot{\delta}_{23} + i(\Omega_L - \frac{\Omega_M}{2} - i \frac{\Gamma^*}{2}) \delta_{23} &= i \frac{b_R}{2} \delta_{13} - i \frac{\Omega_{R_1}}{2} \delta_{12}^* - i \frac{\Omega_{R_2}}{2} (\rho_{22} - \rho_{33}).
 \end{aligned} \tag{1.12}$$

For a laser frequency tuned to the $|2\rangle \rightarrow |3\rangle$ transition and a microwave frequency to $|1\rangle \rightarrow |2\rangle$ (cf. Figure 1.3), the solutions for the coherences (off-diagonal matrix elements) are assumed in the form

$$\begin{aligned}
 \rho_{12} &= \delta_{12} e^{i\omega_M t}, \\
 \rho_{13} &= \delta_{13} e^{i(\omega_L + \omega_M) t}, \\
 \rho_{23} &= \delta_{23} e^{i\omega_L t}.
 \end{aligned} \tag{1.13}$$

The set of equations describing the state populations and coherences of the atomic ensemble is solved under several assumptions. The reduced excited-state lifetime as a result of the buffer-gas collisions yields $\Gamma^* \gg \gamma_1, \gamma_2$. Weak optical and microwave fields are applied to the atomic vapor such that $\Omega_{R_i} \ll \Gamma^*$ and $b_R \ll \Gamma^*$ with small microwave frequency detuning $\Omega_M \ll \Gamma^*$. For a reduced excited-state lifetime and a weak optical field, the population of the excited state is close to zero ($\rho_{33} \approx 0$), while the population distribution is considered to exist between the hyperfine ground states: $\rho_{11} + \rho_{22} \approx 1$. Under the adiabatic approximation, the optical coherences reach the stationary state much faster ($\frac{1}{\Gamma^*} \approx \text{ns}$) than the microwave coherence ($\frac{1}{\gamma_{1,2}} \approx \text{ms}$); thus, the optical coherences ($\dot{\delta}_{13}$ and $\dot{\delta}_{12}$) can be omitted. When the optical-pump frequency is tuned to the optical transition $|1\rangle \rightarrow |3\rangle$, the optical Rabi frequencies are $\Omega_{R_1} \neq 0$ and $\Omega_{R_2} = 0$. Conversely, when the laser is tuned to $|2\rangle \rightarrow |3\rangle$, then $\Omega_{R_1} = 0$ and $\Omega_{R_2} \neq 0$. The solutions for the ground-state population difference $\Delta = \rho_{22} - \rho_{11}$ and coherence δ_{12} are calculated under the aforementioned assumptions and the conditions given by the applied interrogation scheme (CW-DR or POP-DR). The resulting ground-state population difference Δ is detected in clock applications based on the optical detection. In the CW-DR scheme, both fields are applied at the same time: $\Omega_{R_i} > 0$ and $b_R > 0$. In contrast, for the POP-DR scheme, the interactions occur consecutively and each interaction can be evaluated separately with the initial condition given by the solution at the end of the previous interaction phase [69].

1.3.2 Continuous wave scheme

In the CW-DR interrogation approach (cf. Figure 1.4), the Rb atoms in the buffer-gas cell are submitted to both optical and microwave fields simultaneously. We consider here the optical-pump frequency tuned near the optical transition frequency ω_{23} , as illustrated by the model in Figure 1.3 ($\omega_L = \Omega_L - \omega_{23}$), which creates the population inversion $\Delta \approx -1$. The simultaneous microwave field at a frequency coinciding with the ground-state hyperfine splitting frequency ($\omega_M = \Omega_M - \omega_{21}$) repopulates the state $|2\rangle$. The evaluation of the matrix elements in the case of CW-DR interrogation is based on the model described by the equation (1.12) [61, 67]. Under the assumptions given for typical clock operation (cf. section 1.3.1) and when both fields are applied simultaneously, the ground-state coherence δ_{12} and population difference $\Delta = \rho_{22} - \rho_{11}$ are given by [67]

$$\delta_{12} = i \frac{b_R}{2} \frac{\gamma_2 + \Gamma_{p_2}}{(\gamma_2 + \Gamma_{p_2})^2 + (\omega_M - \Delta\omega_{LS} - \omega_{21})^2} \Delta + \frac{b_R}{2} \frac{\omega_M - \Delta\omega_{LS} - \omega_{21}}{(\gamma_2 + \Gamma_{p_2})^2 + (\omega_M - \Delta\omega_{LS} - \omega_{21})^2} \Delta, \quad (1.14)$$

$$\Delta = \frac{\Gamma_{p_2}}{(\gamma_2 + \Gamma_{p_2}) + \frac{b_R^2(\gamma_2 + \Gamma_{p_2})}{(\gamma_2 + \Gamma_{p_2})^2 + (\omega_M - \Delta\omega_{LS} - \omega_{21})^2}}, \quad (1.15)$$

where the optical pumping rate is given by $\Gamma_{p_2} = \frac{\Omega_{R_2}^2}{2\Gamma^*}$ for the optical-pump frequency tuned to transition $|2\rangle \rightarrow |3\rangle$ with $\Omega_L \approx 0$, and $\Delta\omega_{LS} = 2\pi\Delta\nu_{LS}$ represents the light-induced frequency shift contribution, where $\Delta\nu_{LS}$ is given by the equation (1.46).

1.3.2.1 CW-DR signal

The CW-DR signal yields from the transmitted light intensity through the cell according to the Beer-Lambert law (cf. equation (1.4)) and is a measure of the ground-state population difference (Δ) resulting from the CW-DR interaction. The light is absorbed by the atoms that have undergone the DR interaction and has a Lorentzian shape as a function of the microwave frequency detuning $\Omega_M = \omega_M - \omega_{21}$. The spectral lineshape of the CW-DR signal can be written as

$$G(\Omega_M) = g_t - g_0 \frac{S}{S+1} \frac{1}{1 + \frac{\Omega_M^2}{\gamma_2'^2 (S+1)}}, \quad (1.16)$$

where g_t is the transmitted light intensity in the absence of resonant microwave radiation (i.e., background level denoted by B^{CW}), g_0 is the light intensity at the beginning of the vapor cell, and the saturation factor is defined as $S = \frac{b_R^2}{\gamma_1' \gamma_2'}$ with $\gamma_i' = \gamma_i + \frac{\Gamma_{p_i}}{2}$ for $i = 1, 2$.

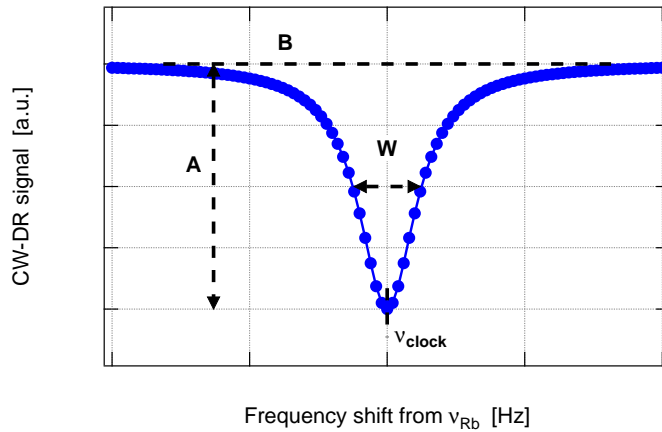


Figure 1.6 – CW-DR signal. The background signal level B corresponds to the case where microwave is OFF. The contrast C is given by the ratio of the signal amplitude A to the background level. The FWHM W is also measured on the DR signal which carries information on the ground-state relaxations.

The amplitude A^{CW} and the FWHM W^{CW} of the CW-DR signal can respectively be written as

$$A^{\text{CW}} = -g_0 \frac{S}{S+1}, \quad (1.17)$$

$$W^{\text{CW}} = \frac{\gamma'_2}{\pi} \sqrt{S+1}. \quad (1.18)$$

For weak optical ($\Omega_R \approx 0$) and microwave ($b_R \approx 0$) fields $S \approx 0$, the FWHM of the CW-DR signal can be approximated to $W^{\text{CW}} \approx \frac{\gamma'_2}{\pi}$, which represents the intrinsic limit of the CW-DR signal linewidth due to ground-state relaxation (cf. section 1.4). The contrast C^{CW} of the signal is defined (see Figure 1.6) as the ratio of the signal amplitude and the transmitted light intensity in the absence of resonant microwave radiation (i.e., background level B^{CW}), which is given by

$$C^{\text{CW}} = \frac{A^{\text{CW}}}{B^{\text{CW}}} = \left| \frac{G(b_R = 0, \Omega_M = 0) - G(b_R, \Omega_M = 0)}{G(b_R = 0, \Omega_M = 0)} \right|. \quad (1.19)$$

Finally, a figure-of-merit (FoM) is defined for the CW-DR signal, written as

$$\text{FoM}^{\text{CW}} = \frac{C^{\text{CW}}}{W^{\text{CW}}}. \quad (1.20)$$

The FoM is inversely proportional to the signal-to-noise ratio limit of the clock stability (cf. equation (1.56)) and is used to optimize the short-term clock stability through the CW-DR signal (cf. chapter 5). The CW-DR signal is optically detected by sweeping the frequency of the microwave field applied to the vapor cell. The strongest absorption occurs for zero microwave detuning with respect to the ground-state hyperfine splitting frequency of the Rb atoms in the vapor cell, i.e., $\Omega_M = \omega_M - \omega_{21} = 0$.

1.3.3 Pulsed-optically pumped scheme

The principal difference of the pulsed-optically pumped scheme from the CW-DR is the separation in time of the microwave interrogation from the optical pumping (cf. Figure 1.5). Therefore, density matrix elements (equation (1.12)) can be separately evaluated in each phase of the interrogation scheme considering the interacting fields during the phase. The initial conditions are given by the previous phase. In this case, the system reduces to a simple two-level model for analysis of the microwave interrogation. Given the low-quality factor of the microwave cavity used in our clock prototypes (cf. chapter 2), the feedback of the microwave cavity on the atoms can be neglected. We consider the optical-pump frequency tuned to the transition $|2\rangle \rightarrow |3\rangle$; thus, the atoms are optically pumped into the state $|1\rangle$.

Optical pumping

During the optical pumping phase, the microwave radiation is off and therefore the microwave Rabi frequency is set to zero $b_R = 0$. In this case, the evolution of the ground-state coherence and of the population difference are given by [69]

$$\dot{\delta}_{12} + (\gamma_2 + \Gamma_{p_2} + i(\Omega_M + \Gamma_{p_2} \Omega'_L)) \delta_{12} = 0, \quad (1.21)$$

$$\dot{\Delta} + (\gamma_1 + \Gamma_{p_2}) \Delta = \Gamma_{p_2}, \quad (1.22)$$

where $\Omega'_L = \frac{2\Omega_L}{\Gamma^*}$ is the normalized laser detuning and $\Gamma_{p_2} = \frac{\Omega_{R_2}^2}{2\Gamma^*}$ is the optical pumping rate.

During this phase, the laser light serves not only to create a population inversion, but also to eliminate the residual coherence that survives the previous interrogation cycle. To diminish the residual coherence before the microwave interrogation, a strong optical-pump pulse is required satisfying the condition $\Gamma_{p_2} t_p \gg 1$, where t_p is the pumping phase duration. In addition, a dead time between two successive cycles, to benefit from the relaxations induced by buffer-gas collisions, can be helpful to reduce the residual coherence before the new Ramsey cycle [70]. For the optical-pump frequency tuned to $|2\rangle \rightarrow |3\rangle$ (cf. Figure 1.3) and a complete population inversion at the end of the pumping phase, the ground-state population before the microwave interrogation is given by $\Delta(t_p) = -1/3$. (In the alternative case, if the optical-pump frequency is tuned to $|1\rangle \rightarrow |3\rangle$, the complete population inversion at the end of the pumping phase would be $\Delta(t_p) = 1/5$.)

Microwave interrogation

During the microwave pulses, the laser light is off; thus, the optical Rabi frequency is set to zero $\Omega_R = 0$, and the ground-state relaxation rates can be neglected with respect to the pulse duration: $t_m \ll \gamma_i^{-1}$ for $i = 1, 2$. The evolution of the ground-state coherence and of the population difference are given by [69]

$$\dot{\delta}_{12} + i\Omega_M \delta_{12} = -\frac{b_R}{2} \Delta, \quad (1.23)$$

$$\dot{\Delta} = 2b_R \text{Re}(\delta_{12}). \quad (1.24)$$

Ramsey time

During the Ramsey time, both radiations are off such that $b_R = 0$ and $\Omega_R = 0$, and the evolution of the ground-state coherence and of the population difference are given by [69]

$$\dot{\delta}_{12} + (\gamma_2 + i \Omega_M) \delta_{12} = 0, \quad (1.25)$$

$$\dot{\Delta} + \gamma_1 \Delta = 0. \quad (1.26)$$

1.3.3.1 Bloch vector representation

During the microwave interrogation (i.e., two microwave pulses separated by the *dark* Ramsey time), the atomic system can be approximated by a two-level model that takes into account only the two ground states $|1\rangle$ and $|2\rangle$. Bloch vector representation is useful to describe the ground-state coherence and population difference during the microwave interrogation phases. In this case, the Bloch vector is defined for

$$R(t) = \begin{bmatrix} \text{Re}(\delta_{12}(t)) \\ \text{Im}(\delta_{12}(t)) \\ \Delta(t) \end{bmatrix} \quad (1.27)$$

Therefore, the microwave interactions during the two pulses and the free evolution during the Ramsey time can be represented by the corresponding transformation matrices [69]. Starting from the Bloch vector, which describes the system at the beginning of the microwave interrogation, the final solutions for the ground-state coherence and population difference at the end of one cycle of POP-DR interaction (cf. Figure 1.5-b) can be calculated by the product of the matrices describing the processes during each phase [69]. In Figure 1.7 the evolution of the ground-state coherence and population is illustrated using the Bloch sphere, neglecting the relaxations that would only introduce damping, for microwave pulses of $\theta = \pi/2$ and $\theta = 0.56 \pi$ and for microwave detunings of $\Omega_M = 0$ and $\Omega_M = \frac{1}{2} \frac{2\pi}{2(t_R + \frac{4t_M}{\pi})}$, which correspond to the central frequency of the central fringe and the frequency at half maximum of the central fringe [51], respectively. The projection of the Bloch vector on the z-axis represents the ground-state population, and the projection on the xy-plane represents the ground-state coherence (cf. equation (1.27)).

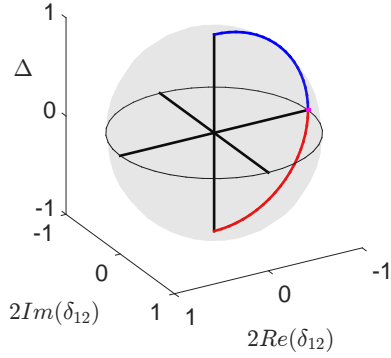
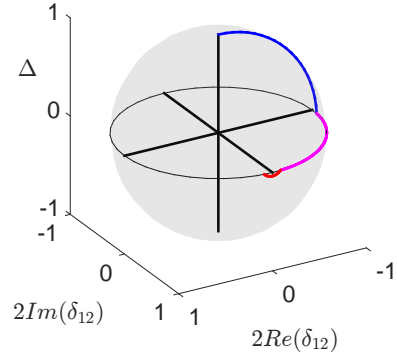
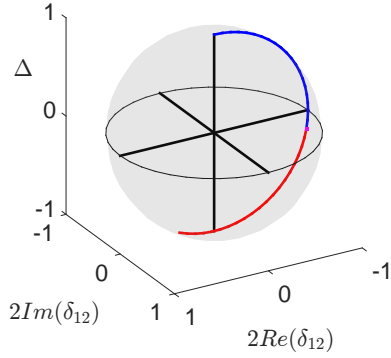
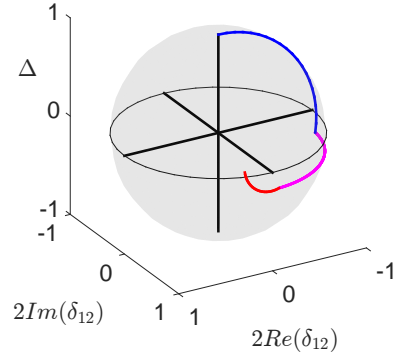

 (a) Zero microwave detuning and $\theta = \pi/2$.

 (b) At half-maximum detuning and $\theta = \pi/2$.

 (c) At zero microwave detuning and $\theta = 0.56 \pi$.

 (d) At half-maximum detuning and $\theta = 0.56 \pi$.

Figure 1.7 – Bloch spheres representing the pulsed microwave interaction with zero detuning (a and c) and a detuning corresponding to the half maximum of the central Ramsey fringe (b and d). Courtesy of W. Moreno for the code used to generate the plots.

1.3.3.2 Ramsey signal

The ground-state population difference at the end of the Ramsey interrogation is optically detected. The transmitted light intensity is related to the number of atoms in the ground-state resonant with the laser light via the Beer-Lambert law (cf. equation (1.4)). The optically detected Ramsey signal is described by a cosine shape and can be fitted with the expression [70]

$$f(\Omega_M) = a_0 + a_1 \cos(a_3 \Omega_M) + a_2 \cos(a_3 2\Omega_M), \quad (1.28)$$

where a_i for $i = 0, 1, 2$ are the i^{th} -order coefficients and $a_3 = t_R + \frac{4t_m}{\pi}$. The amplitude and the FWHM of the central fringe of the Ramsey signal expressed by the equation (1.28) are given by

$$A^{\text{POP}} = 2(a_1 + a_2), \quad (1.29)$$

$$W^{\text{POP}} = \frac{1}{2a_3}. \quad (1.30)$$

Similarly to the CW-DR case, the contrast and figure-of-merit for the central fringe are defined by the equations (1.19) and (1.20).

1.4 Ground-state life time and line broadening

Rb atoms confined in a glass cell with buffer gases suffer collisions with each other and buffer gases. The buffer-gas collisions decrease the mean free path of the Rb atoms, which reduces relaxation due to wall collisions and decreases the Doppler broadening with respect to the applied microwave field [71]. We use a buffer-gas mixture of nitrogen (N_2) and argon (Ar). N_2 quenches the fluorescence radiation of de-exciting Rb atoms, in which case the excitation energy of Rb atoms is transferred to N_2 molecules and converted into the kinetic energy [61]. The excited Rb atoms are transferred to ground states without emitting radiation, which would impact the effectiveness of the optical pumping process. The temperature coefficient of N_2 is compensated by Ar (cf. section 1.5.2). Rb collisions with buffer-gases and with the other Rb atoms and cell walls are sources of relaxation. The line broadening of the optical transitions (with the excited state de-excitation rate Γ^*) caused by buffer-gas collisions are reviewed in section 1.2.3. The buffer-gas collisions, through varying the hyperfine coupling, are also responsible for ground-state population and coherence relaxations [66]. Rb-Rb collisions result in a shift of energy levels (see section 1.5.4) and a broadening by causing ground-state coherence and population relaxations, via the spin-exchange effect [72]. For the buffer-gas cell used in our POP-DR clock, the measured ground-state coherence and population lifetimes are $\gamma_1^{-1} = 3.20 \pm 0.01$ ms and $\gamma_2^{-1} = 3.95 \pm 0.25$ ms [73].

1.5 Clock frequency perturbations

The clock transition frequency used to stabilize the frequency of an external oscillator (cf. Figure 1.1) corresponds to the ground-state hyperfine splitting frequency of the Rb atoms in the clock cell. In the case of a buffer-gas cell, the detected frequency at the end of the cell is an average of the hyperfine splitting frequencies of each atom along the light propagation [47]. Applied external fields and the experimental conditions perturb the atomic structure and induce a frequency shift ($\Delta\nu$) in the ground-state hyperfine splitting of the atoms in the clock cell from the unperturbed ^{87}Rb case (i.e., $\nu_{Rb} = 6'834'682'610.904\ 309$ (8) Hz) [41]. The perturbations on the atomic energy levels arise from the experimental parameters including optical and microwave interaction fields, the static magnetic field, the buffer-gas pressure, the temperature of the vapor cell, and the environmental parameters such as temperature, pressure, and humidity. On one hand, the systematic shifts induced by these experimental and environmental parameters via various physical processes accumulate and produce an average bias between the clock frequency and the unperturbed atomic transition frequency. On the other hand, the fluctuations of these experimental and environmental parameters over time result in fluctuating the frequency shifts through the same physical processes, which degrades the stability of the clock frequency over time.

Evaluation of the accuracy of a clock depends on knowledge of the magnitudes of the frequency shifts and their uncertainties and is crucial for primary frequency standards (i.e., Cs clocks) [8, 10, 74]. Meanwhile, in the case of secondary frequency standards (e.g., Rb vapor-cell clocks), the

fractional frequency fluctuations in time (instability) are the main interest for clock performance analysis. To evaluate the clock frequency instability, the individual contribution of each process is estimated, which is quantified by the clock sensitivity coefficient to the perturbing effect. The detailed analysis of the long-term frequency instability of our POP-DR clock is presented in chapter 3. This section reviews the physical processes that lead to a shift of hyperfine energy levels and thereby the clock frequency and defines the corresponding sensitivity coefficient for each effect, with an emphasis on the POP-DR scheme. The total clock frequency shift is subsequently estimated for the POP-DR clock operation conditions employed in this work.

1.5.1 Second-order Zeeman shift

The hyperfine splitting frequency used as the clock transition is sensitive to the static magnetic field amplitude in the second order via the Zeeman effect, as reflected in the equation (1.3). The frequency shift induced upon the hyperfine splitting by a weak static magnetic field ($B_z = |\mathbf{B}|$) aligned along the z-axis is given by

$$\Delta\nu_{Ze} = C_2 B_z^2 \text{ [Hz]}, \quad (1.31)$$

where $C_2 = 575.14 \cdot 10^8 \text{ Hz/T}^2$ is the quadratic coefficient and B_z is the field amplitude along the z-axis (quantization axis). The relative clock frequency sensitivity to the variations of B_z becomes

$$\frac{\partial\Delta\nu_{Ze} / \nu_{Rb}}{\partial B_z} = \frac{2 C_2 B_z}{\nu_{Rb}} \text{ [1/T]}. \quad (1.32)$$

The magnetic field ($10.7 \mu\text{T}$) [51, 75] applied in our POP-DR clock induces a clock frequency shift of $\Delta\nu_{Ze} = 6.6 \text{ Hz}$ and the linear sensitivity coefficient is estimated as $1.8 \cdot 10^{-4} / \text{T}$.

1.5.2 Buffer-gas density shift

The frequency shift induced by buffer-gas collisions upon the Rb ground-state hyperfine frequency depends on the buffer-gas mixture, pressure, and temperature [61, 76]

$$\Delta\nu_{BG} = P_{cell} (\beta' + \delta' \Delta T + \gamma' \Delta T^2) \text{ [Hz]}, \quad (1.33)$$

where P_{cell} is the buffer-gas pressure, $\Delta T = T_{cell} - T_0$ is the temperature difference between the vapor cell temperature T_{cell} , and T_0 is a reference temperature at which the coefficients β' , δ' , and γ' are given for a buffer-gas mixture. The coefficients for a buffer-gas mixture are obtained by the average of the individual buffer-gas coefficients weighted with respect to the partial pressure ratios. The Rb vapor cells used in this work are filled with N_2 and Ar as buffer gases with a partial pressure ratio of $r = \frac{P_{Ar}}{P_{N_2}} = 1.6$. The individual coefficients for N_2 and Ar and the resulting coefficients for the mixture are provided in Table 1.1. For vapor cells considered here, with a total buffer-gas pressure of 32.54 hPa and at the cell temperature of 62.16°C , the clock frequency shift due to buffer-gas collisions is $\Delta\nu_{BG} = 4247.4 \text{ Hz}$.

Table 1.1 – Buffer-gas shift coefficients for ^{87}Rb using Ar and N_2 gases at $T_0 = 60^\circ\text{C}$ [76].

	$\beta \left[\frac{\text{Hz}}{\text{hPa}} \right]$	$\delta \left[\frac{\text{Hz}}{\text{hPa}\cdot\text{K}} \right]$	$\gamma \left[\frac{\text{Hz}}{\text{hPa}\cdot\text{K}^2} \right]$
Nitrogen	410.97	0.39	$-9.75 \cdot 10^{-4}$
Argon	-44.78	-0.24	$-2.63 \cdot 10^{-4}$
	$\beta' \left[\frac{\text{Hz}}{\text{hPa}} \right]$	$\delta' \left[\frac{\text{Hz}}{\text{hPa}\cdot\text{K}} \right]$	$\gamma' \left[\frac{\text{Hz}}{\text{hPa}\cdot\text{K}^2} \right]$
$r = \frac{P_{\text{Ar}}}{P_{\text{N}_2}} = 1.6$	130.51	$2.3 \cdot 10^{-3}$	$-5.37 \cdot 10^{-4}$

A. Cell temperature coefficient

The relative clock frequency shift sensitivity to cell temperature is given by

$$\frac{\partial \Delta \nu_{BG} / \nu_{Rb}}{\partial T_{cell}} = \frac{P_{cell} (\delta' + 2 \gamma' \Delta T)}{\nu_{Rb}} \quad [/ \text{K}]. \quad (1.34)$$

The Rb vapor cells used in this work are filled with N_2 and Ar. The linear temperature (δ) coefficients with opposite signs of the two gases compensate each other. The clock frequency sensitivity to cell temperature variations can be strongly reduced for a cell temperature, called inversion temperature, at which the coefficient in equation (1.34) cancels. The inversion temperature is given by $T_{inv} = T_0 - \frac{\delta'}{2\gamma'}$. For the Rb clocks, the cell temperature coefficient within an interval of 0.5°C around the T_{inv} is estimated as $\pm 1.3 \cdot 10^{-12} / \text{K}$ at $T_{inv} = 62^\circ\text{C}$.

B. Stem temperature coefficient

The stem in the vapor cells used in our clock setups acts as a reservoir mainly for Rb atoms while kept at a lower temperature with respect to the cell temperature. The buffer-gas density in the vapor cell that contributes to the clock frequency shift changes by the variation of the stem temperature due to the temperature gradient variation between the cell and stem temperatures. This effect results in enhanced temperature sensitivity (ETS) of the vapor cell frequency to the cell temperature, as described in [77]. The relative clock frequency sensitivity coefficient to stem temperature fluctuations is described by

$$\frac{\partial \Delta \nu_{BG} / \nu_{Rb}}{\partial T_{stem}} = \frac{P_{cell} \beta' v_{stem}}{\nu_{Rb} T_{stem}} \quad [/ \text{K}], \quad (1.35)$$

where $v_{stem} = \frac{V_{stem}}{V_{stem} + V_{cell}}$ is the relative stem volume with respect to the total cell-stem volume and T_{stem} is the temperature of the stem around 59.22°C . In the case of our vapor cells, the stem temperature coefficient (TC) is $1.1 \cdot 10^{-12} / \text{K}$.

1.5.3 Barometric effect

Fluctuations of atmospheric pressure lead to fluctuations in the deformation of the cell windows, which translates to a change of the cell length and thereby of the cell volume. This change ultimately results in a variation of the buffer-gas density in the cell [60]. The sensitivity of the clock frequency shift in equation (1.33) to the variations of buffer-gas pressure $P_{cell} = n_{BG} k_B T_{cell}$ is expressed as

$$\frac{\partial \Delta \nu_{BG} / \nu_{Rb}}{\partial P_{cell}} = \frac{\beta' + \delta' \Delta T + \gamma' \Delta T^2}{\nu_{Rb}} \quad [/\text{hPa}]. \quad (1.36)$$

The relative clock frequency sensitivity coefficient to external pressure P_{ext} fluctuations is written as

$$\begin{aligned} \frac{\partial \Delta \nu_{BG} / \nu_{Rb}}{\partial P_{ext}} &= \frac{1}{\nu_{Rb}} \frac{\partial \Delta \nu_{BG}}{\partial P_{cell}} \frac{\partial P_{cell}}{\partial P_{ext}} \\ &= \frac{1}{\nu_{Rb}} \frac{\partial \Delta \nu_{BG}}{\partial P_{cell}} \frac{P_{cell}}{P_{ext}} \frac{\partial V_{cell} / V_{cell}}{\partial P_{ext}} \quad [/\text{hPa}]. \end{aligned} \quad (1.37)$$

The sensitivity coefficient calculated for the vapor cells used in this work is $(8.5 \pm 2.7)10^{-14} / \text{hPa}$ [60] and the coefficient experimentally measured near the atmospheric pressure (between 800 and 1000 hPa) is $(8.2 \pm 0.8)10^{-14} / \text{hPa}$ [51].

1.5.4 Spin-exchange shift

In addition to collisions with the buffer gases (cf. section 1.5.2), Rb atoms in the vapor cell collide also with each other. Rb-Rb collisions may result in an exchange of spins between the atoms, while conserving the total spin of the two-atom system [61]. The shift caused by the spin-exchange (SE) effect to the ground-state hyperfine splitting frequency is given by [72, 78]

$$\Delta \nu_{SE} = -\frac{1}{8\pi} n_{Rb}(T) \bar{v}(T) \lambda_{se} \langle \Delta \rangle \quad [\text{Hz}], \quad (1.38)$$

where $n_{Rb}(T)$ is the rubidium density given by the equation (1.43), $\lambda_{se} = 1.69 \cdot 10^{-19} \text{ m}^2$ is the spin-exchange cross-section [72], $\langle \Delta \rangle$ is the average population inversion between the two ground states of the clock transition ($\Delta = \rho_{22} - \rho_{11}$), and $\bar{v}(T)$ is the mean relative velocity of the two colliding atoms given by $\bar{v}(T) = \sqrt{\frac{8 k_B T}{\pi M}}$, where k_B is the Boltzmann constant and M the atomic mass.

In the POP-DR scheme, the spin-exchange shift primarily impacts the clock frequency during the Ramsey time, that is, via the average population difference during the Ramsey time. The time evolution of the population inversion during the Ramsey time is given by [69]

$$\Delta(t) = -e^{-\gamma_1 t} \tanh\left(\frac{k}{\gamma_1} (1 - e^{-\gamma_1 t}) - \tanh^{-1}(\cos\theta)\right), \quad (1.39)$$

where k is the microwave photon emission rate by an atom, which in turn is given by

$$k = \frac{\mu_0 \mu_B^2 \eta' Q_L n_{Rb}}{\hbar (2I + 1)} \quad [1/s], \quad (1.40)$$

where γ_1 is the ground-state population relaxation time, and θ is the microwave pulse area applied before the Ramsey time. At the beginning of the Ramsey time $t_R = 0$, the initial condition for (1.39) is given by $\Delta(t_R = 0) = \cos\theta$ [69, 72]. For a $\theta = \pi/2$ pulse, the initial population inversion is $\Delta(t_R = 0) = 0$ due to the coherent superposition created by the $\pi/2$ pulse. A microwave pulse larger than the conventional $\pi/2$ pulse yields a residual population difference at the beginning of the Ramsey time; for example, for $\theta = 0.56\pi$, we have $\Delta(t_R = 0) = -0.19$. The time evolution of $\Delta(t)$ during the Ramsey time is presented in Figure 1.8 for different microwave pulse areas, assuming a perfect optical pumping from $|2\rangle$ before the microwave pulse ($\Delta(t = -t_m) = -1$).

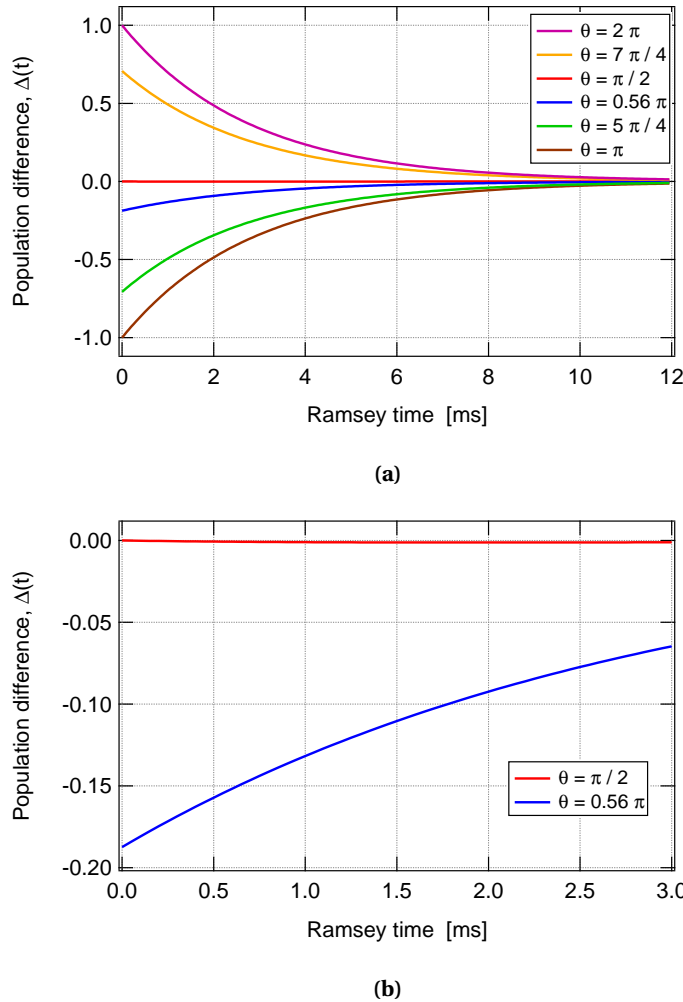


Figure 1.8 – Ground-state population inversion during Ramsey time; for various microwave pulse areas, $k = 1.8$, and $\gamma_1 = 340 \text{ s}^{-1}$. (a) For a Ramsey time extended up to 12 ms. (b) For typical Ramsey time of 3 ms used in the POP-DR clock for $\theta = \pi/2$ and $\theta = 0.56\pi$.

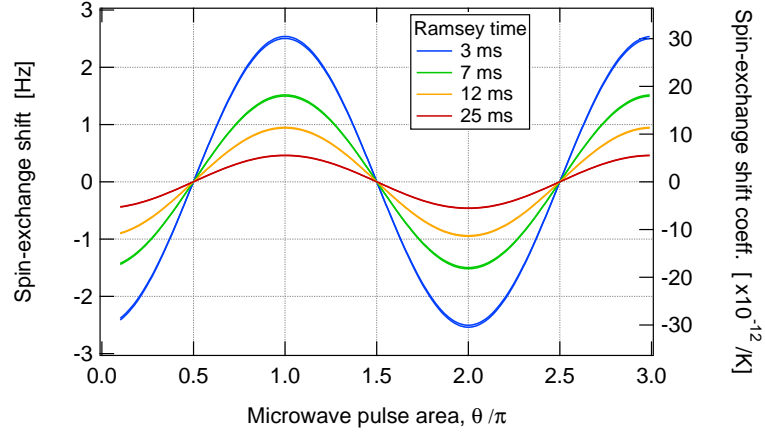


Figure 1.9 – Spin-exchange shift as a function of the microwave pulse area estimated for varied Ramsey times.

The SE shift calculated as a function of the microwave pulse area for different Ramsey times is presented in Figure 1.9. The spin-exchange shift and coefficient can be canceled for microwave pulses of $\theta = \pi/2$. Increased Ramsey time would also result in reducing the SE shift (and coefficient) due to the population difference decrease by relaxation. Under POP-DR clock operation conditions with $\theta = 0.56\pi$, $t_R = 3$ ms and optical pumping from $|2\rangle$, the clock frequency shift induced by the spin-exchange effect is 0.5 Hz.

The Rb density contributing to the clock signal and the mean relative velocity of two colliding Rb atoms are mainly affected by the cell temperature variations. The fluctuations of any of these two parameters lead to fluctuating the clock frequency via the spin-exchange effect. In the next paragraphs, the sensitivity of the POP-DR clock to the fluctuations of these two parameters caused by the cell temperature fluctuations is presented.

A. Contribution of the atomic velocity variations

The mean relative velocity of the two colliding Rb atoms in the thermal vapor cell is given by $\bar{v}(T) = \sqrt{\frac{8k_B T}{\pi M}}$, where k_B is the Boltzmann constant and M is the atomic mass. The clock frequency sensitivity coefficient to Rb velocity fluctuations caused by cell temperature instability is written as

$$\frac{\partial \Delta \nu_{SE} / \nu_{Rb}}{\partial T} = \frac{\partial \Delta \nu_{SE} / \nu_{Rb}}{\partial \bar{v}} \frac{\partial \bar{v}}{\partial T} \quad (1.41)$$

$$= -\frac{1}{8\pi} n_{Rb} \lambda_{se} \langle \Delta \rangle \frac{\partial \bar{v}}{\partial T} \quad [/K]. \quad (1.42)$$

The clock instability contribution of the spin-exchange shift via atomic velocity fluctuations for microwave pulses of $\theta = 0.56\pi$ and the optical pump frequency tuned to the $|2\rangle \rightarrow |3\rangle$ transition is $1.1 \cdot 10^{-13}/K$, which is a negligible level compared to the SE contribution via Rb density fluctuations (see Table 1.2).

B. Contribution of the atomic density variations

The atomic density in the vapor cell for a known cell temperature T is given by [61]

$$n_{Rb}(T) = \frac{9.656 \cdot 10^{18}}{T} 10^{7.43 - \frac{4132}{T}} 10^6 \text{ [m}^{-3}\text{]}, \quad (1.43)$$

In a vapor cell at a temperature 62.16°C, a variation of 1 °C leads to a 8.2 % change in the Rb density. The relative clock frequency sensitivity coefficient to Rb density fluctuations via the spin-exchange effect is written as

$$\frac{\partial \Delta \nu_{SE} / \nu_{Rb}}{\partial T} = \frac{\partial \Delta \nu_{SE} / \nu_{Rb}}{\partial n_{Rb}} \frac{\partial n_{Rb}}{\partial T} \quad (1.44)$$

$$= -\frac{1}{8\pi} \bar{v} \lambda_{se} \langle \Delta \rangle \frac{\partial n_{Rb}}{\partial T} \text{ [/K]}. \quad (1.45)$$

For microwave pulses of $\theta = 0.56 \pi$ and optical pump frequency tuned to the $|2\rangle \rightarrow |3\rangle$ transition, the clock stability limit of the spin-exchange effect via Rb density variations is $< 5.8 \cdot 10^{-12} /K$.

As outlined in Table 1.2, sensitivity to Rb density fluctuations is the dominant contribution to the spin-exchange effect. Due to the residual population resulting from $\theta = 0.56 \pi$ pulses with respect to the case of $\theta = \pi/2$ pulses, the SE coefficient is increased by up to two orders of magnitude and can approach the linear TCs associated to the cell and stem temperature variations (cf. section 1.5.2). For experimental evaluation, the SE effect is not measured separately but included in the measured temperature coefficients of the cell and stem. For the POP-DR clock studied in this thesis, as presented in chapter 3, the temperature variations in the vapor cell remain below 0.5 mK over one day and the induced instability contribution via the SE effect at the level of $3 \cdot 10^{-15}$ (cf. Table 3.5).

Table 1.2 – Spin-exchange coefficients for $\theta = \pi/2$ or 0.56π , optical pumping from $|2\rangle$, and cell at 62.16°C.

Parameter	Temperature sensitivity of the parameter	Pulse area θ	SE shift coefficient
Rb density	$3.0 \cdot 10^{16} \text{ m}^{-3}/K$	$\pi/2$	$4.8 \cdot 10^{-14} /K$
	$3.0 \cdot 10^{16} \text{ m}^{-3}/K$	0.56π	$5.8 \cdot 10^{-12} /K$
Average velocity	0.6 (m/s)/K	$\pi/2$	$8.8 \cdot 10^{-16} /K$
	0.6 (m/s)/K	0.56π	$1.1 \cdot 10^{-13} /K$
Total SE shift coefficient		$\pi/2$	$4.9 \cdot 10^{-14} /K$
		0.56π	$5.9 \cdot 10^{-12} /K$

1.5.5 Light-induced shifts

Laser light applied to the atomic vapor induces a shift in the energy levels, which is known as AC Stark shift [79], or light shift (LS). The optical field coupled with the electric dipole moment results in a change in the energy levels of the states [16, 61]. The induced frequency shift associated to a specific state depends on the laser frequency detuning $\nu'_L = 2\pi\Omega_L$. The total shift of the transition frequency between two states (e.g. $|1\rangle \rightarrow |2\rangle$) is given by the sum of the respective light shifts [67]

$$\begin{aligned}\Delta\nu_{LS} &= \Delta\nu_{LS_2} - \Delta\nu_{LS_1} \\ &= \left(\frac{\Omega_R}{4\pi}\right)^2 \left(\frac{\nu'_{L_2}}{\left(\frac{\Gamma^*}{4\pi}\right)^2 + (\nu'_{L_2})^2} - \frac{\nu'_{L_1}}{\left(\frac{\Gamma^*}{4\pi}\right)^2 + (\nu'_{L_1})^2} \right) \text{ [Hz]}.\end{aligned}\quad (1.46)$$

where $\Delta\nu_{LS_i}$ for $i = 1, 2$ represents the light shift for the corresponding ground-state level $|i\rangle$ and $\nu'_{L_i} = \nu_L - \nu_{i3}$ is the laser frequency detuning from the optical transition frequency from the same ground-state $|i\rangle$. The sensitivity of the clock frequency shift to fluctuations of laser intensity I_L and to frequency ν_L is derived from equation (1.46) and evaluated at a fixed laser frequency and intensity, respectively. The intensity α_{LS} and frequency β_{LS} LS coefficients are given by

$$\alpha_{LS}(\nu_L) = \frac{\partial\Delta\nu_{LS} / \nu_{Rb}}{\partial I_L / I_L} \text{ [%]} \quad \text{for a specific laser frequency } \nu_L, \quad (1.47)$$

$$\beta_{LS}(I_L) = \frac{\partial\Delta\nu_{LS} / \nu_{Rb}}{\partial \nu_L} \text{ [/MHz]} \quad \text{for a specific laser intensity } I_L. \quad (1.48)$$

Light-shift effects are one of the dominant instability sources in optically-pumped atomic clocks and result from the AC Stark shift effect in the presence of the laser light during the microwave interrogation. The impact of LS effects is characterized by the LS coefficients, which in clock applications are determined by measuring the clock frequency shift as a function of light intensity for a specific laser frequency or as a function of laser frequency for a specific light intensity. Light-induced clock frequency shifts manifest in different ways in CW-DR and POP-DR schemes. In the CW-DR scheme, the well-known AC Stark shift effect, occurs, whereas in the POP-DR scheme, this effect is strongly reduced by separating the light from the microwave interrogation phase (cf. section 2.3). However, in this case, the residual coherence at the beginning of the microwave interrogation that survived the optical pumping phase couples the light intensity and frequency to the clock frequency [51, 69]. The impacts of the light-shift effects in the two interrogation schemes are reviewed in the following sections.

A. CW-DR scheme

In the CW-DR scheme, both optical and microwave interactions occur in parallel and at the same time. The energy levels of the atoms interrogated by the microwave radiation are affected by the light field's resonant and off-resonant components via the AC Stark shift effect. The total light shift of the ground-state hyperfine splitting frequency is given by the equation (1.46) and the intensity and frequency LS coefficients are given by the equations (1.47) and (1.48), respectively.

The light-shift coefficients of a similar CW-DR clock to the one studied in this work are in the order of $\alpha_{LS}^{CW} = 1 \cdot 10^{-12} / \%$ and $\beta_{LS}^{CW} = 1.2 \cdot 10^{-11} / \text{MHz}$ [45]. The intensity LS effect can be *suppressed* by detuning the laser frequency such that the α_{LS}^{CW} coefficient decreases [80]. Another approach is to separate the interactions in time such as in the pulsed-optically pumped scheme [44].

B. POP-DR scheme

The impact of the AC Stark shift is significantly reduced in the POP-DR scheme due to the uncoupled optical and microwave interactions. However, the LS effect is not fully suppressed [44, 51, 75]. Furthermore, the analysis of the light-induced effects in the POP-DR scheme should elaborate the combination of different processes occurring during the different phases of the interrogation cycle. The optical-pump pulse serves to create a ground-state population inversion and reduces the microwave coherence at the end of the POP-DR interrogation cycle that survives the weak optical-detection pulse (cf. Figure 2.15). The residual coherence in the ground states at the beginning of the microwave interrogation (before the first microwave pulse) results in a shift of the central Ramsey fringe frequency by inducing an initial phase at the beginning of the Ramsey time [51, 69]. To kill the residual coherence, a strong optical-pump pulse is required $\Gamma_{pi} t_p \gg 1$. A dark time introduced between consecutive cycles would also help to decrease the ground-state coherence via relaxation [70]. During the microwave interrogation, the light is *switched off*, for instance, using an AOM with a typical extinction ratio of 40 dB at Rb optical transition wavelengths. A residual light present during this period impacts the clock frequency via the AC Stark shift effect [75]. Furthermore, the sensitivity to the optical detection light can be attributed to the inhomogeneity of the optical detection light along the atomic vapor and other position-dependent shifts averaged by the detection light [62].

In the POP-DR scheme, the α_{LS}^{POP} and β_{LS}^{POP} coefficients that characterize the light-induced clock frequency shifts are determined by measuring the clock frequency sensitivity to the variations of light intensity or frequency. For the POP-DR clock studied in this thesis, the estimated coefficients are $\alpha_{LS}^{POP} = 2.1 \cdot 10^{-14} / \%$ and $\beta_{LS}^{POP} = 4.6 \cdot 10^{-13} / \text{MHz}$ for the optical-pump frequency tuned to the ground-state transitions from $|2\rangle$ [51]. In the POP-DR scheme, the clock frequency sensitivity coefficients due to light intensity and frequency variations is reduced by about two orders of magnitude compared to the CW-DR scheme (see coefficients given in the previous paragraph).

1.5.6 Microwave-power shift

The microwave field used to interrogate the Rb atoms is applied to the vapor cell using a microwave resonator cavity (see section 2.2.2). In buffer gas cells, the Rb atoms are spatially localized during the microwave interaction and interact with the local microwave field [81, 82]. In the case of an inhomogeneous spatial distribution of the microwave amplitude (i.e., distribution of the microwave power $\sqrt{P_M} \propto b_R$) across the cell, the local microwave interactions yield different frequencies. The resulting clock signal at the end of the cell is a weighted average that depends on the local microwave power. Furthermore, the atoms confined in the buffer gas cell may also exhibit a spatially inhomogeneous distribution of the ground-state hyperfine frequencies because of an inhomogeneous distribution of the applied fields (light intensity and frequency, C-field, and temperature). The atomic hyperfine splitting frequency distribution across the cell depends on

various inhomogeneities, known as the position shift, due to the spatial confinement of Rb atoms in the presence of buffer gases and can be suppressed in vapor cells without buffer gases [83]. The clock signal detected at the end of the vapor cell, and thus its central frequency, is an average of all of the hyperfine splitting frequencies weighted according to the microwave power distribution. As a result, the clock frequency is sensitive to the variations of the microwave power, referred to as the microwave power shift effect [47].

We studied the clock frequency sensitivity to microwave power variations, for the field distribution of the microwave cavity of our POP-DR clock and the various position-dependent clock frequency shifts. The dominant contribution that we identified is the light-induced shift arising from the residual coherence [51, 59]. For a CW-DR clock similar to the one studied in this work, the relative clock frequency sensitivity coefficient to microwave power is in the order of $2.2 \cdot 10^{-12} / \mu\text{W}$ [80]. For the POP-DR clock, the reported MPS sensitivity coefficient of $1.8 \cdot 10^{-12} / \mu\text{W}$ [51] is for $\theta = \pi/2$ microwave pulse areas. By varying the pulse area to $\theta = 0.56 \pi$, the MPS coefficient can be reduced by one order of magnitude to $2 \cdot 10^{-13} / \mu\text{W}$ [84].

1.5.7 Cavity-pulling shift

The microwave cavity is used to radiate the microwave field resonant with the ground-state hyperfine splitting frequency of the Rb atoms. The feedback of the cavity on the atoms with a resonance frequency detuned from the atomic transition frequency leads to a shift in the atomic frequency via the cavity-pulling (CP) effect. The cavity pulling shift in the POP-DR scheme is given by [85]

$$\Delta\nu_{CP} = -\frac{4}{\pi} \frac{Q_L}{Q_a} \Delta\nu_{cav} \ln(\cosh(A(T)) - \text{sgn}(\Delta) \cos(\theta) \sinh(A(T))) \quad [\text{Hz}], \quad (1.49)$$

where Q_L and $Q_a = \frac{\nu_{Rb}}{W}$ are cavity and atomic quality factors, respectively; $\Delta\nu_{cav}$ is the cavity frequency detuning from the atomic frequency; Δ is the ground-state population difference; $\theta = b t_m$ is the microwave pulse area; and

$$A(T) = \frac{k}{\gamma_2} |\Delta| (1 - e^{-\gamma_2 t_R}), \quad (1.50)$$

where k is the microwave photon emission rate of an atom given by the equation (1.40), γ_2 is the ground-state coherence relaxation time, and t_R is the Ramsey time. The cavity resonance frequency in the equation (1.49) is sensitive to variations of the environmental parameters, such as temperature, pressure, and humidity [86]. Moreover, the cavity-pulling shift depends on the applied microwave pulse and the optical-pump frequency, as depicted in Figure 1.10. For the optical-pump frequency tuned to $|2\rangle \rightarrow |3\rangle$ and microwave pulses $\theta = 0.56 \pi$, the frequency shift induced by the cavity-pulling effect is 1.6 mHz.

The cavity-pulling shift coefficients due to the fluctuations of parameter p_i can be written as

$$\frac{\partial \Delta\nu_{CP} / \nu_{Rb}}{\partial p_i} = \frac{\partial \Delta\nu_{CP} / \nu_{Rb}}{\partial \Delta\nu_{cav}} \frac{\partial \Delta\nu_{cav}}{\partial p_i}. \quad (1.51)$$

The sensitivity of our cavity resonance frequency to the environmental temperature, pressure, and humidity is -40 kHz/K [75], -1.6 kHz/hPa, and -38 kHz/(g/m³) [51], respectively. The resonance frequency detuning from the atomic frequency is $\Delta\nu_{cav} = 1.87$ MHz and the quality factor is $Q_L \approx 140$ (cf. section 2.4). The estimated contributions to the clock instability induced by the cavity-pulling effect are reported in Table 1.3 for microwave pulse areas of $\theta = \pi/2$ and $\theta = 0.56\pi$. The use of $\theta = 0.56\pi$ pulses instead of $\theta = \pi/2$ pulses has an important impact on the CP shift coefficients associated to the environmental parameters (temperature, pressure, and humidity). Nevertheless, the clock instability contributions due to the variations of the latter parameters via the CP effect remain at the level of $10^{-17} - 10^{-16}$ at one-day timescale, which are negligible for the POP-DR clock studied in this thesis.

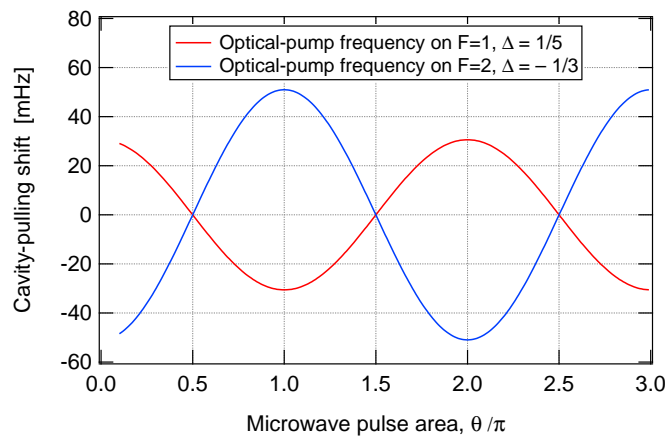


Figure 1.10 – Cavity-pulling shift as a function of the microwave pulse area estimated for the two cases of optical-pump frequency on the D₂ line; $Q_L = 140$, $Q_a = 4.6 \cdot 10^7$, $\Delta\nu_{cav} = 1.87$ MHz, $k = 1.8$, $\gamma_2 = 340$ s⁻¹, $t_R = 3$ ms, and optical-pump frequency tune to $|2\rangle \rightarrow |3\rangle$ transition.

Table 1.3 – Cavity-pulling shift coefficients for $\theta = \pi/2$ and $\theta = 0.56\pi$, optical pumping from $|2\rangle$, cell temperature of 62.16 °C, and at atmospheric pressure. The parameter fluctuations are from [51, 75].

Parameter	Pulse area θ	CP shift coefficient	Parameter fluctuations	Estimated clock instability
Microwave power	$\pi/2$	$5.1 \cdot 10^{-14}$ / μ W	$2 \cdot 10^{-3}$ μ W	$1.0 \cdot 10^{-16}$
	0.56π	$5.6 \cdot 10^{-14}$ / μ W	$2 \cdot 10^{-3}$ μ W	$1.1 \cdot 10^{-16}$
Temperature	$\pi/2$	$1.6 \cdot 10^{-17}$ /K	$5 \cdot 10^{-3}$ K	$7.8 \cdot 10^{-20}$
	0.56π	$-5.1 \cdot 10^{-15}$ /K	$5 \cdot 10^{-3}$ K	$-2.6 \cdot 10^{-17}$
Pressure	$\pi/2$	$6.2 \cdot 10^{-19}$ /hPa	0.06 hPa	$3.7 \cdot 10^{-20}$
	0.56π	$-2.1 \cdot 10^{-16}$ /hPa	0.06 hPa	$-1.2 \cdot 10^{-17}$
Humidity	$\pi/2$	$1.5 \cdot 10^{-17}$ /(g/m ³)	0.2 g/m ³	$2.9 \cdot 10^{-18}$
	0.56π	$-4.8 \cdot 10^{-15}$ /(g/m ³)	0.2 g/m ³	$-9.6 \cdot 10^{-16}$

1.5.8 Summary of clock frequency shifts

The previous sections from 1.5.1 to 1.5.7 discuss the effects that cause a frequency shift to the clock transition frequency with respect to the unperturbed Rb frequency (ν_{Rb}), in view of the resulting clock stability, i.e., variations of the clock frequency over time. The purpose of the present section is to summarize the absolute frequency shifts induced by these effects and estimate the total clock frequency shift (or bias) from the unperturbed Rb frequency, i.e., $\Delta\nu_{clock} = \nu_{clock} - \nu_{Rb}$.

Table 1.4 summarizes the estimated absolute frequency shifts induced by the second-order Zeeman effect ($\Delta\nu_{Ze}$), the buffer-gas collisions ($\Delta\nu_{BG}$), the Rb-Rb collisions (spin-exchange shift, $\Delta\nu_{SE}$), and the cavity-pulling effect ($\Delta\nu_{CP}$) for the POP-DR clock. Two cases of microwave pulse areas are considered, $\theta = \pi/2$ and $\theta = 0.56\pi$, which have a significant impact on the frequency shifts induced by the SE and the CP effects. The dominant frequency shift contribution is due to the buffer-gas collisions. The second-order Zeeman shift, which scales quadratically with the C-field strength, is further reduced in this work (see section 3.3.1). The measured clock frequency shift for the POP-DR clock using microwave pulse areas of $\theta = 0.56\pi$ (see chapter 3) is in agreement with our estimations given that $\Delta\nu_{Ze}$ is reduced to 0.7 Hz.

Table 1.4 – Estimated clock frequency shift of the POP-DR clock for $\theta = \pi/2$ and $\theta = 0.56\pi$ with optical pumping from $|2\rangle$ at atmospheric pressure. The frequency shifts are calculated in sections from 1.5.1 to 1.5.7.

Physical effect	Estimated frequency shift	
	Symbol	Value
<i>In the case of $\theta = \pi/2$ pulses</i>		
Second-order Zeeman	$\Delta\nu_{Ze}$	6.6 Hz
Buffer-gas density	$\Delta\nu_{BG}$	4247.4 Hz
Spin-exchange	$\Delta\nu_{SE}$	$4.5 \cdot 10^{-3}$ Hz
Cavity-pulling	$\Delta\nu_{CP}$	$-5.0 \cdot 10^{-6}$ Hz
Total clock frequency shift	$\Delta\nu_{clock}$	4254.0 Hz
<i>In the case of $\theta = 0.56\pi$ pulses</i>		
Second-order Zeeman	$\Delta\nu_{Ze}$	6.6 Hz
Buffer-gas density	$\Delta\nu_{BG}$	4247.4 Hz
Spin-exchange	$\Delta\nu_{SE}$	$4.8 \cdot 10^{-1}$ Hz
Cavity-pulling	$\Delta\nu_{CP}$	$1.6 \cdot 10^{-3}$ Hz
Total clock frequency shift	$\Delta\nu_{clock}$	4254.5 Hz

1.6 Atomic clock frequency instability

Frequency standards provide an oscillating signal at a known frequency that is stabilized to the atomic transition frequency. The instantaneous frequency of an atomic clock output signal at time t can be written as

$$f(t) = f_0(1 + \epsilon + y(t)), \quad (1.52)$$

where f_0 is the reference (or nominal) frequency (e.g the unperturbed ground-state hyperfine transition frequency ν_{Rb}), ϵ is the fractional frequency bias that results from the systematic frequency shifts (cf. section 1.5.8), and $y(t) = \frac{\Delta f(t)}{f_0}$ reflects the time-dependent fractional frequency fluctuations. The *accuracy* represents how close to the reference frequency the clock output frequency is and is characterized via the analysis of ϵ . The *stability* of a frequency standard gives a measure of its ability to reproduce the same frequency over a given time interval. Frequency stability analysis is based on evaluation of the (dimensionless) variable $y(t)$. The secondary frequency standards, such as the Rb vapor-cell clock, are primarily characterized by their fractional frequency stability.

In the time domain, the clock frequency instability is expressed in terms of the Allan deviation ($\sigma_y(\tau)$) [56] as a function of the averaging time τ . Clock frequency instability is often studied in three regions according to the averaging timescales. The first region is the short-term timescales of τ between 1 and 100 s, when the clock stability is predominantly limited by the signal-to-noise ratio of the detection (dominated by the white frequency noise). The second region corresponds to medium-term timescales of τ ranging from 100 to 10'000 s and the third region corresponds to long-term timescales of $\tau > 10^4$ s up to 1 day (86'400 s). On medium- and long-term timescales, the main sources of clock frequency instability originate from the slow fluctuations of the sensitive parameters that perturb the atomic transition frequency via the physical effects reviewed in section 1.5. The impact of the fluctuating parameters is quantified by the sensitivity coefficient of the clock frequency with respect to the parameter and the amplitude of the fluctuations of the parameter (cf. section 1.6.3). On long-term timescales, the clock stability may additionally be limited by the aging processes yielding a frequency drift.

In this thesis, we study the limitations of the clock stability that arise on the short-term timescales from various noise sources (cf. chapter 5) and on the medium-to-long term timescales from the slow fluctuations of the systematic frequency shifts (cf. chapter 3). This section first presents the statistical tool used for the clock stability analysis: (overlapping) Allan deviation. Secondly, the instability sources degrading the clock stability on the short-term timescales are described. Then, the medium-to-long term clock stability limitations due to the systematic frequency shift fluctuations are outlined.

1.6.1 Overlapping Allan deviation

The statistical tool to characterize the frequency instability of an atomic clock is the Allan deviation [56], which is the square root of the two-sample variance, or Allan variance $\sigma_y^2(\tau)$. The characterization of the clock frequency instability is based on the measurement of its fractional frequency fluctuations $y(t)$ in time. This frequency data can be divided into equal time intervals of duration $\tau = t_{i+1} - t_i$. The fractional frequency fluctuation averaged over the time interval τ is written as

$$\bar{y}_i = \frac{1}{\tau} \int_{t_i}^{t_{i+1}} y(t) dt. \quad (1.53)$$

For N samples \bar{y}_i averaged over time intervals of τ , the Allan deviation is calculated with [87]

$$\sigma_y(\tau) = \sqrt{\frac{1}{2(N-1)} \sum_{i=1}^{N-1} (\bar{y}_{i+1} - \bar{y}_i)^2}. \quad (1.54)$$

Rather than drawing the frequency samples consecutively, the use of overlapping samples increases the statistical confidence of the frequency instability estimation. Indeed, the most commonly used frequency instability measure for atomic frequency standards is the overlapping Allan deviation. For N frequency samples acquired with the measurement time τ_0 , the overlapped samples are considered for the averaging time τ , which is an integer multiple of τ_0 such that $\tau = m \tau_0$. The overlapping Allan deviation is written as [87]

$$\sigma_y(\tau) = \sqrt{\frac{1}{2m^2(N-2m+1)} \sum_{j=1}^{N-2m+1} \left(\sum_{i=j}^{j+m-1} (\bar{y}_{i+m} - \bar{y}_i) \right)^2}. \quad (1.55)$$

We use the overlapping Allan deviation to evaluate the instability of the frequency standards and those of the physical parameters that impact the clock frequency stability. We also use the ThêoH (ThêoH) statistic [88], in particular in chapter 3 where the long-term clock instability sources are evaluated up to one-day timescale. The ThêoH statistic combines the overlapping Allan, used for short- and medium-term averaging times, and Thêo1, used for long-term averaging times, and includes a bias removal algorithm [89] to correct the bias from Thêo1 with respect to the overlapping Allan variance, which can exist for the noise types except white FM noise [87]. The Thêo1 statistic provides an analysis up to an averaging time of 75 % of the full measurement duration, where the measurement sampling time (τ_0) is separated from the statistical averaging time τ such that $\tau = 0.75 m \tau_0$. Therefore, the Thêo1 statistic allows to extend the analysis to a larger averaging time and get significantly more information on the stability level of a fluctuating parameter than the overlapping Allan statistics while using the same data set. The ThêoH statistics is extensively used in chapter 3 to analyze the instability of the clock frequency stability and of the various physical parameters impacting the long-term clock stability.

1.6.2 Short-term clock frequency instability

On short-term timescales (1 to 100s), the clock frequency instability is governed by the signal-to-noise ratio of the detection signal. In addition, the noise of the optical and microwave sources degrades the clock frequency stability via different effects depending on the interrogation scheme. Chapter 5 presents a detailed evaluation of the various noise contributions to the short-term clock stability of a CW-DR clock using a frequency-doubled laser for optical pumping and detection. In the following sections, we provide an overview of the noise contributions to the short-term clock instability with an emphasis on the CW-DR interrogation scheme.

1.6.2.1 Optical detection noises

In vapor-cell clocks based on optical pumping and detection, both the laser and detector noises contribute to the measured clock frequency instability. The short-term clock frequency stability limited by the signal-to-noise ratio of the detection signal is given by [90]

$$\sigma_{\text{SNR}}(\tau) = \frac{S_n}{\sqrt{2} D_s \nu_{Rb}} \tau^{-1/2}, \quad (1.56)$$

where S_n is the optical detection noise power spectral density and D_s is the discriminator slope of the detected signal. Under typical laser operation conditions (well above the threshold current), the clock detection noise is proportional to the applied optical power and is dominated by the laser noise. Nevertheless, the clock detection noise is only weakly sensitive to the variations of the microwave power (see Appendix A for more information). The detected optical power of the CW-DR signal is associated with the background level B^{CW} defined in section 1.3.2.1. The discriminator slope of the error signal concurrently depends on the optically detected signal and on the waveform and properties of the reference signal used for synchronous detection. Assuming a square-wave modulation signal applied with a modulation depth corresponding to a third of the optically detected signal's FWHM ($f_{\Delta} \approx 0.3 W^{\text{CW}}$), the discriminator slope is proportional to the ratio $D_s = K \frac{A^{\text{CW}}}{W^{\text{CW}}}$ where K is a factor depending on the modulation signal waveform and properties. Thus, SNR limited clock stability $\sigma_{\text{SNR}} \propto \frac{S_n}{D_s} \propto \frac{1}{FOM^{\text{CW}}}$ is inversely proportional to the figure-of-merit defined in equation (1.20) for specific experimental conditions. It is therefore useful to optimize the clock operational parameters to maximize the FoM of the optically detected signal in order to improve short-term clock frequency stability.

The photodetector noise in the absence of light S_{det} determines the floor level of noise and should not limit the optical detection signal. The shot-noise $S_{\text{shot-noise}} = \sqrt{2 e I_{\text{DC}}}$ at detection sets the ultimate physical limit for achievable short-term clock frequency stability. While laser intensity noise, or amplitude modulation (AM) noise, S_{AM} , contributes directly to the optical detection noise, its frequency modulation (FM) noise is converted across the atomic vapor to AM noise $S_{\text{FM-AM}}$ [90, 91]. In fact, the atomic vapor in the cell acting as a frequency discriminator transfers the optical frequency modulation into amplitude modulation (see Figure 1.11). The atomic discriminator, the rate of the FM-to-AM noise conversion, is defined as the local slope $D_{\text{FM-AM}}$ at the specific laser frequency and depends on experimental conditions such as laser intensity and cell temperature. This phenomenon is called FM-to-AM noise conversion and forms the dominant contribution to

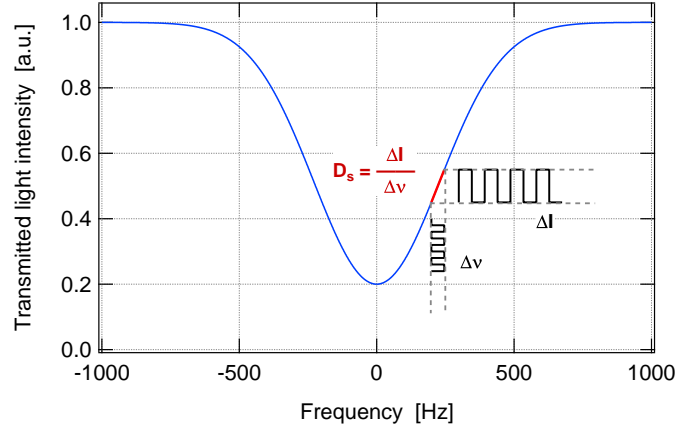


Figure 1.11 – Laser frequency-modulation conversion to amplitude-modulation via an atomic frequency discriminator; $D_{FM-AM} = \frac{\Delta I}{\Delta \nu}$.

the optical detection noise in many *hot* vapor-cell clock experiments [44, 45, 92]. The individual noise processes are considered independent and are added, as reported in Appendix A.

1.6.2.2 Light shift effects

Laser intensity and frequency fluctuations also contribute to the clock frequency instability via the light-shift effects (see section 1.5.5). On short-term timescales, the laser noise contribution to the optical detection noise in the CW-DR scheme is scaled with the associated light-shift coefficient (α_{LS}^{CW} or β_{LS}^{CW}). The contribution of the laser intensity noise to the short-term clock instability via the intensity LS effect expressed in terms of relative intensity noise (RIN) is given by [93]

$$\sigma_{\alpha_{LS}}(\tau) = \frac{\alpha_{LS}^{CW} I_L \sqrt{S_{RIN}}}{\sqrt{2} \nu_{Rb}} \tau^{-1/2}, \quad (1.57)$$

where α_{LS}^{CW} is the intensity LS coefficient (absolute, in Hz/ μ W), P_L is the optical power, and $S_{RIN} = \frac{S_{AM}^2}{I_{DC}^2}$ is the laser RIN (in Hz⁻¹) determined for the measured AM noise S_{AM} of the photodetector current I_{DC} (cf. section 2.1.1.1). The contribution to short-term clock instability of the laser frequency noise via the frequency LS effect is given by [93]

$$\sigma_{\beta_{LS}}(\tau) = \frac{S_{FM} \beta_{LS}^{CW^2}}{\sqrt{2} \nu_{Rb}} \tau^{-1/2}, \quad (1.58)$$

where β_{LS}^{CW} is the frequency LS coefficient (absolute, in Hz/MHz) and S_{FM} is the laser frequency noise power spectral density (in Hz²/Hz, see section 2.1.1.1). Assuming independent and uncorrelated effects, the total impact of the light-shift effects is estimated as follows:

$$\sigma_{ls}(\tau) = \sqrt{\sigma_{\alpha_{LS}}^2(\tau) + \sigma_{\beta_{LS}}^2(\tau)}. \quad (1.59)$$

1.6.2.3 Microwave phase noise

The resonance frequency of the vapor cell is detected using the synchronous detection method. The optical detection signal is demodulated at the modulation frequency of the microwave frequency interrogating the atoms. Under closed-loop clock mode, the demodulated signal is used to stabilize the frequency of an external local oscillator. The phase noise of the LO contributes to the clock noise due to the microwave frequency modulation via intermodulation effects [94, 95]. In the CW-DR scheme, the contribution of the phase noise of the LO output modulated at f_{mod}^{CW} to the clock instability is given by [96]

$$\sigma_{LO}(\tau) = \sqrt{\sum_{n=1}^{\infty} C_{2n}^2 S_{\phi}(2nf_{mod}^{CW})} \tau^{-1/2}, \quad (1.60)$$

where

$$C_{2n} = \frac{2n}{(2n-1)(2n+1)} \frac{f_{mod}^{CW}}{\nu_{Rb}}, \quad (1.61)$$

and $S_{\phi}(2nf_{mod}^{CW})$ is the microwave phase noise spectral density of the $(2n)^{th}$ -harmonic. The clock stability limit caused by the LO phase noise depends on the microwave modulation frequency. The LO phase noise and the modulation conditions are presented in section 2.3 for the CW-DR clock.

1.6.2.4 Short-term clock instability budget

The short-term frequency stability of a vapor-cell clock based on optical detection is ultimately limited by the shot noise in the detection. However, the noise of the employed optical and microwave sources degrade the achievable short-term clock stability via the effects described in the previous sections (from section 1.6.2.1 to 1.6.2.3). Given that the noise contributions are independent from each other, the total short-term clock frequency instability can be estimated by the quadratic sum of all individual noise contributions as

$$\sigma_y(\tau) = \sqrt{\sigma_{SNR}^2(\tau) + \sigma_{LS}^2(\tau) + \sigma_{LO}^2(\tau)}. \quad (1.62)$$

The short-term clock stability limits arising from the independent noise sources can be evaluated in a budget as the one presented in Table 1.5. The short-term budget of Table 1.5 is given based on the previous work [80] using a CW-DR clock similar to the one studied in this work (cf. section 2.3). The primary difference between the two clocks is the optical source. In [80], the clock employs a 780-nm laser diode, while in this work, frequency-doubled telecom lasers initially emitting at 1560 nm are used for optical pumping and detection. The short-term stability optimization and the analysis of the different noise contributions for the CW-DR clock based on the telecom laser are presented in chapter 5.

1.6. Atomic clock frequency instability

Table 1.5 – Short-term instability budget at $\tau = 1$ s for the state-of-the-art CW-DR Rb clock. The budget is based on a similar CW-DR clock [80] to the CW-DR clock studied in this thesis. A laser diode emitting at 780 nm stabilized to $|2\rangle$ hyperfine component transitions is used.

j	Noise source	Remark	Noise	Estimated clock instability
1	Detector noise		$0.36 \text{ pA}/\sqrt{\text{Hz}}$	$2.5 \cdot 10^{-14}$
2	Shot-noise limit		$0.71 \text{ pA}/\sqrt{\text{Hz}}$	$4.9 \cdot 10^{-14}$
3	Microwave noise		$0.74 \text{ pA}/\sqrt{\text{Hz}}$	$5.1 \cdot 10^{-14}$
4	Laser noises (AM & FM-to-AM)		$1.46 \text{ pA}/\sqrt{\text{Hz}}$	$1.0 \cdot 10^{-13}$
5	SNR limit	including $j=1,3,4$	$1.68 \text{ pA}/\sqrt{\text{Hz}}$	$1.2 \cdot 10^{-13}$
6	Dick effect		$0.74 \text{ pA}/\sqrt{\text{Hz}}$	$7.5 \cdot 10^{-14}$
7	Intensity LS	$\alpha_{LS}^{\text{CW}} = 1.0 \cdot 10^{-12} \%$	$3 \cdot 10^{-3} \%$	$3.0 \cdot 10^{-15}$
8	Frequency LS	$\beta_{LS}^{\text{CW}} = 1.2 \cdot 10^{-11} \text{ /MHz}$	$3.0 \cdot 10^{-3} \text{ MHz}$	$3.6 \cdot 10^{-14}$
Total estimated clock frequency instability at $\tau = 1$ s			$\sigma_y(\tau) = \sqrt{\sum_{j=5}^8 \sigma_j^2(\tau)}$	$1.4 \cdot 10^{-13}$

1.6.3 Medium-to-long term clock instability

Fluctuations in environmental and experimental parameters degrade the clock frequency stability on the medium-to-long term timescales. The sensitive parameters include the laser intensity and frequency, microwave and static magnetic field amplitudes, cell and stem temperatures, and external pressure and humidity. The physical effects through which the parameter fluctuations perturb the clock frequency are characterized by the sensitivity coefficients, as described in section 1.5. The clock stability limit of each sensitive parameter p_i can be estimated using

$$\sigma_i(\tau) = \frac{\partial \Delta \nu_i / \nu_{Rb}}{\partial p_i} \sigma_{p_i}(\tau), \quad (1.63)$$

where the first term represents the clock frequency sensitivity coefficient associated with one of the effects and the second term represents the fractional fluctuations of the specific sensitive parameter. Assuming that the parameter fluctuations are independent, the total long-term clock frequency variance can be estimated as the sum of the squares of all of the independent contributions such that the total Allan deviation is given by

$$\sigma_y(\tau) = \sqrt{\sum_i \sigma_i^2(\tau)}. \quad (1.64)$$

The total clock instability can be evaluated in a clock instability budget that lists all of the different clock instability contributions. Table 1.6 details the preliminary long-term instability budget at $\tau = 10^4$ s of our POP-DR clock as estimated at the beginning of this thesis. The total clock stability limit is estimated at $2.1 \cdot 10^{-14}$ at $\tau = 10^4$ s after adding the contributions in lines 1 – 7. The impact of the SE and CP effects are assumed to be included in the experimentally determined cell TC, barometric coefficient, and MPS coefficient. The sensitivity coefficients on lines 1 – 3 and 8 – 13 are calculated as described in section 1.5. The sensitivity coefficients of lines 4, 5, 6, 7 were measured or estimated in the previous work [51, 75] as well as the fluctuations of all physical parameters. The parameter fluctuations and the long-term instability budget of our POP-DR clock are consolidated in the detailed analysis presented in chapter 3.

1.7 Conclusion

This chapter provided an overview of the basic physics required to understand the principle of double-resonance atomic frequency standards. First, the chapter detailed the atomic structure of Rb and introduced the simplified three-level model. The optical and microwave double-resonance interaction was described for two schemes: continuous wave operation and pulsed-optically pumped operation. Furthermore, the effects perturbing the Rb structure and thus leading to shifts in the clock frequency from the unperturbed Rb transition frequency were presented. Finally, the chapter introduced the clock frequency instability characterization tool, the Allan variance, and described the instability contributions on different timescales. In addition, the preliminary clock frequency instability budgets were presented for short and medium-to-long terms for two different clock prototypes, CW-DR and POP-DR. The basic principles reviewed in this section are critical for understanding and evaluation of the results obtained in this thesis. The preliminary clock instability budgets are consolidated in the studies presented in the subsequent chapters.

Table 1.6 – Preliminary long-term instability budget at $\tau = 10^4$ s for the POP-DR clock, operated at atmospheric pressure using microwave pulses of $\theta = 0.56\pi$ and optical pumping from $|2\rangle$ hyperfine component. The total clock instability is estimated by the quadratic sum of the contributions from line $j = 1$ to $j = 7$, assuming the contributions of the effects in lines $j = 8$ to $j = 12$ are experimentally included in the lines above. The (absolute and relative) sensitivity coefficients are calculated as described in section 1.5 except for lines $j = 4, 5, 6, 7$. The fluctuations of the sensitive parameters ($\sigma_p(\tau)$) given for $\tau = 10^4$ s are estimated based on previous works [51, 75]. ^(a) experimental coefficients based on previous work [51].

j	Physical effect	Sensitive parameter	Sensitivity coefficient	Relative sensitivity coefficient	Parameter fluctuations	Estimates clock instability
1	2 nd -order Zeeman shift	C-field	$1.2 \cdot 10^6$ Hz/T	$1.8 \cdot 10^{-4}$ /T	$5 \cdot 10^{-11}$ T	$9.0 \cdot 10^{-15}$
2	Buffer-gas density shift	T_{cell}	$\pm 8.7 \cdot 10^{-3}$ Hz/K	$\pm 1.3 \cdot 10^{-12}$ /K	$5 \cdot 10^{-3}$ K	$6.4 \cdot 10^{-15}$
3	Stem TC	T_{stem}	$7.6 \cdot 10^{-3}$ Hz/K	$1.1 \cdot 10^{-12}$ /K	$5 \cdot 10^{-3}$ K	$5.6 \cdot 10^{-15}$
4	Barometric ^(a)	P_{ext}	$5.6 \cdot 10^{-4}$ Hz/hPa	$8.1 \cdot 10^{-14}$ /hPa	$6 \cdot 10^{-2}$ hPa	$4.9 \cdot 10^{-15}$
5	Intensity light shift ^(a)	I_L	$-3.3 \cdot 10^{-4}$ Hz/%	$-4.9 \cdot 10^{-14}$ /%	0.3 %	$1.5 \cdot 10^{-14}$
6	Frequency light-shift ^(a)	ν_L	$7.3 \cdot 10^{-5}$ Hz/MHz	$1.1 \cdot 10^{-14}$ /MHz	$4 \cdot 10^{-3}$ MHz	$4.3 \cdot 10^{-17}$
7	Microwave power shift ^(a)	P_M	$2.1 \cdot 10^{-2}$ Hz/ μ W	$3.1 \cdot 10^{-12}$ / μ W	$2 \cdot 10^{-3}$ μ W	$6.1 \cdot 10^{-15}$
8	Spin-exchange	T_{cell}	$4.0 \cdot 10^{-2}$ Hz/K	$5.9 \cdot 10^{-12}$ /K	$5 \cdot 10^{-3}$ K	$3.0 \cdot 10^{-14}$
9	Cavity-pulling	P_M	$3.8 \cdot 10^{-4}$ Hz/ μ W	$5.6 \cdot 10^{-14}$ / μ W	$2 \cdot 10^{-3}$ μ W	$1.1 \cdot 10^{-16}$
10	Cavity-pulling	T_{cav}	$-3.5 \cdot 10^{-5}$ Hz/K	$-5.1 \cdot 10^{-15}$ /K	$5 \cdot 10^{-3}$ K	$2.6 \cdot 10^{-17}$
11	Cavity-pulling	P_{ext}	$-1.4 \cdot 10^{-6}$ Hz/hPa	$-2.1 \cdot 10^{-16}$ /hPa	$6 \cdot 10^{-2}$ hPa	$1.2 \cdot 10^{-17}$
12	Cavity-pulling	H_{ext}	$-3.3 \cdot 10^{-5}$ Hz/(g/m ³)	$-4.8 \cdot 10^{-15}$ /(g/m ³)	0.2 g/m ³	$9.6 \cdot 10^{-16}$

Total estimated clock frequency instability at $\tau = 10^4$ s		$\sigma_y(\tau) = \sqrt{\sum_{j=1}^7 \sigma_j^2(\tau)}$	$2.1 \cdot 10^{-14}$
($\theta = 0.56\pi$, optical pumping from $ 2\rangle$, in hermetic chamber at ~ 960 hPa)			

2 Experimental setups

This chapter presents the key properties of the experimental setups for the optical and microwave frequency standards studied in this thesis: the optical sources, (microwave) local oscillators, the physics package (PP) assemblies accommodating the Rb vapor cell, and the microwave cavity. The optical sources include a compact laser head (LH-CW) for the CW-DR clock and a second compact laser head (LH-POP) with an integrated AOM for the POP-DR clock. The LHs make use of a distributed-feedback (DFB) laser diode emitting at 780 nm and a ^{87}Rb vapor cell that provides atomic frequency references to stabilize the laser frequency. These LHs were designed and mounted at LTF [58], and the vapor cells were produced at LTF [97]. In this thesis, two additional laser systems are studied (cf. chapters 4 and 5), which are based on laser diodes emitting in the telecom window C-band at 1560 nm. Frequency-doubling technology enables the use of such lasers in experiments that deal with or benefit from the Rb resonances. The first frequency-doubled (FD) laser system is based on a DFB laser diode (FD-DFB), which was previously studied in a different setup for space-borne CO_2 detection applications [51, 98, 99]. The second FD laser system studied and optimized in this thesis makes use of an external cavity laser (ECL) formed by a gain medium and a Bragg grating integrated on a planar light circuit (FD-ECL) [100]. The PPs used in the CW-DR clock (PP-CW) and in the POP-DR clock (PP-POP) comprise a vapor cell containing ^{87}Rb and buffer gases [97] and a compact magnetron-type microwave cavity, which was designed and developed in the framework of a collaboration project [75, 80]. The local oscillators are based on a 5 or 10-MHz crystal oscillator (XO) and a frequency multiplication chain to reach the ^{87}Rb ground-state hyperfine splitting frequency near 6.835 GHz. Two different LOs are used in this thesis: the LO dedicated to the CW-DR clock (LO-CW) is a commercially available frequency synthesizer, and the LO dedicated to the POP-DR clock (LO-POP) is integrated in the clock control electronics developed by C. Calosso (INRIM) in the framework of a collaboration project [101]. The frequency instability characterization of optical or microwave frequency standards consists of comparing the frequency output to a frequency reference with a better and known frequency stability.

In the following sections, we first present the optical sources and physics packages. Then, the key properties of the CW-DR and POP-DR vapor-cell clocks studied in this thesis are reviewed. Finally, the methods used to characterize the frequency instability of the vapor-cell clocks and the optical sources are described.

2.1 Laser systems

This section reviews the laser systems that are used as optical frequency references in this work: LH-CW, LH-POP, FD-DFB, and FD-ECL. The laser systems comprise a semiconductor laser diode, a ^{87}Rb vapor cell used to frequency stabilize the LD on atomic frequency references, and the fiber or free-space optical components. In this section, we review the spectral properties of the LH-CW and LH-POP based on LDs emitting at 780 nm that have an impact on the performance of Rb vapor-cell clocks. For the laser systems based on frequency-doubled telecom lasers, FD-ECL and FD-DFB, we describe in this section the properties of the experimental setups for which the detailed spectral characterization and evaluation are presented in chapter 4.

2.1.1 Laser heads based on 780-nm laser diodes

Compact laser heads include a LD emitting at 780 nm, a ^{87}Rb vapor cell, optics, and photodetectors with pre-amplification electronics [58]. Two different laser heads are used in this work: LH-CW and LH-POP, shown in Figures 2.1 and 2.2, respectively. The main difference between the two LHs is the AOM integrated in the LH-POP, which is required to pulse the output light. The integration of the AOM degrades the frequency and intensity instability of the output light at all timescales (cf. Table 2.1) and increases the overall volume compared to LH-CW.

LHs employ a DFB laser diode (from eagleyard Photonics) mounted in a TO3 package and temperature controlled via a thermo-electric cooler. The LD emits linearly polarized light at the wavelength of 780.24 nm (384.231 THz), coinciding with the ^{87}Rb D₂ line. The temperature and the drive current of the LD are controlled via home-built electronics exhibiting a current source noise of $1 \text{ nA}/\sqrt{\text{Hz}}$. The laser frequency is stabilized on a Rb transition using the Doppler-free absorption spectrum of a ^{87}Rb cell and a lock-in amplifier. The laser current is modulated with a 50-kHz reference signal, and the photo-detected absorption signal is demodulated using the reference signal to generate the error signal through synchronous detection. A proportional-integral (PI) servo controller is used to apply the feedback to the laser drive current.

The ^{87}Rb vapor cell used to stabilize the laser frequency to Rb transitions, shown in Figure 2.6a, is referred to as reference Rb cell in this work. It also constitutes the heart of the frequency reference units (FRUs) employed in FD laser systems (cf. section 2.1.2). The reference Rb cell consists of a cylindrical glass cell with a 10-mm diameter and 19-mm length filled with ^{87}Rb vapor. The temperature of reference Rb cells is stabilized at 40°C. Magnetic coils surround the cell to apply a stabilized magnetic field and two-layers of μ -metal shields in order to reduce the coupling of the environmental static magnetic field inside the cell. The baseplate carrying the LD, the vapor cell, and the optics for the Doppler-free spectroscopy are temperature stabilized at 28°C.

The LH-CW is an optical frequency reference at 780 nm based on the Doppler-free absorption spectroscopy (cf. section 1.2.2) using a reference ^{87}Rb cell, as presented in Figure 2.1. The LD output light is split into two beams. One beam reaches a photodetector to monitor the reference Rb cell input light, while the other splits into two. One part of the latter is retro-reflected through the vapor cell and the Doppler-free absorption spectrum is detected using the second PD. The second part is the output light at 780 nm. The LH-CW has a volume of 0.63 dm^3 and a mass of 0.6 kg [80].

The LH-POP, shown in Figure 2.2, exhibits a similar configuration to the LH-CW for the Doppler-free absorption scheme using a reference ^{87}Rb cell and additionally includes an AOM. The LD output is split into two parts. One part is sent to the Doppler-free absorption scheme and the other part to the AOM. The AOM is used in double-pass configuration, whereby the light passes through twice and then is directed to the output of the LH-POP. The AOM is driven by a radio frequency (RF) source at 75 MHz, leading to a total frequency shift of -150 MHz at the output light with respect to the LD output light. The AOM also serves as an optical switch for the pulsed clock operation. An extinction ratio of > 40 dB and a rise/fall time of $4.5 \mu\text{s}$ are measured [75, 102]. The LH-POP has a volume of 2.3 dm^3 and a mass of 1.4 kg [80].

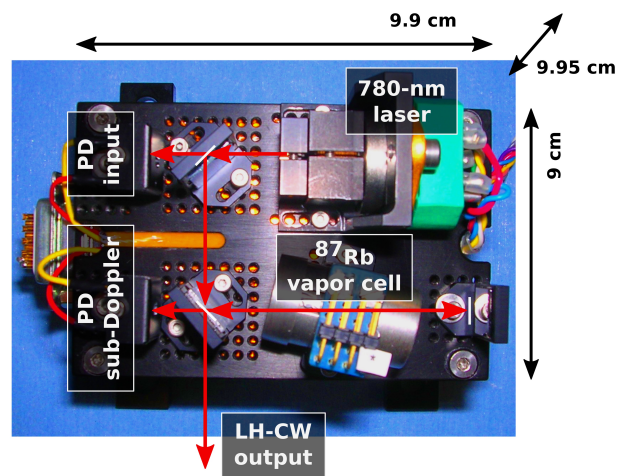


Figure 2.1 – Photography of the continuous-wave optical source: *LH-CW*. PD: photodetector.

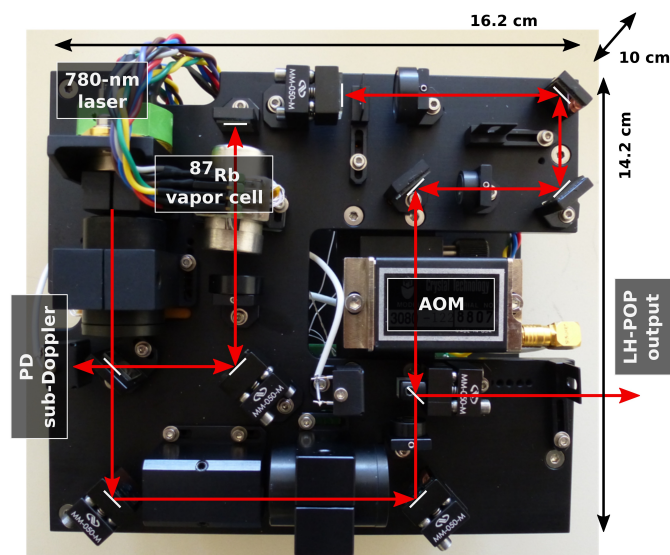


Figure 2.2 – Photography of the pulsed optical source: *LH-POP*, including an AOM. PD: photodetector.

2.1.1.1 Laser spectral characterization

The spectral properties of the laser used for optical pumping and detection in vapor-cell clocks are crucial for the clock performance and require a thorough characterization. The emission frequency of the LD can be tuned across the optical transition frequencies by varying the drive current or the LD temperature. The single-mode emission is characterized by a side-mode suppression ratio (SMSR), which is defined by the ratio of the lasing mode power (P_{las}) with respect to the next strongest mode power (P_{adj}), given by $SMSR = 10 \log \left(\frac{P_{cen}}{P_{adj}} \right)$. The narrow linewidth (LW) of the laser emission is important to resolve the Doppler-free spectral features used to frequency stabilize the LD. The laser LW of 1 – 2 MHz is measured using the heterodyne beat-note method (cf. section 2.5.2). As an alternative, the beta-line method [103], which is used in section 4.2.4, can also be applied to the FM noise spectra of the lasers.

Random fluctuations of the laser intensity and frequency, referred to as noise, may become dominant factors in the clock detection noise (cf. section 1.6.2.1). Laser noise can be described by a power spectral density (PSD) as a function of the Fourier frequency (normalized for a 1-Hz bandwidth). Laser intensity noise is measured using a photodetector that generates a photocurrent (I_{DC}) proportional to the detected optical power, which is subsequently converted into a voltage. The fluctuations of the electrical signal are processed using a fast Fourier transform (FFT) spectrum analyzer to provide the noise PSD (S_n) of the electrical signal voltage in $V/\sqrt{\text{Hz}}$ or in terms of the photocurrent in $A/\sqrt{\text{Hz}}$. The photodetector should operate in the linear response regime so that the measured noise effectively represents the laser intensity noise. Laser intensity noise is often expressed in relative intensity noise (RIN), which is defined by the optical power noise normalized to the average optical power ($S_{RIN} = \frac{S_n^2}{I_{DC}^2}$).

The measurement of laser frequency noise requires a frequency discriminator to convert the FM noise into AM noise that can be measured using a photodetector. For this purpose, in this thesis we make use of the atomic absorption obtained through a vapor cell (cf. Figure 1.11). Subtracting the laser AM noise off-resonance of the vapor cell from the in-resonance noise PSD yields the contribution of the FM-to-AM noise conversion, which is then converted to FM noise PSD using the atomic frequency discriminator. Laser intensity fluctuations on longer timescales are measured via the detected optical power fluctuations expressed in relative [%], while frequency fluctuations are obtained from the heterodyne beat-note frequency measurements using a frequency counter referenced to H-maser (cf. section 2.5.2). More details on laser spectral characterization in view of high-performance vapor-cell clock applications are given in chapter 4 and [104].

The spectral properties of the LHs summarized in Table 2.1 are measured in the CW operation mode, i.e., for the LH-POP, the measurements are performed at the AOM output while the RF power to the AOM is continuously applied. The double passage through the AOM, even in CW operation mode, degrades the light intensity and frequency stabilities by one order of magnitude compared to the LH-CW output (without AOM). The LH-CW is used as the optical frequency reference for the evaluation of frequency-doubled laser systems in chapter 4. The LH-CW is also used in the CW-DR clock described in section 2.3). The LH-POP is employed as the pulsed light source in the POP-DR clock described in section 2.4.

Table 2.1 – Spectral characteristics of the LH-CW (see Figure 2.1) and LH-POP (see Figure 2.2). The results for the LH-CW are essentially presented in chapter 4 and in [105] for the LH-POP data. The LH-POP parameters are measured at the AOM output operated in CW mode.

Parameter	Remark	Unit	LH-CW	LH-POP
Current coeff.		[GHz/mA]	-1	-1
Temperature coeff.		[GHz/K]	-25	-30
SMSR		[dB]	> 40	> 40
RIN	$f = 100$ Hz	[Hz ⁻¹]	$< 1 \cdot 10^{-11}$	$< 2 \cdot 10^{-11}$
FM noise	$f = 100$ Hz	[Hz ² /Hz]	$< 1 \cdot 10^9$	$< 1 \cdot 10^9$
Linewidth		[MHz]	2.1	1.7
Intensity instability	$\tau < 100$ s	[%]	$< 1 \cdot 10^{-2}$	$4 \cdot 10^{-1}$
	$100 < \tau < 10^4$ s	[%]	$< 2 \cdot 10^{-2}$	$< 5 \cdot 10^{-1}$
Frequency instability	$\tau < 100$ s	—	$< 5 \cdot 10^{-12}$	$1.5 \cdot 10^{-11}$
	$100 < \tau < 10^4$ s	—	$< 1 \cdot 10^{-11}$	$< 1 \cdot 10^{-11}$

2.1.2 Frequency-doubled laser systems

This section presents the optical frequency references based on a laser diode emitting at the telecom C-band and a nonlinear crystal that is used to double the laser frequency in order to reach Rb D₂ line transitions around 780 nm [106, 107]. Two frequency-doubled (FD) laser systems described in this section are thoroughly characterized in chapter 4 and evaluated in the CW-DR clock in chapter 5. The first laser system, labeled in this thesis FD-ECL, employs a gain medium and a planar waveguide including a Bragg grating (from RIO) to form a compact ECL. The second laser system, labeled FD-DFB, employs a DFB LD (from EMCORE). The LDs are mounted in a 14-pin butterfly package with a fiber-coupled output. The temperature and the drive current of the LDs are controlled via home-built laser control electronics (noise level of 1 nA/ $\sqrt{\text{Hz}}$). The planar ECL technology allows a single-mode emission exhibiting in particular a lower FM noise and a narrower linewidth compared to DFB lasers while preserving a smaller volume compared to other ECL technologies [100].

LDs emitting at 1560 nm are implemented in two nominally identical fiber-coupled optical setups for frequency doubling and stabilization on Rb frequency references. Figure 2.3 presents the schematic of the FD laser systems. The 1560-nm output of the laser is injected into a periodically-poled lithium niobate (PPLN) waveguide (from NTT Electronics) for second-harmonic generation (SHG). The PPLN output light at 780 nm is then coupled in the frequency reference unit. Two fiber-coupled beam splitters (BSs) give access to two Rb-stabilized frequency reference outputs, one each at 1560 and 780 nm. The BS at 1560 nm is primarily used for spectral characterization (chapter 4) and is removed for Rb clock applications (chapter 5). All of the fiber components are based on single-mode (SM) polarization-maintaining (PM) fiber optics.

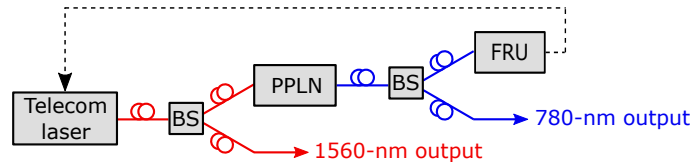


Figure 2.3 – Schematic of the FD laser system stabilized on Rb frequency reference. Red lines: 1560-nm fiber. Blue lines: 780-nm fiber. Dashed black line: electrical. BS: fiber-coupled beam splitter. PPLN: periodically-poled lithium niobate. FRU: frequency reference unit.

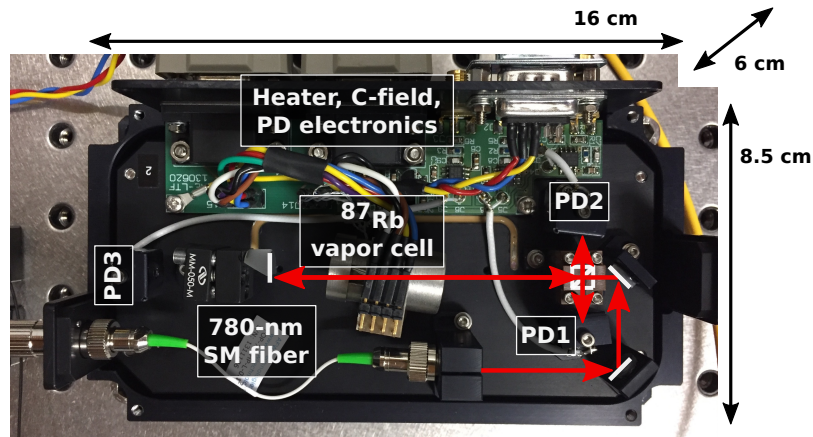


Figure 2.4 – Photography of the frequency reference unit: FRU. Red line shows the optical path. PD: Photodetector. SM: single-mode.

The FRU, depicted in Figure 2.4, accommodates a Doppler-free absorption scheme using a reference cell filled with ^{87}Rb vapor (cf. Figure 2.6a), which is similar to the design of the LHs. The light at the fibered input of the FRU is coupled into free space via a collimation lens, and is then split into two parts using a free-space beam splitter. One part reaches a first photodetector (PD1) for reference cell input light monitoring, whereas the second part is retro-reflected through the reference ^{87}Rb cell and reaches a second photodetector (PD2). A third photodetector (PD3) can also be placed to monitor the Doppler-broadened transmission.

The optical power of the second harmonic at 780 nm (i.e., PPLN output power P_{780nm}), is the quadratic function of the 1560-nm input power P_{1560nm} via

$$P_{780nm} = \eta P_{1560nm}^2, \quad (2.1)$$

where η is the conversion efficiency, which depends on the waveguide temperature. The conversion efficiency of the PPLN at the optimized temperature of 49°C (cf. Figure 2.5) is $\eta = 2.87 \text{ /W}$.

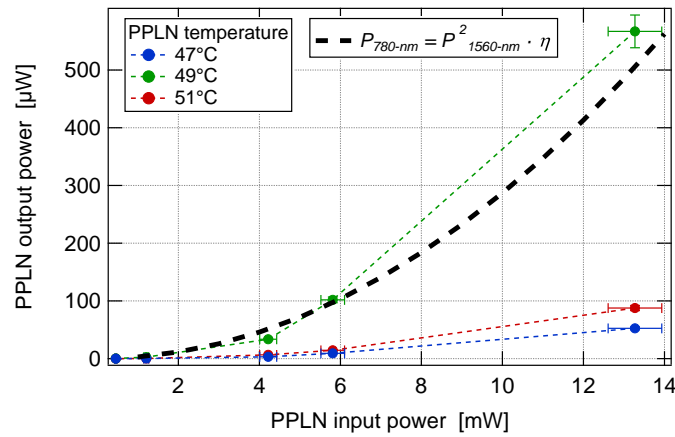


Figure 2.5 – PPLN output optical power as a function of the input power for different PPLN temperature. Black dashed line shows the expected output power at 780-nm output, calculated using equation (2.1).

2.2 Physics packages

At the heart of each DR clock prototype is the physics package [75] that holds the glass cell filled with Rb and buffer gases and the compact microwave cavity. A copper solenoid placed around the cavity and driven by a DC current (C-current) generates the so-called C-field parallel to the cell symmetry axis. The C-field lifts the degeneracy of the hyperfine ground states, allowing to address the clock transition, and sets the quantization axis. The optical electric field and the microwave magnetic field are aligned orthogonally and parallel, respectively, to the C-field orientation to realize the DR interrogation scheme. The laser beam at the PP input is expanded by a diffuser and focused by a bi-convex lens. The enlarged laser beam, with a diameter of 19 mm, traveling along the vapor cell ensures coverage of a large portion of the atoms inside for a high-contrast signal. At the end of the vapor cell, the beam is collimated on the photodetector, generating an electric current proportional to the optical power, which is then measured as a voltage at the output of a pre-amplification circuit. To reduce the coupling of the external magnetic-field and temperature fluctuations to the vapor cell, μ -metal magnetic shielding and thermal insulation layers surround the cell-cavity assembly. The assembled PPs have a volume of 0.8 dm^3 and a mass of 1.4 kg [80]. The next sections describe the common components and the principal characteristics of the PPs implemented in the CW-DR and POP-DR clocks. The dissimilarities of individual PPs and their implementation in distinct clock setups are reviewed in sections 2.3 and 2.4 for the CW-DR and the POP-DR clock, respectively.

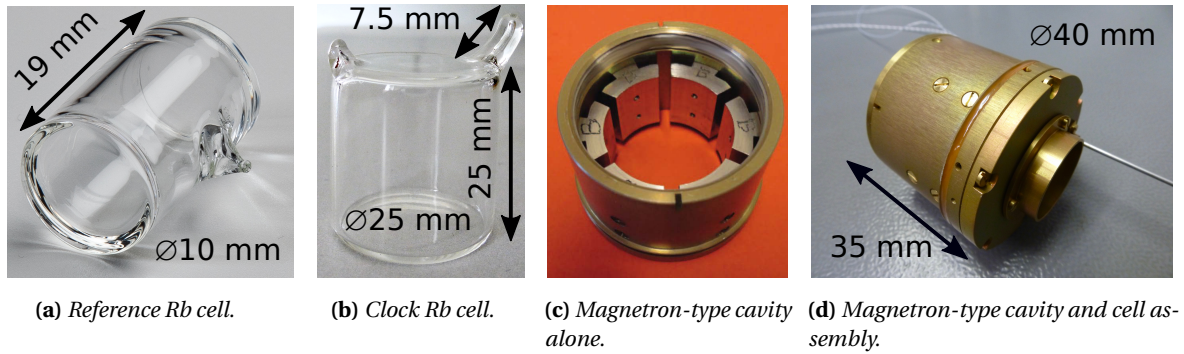


Figure 2.6 – Photography of the vapor cell (a) and (b) and the magnetron-type microwave cavity (c) and (d). Reference Rb cell (a) is implemented in LHs and FRU for laser frequency stabilization. Clock Rb cell (b) containing buffer gases is one of the key component used in the PPs of CW-DR and POP-DR clocks.

2.2.1 Buffer-gas cell

The Rb cells used in clock prototypes, which are filled with Rb and buffer gases, are referred to as clock Rb cells in this work. The buffer gas cells depicted in Figure 2.6b are made of a 25-mm-long borosilicate glass tube with an external diameter of 25 mm. Flat windows of 1-mm thickness are sealed at both ends. A stem reservoir of 7.5 mm in length is located at one side. The buffer gas, produced at LTF [97], contain Ar and N₂ as buffer gases with a partial pressure ratio of $r = \frac{P_{Ar}}{P_{N_2}} = 1.6$ and a total pressure of 32.54 hPa. The buffer-gas density shift effect is the primary clock frequency shift source in vapor-cell clocks (cf. Table 1.4). Hence, it also couples the clock frequency to the fluctuations of the vapor-cell temperature and internal pressure. As such, we actively stabilize the cell and stem temperatures, which is discussed in section 2.2.4.

2.2.2 Magnetron-type cavity

The microwave cavities implemented in both PPs are based on a magnetron-type resonator [57, 108], also known as a loop-gap resonator [109], which allows reducing the volume of the resonator cavity in comparison to simple cylindrical forms. In this way, they enable compact and reliable solutions for high-performance vapor-cell clocks destined for ground-based or in-space applications [22, 80, 110]. The magnetron-type cavity has a cylindrical shield, where six electrodes are placed in rotational symmetry [57]. Photographs of the cavity alone and assembled with the Rb- and buffer gas-filled clock cell are presented in Figures 2.6c and 2.6d, respectively. Cut-off tubes of 20-mm diameter are fixed at both ends to reduce the microwave power loss from the openings required for light propagation.

In DR vapor-cell clocks, the microwave signal resonant with the clock transition $|F = 1, m_F = 0\rangle \leftrightarrow |F = 2, m_F = 0\rangle$ is generated by the LO. The microwave cavity is used to apply the microwave field to the atoms residing in the buffer gas cell that is inserted in the cavity. For the magnetron-type cavity, the resonant mode coinciding with the atomic transition frequency is obtained with a TE₀₁₁-like mode; the magnetic field is aligned in the axial direction parallel to the C-field and the light propagation vector, while the electric field is confined between the electrodes. The quantization axis determined by the applied static magnetic field (C-field) is defined along the z-axis parallel to

Table 2.2 – Key parameters of the simulated microwave performance of the magnetron cavity [80].

Mode	–	TE ₀₁₁
Resonance frequency	ν_{cav}	6.831 GHz
Filling factor	η'	0.136
Field orientation factor	ξ	0.877
Volume	V_{cav}	0.044 dm ³
Q-factor (unloaded)	Q_u	488
Q-factor (loaded)	Q_l	185

the cell symmetry axis. The microwave (magnetic) field H should be parallel to the quantization axis along the cell length in order to have a high-contrast signal. Furthermore, the field amplitude should be homogeneous throughout the cell volume in order to maximize the number of atoms experiencing the same microwave interaction and thereby reduce the position-dependent shifts in the buffer gas cell [83]. The distribution of the microwave magnetic field inside the cavity is characterized by the filling factor η' , which is defined as the efficiency ratio of the magnetic field energy coupled in the vapor cell and that is useful for the clock transition with respect to the total energy stored inside the cavity [61]. The homogeneity of the microwave field orientation along the z-axis inside the vapor cell is characterized by the field orientation factor (FoF) denoted by ξ [57]. The FoF is defined as the ratio of the microwave magnetic field component parallel to the z-axis H_z , which is useful to drive the clock transition ($\Delta m_F = 0$), to the total field energy inside the vapor cell (including both parallel and orthogonal components to the z-axis). The FoF is experimentally determined from the atomic response via the Zeeman spectrum [57], where the transitions for $\Delta m_F = 0$ (π) or $\Delta m_F = \pm 1$ (σ) are governed respectively by the parallel or orthogonal orientation of the microwave magnetic field with respect to the quantization axis.

The quality factor (Q-factor) of a resonator represents the ratio between the average energy stored in the cavity and the energy losses, for example, due to the coupling circuit, cavity walls, and glass cell. The unloaded Q-factor Q_u is defined for the cavity alone (i.e., without the glass cell), whereas the loaded Q-factor Q_l takes into account the glass cell body containing the Rb and buffer gases. A high Q-factor may present a limitation in the medium-to-long-term clock frequency stability due to the increased sensitivity coefficient of the cavity-pulling effect (cf. section 1.5.7) compared to a low Q-factor, such as for the magnetron-type cavity. Table 2.2 outlines the simulated microwave performance of the magnetron-type cavity employed in our DR clock prototypes. For more information on the microwave performance simulations, one may refer to the references [57, 80]. The experimental characteristics determined for the individual cavities used in the CW-DR and POP-DR clocks are presented in sections 2.3 and 2.4.

2.2.3 C-field coils and magnetic shielding

To ensure a uniform magnetic field inside the cell, a solenoid surrounds the cell-cavity assembly. The static magnetic field applied to the cell can be determined from the applied current amplitude via Ampere's law for the solenoid configuration of our PPs. This method relies on the core geometry and the accuracy of the applied current value and may not represent the actual field coupled in the cell. Alternatively, the actual strength of the C-field residing in the vapor cell can be deduced from the atomic response via the Zeeman spectrum. The frequency shifts between the transmission peaks associated with the Zeeman transitions (cf. section 1.1) offer a more accurate measure of the C-field felt by the atoms in the vapor cell. Therefore, in this thesis we deduce the applied C-field from the experimental Zeeman spectra and determine the conversion factor in order to assess the C-field actually felt by the atoms from the C-current applied to the solenoid.

The C-current responsible for the C-field inside the vapor cell is stabilized via control electronics and the cell-cavity assembly is placed in two layers of cylindrical μ -metal shielding to isolate the vapor cell from the environmental magnetic field. The two-layers of μ -metal present a longitudinal shielding factor of 3067, which corresponds to a 70-dB attenuation [80]. The fluctuations of the C-field inside the vapor cell may become an important clock instability source in the medium-to-long term via the second-order Zeeman effect, which is studied in chapter 3 for the POP-DR clock presented in section 2.4.

2.2.4 Temperature control

As reviewed in sections 1.5 and 1.6.2, temperature fluctuations in the cell or stem, and also of the cavity, may have an important degrading impact on the clock stability performance. We stabilize the temperature in the PPs at three sensitive locations: the cell-cavity assembly, the stem, and the external shielding. The temperature at these locations is measured by a negative temperature coefficient (NTC) thermistor and stabilized via a servo controller acting on a resistive heater. NTCs used in our PPs generally have an accuracy of $\pm 0.2^\circ\text{C}$. In addition, polyethylene or polystyrene foam layers surround the cell-cavity assembly to insulate from the environmental temperature fluctuations.

The PP implemented in the CW-DR clock setup has additional NTCs for monitoring that are installed on the outer surface of the microwave cavity. We use one NTC on the front (where the light enters the cell) and one on the back (where the light hits the photodetector) of the cavity, disposed as depicted in Figure 2.7, to assess the temperature fluctuations of the cell-cavity assembly. Temperature fluctuations simultaneously measured in the PP environment and by these two monitoring NTCs on the cavity at 60°C are reported in Figure 2.8. Due to the insulation layers, peak-to-peak temperature variations above 0.4°C measured in the PP external environment are attenuated by more than three orders of magnitude as measured on the cavity close to the apertures for light propagation. The measured temperature instability of 0.5 mK over one day (in terms of Allan deviation) is one order of magnitude lower than the previously estimated values (between 5 and 10 mK) for similar PPs [51, 75, 80], corresponding to a clock stability limit that is one order of magnitude lower (cf. preliminary long-term budget shown in Table 1.6).

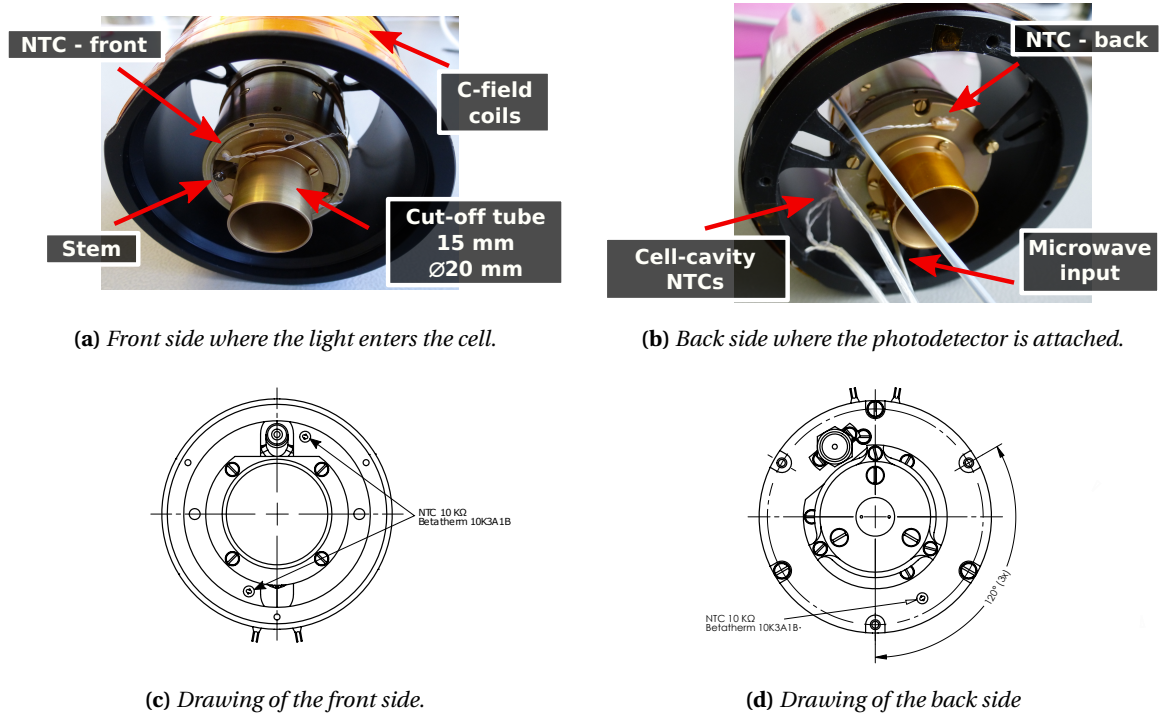


Figure 2.7 – Photography and drawings of the microwave cavity with additional monitoring NTCs. Cavity is 35-mm long and its external diameter is 40 mm. The C-field coil has an internal diameter of 80 mm and length of 47 mm.

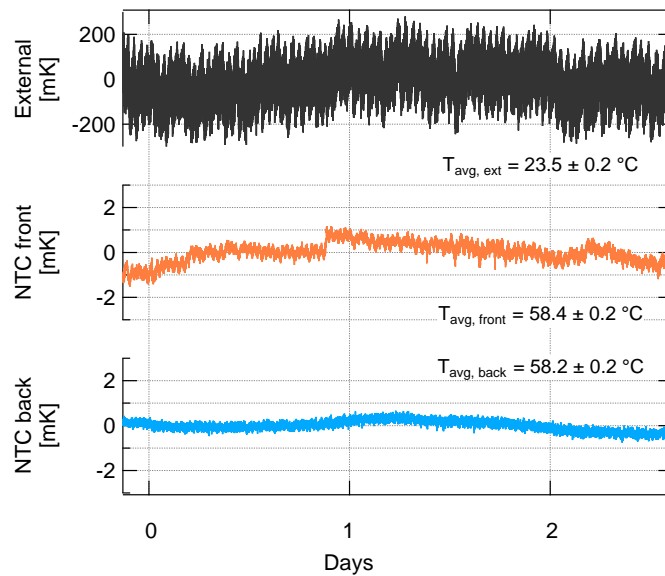


Figure 2.8 – Temperature fluctuations measured in simultaneous in the laboratory and on the microwave cavity. Front and back NTCs correspond to the ones shown in Figure 2.7. During the measurement the cell-cavity assembly's temperature is stabilized at 60°C and the stem at 45°C.

2.3 CW-DR Rb vapor-cell clock

This section presents the CW-DR Rb clock setup that is used to evaluate the frequency-doubled laser systems. The schematic of the CW-DR Rb vapor-cell clock is illustrated in Figure 2.9. The CW-DR clock setup is formed from three parts: the laser system (FD-ECL or FD-DFB), the physics package (PP-CW), and the local oscillator (LO-CW). The following paragraphs review the characteristics of the main components of the CW-DR clock setup.

2.3.1 Optical sources (FD-ECL, FD-DFB, LH-CW)

The CW-DR clock exploits the two FD laser systems (FD-ECL and FD-DFB) based on fiber-coupled laser diodes emitting at 1560 nm (cf. section 2.1.2). We also use the LH-CW, based on a DFB laser diode emitting at 780 nm, (cf. section 2.1.1) in the CW-DR clock to assess the performance of the FD laser systems. As described in section 2.1.2, the 1560-nm output of the laser diode is frequency doubled using a PPLN. One part of the 780-nm output of the PPLN is used to stabilize the laser frequency via the FRU (cf. Figure 2.4) and the other part is guided to the PP-CW for optical pumping and detection. For CW-DR clock applications, the BS at 1560 nm depicted in Figure 2.3 is omitted. The components of the FD laser system (fibered laser, PPLN, and FRU) used in the CW-DR clock occupy in total a volume of 2.0 dm³ and have an estimated mass of 1.2 kg. The detailed spectral characterization of the two FD laser systems is presented in chapter 4 and their application in the CW-DR Rb clock is presented in chapter 5.

2.3.2 Physics package (PP-CW)

The physics package of the CW-DR clock comprises two key elements: the clock Rb cell and the magnetron-type microwave cavity. The microwave signal resonant with the ⁸⁷Rb ground-state hyperfine splitting frequency is generated by the local oscillator (LO-CW described in the next paragraph) and fed into the cavity. The laser light reaching the photodetector at the end of the cell is used to stabilize the LO-CW's frequency via a lock-in amplifier and a servo controller, which closes the clock loop. The general description of the PPs implemented in clock setups is given in section 2.2. This paragraph outlines the specific characteristics of the PP-CW.

The cell temperature is stabilized at 60°C and the stem at 45°C, optimizing the optical absorption of the buffer gas cell. The transmitted light intensity as a function of laser frequency at the end of the buffer gas cell is reported in the top plot of Figure 2.10. The Doppler-free absorption spectrum obtained using the reference Rb cell is illustrated in the bottom plot. The laser frequency is stabilized on one of the optical frequency references provided by the Doppler-free peaks of the direct or cross-over transitions of the two ground states $|F_g = 1\rangle$ and $|F_g = 2\rangle$. The labels indicated on the plot for the optical frequency references are extensively used in the next chapters. The optical transmission spectrum of the clock Rb cell is shifted and broadened by collisional effects. The laser frequency fluctuations are converted into intensity fluctuations through the clock Rb cell and the optical transmission spectrum acts as a frequency discriminator (see section 1.6.2.1). The optical frequency references, corresponding to different frequency discriminators, are used to evaluate the impact of the laser noise on the short-term clock frequency stability in chapter 5.

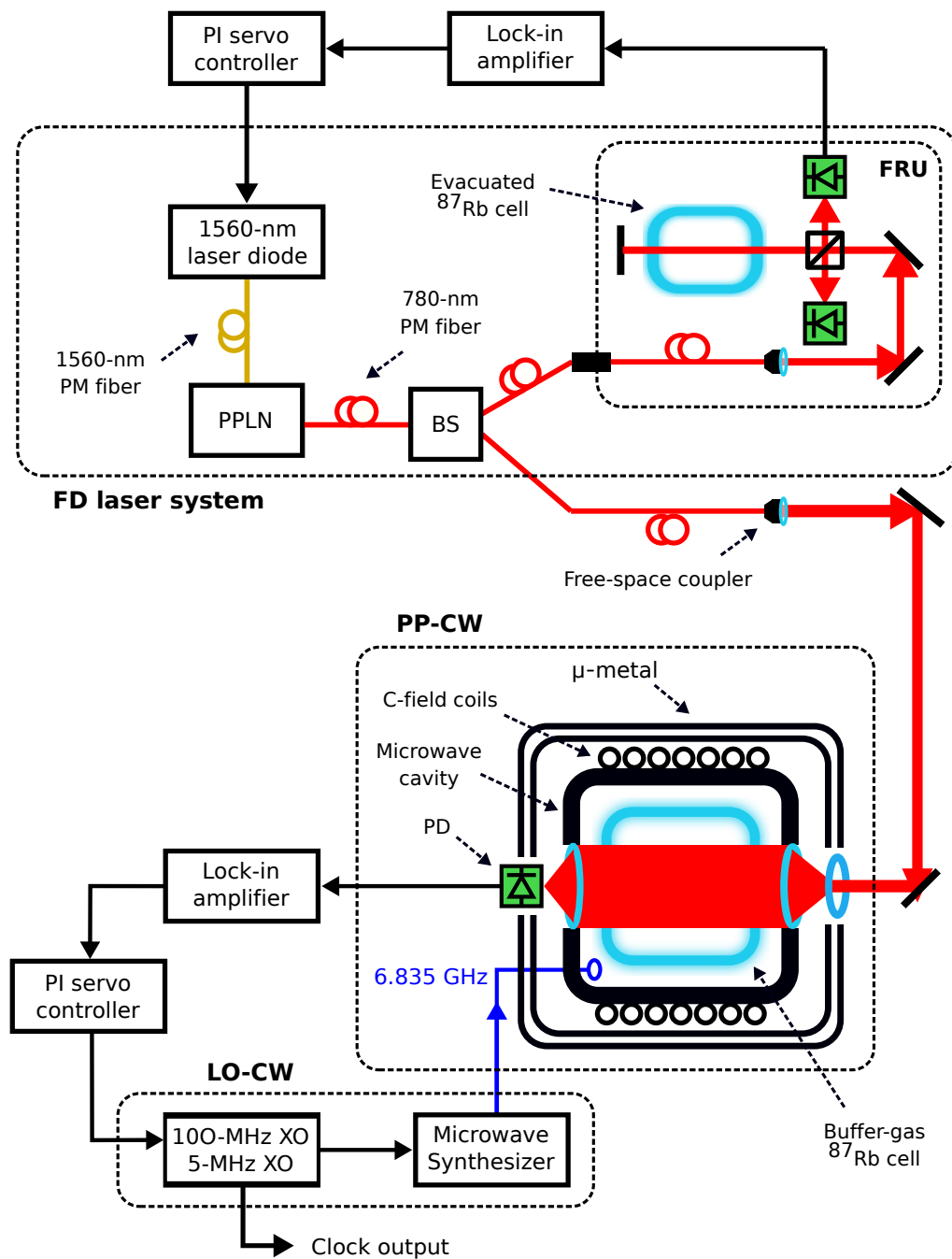


Figure 2.9 – Schematic of the CW-DR clock setup employing the frequency-doubled laser system, PP-CW, and LO-CW. PPLN: periodically-poled lithium niobate. BS: fiber-coupled beam splitter. PD: Photodetector. Black arrows: electrical signal. Red arrows: Free-space 780-nm light. One part of the frequency-doubled 1560-nm laser output is injected into the FRU to stabilize the laser frequency, while the other part is coupled in free-space and guided toward the CW-DR clock PP. In the presence of resonant microwave radiation in the cavity, the optically detected DR signal serves to stabilize the LO-CW frequency at 10 MHz.

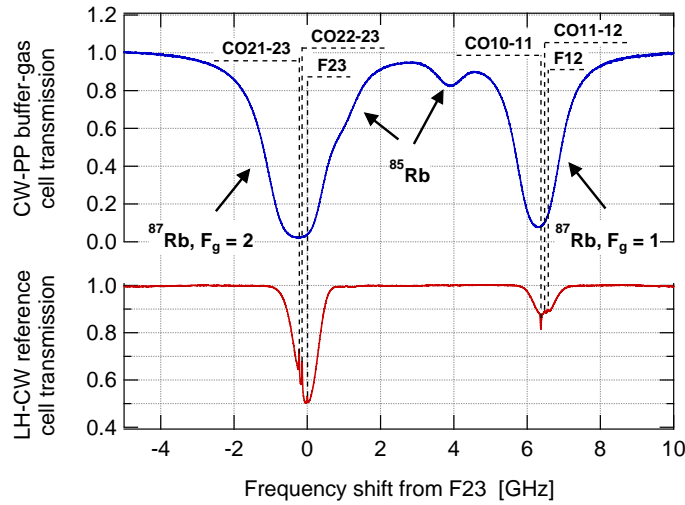


Figure 2.10 – Transmission signals of the LH-CW reference cell (bottom) and the CW-DR clock cell (top). The sub-Doppler resolution of the optical transitions obtained through the reference cell serve to stabilize the laser frequency. The labels for the transitions used in this thesis as frequency references are given. On the transmission signal of the clock cell traces of the isotope ^{85}Rb absorption are notable.

The solenoid used to apply the C-field to the vapor cell is 47-mm long and is made of a 0.25-mm diameter wire making 334 turns. The Zeeman spectrum reported in Figure 2.11 is measured using the FD-ECL for a C-current of 0.25 mA. The frequency shifts between the Zeeman transition peaks indicate that an average C-field amplitude of $2 \mu\text{T}$ is applied to the vapor cell, corresponding to a conversion factor of $8.1 \cdot 10^{-3} \text{ T/A}$ between the applied C-current and the actual C-field inside the vapor cell of the PP-CW.

The microwave cavity holding the clock Rb cell used in the CW-DR clock is a magnetron-type cavity (cf. section 2.2.2). The resonance frequency of the cavity is fine tuned to coincide with the atomic transition frequency at 6.835 GHz. We deduce the FoF of $\xi_{exp} = 0.89$ (89 %) for the magnetron-type cavity of the PP-CW from the Zeeman spectrum depicted in Figure 2.11 (cf. section 2.2.2). The resonance of the cavity has a FWHM of 90 MHz, yielding a loaded quality factor of 80 determined at a cavity temperature of 65°C [75]. The measured temperature sensitivity of the cavity resonance frequency is -33 kHz/K . The sensitivity of the cavity resonance frequency has an impact on the clock frequency stability via the cavity-pulling effect (cf. section 1.5.7). The contribution to clock instability of the CP effect may become a limiting factor, for example, in the case of a high Q-factor or a large frequency detuning between the cavity resonance and the atomic transition. The temperature sensitivity of the cavity resonance frequency with the low Q-factor and small frequency detuning of our cavity yield a CP shift coefficient of $-5.7 \cdot 10^{-14} / \text{K}$ [75].

2.3.3 Local oscillator (LO-CW)

The microwave signal fed into the microwave cavity in CW-DR clock experiments is generated by a commercial frequency synthesizer (RB-1 from SpectraDynamics [111]). The LO-CW has two low-noise quartz oscillators at 5 and 100 MHz in the multiplication chain to reach the 6.835 GHz

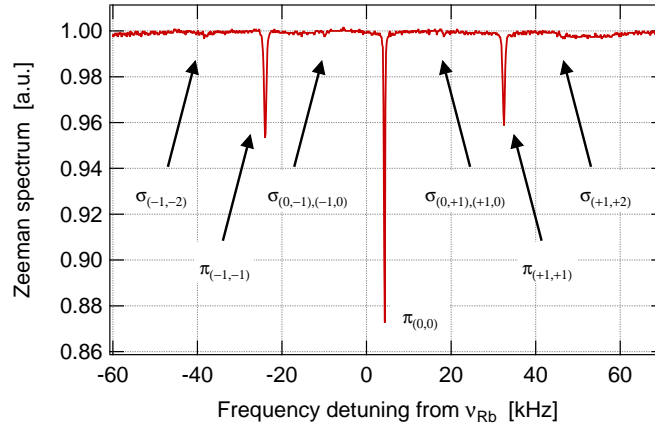


Figure 2.11 – Zeeman spectrum measured using the PP-CW and the FD-ECL. Laser frequency is tuned to the cross-over peak CO10-11 with an optical power of $65 \mu\text{W}$. Microwave power is -36.4 dBm and the C-field amplitude, determined from the detuning between Zeeman peaks, is $2 \mu\text{T}$.

signal resonant with the atomic transition frequency. The 10-MHz output of the LO-CW is obtained by multiplying the 5-MHz reference signal by two. The 100-MHz signal serves as a reference in the multiplication chain of the 6.835 GHz. The frequency of the output signal around 6.835 GHz can be modulated, via the multiplication chain, in a range of $\pm 3 \text{ MHz}$ with $1\text{-}\mu\text{Hz}$ resolution, which covers the clock frequency shift and full Zeeman spectrum measurements (for C-field amplitudes up to 0.1 mT). LO-CW can be operated in two configurations via a computer interface: open loop and closed loop. In the first case, the LO-CW frequency is either only swept or swept and modulated for CW-DR spectroscopy studies, whereas in the second case, the LO-CW frequency is modulated and stabilized to an atomic transition by demodulation of the clock signal. The frequency sweep is achieved with a minimum step size of $1\text{-}\mu\text{Hz}$. The frequency is modulated applying a square-wave signal at the modulation frequency $f_{\text{mod}}^{\text{CW}}$ and depth $\pm f_{\Delta}^{\text{CW}}$, obtained from an external waveform generator. The optically detected CW-DR signal is demodulated by phase-sensitive detection using a lock-in amplifier. The resulting error signal can be approximated by the derivative of the Lorentzian CW-DR signal and the atomic transition frequency at the center of the CW-DR signal is deduced from the error signal. The slope at the center of the error signal is maximized for $f_{\Delta}^{\text{CW}} \approx 0.3 W^{\text{CW}}$ (cf. Appendix B). The modulation frequency must not be faster than the atomic relaxation rates $\gamma_{1,2}$ in order to have a DR interrogation in quasi-static conditions [61]. In this work, the optimal microwave modulation frequency and depth are in the order of 70 Hz and $\pm 70 \text{ Hz}$ for the typical CW-DR signal with a FWHM of $\sim 200 \text{ Hz}$. The frequency shift of the LO-CW with respect to the atomic transition frequency detected using the error signal is corrected using a PI servo controller and acting on the quartz oscillator that has a tuning coefficient of 0.5 Hz/V . The clock output constitutes the 10-MHz signal of the LO-CW operated in a closed loop (i.e., frequency-stabilized on the atomic transition frequency).

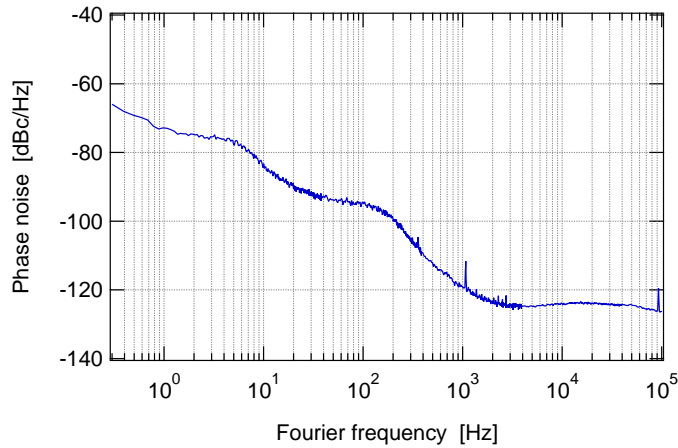


Figure 2.12 – Phase noise measured at the 6.835 GHz output of the LO-CW. Courtesy of C. Affolderbach, LTF

Figure 2.12 depicts the phase noise measured at the 6.835-GHz output of the LO-CW. The phase noise of the LO-CW contributes to the short-term clock frequency instability via the Dick effect (in CW-DR scheme) according to the equation (1.60). In the case of the CW-DR clock scheme used in this research ($f_{\text{mod}}^{\text{CW}} = 70$ Hz and $f_{\Delta}^{\text{CW}} = \pm 70$ Hz), the clock stability limit due to the Dick effect and with the employed LO-CW is $1.6 \cdot 10^{-13}$ when taking into account the even harmonics of the modulation frequency up to 10 kHz.

2.4 POP-DR Rb vapor-cell clock

In the pulsed-optimally pumped scheme, the microwave interrogation and the optical pumping and detection phases are separated in time in order to reduce the impact of the AC Stark shift effect (cf. section 1.3.3). Figure 2.13 illustrates the schematic of the POP-DR Rb vapor-cell clock. The three main parts of the POP-DR clock are the laser system (LH-POP), the physics package (PP-POP), and the local oscillator (LO-POP). The principal difference of the POP-DR clock compared to the CW-DR clock (cf. Figure 2.9) is the AOM implemented as an optical and a RF switches to realize the pulsed interrogation. The optical powers in the pump and detection pulses can be individually adjusted via the RF power injected into the AOM. The timing of the pulses is controlled by the switches for the AOM and microwave cavity input powers using the pattern indicated on a computer interface. We evaluate the frequency instability sources and limitations on the long-term timescale of the POP-DR clock in chapter 3. In the next paragraphs, we review the characteristics of the main components of the POP-DR clock.

2.4.1 Optical source (LH-POP)

The optical source of the POP-DR clock prototype is the LH-POP with the integrated AOM. The LH-POP is described and characterized in section 2.1.1.

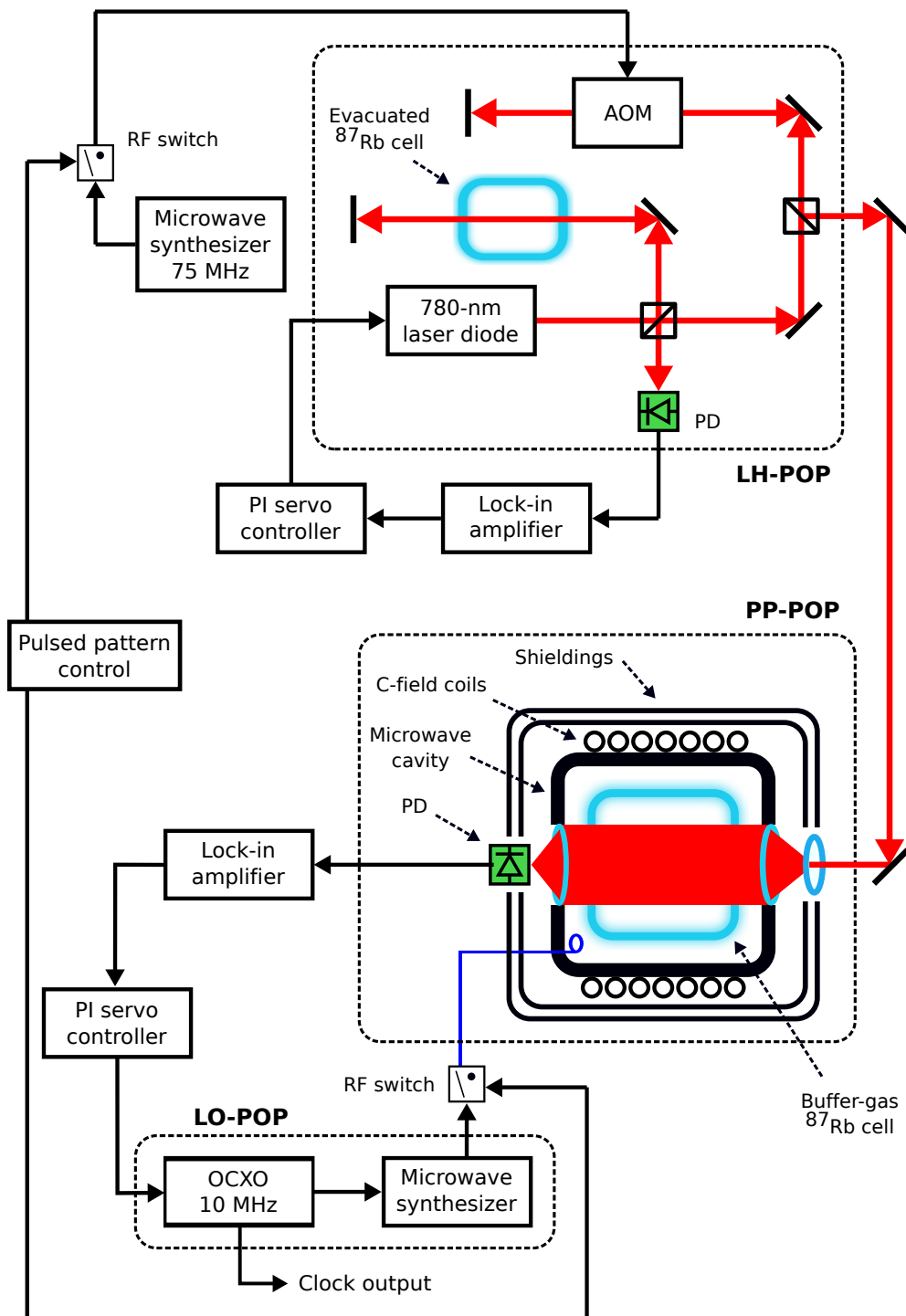


Figure 2.13 – Schematic of the POP-DR clock setup employing the 780-nm LH-POP as the optical source. One part of the 780-nm laser output is frequency stabilized via the reference ^{87}Rb -vapor cell, while the other part, following the double-passage through the AOM is guided to the PP-POP. LO-POP used to generate the 6.835-GHz signal, the clock stabilization loop (lock-in amplifier and servo controller), and the pulsed pattern control are integrated within the clock control electronics [101], which is used to apply the pattern shown in Figure 2.15 using the RF switches. The optically detected POP-DR (Ramsey) signal serves to stabilize the LO-POP frequency.

2.4.2 Physics package (PP-POP)

The physics package of the POP-DR clock, PP-POP, is nominally identical to the PP-CW (cf. section 2.3.2). Section 2.2 provides the general description of the PP-POP, which contains the clock Rb cell and the microwave cavity. In this paragraph, we outline the key parameters of the PP-POP. In order to reduce the clock frequency sensitivity to cell temperature variations (cf. section 3.3.2), we stabilize the temperature of the cell volume at 62.16°C and the stem temperature is stabilized at 59.22°C. The solenoid of 48-mm in length and formed by a 0.30-mm diameter wire making 284 turns is used to apply a C-field of 10.7 μT to the vapor cell of the PP-POP. The corresponding conversion factor between the applied C-current and the C-field strength in the cell is $6.7 \cdot 10^{-3} \text{ T/A}$, in agreement with previously reported data on the same PP [75]. This conversion factor is used to determine the actual C-field in the cell for various C-currents (e.g. in Figure 3.2). The preliminary measurement of the long-term C-field fluctuations performed using the PP-POP reports an instability of $5 \cdot 10^{-11} \text{ T}$ for averaging times of 10^4 s [51]. The contribution of the C-field fluctuations inside the vapor cell to clock frequency instability, via the second-order Zeeman shift effect, is further studied and optimized in section 3.3.1.

In the pulsed scheme the clock signal can be detected in two modes: either via the optical transmission through the vapor cell or via the decay signal of the excited Rb atoms, which can be detected in the microwave domain [69]. In the latter case, the atomic decay signal is coupled out of the cavity through the coupling loop used to couple the microwave field into the cavity. Thus, the microwave detection scheme requires a cavity with a high-quality factor in order to achieve a sufficiently strong SNR. Furthermore, the cavity resonance frequency detuning from the unperturbed atomic transition frequency induces a clock frequency shift via the cavity-pulling shift effect (cf. section 1.5.7). The impact of the latter effect is proportional not only to the frequency detuning, but also to the loaded Q-factor of the cavity. The optical detection method relaxes the requirement of a high Q-factor, which moreover yields a reduced impact of the cavity-pulling shift effect. In our POP-DR clock, we use the optical detection method and the magnetron-type cavity with a low (loaded) Q-factor (< 200).

The resonance frequency and the loaded Q-factor of the microwave cavity are experimentally determined from the input reflection coefficient, also known as the S_{11} parameter. We measure the S_{11} parameter (see Figure 2.14) for the magnetron-type cavity of the PP-POP using a network analyzer under experimental conditions optimizing the long-term clock stability (cf. Table 3.6). The resonance frequency is detected by the power drop of the cavity input reflection. The detuning from the unperturbed Rb ground-state hyperfine frequency is $\Delta\nu_{cav} = 1.87 \text{ MHz}$. The FWHM of the cavity resonance is $W_{cav} = 51 \text{ MHz}$. The loaded quality factor of the cavity containing the glass cell filled with Rb and buffer gases is given by the ratio $Q_l = \frac{\nu_{cav}}{W_{cav}} \approx 140$. The FoF is experimentally determined from the Zeeman spectrum, as described in section 2.2.2 and demonstrated in section 2.3.2 for the case of the PP-CW. The experimental FoF is $\xi_{exp} = 0.92$ (i.e., 92 %) [75].

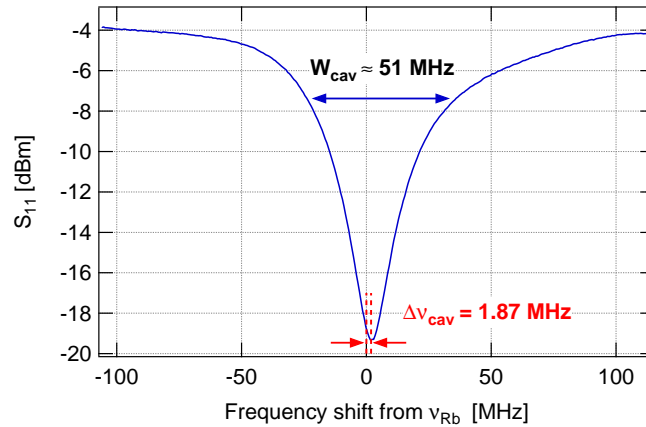


Figure 2.14 – Microwave cavity resonance under optimized clock operating conditions (cf. Table 3.6).

Table 2.3 – Environmental sensitivity coefficients of the resonance frequency ν_{cav} of the magnetron-type cavity implemented in PP-POP. Parameter fluctuations are given for averaging time of 10^4 s: Cavity temperature instability from section 3.3.2.2, chamber internal pressure instability from section 3.3.3, and environmental humidity instability provided by MeteoSwiss¹. ^(a) [75]. ^(b) [51].

Parameter	Parameter fluctuations	Sensitivity coefficient
Temperature	$5 \cdot 10^{-4}$ K	$-40 \cdot 10^3$ Hz/K ^(a)
Pressure	$3 \cdot 10^{-2}$ hPa	$-1.6 \cdot 10^3$ Hz/hPa ^(b)
Humidity	0.4 g/m ³	$-37.5 \cdot 10^3$ Hz/(g/m ³) ^(b)

The resonance mode and frequency of a cavity are sensitive to the environmental parameters via the electrical properties (i.e., dielectric constant) of the medium that fills the cavity's internal volume [86]. For our clock prototype operated in air under ambient conditions, the glass cell with Rb atoms, together with the air filling the cavity, undergoes changes in the dielectric constant arising from fluctuations of the environmental parameters. The measured temperature sensitivity coefficient of the cavity resonance frequency is $-40 \cdot 10^3$ Hz/K [75]. The pressure and humidity sensitivity coefficients calculated for our microwave cavity according to [86] are $-1.6 \cdot 10^3$ Hz/hPa and $-37.5 \cdot 10^3$ Hz/(g/m³), respectively [51]. The environmental sensitivity coefficients of the cavity resonance frequency are collected in Table 2.3 for the magnetron cavity implemented in the POP-PP and typical parameter fluctuations at 10^4 s.

¹Acknowledgments to MeteoSwiss, the Swiss Federal Office of Meteorology and Climatology for the environmental parameters data.

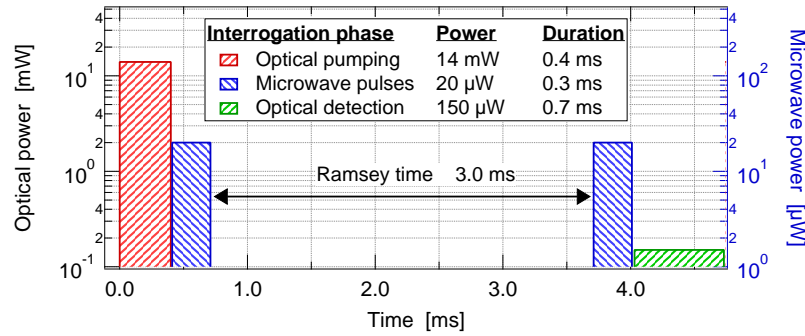


Figure 2.15 – Pulsed interrogation pattern of the POP-DR clock. Left axis: optical pump (red) and detection (green) power. Right axis: microwave (blue) applied to the vapor cell.

2.4.3 Local oscillator (LO-POP)

The local oscillator of the POP-DR clock, LO-POP, is integrated with the clock control electronics, which are used to control the pulsed operation and the clock stabilization loop. The 6.835-GHz signal is generated from a 10-MHz oven-controlled XO (OCXO) via a frequency multiplication chain [101]. A computer interface enables to operate the LO-POP in open- or closed-loop configurations (similarly to those in section 2.3.3) with a customizable pattern for the applied fields. The error signal is derived from the optically detected Ramsey signal and the microwave frequency correction is applied via the PI servo controller. The 10-MHz output of the LO-POP, provided by the OCXO, is used for the metrological and instability characterization of the POP-DR clock (cf. section 2.5).

In the POP-DR interrogation scheme, a Ramsey interrogation scheme is applied in the time domain to the atomic vapor confined in the vapor cell (cf. section 1.3.3). First, a strong optical pulse is applied to optically pump the atoms and reduce the residual microwave coherence. Secondly, two microwave pulses are applied separated in time by a *dark* Ramsey time, when the atoms evolve freely before the second microwave pulse. Thirdly, a weak optical pulse is applied to probe the atoms and detect the clock signal. The pulse timing pattern shown in Figure 2.15 is optimized in order to improve the short-term stability of the POP-DR clock [75]. One cycle of the pattern has a period of $t_C = 4.74$ ms. For the Ramsey signal, the pattern is applied iteratively while sweeping the LO-POP frequency with a minimum step size of 1 μ Hz and in a range of 1.5 GHz. The LO-POP frequency is modulated at each iteration cycle such that the modulation frequency is given by $f_{mod}^{POP} = \frac{1}{t_C} \approx 211$ Hz, with a modulation depth of $f_{\Delta}^{POP} = \pm 80$ Hz. The clock frequency stability limit of the Dick effect in this case is estimated as $1.8 \cdot 10^{-13} \tau^{-1/2}$ [51].

The microwave power fluctuations are measured using a power detector at the 6.835-GHz output of the LO-POP operated in CW mode [51]. In this case, the microwave power instability is 2 nW (0.01 % relative) at 10^4 s averaging time. The fluctuations of the microwave power coupled into the cavity contribute to the clock frequency instability via the microwave power shift effect (cf. section 1.5.6). Therefore, it is important to determine the actual microwave power fluctuations that the atoms feel inside the vapor cell in the pulsed interrogation scheme. To this end, we make use of the atoms and their sensitivity to microwave power fluctuations in this thesis. This measurement and the impact of the MPS on the long-term clock frequency instability are evaluated in chapter 3.

2.4.4 Hermetic chamber

The properties of the key components of the Rb vapor-cell clock are sensitive to variations in environmental parameters, which leads to a coupling between the parameter instability and the clock frequency instability. The long-term stability of vapor-cell clocks is primarily limited by fluctuations in sensitive parameters, which impact clock frequency via different physical effects. In particular, pressure fluctuations perturb the clock frequency via the cavity-pulling shift effect due to the sensitivity of the microwave cavity's resonance frequency to pressure. The impact of this effect is reduced with a low-Q cavity. An additional effect coupling the pressure fluctuations to clock frequency via the vapor cell (volume and pressure variations) is the barometric effect, which may become a dominant limiting factor of the clock stability [60]. The barometric sensitivity of the vapor cell can be optimized based on the cell dimensions, glass material, or buffer gas mixture. Placing the microwave cavity and clock Rb cell in a vacuum environment would drastically reduce the clock sensitivity to pressure fluctuations, but makes the system bulky and power consuming in some applications.

In this thesis, we employ a hermetic chamber to passively stabilize the pressure fluctuations external to the clock cell. We place only the PP-POP, which principally comprises the microwave cavity and the clock Rb cell (cf. section 2.4.2), on a baseplate in the hermetic chamber. The chamber door is tightly closed by an initial pumping to half atmospheric pressure (around 500 hPa) then the pump is stopped. Following a degassing period, the hermetic chamber's internal pressure is stabilized around 535.3 hPa. The temperature of the baseplate, where the PP-POP is placed, is actively stabilized at 27°C. A pressure sensor (Baratron) is used to monitor the internal pressure of the hermetic chamber and an NTC hanging on top of the PP-POP to monitor the internal temperature. Figure 2.16a presents the pressure fluctuations measured simultaneously inside the hermetic chamber and the atmospheric pressure data provided by MeteoSwiss² at a similar altitude as our laboratory (~485 m). The hermetic chamber reduces the peak-peak pressure variations by more than a factor of 10 (and two orders of magnitude over one day in terms of Allan deviation of pressure fluctuations, cf. Figure 3.7a). Due to the reduced pressure fluctuations external to the clock Rb cell, the clock stability limitation via the barometric effect is reduced to few 10^{-15} at one day, and allows the evaluation of the other stability limitations at the level of 10^{-14} or below (see chapter 3) on long-term timescales (up to one day).

The internal temperature of the hermetic chamber and the external temperature (i.e., measured in the laboratory) are shown in Figure 2.16b. External temperature peak-peak variations of 0.5 K are attenuated by a factor of five in the chamber compared to temperature fluctuations in the laboratory. The internal pressure fluctuations are clearly correlated with the internal temperature fluctuations (0.02 K over one day), which represents the main limitation of the hermetic chamber pressure instability. The internal pressure data are reported in Figure 2.17 as a function of internal temperature, with the color map indicating the measurement time scale. According to the ideal gas law, the slope of the linear fit applied to the curve is linearly proportional to the air density inside the hermetic chamber (ρ_{ch}) by a factor equal to the gas constant $R = 287.05 \text{ J}/(\text{kg}\cdot\text{K})$. We estimate the air density inside the chamber to be $\rho_{ch} = 0.5 \pm 0.1 \text{ kg}/\text{m}^3$ for an average temperature

²Acknowledgments to MeteoSwiss, the Swiss Federal Office of Meteorology and Climatology for the environmental parameters data.

Chapter 2. Experimental setups

$T_{avg,int} = 24.8 \pm 0.1$ °C and $P_{avg,int} = 535.3 \pm 0.1$ hPa, which is in agreement for dry air density (~ 0.6 kg/m³) at half atmosphere and 25°C temperature.

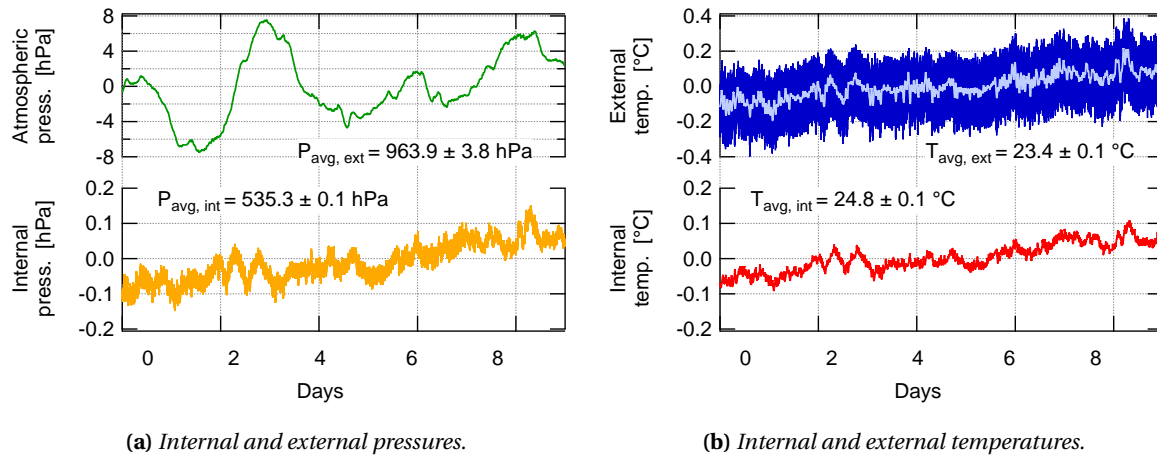


Figure 2.16 – Temperature and pressure fluctuations measured inside and outside the hermetic chamber.

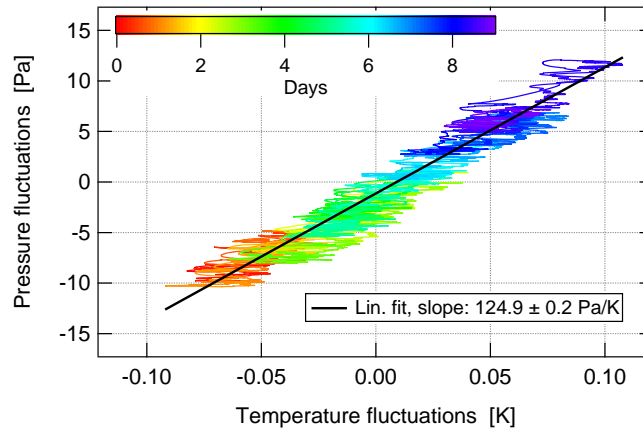


Figure 2.17 – Chamber internal pressure fluctuations as a function of chamber internal temperature fluctuations. Chamber internal mean temperature $T_{avg,int} = 24.8 \pm 0.1$ °C and mean pressure $P_{avg,int} = 535.3 \pm 0.1$ hPa. The air density inside the chamber deduced from the linear fit slope using $R = 287.05$ J/(kg.K) is $\rho_{ch} = 0.5 \pm 0.1$ kg/m³.

2.5 Frequency instability characterization methods

The frequency instability of a frequency standard can only be characterized through comparison to a frequency standard with similar or better and known stability [17] used as the frequency reference. The following sections review the frequency stability characterization methods for microwave and optical frequency standards studied in this thesis.

2.5.1 Microwave frequency standards

At LTF, the frequency reference is provided by an active H-maser (iMaser3000 from T4Science [40]) monitored against the GPS time to correct the long-term frequency variations. The frequency reference is delivered to each post of the laboratory via a low-noise frequency distribution system (from SpectraDynamics). This equipment available at LTF enables (relative) frequency instability measurements with high precision, i.e., $\leq 1 \cdot 10^{-13}$ at 1 s averaging down to few 10^{-16} over one day. The black dotted curve in Figure I3 depicts the typical frequency stability measurement limit given by the performance of the active H-maser. The frequency instability of the microwave frequency standards is characterized at the output of the LO, which is stabilized on the atomic transition frequency against the frequency reference. A low-noise phase comparator (from Miles Design) detects the relative phase (or frequency) difference of the clock output with respect to the frequency reference provided by the AHM. The measurement limit given by the phase comparator residual noise is $1 \cdot 10^{-13}$ at 1 s and around $1 \cdot 10^{-15}$ over one day.

2.5.2 Optical frequency standards

For the instability characterization of the optical frequency standards, such as LHs and FD laser systems, we apply the heterodyne beat method [17]. In this case, as illustrated in Figure 2.18a, one part of the frequency-stabilized lights of two laser systems are overlapped via a fiber-optic beam combiner. When the two laser lights with slightly different frequencies and parallel polarization states are superimposed spatially on a fast photodetector, the photodetector delivers the beat-note signal at a frequency equal to the difference of the two optical frequencies. We stabilize the frequency of the lasers on different atomic frequency references that are obtained using reference Rb cells, as presented in Figure 2.10. The beat-note frequency corresponds to the frequency detuning between two frequency references (cf. Figure 1.2), typically in the RF region. The frequency instability of the beat note is measured using a frequency counter. In this scheme, the H-maser's 10-MHz signal provides a reference for the frequency counter. The LH-CW, with a known frequency instability, provides the reference to evaluate the performance of the two laser systems under study.

Assuming uncorrelated frequency fluctuations between the laser systems, the frequency instability of the beat note corresponds to the sum of squared variances of each laser system's frequency fluctuations. Thus, if one of the lasers is more stable than the other, the beat-note instability is dominated by the worse laser stability. An alternative beat-note scheme, depicted in Figure 2.18b, is based on the simultaneous measurement of three beat notes established between three laser systems at three different frequencies. In this case, the three-cornered hat [112] method can in principle be used to assess the frequency fluctuations of the individual laser systems under the

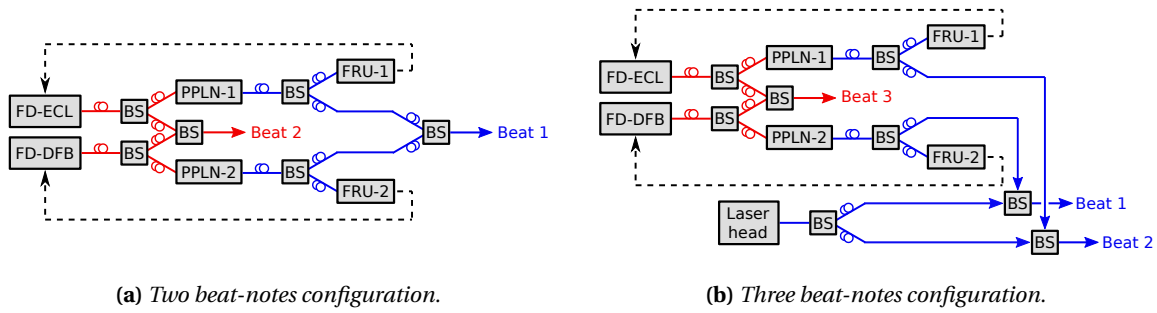


Figure 2.18 – Schematics of beat-note measurement setups, including two lasers or three lasers.

condition that the three beat-note measurements are performed simultaneously and laser systems exhibit independent frequency fluctuations at similar levels. However, considering the laser systems studied in this thesis in chapter 4 the analysis using the three-cornered hat method did not lead to reasonable results. The reason for that is that one of the laser systems under study (FD-ECL) exhibits one to two orders of magnitude lower frequency instability compared to the other two laser systems (FD-DFB and LH-CW).

The beat-note method is also employed for laser linewidth measurements (cf. section 4.2.2) in the configuration shown in Figure 2.18b. In this case, instead of a frequency counter, an RF spectrum analyzer scans the spectral distribution of the beat-note signal of two laser outputs. Assuming uncorrelated frequency noise, the beat-note signal linewidth corresponds to the square root of the sum of squared linewidths of the individual laser systems.

2.6 Conclusion

In this chapter, we described the experimental apparatus employed within this thesis. Two distinct clock prototypes are presented: the CW-DR clock and the POP-DR clock. Both involve a buffer gas cell and a magnetron-type cavity, and both use a frequency-stabilized laser system for optical pumping and detection. The main difference between the two clocks is the laser system. The POP-DR clock employs the LH-POP, which is based on a laser diode emitting directly at the Rb D₂ line at 780 nm and is operated in pulsed mode. Meanwhile, the CW-DR clock employs the frequency-doubled laser system, which is based on a laser diode emitting in the telecom C-band region at 1560 nm.

The metrological and stability properties of Rb clocks and laser systems presented in this chapter are studied in the next chapters. First, we analyze the effects perturbing the POP-DR clock frequency and evaluate the arising limitations of the clock stability at the level of 10^{-14} up to 1 day (in chapter 3). The spectral properties of the frequency-doubled laser systems, FD-ECL and FD-DFB, are then extensively characterized as regards their implementation in high-precision applications at 780 and 1560 nm (in chapter 4). Finally, we evaluate the exploitation potential of the FD-ECL and FD-DFB in high-performance Rb clocks using the CW-DR clock and study the short-term clock stability limitations arising from the laser noise (in chapter 5). The LH-CW is also used in the CW-DR clock to assess the performance achieved with FD laser systems.

3 Evaluation of long-term instabilities in a POP-DR Rb cell clock

The frequency stability of vapor-cell clocks on long-term timescales is mostly governed by fluctuations of the experimental and environmental parameters via the physical effects reviewed in section 1.5). The impact of the perturbing effect is characterized by the clock frequency sensitivity coefficient to the varying physical parameter. The instability contributions of the independent effects are evaluated in an instability budget, which serves to identify the dominant contributions limiting the clock stability. In this chapter, we present an analysis of the limitations and a detailed budget of the long-term instability for our compact POP-DR Rb vapor-cell clock (cf. section 2.4).

The preliminary long-term clock instability budget of our POP-DR clock, presented in Table 1.6 based on previous studies [51, 75], indicates the main instability sources as the second-order Zeeman shift effect and the stem temperature coefficient. In view of improving the long-term clock stability, the limitations of these two effects are analyzed and their contributions are reduced and consolidated. In addition, we evaluate the instability contributions of all important physical effects and quantify the resulting clock stability limits on long-term timescales. The fluctuations of the involved parameters are measured, via the atomic response when possible, and the clock frequency sensitivity coefficients are evaluated under optimized conditions.

First, this chapter discusses the Ramsey signal parameters and the optical-pump frequencies in view of improving the long-term clock stability. Secondly, the contributions of the different processes to the long-term clock instability are evaluated. We then present the comprehensive long-term instability budget for our POP-DR clock, including all known physical effects relevant on timescales from 10^4 s up to 10^5 s (one day) of averaging time. Finally, we present and discuss the measured clock frequency instability. Sections 3.3 and 3.4 are essentially based on our article [113]. The text and figures in these two sections are adapted from [113].

3.1 Ramsey signal

Figure 3.1 shows the measured Ramsey signals for the POP-DR scheme with microwave pulse areas of $\theta = 0.56\pi$ and $\theta = \pi/2$. The frequency shift of the central fringe central frequency (ν_{clock}) from the unperturbed Rb ground-state hyperfine splitting frequency ν_{Rb} , induced via the physical effects reviewed in section 1.5, is largely dominated by the buffer-gas density shift of $\Delta\nu_{BG} = 4247.4$ Hz (cf. Table 1.4). The key parameters of the central fringes of the two Ramsey signals are outlined in Table 3.1. The signal amplitude and thus the contrast are decreased by $\sim 2\%$ for microwave pulse areas slightly different than $\theta = \pi/2$. At the end of the microwave interrogation using $\theta = 0.56\pi$ pulses, the population is not entirely inverted and yields a residual coherence at the beginning of the optical detection phase, which is described by the Bloch vector representation in Figure 1.7c. The contrast of the Ramsey central fringe has an impact on the clock performance on short-term timescales (cf. section 1.6.2.1). The short-term clock stability degradation induced by the ($\sim 2\%$) reduced signal contrast is estimated in the order of $\sim 5\%$. Nonetheless, microwave pulse areas of $\theta = 0.56\pi$ lead to an optimized MPS coefficient, reducing the long-term clock stability limit of the microwave power fluctuations by approximately one order of magnitude [51].

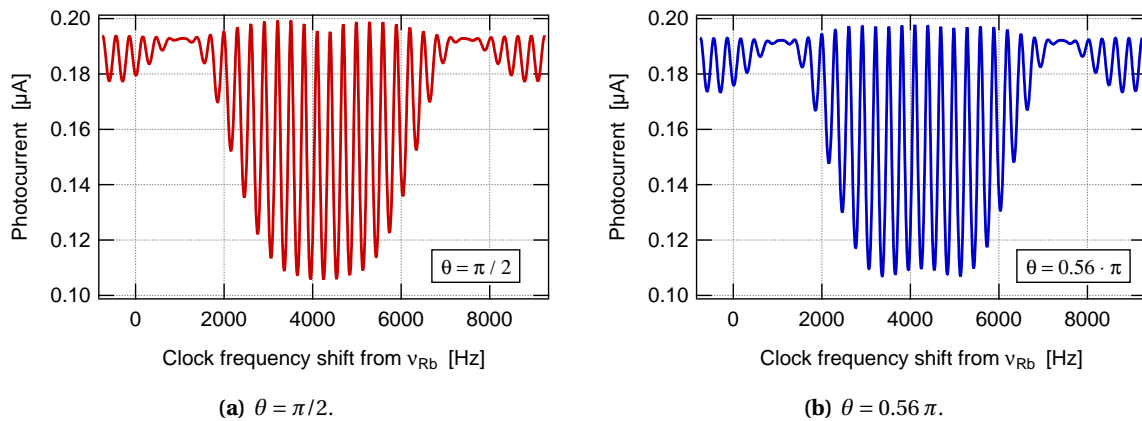


Figure 3.1 – Ramsey spectra measured for microwave pulses of $\theta = \pi/2$ and $\theta = 0.56\pi$ by varying the applied microwave power for fixed pulse duration of 0.3 ms and the Ramsey time is 3 ms. All other experimental conditions are kept identical.

Table 3.1 – Key parameters of the central Ramsey fringes measured for $\theta = \pi/2$ and $\theta = 0.56\pi$ pulses. The parameters are deduced from the signals shown in Figure 3.1 applying the fit function of the equation (1.28).

Signal parameters	Unit	$\theta = \pi/2$	$\theta = 0.56\pi$
Amplitude	[nA]	89.1	87.5
Contrast	[%]	45.6	44.3
FWHM	[Hz]	146.5	146.5
Approx. D_s	[nA/Hz]	1.5	1.4

3.2 Trade-off between short- and long-term clock stability

The experimental parameters (optical, microwave, and C-field amplitudes and cell and stem temperatures) impact the clock frequency stability at all timescales. A trade-off usually is necessary to optimize the clock performance given the timescale of interest. The SNR-limited short-term stability of the POP-DR clock was optimized through considering the duration and amplitude of the applied fields [75]. In the present work, the emphasis is on long-term timescales up to 1 day. The MPS-limited long-term instability of our POP-DR clock is optimized for the laser frequency tuned to $|5^2S_{1/2}, F = 2\rangle$ ground-state transitions and microwave pulses of $\theta = 0.56\pi$ [84]. This results in a weak loss in the signal contrast and degrades the short-term stability by $\sim 5\%$ (cf. section 3.1).

In the short term, one of the main instability contributions arises from the optical detection noise, comprising laser intensity noise and FM noise converted to AM noise through the atomic vapor (cf. section 1.6.2.1). The contribution of the FM-to-AM noise conversion [90, 91], which is quantified by the frequency discriminator slope obtained from the atomic absorption line, depends on the experimental conditions: laser intensity and frequency and vapor cell temperature. Table 3.2 summarizes the frequency discriminators of the FM-to-AM noise conversion associated with the direct or cross-over resonances obtained between the $|5^2S_{1/2}, F = 2\rangle$ ground state and the excited states on D₂ line, measured at an optical power of 14 μ W and a cell temperature of 62.16°C. Under unchanged experimental conditions (except for the laser frequency) and assuming equivalent laser intensity and frequency noises for the three optical frequencies, the optical detection noise is mainly affected by the frequency discriminator slope associated with the FM-to-AM noise conversion phenomenon. The converted noise adds quadratically to the laser intensity and detector noises (cf. Appendix A), yielding the total clock optical detection noise.

In the long term, the laser frequency has an impact on the clock instability via light-induced effects (cf. section 1.5.5). The intensity LS coefficient of the POP-DR clock is minimized for the laser frequency tuned to the CO21-23 cross-over resonance (cf. Table 3.3). The instability contribution of the LS effect adds quadratically to the contributions of the other effects (studied in the next section 4.3). In order to improve the long-term clock stability, the laser frequency CO21-23 (minimizing the LS contribution) is used, which results into a short-term clock stability degradation by a factor of two compared to the use of CO22-23. This drawback may be avoided by using a lower FM noise laser source.

Table 3.2 – Discriminator slope (D_{FM-AM}) of the FM-to-AM noise conversion via the clock Rb cell for laser frequency tuned to one of the $|5^2S_{1/2}, F = 2\rangle$ ground-state transitions.

Laser frequency	D_{FM-AM} [nA/MHz]
CO21-23	-0.44
CO22-23	-0.13
F23	0.28

3.3 Analysis of long-term clock instability sources

The vapor-cell clock frequency is sensitive to fluctuations of the experimental and environmental parameters [47] via different physical processes [67] characterized by the respective sensitivity coefficients. In this section, we evaluate the impact of these processes (see section 1.5) on our clock's stability performance on long-term timescales and discuss the related limitations.

3.3.1 Second-order Zeeman shift

The magnetic field fluctuations inside the vapor cell contribute to the clock frequency instability via the second-order Zeeman effect. The clock frequency sensitivity coefficient being linearly proportional to the C-field amplitude (cf. section 1.5.1) can be reduced by decreasing the C-field strength B_z applied to the vapor cell. The second-order Zeeman effect was identified as one of the dominant instability sources that limits the long-term stability performance of our POP-DR clock [51] (cf. preliminary budget shown in Table 1.6). The applied C-field amplitude was $10.7 \mu\text{T}$, corresponding to a second-order Zeeman shift coefficient of $1.8 \cdot 10^{-4} / \text{T}$ ($1.2 \cdot 10^6 \text{ Hz/T}$) that was deduced from the linear fit locally applied to the quadratic function of clock frequency shift depicted in Figure 3.2. A reduction¹ of the applied C-field to $3.5 \mu\text{T}$ (by a factor of three) yielded a second-order Zeeman shift coefficient of $5.8 \cdot 10^{-5} / \text{T}$ ($4.0 \cdot 10^5 \text{ Hz/T}$) and the clock instability contribution decreased by a factor of three given unchanged field fluctuations. Meanwhile, the absolute clock frequency shift induced by the second-order Zeeman shift $\Delta\nu_{Ze}$ was also reduced to 0.7 Hz from 6.6 Hz corresponding to the C-field amplitude of $10.7 \mu\text{T}$ (cf. Table 1.4).

To assess the magnetic field fluctuations inside the PP-POP vapor cell, we exploit the atomic response to magnetic field variations. To do so, we increase the second-order Zeeman shift sensitivity of the clock frequency by stabilizing the LO-POP frequency on the Zeeman transition $|5^2S_{1/2}, F=1, m_F=-1\rangle \leftrightarrow |5^2S_{1/2}, F'=2, m_F=-1\rangle$. The transition frequency between Zeeman sub-levels with $m_F \neq 0$ is sensitive to magnetic field variations in the first order (cf. equation (1.3)). In such a configuration, the clock frequency fluctuations are dominated by the magnetic field fluctuations via the sensitivity coefficient given by $(m_F^{F=1} + m_F^{F=2}) 7 \cdot 10^9 \text{ Hz/T}$. The measured C-field fluctuations are reported in Figure 3.3 along with those of the typical external magnetic field measured outside of the PP-POP using a fluxgate sensor. Figure 3.3 also demonstrates the C-current applied to the solenoid around the clock cell, expressed in terms of magnetic field fluctuations (left axis). The right axis scales the corresponding clock stability limit estimated with the sensitivity coefficient for a C-field of $3.5 \mu\text{T}$. On short-term timescales, magnetic field fluctuations in the clock cell are limited by the noise of the current source. On long-term timescales, field fluctuations in the clock cell are on the level of 20 pT, limited by the external field fluctuations that are attenuated by the magnetic shielding factor of ~ 300 deduced from simultaneously measured field variations.

¹The *high* C-field amplitude of $10.7 \mu\text{T}$ was initially chosen to avoid the superimposition of neighboring sigma transitions on the clock transition ($|5^2S_{1/2}, F=1, m_F=0\rangle \leftrightarrow |5^2S_{1/2}, F'=2, m_F=0\rangle$), which may occur in a case where the sigma transition lines are largely broadened due to field inhomogeneities. For the microwave cavity of our POP-DR clock, the microwave field has a high uniformity along the quantization axis defined by the C-field (FoF of 92 %, cf. section 2.4.2). The narrow Zeeman transition lines allow to decrease the C-field such that the clock transition frequency sensitivity to second-order Zeeman effect reduces while avoiding the superimposition of neighboring Zeeman (sigma) transitions in the clock transition.

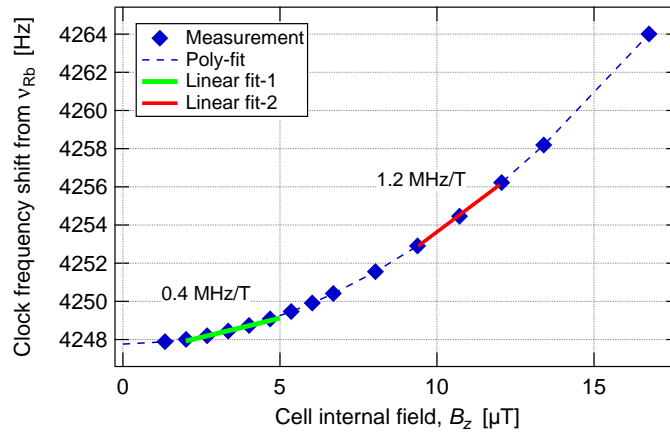


Figure 3.2 – Clock frequency shift as a function of the applied C-field, the second-order Zeeman shift $\Delta\nu_{Ze}$. Figure adapted from [113].

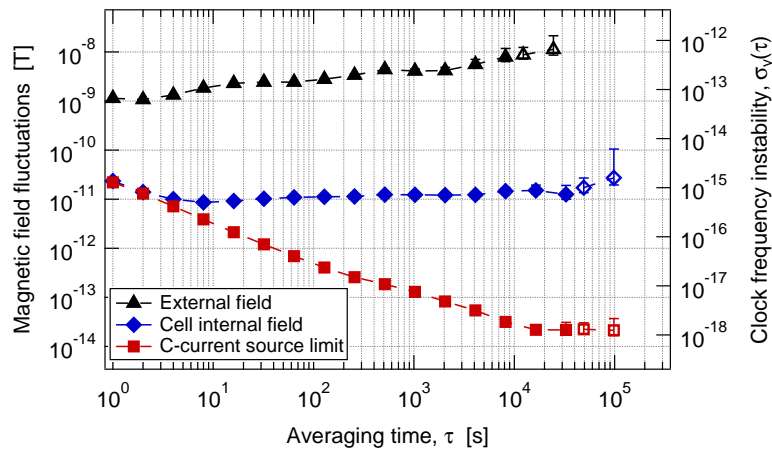


Figure 3.3 – Magnetic field fluctuations and clock stability limit via second-order Zeeman shift effect. Stability analysis performed using ThèoH statistics (cf. section 1.6.1); filled markers: overlapping Allan deviation; empty markers: Thèo1. Figure adapted from [113].

3.3.2 Buffer-gas density shift

Fluctuations of the cell volume temperature perturb the clock frequency through the temperature-dependent buffer-gas pressure shift [76] and fluctuations of the stem temperature perturb the clock frequency via the buffer-gas density change resulting from the temperature gradient between the cell volume and stem [77]. Furthermore, the fluctuations of the cell volume induced by the barometric effect also act on the buffer-gas density via cell internal pressure variations (cf. section 3.3.3). The temperature-dependent spin-exchange shift effect [72, 78] and its impact on the clock frequency stability is discussed in section 3.3.4. In this section, we focus on the temperature sensitivities of the cell volume and stem due to the buffer-gas collisions and the induced clock frequency instabilities (cf. section 1.5.2).

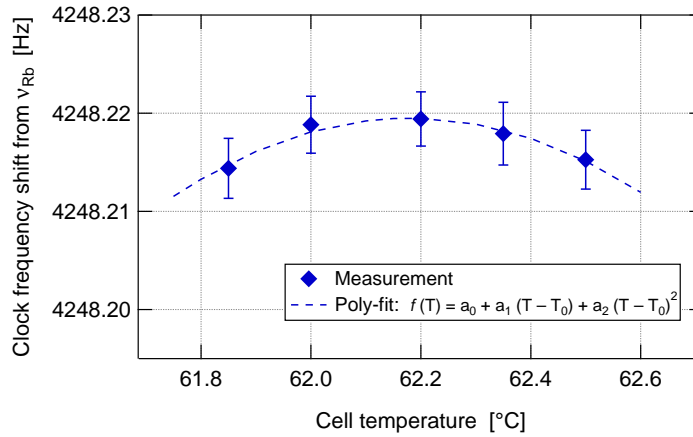


Figure 3.4 – Clock frequency shift as a function of the clock cell temperature, the buffer-gas density shift $\Delta\nu_{\text{BG}}$. Figure adapted from [113].

3.3.2.1 Cell and stem temperature coefficients

The buffer-gas mixture of argon and nitrogen with a ratio of $r = \frac{P_{\text{Ar}}}{P_{\text{N}_2}} = 1.6$ of the clock Rb cells reduces the first-order cell temperature coefficient (TC) (cf. Table 1.1). The clock frequency shift measured as a function of the cell temperature while keeping the stem temperature constant at 59.22°C is reported in Figure 3.4. The cell temperature that minimizes the first-order cell TC is obtained at the inversion temperature (T_{inv}) of the quadratic fit applied to the data and the associated first-order cell TC is obtained with its derivative evaluated at T_{inv} . The inversion temperature for our clock cell is $62.16 \pm 0.2^\circ\text{C}$ and the first-order cell TC evaluated in the interval of $T_{\text{inv}} \pm 0.25 \text{ K}$ is $\pm 2.3 \cdot 10^{-12} / \text{K}$.

The clock frequency sensitivity to stem temperature variations, which cause a buffer-gas density change in the vapor cell, is measured while keeping the cell volume temperature constant. Figure 3.5 presents the clock frequency shift as a function of the stem temperature; the stem TC determined by the slope is $1.2 \cdot 10^{-12} / \text{K}$. Each data point is the average of the clock frequency shift measurement of 100 s at varied stem temperatures. According to [80], on these *fast* timescales, it is mainly the buffer-gas density change in the cell volume that dominates in the case of vapor cells with a stem, while the Rb density change contributes only weakly. Furthermore, the contribution of the spin-exchange shift effect is included in principle in the experimentally determined temperature coefficients of our clock cell.

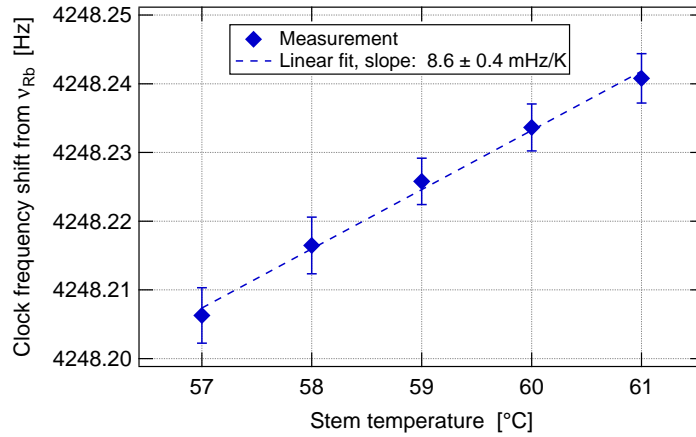


Figure 3.5 – Clock frequency shift as a function of the stem temperature.

3.3.2.2 Temperature fluctuations

In order to estimate the contribution to the clock instability of the buffer-gas density shift, we study the temperature fluctuations of the vapor cell and stem. In principle, temperature fluctuations inside the vapor cell can also be assessed by measuring the clock frequency fluctuations using a cell temperature corresponding to an increased cell TC. Nevertheless, for temperature fluctuations to become the dominant clock instability source, the cell temperature should change by more than $\pm 5^\circ\text{C}$, which is impractical in our clock. Instead, we make use of NTCs implemented in the PPs to assess the cell and stem temperature fluctuations.

As demonstrated in Figure 3.6, the typical temperature instability of the PP-CW under ambient laboratory conditions, measured using the monitoring NTCs placed on the microwave cavity of the PP-CW (cf. Figure 2.7), is below 0.5 mK over one day. In the PPs, the cell (or stem) temperature is detected using two NTCs in a Wheatstone bridge configuration and stabilized with a feedback on the heater current. In order to determine the cell temperature fluctuations using an independent NTC whose response is not included in the feedback loop, we modify the Wheatstone bridge into two separate and simpler resistance measurement circuits. One of the NTC measurements serves to stabilize the cell temperature and the other serves to monitor the temperature fluctuations independently from the feedback loop. These modifications were performed on the cell and stem temperature control circuits of the PP-POP in order to assess the temperature fluctuations more precisely. The cell and stem temperature instability measured using the independent NTCs using PP-POP placed in the hermetic chamber are depicted in Figure 3.6. A stability level below 10 μK over one day is determined for both cell and stem, which would lead to a clock stability limit well below 10^{-16} due to the buffer-gas collisions. The right axis in Figure 3.6 presents the clock stability limit estimated using the cell TC of $2.3 \cdot 10^{-12} / \text{K}$ determined in the previous section 3.3.2.1. In view of operating our POP-DR clock under ambient laboratory conditions, the temperature instability measured using the PP-CW offers a reliable estimation of the upper limit of cell and stem temperature fluctuations. Thus, given the temperature fluctuations of the POP-DR clock cell at the level of 0.5 mK, the estimated clock stability limits using the cell and stem TCs are $\leq 10^{-15}$ for the one-day timescale.

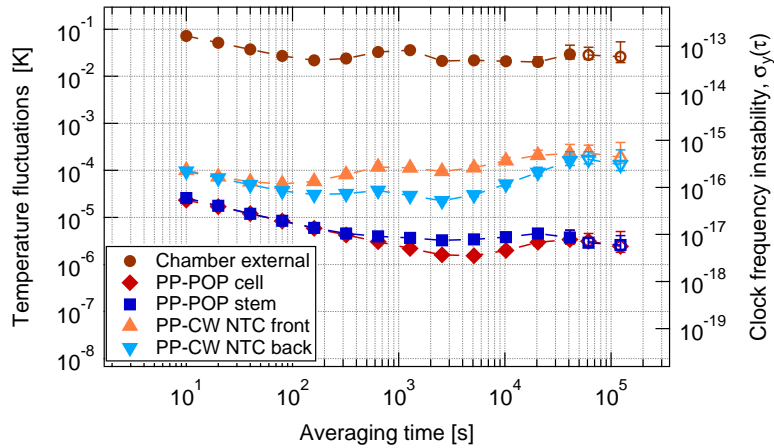


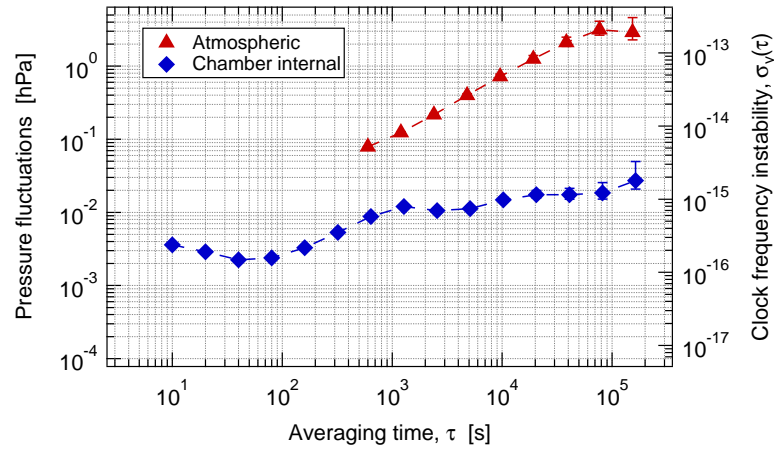
Figure 3.6 – Temperature fluctuations measured on the cell and stem of the PP-POP (placed in the hermetic chamber) and on the microwave cavity of the PP-CW (placed outside the chamber). PP-CW temperature fluctuations are shown in Figure 2.8. Left axis: temperature fluctuations in K. Right axis: estimated relative clock stability limit. Stability analysis performed using ThèoH statistics (cf. section 1.6.1); filled markers: overlapping Allan deviation; empty markers: Thèo1. Figure adapted from [113] and includes additional data.

3.3.3 Barometric effect

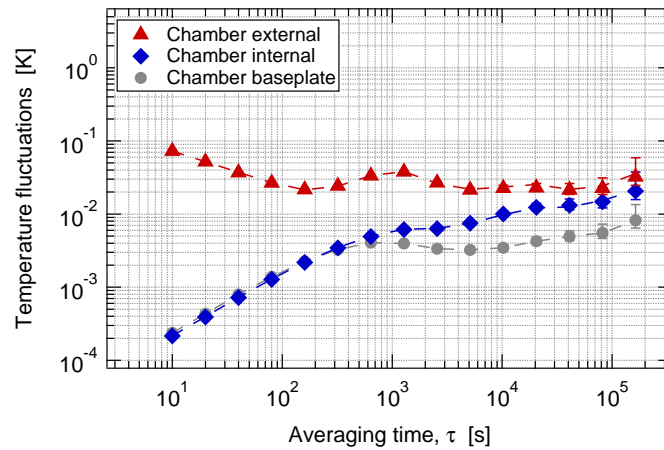
In the POP-DR clock, the dominant contribution is the barometric effect due to the variation of the buffer-gas pressure in the cell, which is induced by the bending of the cell windows in response to varying external pressure [60] (cf. section 1.5.3). Typical atmospheric pressure fluctuations can reach 3 hPa (in terms of Allan deviation) over one day and result in a clock instability contribution at a level of $2 \cdot 10^{-13}$ (see Figure 3.7). In order to decrease the barometric effect-induced clock stability limit below $2 \cdot 10^{-14}$ over one day, we must reduce the barometric sensitivity coefficient of the vapor cell, which depends on the glass cell's dimensions and material [51], by a factor of ten. For example, increasing the glass wall thickness by a factor of 2.2 or decreasing the cell diameter by a factor of 1.8 would lead to an approximately ten times lower barometric sensitivity. As an alternative, we employ a hermetic chamber in this thesis to passively stabilize the pressure fluctuations in the PP-POP vapor cell environment (cf. section 2.4) while keeping the same cell.

Figure 3.7 presents the simultaneously measured internal and external chamber pressure and temperature fluctuations in terms of overlapping Allan deviation. In this case, the pressure fluctuations in the PP-POP vapor cell environment (internal chamber pressure) are reduced by two orders of magnitude (to 0.03 hPa, see Figure 3.7) and the induced clock stability limit is reduced to $2 \cdot 10^{-15}$ up to a one-day timescale. The internal temperature of the chamber is controlled via an actively stabilized baseplate temperature in the short term; on long-term timescales, it is governed by the residual external temperature fluctuations transferred inside the chamber. The pressure fluctuations inside of the chamber are limited by the internal temperature fluctuations via the ideal gas law. The simultaneously measured chamber temperature and pressure fluctuations presented in Figure 2.16 (bottom plots of the two graphs) present highly correlated variations.

3.3. Analysis of long-term clock instability sources



(a) Left: Pressure fluctuations. Right: Estimated clock stability limit via the barometric effect.



(b) Temperature fluctuations.

Figure 3.7 – Chamber internal and external pressure and temperature fluctuations. Figures adapted from [113] and (b) includes additional data (Chamber baseplate temperature).

The clock frequency fluctuations measured following the chamber pressure change (see Figure 3.8a) demonstrate an equilibration process with a time constant of 1.2 ± 0.2 days. The chamber pressure (see Figure 3.8b) presents a stabilization period with a time constant of 1.71 ± 0.01 days due to the degassing process. The clock frequency variation during the pressure stabilization in the chamber is notably dominated by the pressure variation in the chamber, which occurs via the barometric effect. The peaks of the measured clock frequency and the oscillations of the pressure appear to originate from temperature fluctuations. The barometric sensitivity coefficient of the clock frequency is deduced from the linear fit depicted in Figure 3.9. The coefficient of $(6.6 \pm 0.2) \cdot 10^{-14}$ /hPa measured under reduced pressure conditions is slightly lower than the coefficient $((8.1 \pm 0.7) \cdot 10^{-14}$ /hPa) measured under atmospheric pressure [51].

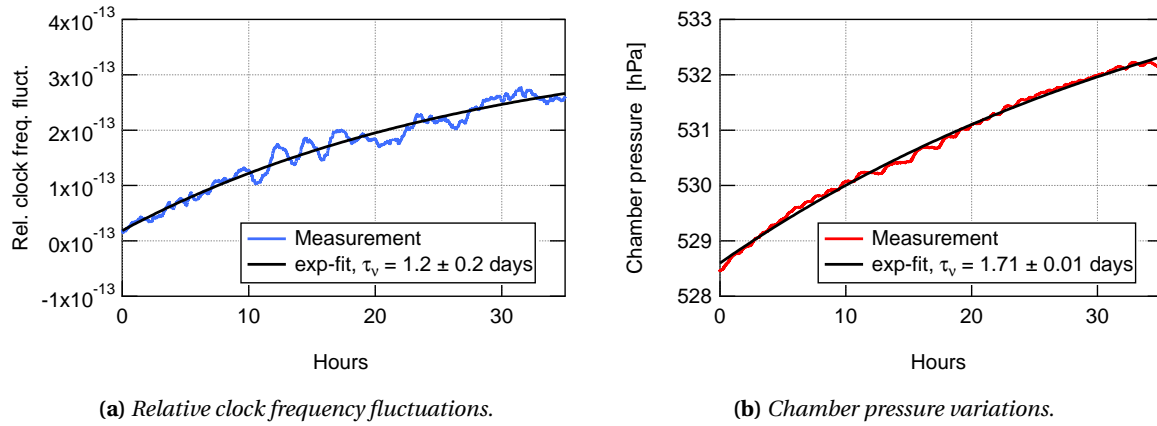


Figure 3.8 – Relative clock frequency fluctuations and chamber pressure variations. Both data are recorded simultaneously following the depressurization of the chamber.

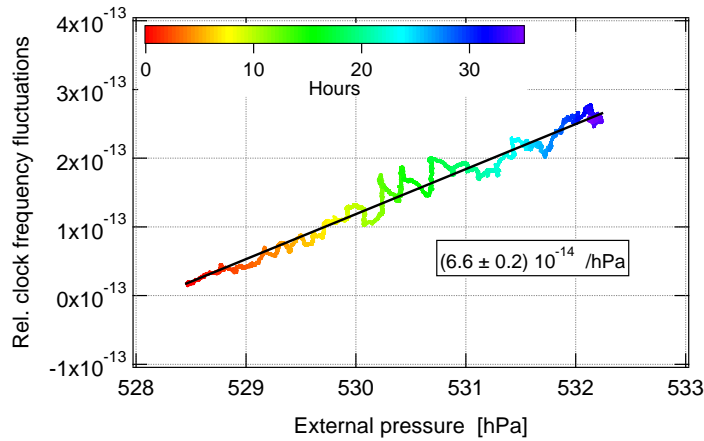


Figure 3.9 – Relative clock frequency shift versus chamber pressure recorded simultaneously.

3.3.4 Spin-exchange shift

The temperature-dependent Rb density and velocity variations contribute to the clock frequency instability via the spin-exchange effect (see section 1.5.4). In vapor-cell clocks, the clock frequency sensitivity to cell temperature variations is dominated by the buffer-gas density shift effect (see Figure 3.4). The spin-exchange shift contributes linearly to the quadratic buffer-gas density shift, which has an impact on the linear fit parameter. Thus, in vapor-cell clocks, the experimental determination of the SE coefficient is limited by the buffer-gas density shift effect, though it can be calculated (cf. section 1.5.4) assuming ideal optical pumping and homogeneous microwave field application. Taking into account the optimized clock experimental conditions (optical-pump frequency on $|2\rangle \rightarrow |3\rangle$ transitions and microwave pulses of $\theta = 0.56 \pi$), the calculated clock frequency sensitivity coefficient is $< 6.0 \cdot 10^{-12} /K$. This coefficient is at the same level as that reported for a similar vapor cell with a larger stem volume where the CW-DR scheme is applied [80]. The clock stability limit of the spin-exchange shift due to the cell temperature fluctuations < 0.5 mK over one day (see Figure 3.6) is estimated below $3 \cdot 10^{-15}$.

3.3.5 Light-induced shifts

In the POP-DR scheme where the optical and microwave interactions are separated in time, the impact of the AC Stark shift effect is strongly reduced compared to the case where the CW-DR scheme is applied (cf. section 1.5.5). However, light-induced clock frequency shift ($\Delta\nu_{LS}$) is not fully suppressed and the remaining sensitivity results from a combination of different processes that correspond to each phase of the interrogation scheme: residual coherence due to non-ideal optical pumping in the vapor cell [69] and the residual light during the microwave interrogation due to non-perfect light extinction, via the AC Stark shift effect [75].

Figure 3.10 reports on the clock frequency shift as a function of the optical pump and detection powers, varied by the same ratio in all phases of the POP-DR interrogation scheme, for the laser frequency tuned to the sub-Doppler peaks from $|5^2S_{1/2}, F = 2\rangle$ ground state. In the optical power region corresponding to the typical clock operation conditions (14 mW optical pump power), the clock frequency varies linearly with light intensity. The clock frequency sensitivity to light intensity fluctuations characterized by the α_{LS}^{POP} coefficient is deduced for a fixed laser frequency through applying the linear fit illustrated for CO22-23 in Figure 3.10. Figure 3.11 presents the clock frequency shift as a function of the laser frequency detuning from $|5^2S_{1/2}, F = 2\rangle \rightarrow |5^2S_{1/2}, F' = 3\rangle$ measured for fixed optical pump and detection powers. The β_{LS}^{POP} coefficient characterizing the clock frequency sensitivity to laser frequency fluctuations is deduced from the slope of the linear fit in Figure 3.11). Table 3.3 summarizes the experimental LS coefficients. Both coefficients are reduced by one order of magnitude compared to the CW-DR [45] and CPT [114] interrogation schemes and are of the same order of magnitude as the ones reported for similar pulsed DR [44] and CPT schemes [52].

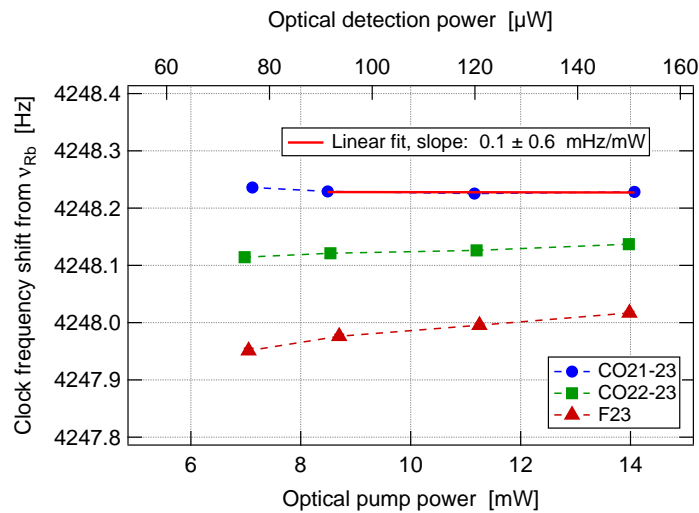


Figure 3.10 – Clock frequency shift as a function of the optical pump and detection powers for laser frequencies tuned to the $|5^2S_{1/2}, F = 2\rangle$ ground-state transitions. Red solid line: linear fit to deduce the intensity LS coefficient at a fixed laser frequency. Figure adapted from [113].

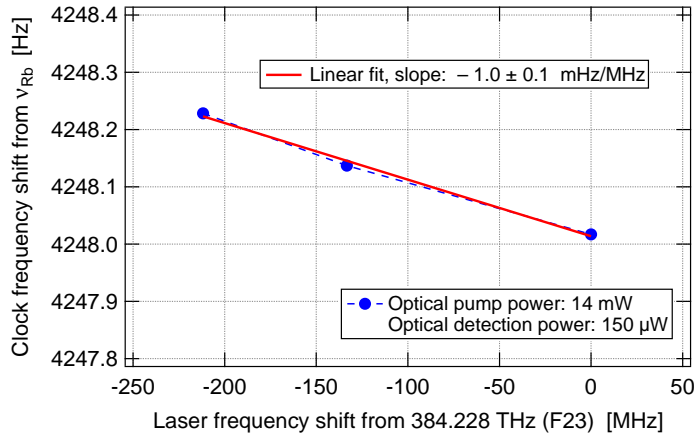


Figure 3.11 – Clock frequency shift as a function of laser frequency on the $|5^2S_{1/2}, F = 2\rangle$ ground-state transitions. Red solid line: linear fit to deduce the frequency LS coefficient.

Table 3.3 – Light –intensity and frequency– induced clock frequency sensitivity coefficients. The coefficients are deduced from the data shown in Figures 3.10 and 3.11, for optical-pumping from the $|5^2S_{1/2}, F = 2\rangle$ ground-state transitions. Table adapted from [113].

Parameter	α_{LS}^{POP} [/%]	β_{LS}^{POP} [/MHz]
CO21-23	$< 2.3 \cdot 10^{-14}$	
CO22-23	$(7 \pm 2) \cdot 10^{-14}$	$(-1.5 \pm 0.1) \cdot 10^{-13}$
F23	$(1.6 \pm 0.1) \cdot 10^{-13}$	

Figure 3.12 presents the relative optical power fluctuations measured at the clock cell input under pulsed operation conditions of the POP-DR interrogation (cf. Figure 2.15). For this measurement, we used the residual transmitted light at the back of a dielectric mirror, which conducts the light to the clock cell of the PP-POP. The optical power fluctuations are below 0.7 % at one day. For the α_{LS}^{POP} coefficients listed in Table 3.3, the clock stability limit of the intensity LS effect is at the 10^{-14} level. In the POP-DR clock, the laser intensity is not actively stabilized and its fluctuations represent the main instability source on long-term timescales. Laser intensity fluctuations are affected by environmental parameters such as the temperature, pressure, or humidity, which can affect the AOM, optics, and electronics. The laser frequency-stabilization loop can also contribute to light intensity fluctuations, as it acts on the laser current to regulate its frequency. Active laser intensity stabilization is required in order to reduce these long-term instability contributions due to light intensity fluctuations and can be implemented, for example, by acting on the laser temperature or via the AOM drive power. Given that the relative laser intensity fluctuations can be drastically reduced to the level of $2 \cdot 10^{-5}$ at $\tau = 10^4$ s using a temperature-stabilized AOM, as demonstrated in [115], with a stabilization loop via the RF power of the employed AOM, our clock’s stability limit of the intensity LS effect would decrease by more than three orders of magnitude to $5 \cdot 10^{-17}$.

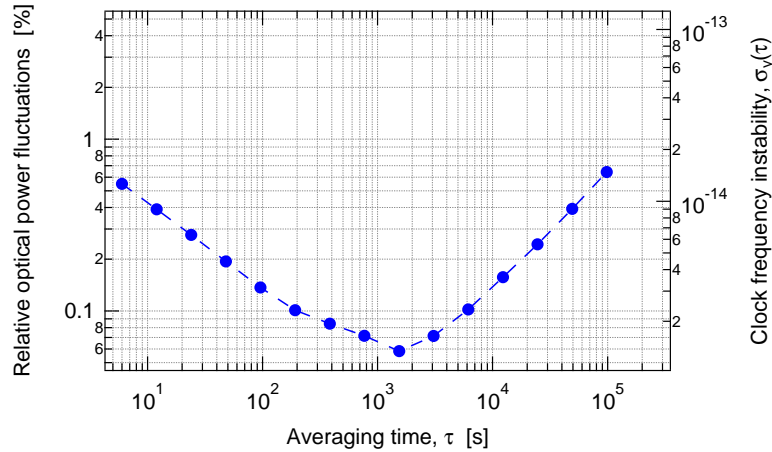


Figure 3.12 – Left-hand axis: Relative optical power fluctuations measured at the clock cell input in the pulsed operation mode. Right-hand axis: estimated clock frequency stability limit via the intensity LS effect. Courtesy of F. Gruet, LTF

In addition to decreasing the laser intensity fluctuations, detailed investigation of the processes that contribute to the light shifts in the POP scheme, particularly in view of reducing the residual coherence via a stronger optical pumping [69], would help to improve the clock stability limits due to this effect. Moreover, composite interrogation protocols based on the time-domain Ramsey scheme [52, 116], which have been widely exploited to reduce the light-shift effects in recent high-performing CPT-based vapor-cell clock demonstrations, may also be an interesting alternative to consider in future studies.

The frequency instability of the LH-POP is 4 kHz at one day ($< 10^{-11}$ in relative, cf. Table 2.1) and leads to a clock stability limit below the 10^{-15} level when taking into account the measured β_{LS}^{POP} coefficients. This laser frequency instability measurement was performed at the LH output in the CW operation mode (AOM does not function as an optical switch, but continuously). When operating the LH-POP in the pulsed mode according to the scheme of Figure 2.15, the switching of the AOM could degrade the frequency stability at the LH-POP output (similarly to the intensity stability degradation in the pulsed operation). In this case, the estimated clock stability limit from the laser frequency fluctuations may be underestimated and requires validation in future work.

3.3.6 Microwave-power shift

The microwave-power shift [47] arises from the inhomogeneity of the applied microwave field amplitude across the clock cell and in the case of spatially varying frequency shifts of the Rb atoms that are effectively localized in the buffer gas [83]. For the POP-DR clock, numerical studies have identified the greatest contribution to the MPS effect as the inhomogeneity of the light shift caused by the residual coherence [51, 59]. The clock stability limit of the microwave power fluctuations via the cavity-pulling effect is further discussed in section 3.3.5.

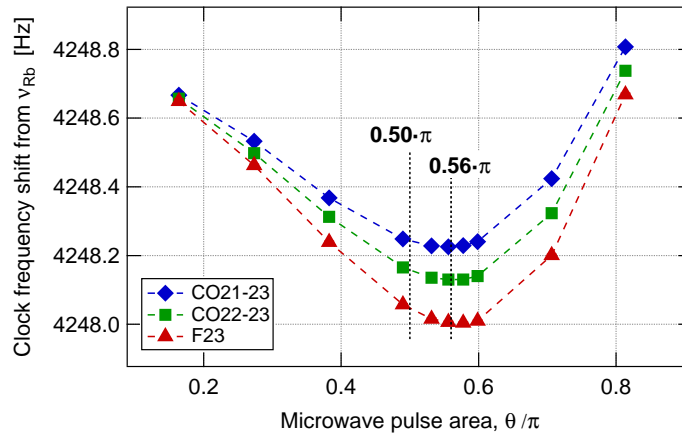


Figure 3.13 – Clock frequency shift as a function of the applied microwave pulse area, for optical-pump frequencies tuned to the $|5^2S_{1/2}, F = 2\rangle$ ground-state transitions. Figure adapted from [113].

The clock frequency shift measured as a function of the pulse area $\theta = b_R \cdot t_m \propto \sqrt{P_M} \cdot t_m$ for optical-pump frequencies tuned to the sub-Doppler peaks from $|5^2S_{1/2}, F = 2\rangle$ ground state is reported in Figure 3.13. The microwave Rabi frequency is proportional to the square root of the microwave power, P_M , applied during the pulse. Thus, the microwave pulse area is varied by changing the applied microwave power P_M at a constant pulse duration t_m . The product $\theta = \sqrt{P_M} \cdot t_m$ is scaled via the Rabi oscillation measurement under the assumption that the maximum contrast in Rabi oscillation is obtained for $\theta = \pi/2$ [59]. At a microwave pulse area of $\theta = 0.56\pi$, slightly larger than the $\pi/2$ pulses, the clock frequency sensitivity to microwave power fluctuations is reduced by one order of magnitude ($< 4 \cdot 10^{-13} / \mu\text{W}$). Nevertheless, $\theta = 0.56\pi$ pulses result in a slightly reduced central fringe contrast, as discussed in section 3.1, and shifts the clock frequency by < 25 mHz compared to the case of ideal $\pi/2$ pulses.

In order to measure the microwave power fluctuations in the vapor cell, we make use of the atomic response. To do so, we operate the clock with $\theta \approx 0.8 \cdot \pi$ pulses, corresponding to an enhanced MPS coefficient of $6 \cdot 10^{-12} / \mu\text{W}$. During the measurement shown in Figure 3.14, the intensity light-shift contribution is estimated to be lower than the MPS effect by more than a factor of two and all other effects are at least one order of magnitude lower. Deduced microwave power fluctuations, as shown on the left axis of Figure 3.14, are below $1.5 \cdot 10^{-2} \mu\text{W}$ (0.08 %) up to one day. The right-hand axis of Figure 3.14 presents the clock stability limit estimated for our POP-DR clock operation conditions using microwave pulses of $\theta = 0.56\pi$. The MPS induced clock instability remains below $6 \cdot 10^{-15}$ up to one day and does not currently represent a dominant instability source. Furthermore, an active microwave power stabilization scheme that can benefit from the pulsed interrogation approach and from the atoms' response may be useful to decrease the microwave power fluctuations [117]. In this case, not only the contribution of the MPS effect, but also that of the cavity-pulling effect (see section 3.3.5) via fluctuations of θ would be reduced.

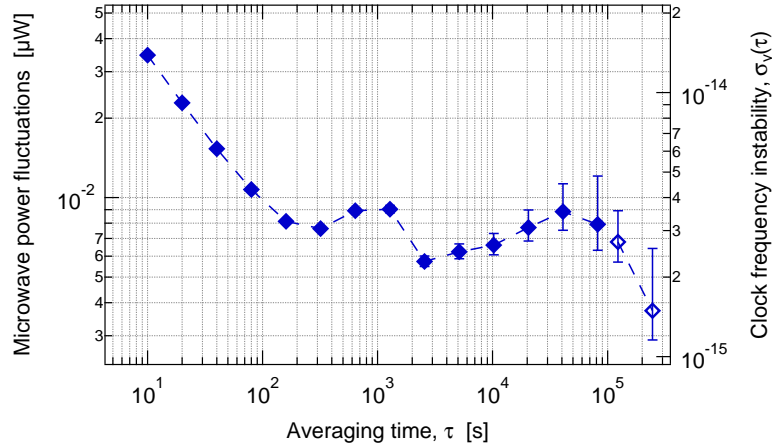


Figure 3.14 – Microwave power fluctuations and clock stability limit via MPS effect. Stability analysis performed using ThèoH statistics (cf. section 1.6.1); filled markers: overlapping Allan deviation; empty markers: Thèo1. Figure adapted from [113].

3.3.7 Cavity-pulling shift

The clock frequency is coupled to the physical parameters – such as the cavity temperature, pressure, and humidity – via the CP shift effect (cf. section 1.5.7). The sensitivity of the microwave cavity resonance frequency ν_{cav} to these parameters is characterized by the tuning coefficients listed in Table 2.3. The instability contribution of the CP shift effect may become the main clock stability limitation, for example, for high Q-factor cavities [118]. Due to the low Q-factor of the magnetron-type cavity $Q_l \approx 140$ and the small detuning of the resonance frequency from the atomic transition frequency $\Delta\nu_{cav} \approx 1.87$ MHz (cf. section 2.4), the impact of the CP shift effect in our POP-DR clock remains a negligible contribution.

The fluctuations of the sensitive parameters at one day and the cavity-pulling shift coefficients calculated for the PP-POP’s magnetron-type cavity for the optical-pump frequency tuned to the cross-over $|5^2S_{1/2}, F=2\rangle \rightarrow |5^2P_{3/2}, F=1,3\rangle$ and microwave pulse areas of $\theta = 0.56\pi$ are listed in Table 3.4. The estimated clock stability limit due to the cavity-pulling effect is dominated by the humidity sensitivity of the cavity and the microwave power fluctuations that is one order of magnitude lower than the MPS effect. The remaining instability contributions via the cavity-pulling effect are negligible. Even under ambient laboratory conditions, the clock instability contribution arising from atmospheric pressure fluctuations of 3 hPa via the CP shift effect is negligible at $6 \cdot 10^{-16}$ and results in a (total) CP shift limit at $2.2 \cdot 10^{-15}$.

Table 3.4 – *Cavity-pulling shift coefficients and estimated clock stability limits for the experimental parameter fluctuations. Microwave power instability is determined in section 3.3.6, cavity temperature instability in section 3.3.2.2, chamber internal pressure instability in section 3.3.3, and environmental humidity instability provided by MeteoSwiss². Table adapted from [113].*

$\tau = 10^4$ to 10^5 s	CP shift coefficient	Parameter fluctuations	Clock instability contribution
Microwave power	$5.6 \cdot 10^{-14} / \mu\text{W}$	$1.5 \cdot 10^{-2} \mu\text{W}$	$8.3 \cdot 10^{-16}$
Temperature	$-5.1 \cdot 10^{-15} / \text{K}$	$5 \cdot 10^{-4} \text{ K}$	$2.6 \cdot 10^{-18}$
Pressure	$-2 \cdot 10^{-16} / \text{hPa}$	$3 \cdot 10^{-2} \text{ hPa}$	$6 \cdot 10^{-18}$
Humidity	$-4.8 \cdot 10^{-15} / (\text{g}/\text{m}^3)$	$0.4 \text{ g}/\text{m}^3$	$1.9 \cdot 10^{-15}$
Total			$2.1 \cdot 10^{-15}$

3.3.8 Other shifts

In this section, we evaluate two additional effects that induce a shift of the atomic energy levels and thereby contribute to the clock instability, although at negligible levels. First, the blackbody radiation (BBR) shift $\Delta\nu_{BBR}$ for ^{87}Rb is given in relative terms by [119]

$$\frac{\Delta\nu_{BBR}}{\nu_{Rb}} = -1.26 \cdot 10^{-14} \left(\frac{T_{cell}}{300} \right)^4, \quad (3.1)$$

where T_{cell} is the vapor-cell temperature. The resulting sensitivity coefficient at the cell temperature of 62.16°C is calculated as $-2.3 \cdot 10^{-16} / \text{K}$. Considering the cell temperature fluctuations at the level of 0.5 mK (see section 3.3.2.2), the clock stability limit of the BBR shift effect is estimated as $1.2 \cdot 10^{-19}$ at one day. For temperature fluctuations up to 1 K , the clock stability limit is well below 10^{-15} .

Secondly, a static electric field applied on the atomic vapor shifts the energy levels through the DC Stark shift effect. For the clock transition of ^{87}Rb , the DC Stark shift is given by [120]

$$\frac{\Delta\nu_{DC}}{\nu_{Rb}} = -1.8 \cdot 10^{-16} E_0^2, \quad (3.2)$$

where E_0 is the electric field strength expressed in Volt per centimeter. For our cm-scale vapor cell, taking into account an environmental electric field up to $3 \text{ V}/\text{cm}$, the impact of the DC Stark shift effect is below $1.1 \cdot 10^{-15}$.

²Acknowledgments to MeteoSwiss, the Swiss Federal Office of Meteorology and Climatology for the environmental parameters data.

3.4 Long-term clock instability budget

Table 3.5 summarizes the principal physical effects that impact the long-term frequency stability of our POP-DR Rb-cell clock with experimental sensitivity coefficients and parameter fluctuations under optimized clock operation conditions (i.e., in the hermetic chamber), as listed in Table 3.6. The impact of the SE and CP effects are assumed to be included in the experimentally determined cell TC, barometric coefficient, and MPS coefficient. Thus, the total clock stability limit is the quadratic sum of the contributions of lines 1 – 7 given for averaging times from 10^4 to 10^5 s (one day). The clock instability of $1.7 \cdot 10^{-14}$ is estimated, in reasonable agreement with the measured instability (cf. Figure 3.15).

The long-term clock stability was initially optimized by optimizing the experimental parameters, such as the optical-pump frequency and the applied microwave pulse areas. The instability contribution of the MPS effect is reduced by optimizing the sensitivity coefficient for microwave pulses areas of 0.56π , at the expense of a slightly increased clock frequency shift and reduced contrast of the central Ramsey fringe characterized in section 3.1. The barometric effect is reduced employing the hermetic chamber to isolate the clock Rb cell from atmospheric pressure fluctuations. Furthermore, the dominant contribution of the second-order Zeeman shift effect is diminished due to the reduced clock frequency sensitivity coefficient. The simultaneous cell and stem temperature measurements are used to consolidate the clock stability limits of the buffer-gas density shift effect. Thus, their contributions, along with those induced by the cavity-pulling and spin-exchange effects, currently remain at the level of 10^{-15} or below.

According to the budget in Table 3.5, the dominant clock instability contribution arises from laser optical power fluctuations. All of the parameter fluctuations are assessed using the POP-DR scheme under the optimized clock parameters outlined in Table 3.6 (i.e., in the hermetic chamber), except the laser frequency instability measured in the CW mode. The experimental validation of the instability in the pulsed operation mode of the POP-DR clock is required to further confirm the long-term clock budget. We suspect that the contribution of the frequency light-shift effect may be underestimated in this budget. In addition, the optical power could not be simultaneously measured with the clock frequency and is necessary to confirm its limitation. Given the contributions from all other known effects consolidated in this work, we suspect that the observed bump in Figure 3.15 around 10^4 s arises from the light-shift effects. In order to overcome the limitation due to the laser intensity fluctuations, one straightforward solution is to implement an active stabilization loop, for example, acting on the laser chip temperature or on the RF power of the AOM.

Reducing the optical power fluctuations by a factor of three will be sufficient for reaching a $< 10^{-14}$ clock stability level at one day. Alternatively, detailed analyses of the light-induced clock frequency sensitivities in the POP-DR scheme will help to identify the physical processes at the origin of this dominant contribution and to reduce the sensitivity coefficient. Solutions that employ a second laser light to reduce the light-shift effect, as demonstrated in [121], could ultimately present an effective approach to efficiently pump the atoms in the cell and reduce the light-induced sensitivities as well as the sensitivities related to the residual coherence.

Table 3.5 – Long-term instability budget at $\tau = 10^4$ to 10^5 s for the POP-DR clock. Microwave pulses of $\theta = 0.56\pi$ and optical pumping from $F_g = 2$ ground state with the PP-POP placed in the hermetic chamber at 535 hPa. The clock sensitivity coefficients and the physical parameter instability ($\sigma_p(\tau)$) are presented and discussed in the previous section 3.3. The total clock stability limit is estimated taking into account the effects in lines $j = 1 - 7$, assuming uncorrelated effects. ^(a) contributions of these effects are included in another effect associated to the same sensitive parameter, e.g. temperature, pressure, or microwave power.

j	Physical effect	Sensitive parameter	Sensitivity coefficient	Relative sensitivity coefficient	Parameter fluctuations	Clock instability contribution
1	2 nd -order Zeeman shift	C-field	$4.0 \cdot 10^5$ Hz/T	$5.8 \cdot 10^{-5}$ /T	$2 \cdot 10^{-11}$ T	$1.2 \cdot 10^{-15}$
2	Buffer-gas density shift	T_{cell}	$\pm 1.6 \cdot 10^{-2}$ Hz/K	$\pm 2.3 \cdot 10^{-12}$ /K	$5 \cdot 10^{-4}$ K	$1.2 \cdot 10^{-15}$
3	Stem TC	T_{stem}	$8.2 \cdot 10^{-3}$ Hz/K	$1.2 \cdot 10^{-12}$ /K	$5 \cdot 10^{-4}$ K	$6.0 \cdot 10^{-16}$
4	Barometric	P_{ext}	$4.5 \cdot 10^{-4}$ Hz/hPa	$6.6 \cdot 10^{-14}$ /hPa	$3 \cdot 10^{-2}$ hPa	$2.0 \cdot 10^{-15}$
5	Intensity light shift	I_{laser}	$\pm 1.6 \cdot 10^{-4}$ Hz/%	$\pm 2.3 \cdot 10^{-14}$ /%	0.7 %	$1.6 \cdot 10^{-14}$
6	Frequency light shift	ν_{laser}	$-1.0 \cdot 10^{-3}$ Hz/MHz	$-1.5 \cdot 10^{-13}$ /MHz	$4 \cdot 10^{-3}$ MHz	$6.0 \cdot 10^{-16}$
7	Microwave power shift	P_M	$2.7 \cdot 10^{-3}$ Hz/ μ W	$4.0 \cdot 10^{-13}$ / μ W	$1.5 \cdot 10^{-2}$ μ W	$6.0 \cdot 10^{-15}$
8	Spin-exchange shift ^(a)	T_{cell}	$4.0 \cdot 10^{-2}$ Hz/K	$5.9 \cdot 10^{-12}$ /K	$5 \cdot 10^{-4}$ K	$3.0 \cdot 10^{-15}$
9	Cavity-pulling shift ^(a)	P_M	$3.8 \cdot 10^{-4}$ Hz/ μ W	$5.6 \cdot 10^{-14}$ / μ W	$1.5 \cdot 10^{-2}$ μ W	$8.3 \cdot 10^{-16}$
10	Cavity-pulling shift ^(a)	T_{cav}	$-3.5 \cdot 10^{-5}$ Hz/K	$-5.1 \cdot 10^{-15}$ /K	$5 \cdot 10^{-4}$ K	$2.6 \cdot 10^{-18}$
11	Cavity-pulling shift ^(a)	P_{ext}	$-1.4 \cdot 10^{-6}$ Hz/hPa	$-2.1 \cdot 10^{-16}$ /hPa	$3 \cdot 10^{-2}$ hPa	$6.0 \cdot 10^{-18}$
12	Cavity-pulling shift ^(a)	H_{ext}	$-3.3 \cdot 10^{-5}$ Hz/(g/m ³)	$-4.8 \cdot 10^{-15}$ /(g/m ³)	0.4 g/m ³	$1.9 \cdot 10^{-15}$
Total estimated clock frequency instability at $\tau = 10^4$ to 10^5 s						
					$\sigma_{y_j}(\tau) = \sqrt{\sum_{j=1}^7 \sigma_j^2(\tau)}$	$1.7 \cdot 10^{-14}$
					including lines $j = 1$ to 7	

3.5 Measured long-term clock instability

This section presents the measured long-term clock frequency instability and the simultaneously measured parameter fluctuations. The experimental parameters used to operate the clock, which are optimized as presented in previous sections, are outlined in Table 3.6. Under these conditions, the measured clock frequency instability is reported in Figure 3.15. The measurement has a duration of three days; the full range of data is analyzed using the Thêo-H statistic [88], which combines the overlapping Allan (filled circles) and Thêo1 (empty circles) variances (cf. section 1.6.1).

The short-term instability of $4.8 \cdot 10^{-13} \tau^{-1/2}$ is limited by the SNR of the optical detection [51]. The linear drift of $-4.3 \cdot 10^{-15}$ /day, well below the measured instability at one day, is not removed from the data shown in Figure 3.15. The measured clock instability remains $< 2 \cdot 10^{-14}$ at the averaging times of $10^4 - 10^5$ s, in agreement with the estimated clock instability according to the budget in Table 3.5.

Table 3.6 – Clock experimental parameters in view of optimized long-term stability performance.

Laser frequency (CO21-23)		384.227 903 THz
AOM frequency shift		$-2 \cdot 75$ MHz
Optical pump pulse	$t_p = 0.4$ ms	$P_p = 14$ mW
Optical detection pulse	$t_d = 0.7$ ms	$P_d = 150$ μ W
Microwave pulses (0.56π)	$t_m = 0.3$ ms	$P_M = 20$ μ W
Free evolution time	$t_R = 3.0$ ms	
Total cycle time	$t_C = 4.74$ ms	
LO-POP modulation frequency		$f_{mod} = 211$ Hz
LO-POP modulation depth		$f_{\Delta} = \pm 80$ Hz
C-field		3.5 μ T
Cell temperature		62.16°C
Stem temperature		59.22°C
Chamber average pressure		535.3 hPa
Chamber average temperature		24.86°C

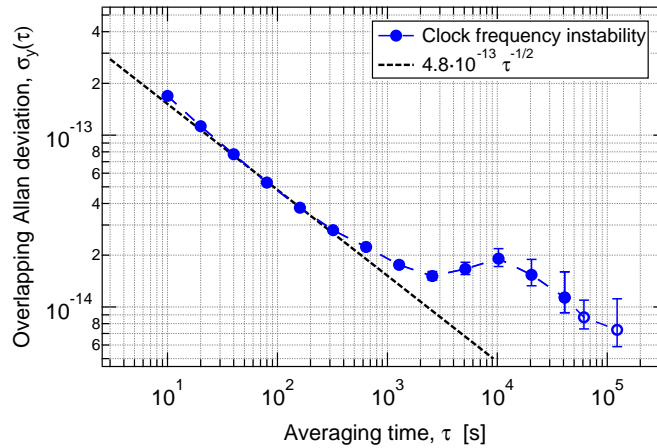


Figure 3.15 – Measured long-term clock frequency instability. The drift of $-4.3 \cdot 10^{-15}$ /day is not removed. Stability analysis performed using ThéoH statistics (cf. section 1.6.1); filled markers: overlapping Allan deviation; empty markers: Théo1. Figure adapted from [113].

Simultaneous measurement of the experimental and environmental parameters along with the clock frequency is crucial to confirm the dominant contribution to the clock frequency fluctuations through a correlation analysis. Figure 3.16 reports the clock frequency and the simultaneously measured parameters such as: chamber pressure; the LH-POP reference-cell transmission signal obtained in the Doppler-free configuration; and the temperature fluctuations of the cell, stem, and laboratory. The recorded data are smoothed with a moving average algorithm in order to reveal the underlying form of the fluctuations. The chamber pressure is measured using a pressure sensor. The LH-POP reference signal corresponds to the Doppler-free absorption signal used to stabilize the laser frequency. Before entering the PP, the frequency-stabilized laser output travels through several more passive optical elements and the AOM in double-pass configuration. The cell and stem temperatures are measured using the monitoring NTCs (in open loop). For the temperatures of the cell, stem, and laboratory, the absolute fluctuations around the respective mean values are indicated ($T_{cell} = 62.1^\circ\text{C}$, $T_{stem} = 59.2^\circ\text{C}$, and $T_{lab} = 21.3^\circ\text{C}$). The accuracy bias of the mean values measured by the monitoring NTCs from the temperatures indicated in Table 3.6 is in the uncertainty limit of the employed NTCs ($\pm 0.2^\circ\text{C}$).

The evident correlation of the chamber pressure with the laboratory temperature fluctuations is a result of the heat transfer through the chamber walls, which was characterized in section 2.4.4. In fact, for the clock frequency fluctuations, no clear correlation with any other recorded signal is observed, indicating that the clock frequency instability is dominated neither by the barometric effect nor the temperature sensitivities. However, the optical power was not measured simultaneously at the PP input but at that of the reference Rb cell of the LH-POP. Thus, even though this data does not correspond to the light entering the PP-POP, it is still useful to estimate the fluctuations at the PP input given that the additional optical components, and particularly the AOM (even in continuous-wave operation), degrade the long-term laser intensity stability (in relative) by one order of magnitude (cf. Table 2.1). Taking into account this factor of ten, the relative optical power fluctuations level at the PP-POP input ΔP_{PP} is qualitatively estimated from the relative optical

power fluctuations measured before the AOM in the LH-POP ΔP_{LH} using

$$\frac{\Delta P_{PP}}{P_{PP}} = 10 \frac{\Delta P_{LH}}{P_{LH}}. \quad (3.3)$$

The induced clock frequency stability limit is subsequently estimated using the α_{LS}^{POP} light-shift coefficient (cf. Table 3.3) and presented (with the blue triangles) in Figure 3.17. For other sensitive parameters, whose fluctuations are directly recorded in parallel to the clock frequency, the stability limits are estimated using the corresponding sensitivity coefficients. The calculated clock frequency fluctuations are presented in Figure 3.17. The estimated clock instability contribution from the light shift effects due to the laser intensity fluctuations reaches the 10^{-14} level at the averaging times $> 10^4$ s. For an ultimate validation of the long-term clock stability limitation due to the intensity LS effects, the optical power at the PP-POP input should be measured simultaneously with the clock frequency. In this case, we would expect to observe a significant correlation between the two simultaneously recorded data.

The LH-POP, placed in a thermal isolation box in the laboratory, operates under atmospheric conditions. Therefore, light intensity and frequency may suffer from variations of the environmental parameters via the reference cell, AOM, or optical elements. Figure 3.18 reports the LH-POP reference cell signal along with the atmospheric pressure and humidity variations recorded in Neuchâtel³ and the temperature fluctuations in its environment. The detected optical power fluctuations appear to be correlated with those of the atmospheric pressure and humidity, whereas no significant correlation with the temperature can be distinguished. In particular, the optical power detected via the photodetector current (-0.33 A/W) through the reference Rb cell of the LH-POP reveals a linear sensitivity coefficient to the fluctuations of the atmospheric pressure ~ -0.01 $\mu\text{W}/\text{hPa}$ (~ 3.3 nA/hPa). The sensitivity of the optical power to the fluctuations of the environmental parameters may originate at different stages of the LH-POP, for example optical components' reflectivity, air's refractive index, or reference cell temperature. Further investigations are required to identify the dominant contribution and thus to reduce the laser intensity fluctuations while still operating the LH-POP under ambient atmospheric conditions.

³Acknowledgments to MeteoSwiss, the Swiss Federal Office of Meteorology and Climatology for the environmental parameters data.

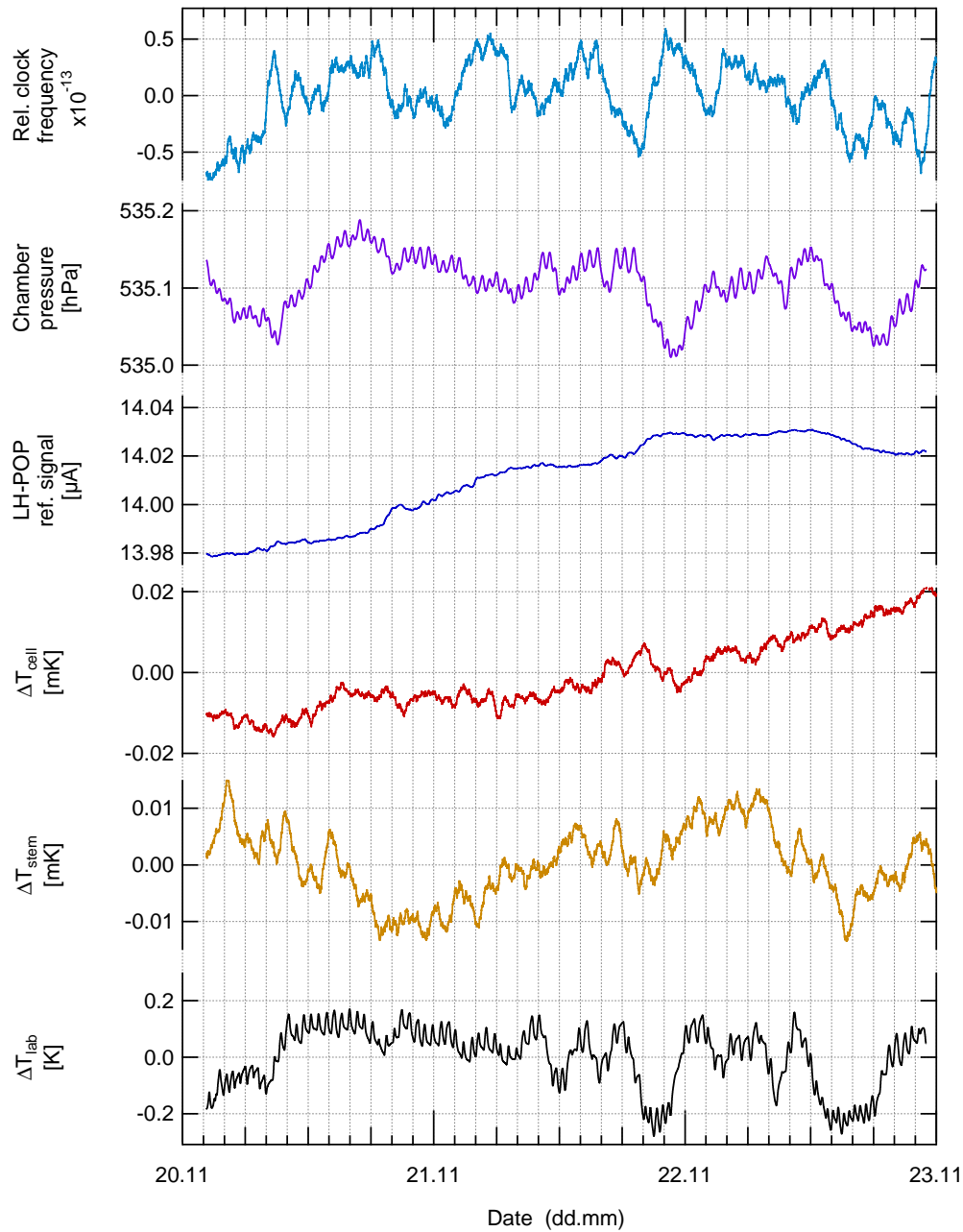


Figure 3.16 – Relative clock frequency and simultaneously measured experimental parameters: chamber pressure, LH-POP Doppler-free absorption, and temperature fluctuations of the cell, stem, and in the laboratory. Mean temperatures for cell, stem, and in the laboratory are $T_{cell} = 62.1^\circ\text{C}$, $T_{stem} = 59.2^\circ\text{C}$, $T_{lab} = 21.3^\circ\text{C}$, respectively. The relative clock frequency and the cell and stem temperature data are smoothed over 3'000 s, the chamber pressure and LH-POP signal data are smoothed over 1'000 s, and the laboratory temperature data is smoothed over 7'000 s.

3.5. Measured long-term clock instability

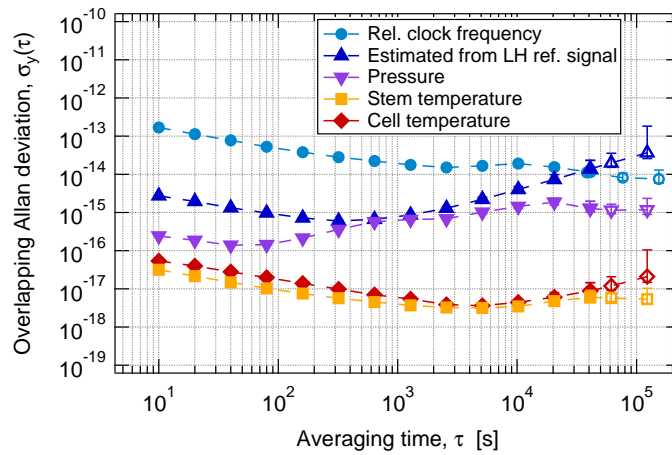


Figure 3.17 – Estimated clock frequency fluctuations induced by the temperature, barometric, and light intensity sensitivities. The clock frequency sensitivity coefficients are applied to the simultaneously recorded parameters to estimate the contributions to the clock frequency fluctuations. Stability analysis performed using ThêoH statistics (cf. section 1.6.1); filled markers: overlapping Allan deviation; empty markers: Thêo1.

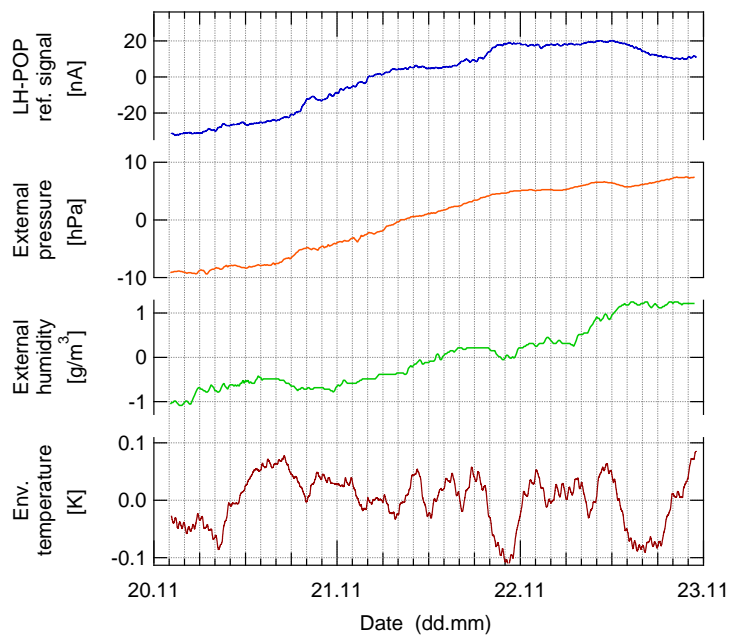


Figure 3.18 – Absolute fluctuations of the LH-POP Doppler-free absorption, the atmospheric pressure and humidity, and the temperature in the LH-POP surroundings.

3.6 Conclusion

In this chapter, we analyzed the long-term stability limitations in our compact Rb vapor cell clock where the POP-DR interrogation scheme is applied. We evaluated and optimized the clock frequency sensitivity to experimental parameter fluctuations in view of improving the long-term clock stability. A clock instability below $2 \cdot 10^{-14}$ at $\tau = 10^4$ to 10^5 s timescales was demonstrated under optimized experimental conditions. The instability contribution of the second-order Zeeman effect, which was one of the principal clock stability limits, was reduced by decreasing the clock frequency sensitivity at a lower C-field. The impact of clock Rb cell temperature fluctuations on the long-term clock instability via buffer-gas density shift and spin-exchange shift effects are assessed through simultaneous monitoring of the temperature at the level of 10^{-15} or below.

We evaluated the various contributions in the long-term clock instability budget. The clock frequency sensitivity coefficients were experimentally determined under optimized experimental parameters. The fluctuations of the parameters were measured using the atomic response when possible and under similar conditions to the clock operation (see Table 3.6). The dominant instability contribution to the measured clock frequency instability was estimated at the level of $1.6 \cdot 10^{-14}$ arising from variations of the light intensity through the LS effects. The second highest contribution was the microwave power shift effect at the level of $6.0 \cdot 10^{-15}$. For all other relevant effects, the contribution remained well below $5.0 \cdot 10^{-15}$.

In our POP-DR clock, the laser intensity is not actively stabilized. The laser frequency is stabilized via the laser drive current, and therefore may lead to light intensity variations if the intensity is not stabilized in a separate loop. The laser intensity fluctuations can be reduced through an active stabilization loop via the AOM [115] up to three orders of magnitude, yielding a clock stability limit below 10^{-16} . Nevertheless, adding a servo loop on each parameter would make the system relatively more complicated and power consuming. In view of clock prototype with a small SWaP, it is more interesting to identify the origin of high intensity fluctuations and have a better control of the light intensity stability while keeping the number of servo loops to a minimum. Our preliminary results suggest that the Doppler-free absorption signal used to frequency stabilize the laser light appears sensitive to the variations of the environmental pressure and humidity. In this case, such environmental parameters may perturb the light intensity by different means, for instance through the optical components' reflectivity, air's refractive index, or reference cell temperature. Moreover, frequency-stabilized laser light, serving for the optical pumping and detection in the clock, passes through additional components (e.g., AOM) before reaching the clock Rb cell, and therefore is expected to be more sensitive to such environmental parameters' variations than the Doppler-free signal. Further investigations are required in order to identify the main origin of the dominant contribution and then implement an adequate stabilization servo loop if necessary.

Finally, the long-term clock instability budget consolidated in this thesis includes the sensitivity coefficients and parameter fluctuations measured under similar experimental conditions to the clock instability measurement, except for the laser frequency. The laser frequency fluctuations measured at the PP-POP input in CW operation mode may be underestimated for the pulsed operation mode of the POP-DR clock and should be further studied.

4 Optical sources for Rb clocks based on frequency-doubled telecom lasers

In laser-pumped vapor-cell clocks, the LD emission used to optically pump the atoms often also serves to detect the atomic resonance resulting from the microwave interrogation. In this case, one of the main clock instability contributions on short-term timescales is the detection signal-to-noise ratio (cf. section 1.6.2.1). While the signal properties largely rely on the atomic density, interrogation scheme, and other experimental parameters (e.g. optical and microwave powers, cell temperature), the optical detection noise is dominated by the laser noise (AM and FM-to-AM conversion noise). Furthermore, the fluctuations of the light intensity and frequency degrade the clock frequency stability via the LS effects (cf. section 1.5.5) and may become a serious long-term clock instability source. The requirements on the laser spectral properties for such applications in order to reach a clock frequency stability of 10^{-13} at $\tau = 1$ s and 10^{-14} at $\tau = 10^4$ s (1 day) are the following:

- Collimated and single-mode emission at the wavelength of the ^{87}Rb D₁ or D₂ line with a mode-hop free tuning range covering several GHz across the optical resonances from the hyperfine ground states and a linewidth below 5 MHz to resolve the Doppler-free spectroscopy of the excited states;
- In the CW-DR scheme, an optical power in the order of a few hundreds of μW ; in the POP-DR scheme, typically 15 to 20 mW for optical pumping and a few hundreds of μW for detection;
- Relative intensity noise of 10^{-11} Hz^{-1} at Fourier frequencies corresponding to the modulation frequency of the clock detection, typically between 50 Hz and 500 Hz;
- Frequency noise below $10^{10} \text{ Hz}^2/\text{Hz}$ at Fourier frequencies corresponding to the modulation frequency of the clock detection, typically between 50 Hz and 500 Hz;
- Given the LS coefficients measured in the CW-DR scheme (reported in Table 3.3 of reference [75]), the relative laser frequency, and intensity instabilities $< 3 \cdot 10^{-12}$ and $< 3 \cdot 10^{-4}$ over one day, and considering those measured in the POP-DR scheme (global α and β light-shift coefficients reported in Tables 3.6 and 3.7 of reference [51]), relative frequency and intensity instabilities of $< 3 \cdot 10^{-10}$ and $< 7 \cdot 10^{-4}$.

DFB laser diodes emitting at 780 nm that are employed in Rb vapor-cell clocks typically provide a mode-hop free tuning range of several GHz and an optical power of several tens of mW while exhibiting a linewidth in the order of a few MHz (cf. section 2.1.1). Meanwhile, the progress in the telecommunications resulted in an extensive research and development of optical sources and

components operating in the telecom spectral regions, among which the so-called conventional (or erbium) window (known as the C-band around 1560 nm) is the most widely used window for optical fiber communications. This is because in this spectral region the losses are the lowest in silica fibers and the fiber lasers and amplifiers based on erbium are available, which offer high performances and especially for long-distance transmission. Working at larger wavelengths, around 1560 nm instead of 780 nm, has also a practical advantage in the processing of frequency selective structures at the wavelength scale, which are used in single-mode (DFB, DBR, or external cavity) lasers and to narrow the laser linewidth. Working with Rb atoms offers the possibility to benefit from the superior spectral properties and higher reliability of optical sources and components at 1560 nm, which coincides with the twofold optical transition wavelengths of ^{87}Rb atoms at 780 nm.

In this chapter, we investigate two frequency-doubled telecom lasers based on different laser chip technologies (cf. section 2.1.2) for their potential exploitation in high-performance Rb vapor-cell clocks. First, we present an overview of high-precision applications that benefit from such laser systems. Then, we study in detail the spectral properties and long-term fluctuations of the laser systems based on frequency doubling. Finally, we discuss their implementation in Rb vapor-cell clocks in view of short- and long-term clock frequency instability. The following sections, except for sections 4.2.1 and 4.6, are essentially based on our article [122] with the inclusion of additional studies and discussion. The text and figures are adapted from [122].

4.1 Telecom lasers in atomic physics

Frequency-stabilized 780-nm optical sources play a crucial role in many high-precision applications in metrology [67], atomic physics and spectroscopy [123], atmospheric sensing [124], and optical telecommunication [125]. Advances in scientific research and industrial development in these fields reflect the increasing interest in compact, reliable, and highly stable laser sources satisfying stringent spectral requirements specific to each application. For semiconductor laser diodes emitting at 780 nm, a widely used frequency stabilization technique is based on the atomic frequency references obtained through a rubidium vapor cell to generate the correction signal [126]. Improved laser frequency stabilities are achieved by resolving the ^{87}Rb atomic transition lines close to their natural linewidths in Doppler-free spectroscopy schemes [127, 128].

At twice the wavelength of the 780-nm Rb D_2 line, corresponding to the telecommunication C-band at 1560 nm, reliable and low-cost components are available (e.g. low-noise laser diodes, amplifiers, modulators). Thus, thanks to the second harmonic generation [106, 107], telecom lasers emitting at 1560-nm can also benefit from the Rb atomic frequency reference stability at 780 nm. This concept has been largely exploited in the last two decades for optical frequency references in optical telecommunication applications at 1560 nm [129, 130]. Numerous applications at 780 nm have also leveraged this idea: the use of the frequency-doubled laser systems is demonstrated in Rb fountain clocks [131], in compact Rb clocks based on 778-nm two-transition transition [132], in laser cooling for atom interferometry [133–136], in space-borne applications [137–139], in ground-based gravimeters [140], and in manipulation of the Rb with short pulses [141]. High-precision applications require reliable and reproducible low-noise optical sources with a long lifetime. The availability of such lasers emitting directly at 780 nm presents a limitation for the industrialization

of laser-pumped Rb clocks. The LDs of the telecom C-band thus present attractive alternatives to 780-nm LDs owing to the availability of reliable and reproducible high-performance components in this wavelength region.

Our group has previously developed compact and robust optical sources based on a DFB LD emitting directly at 780 nm and Doppler-free stabilization, such as the LH-CW and LH-POP, for applications in high-performance Rb vapor-cell clocks [58]. These optical sources exhibit a frequency instability below 10^{-11} up to one day of averaging time. Our group has also previously demonstrated a compact laser system based on a frequency-doubled 1560-nm LD stabilized to a Rb cell reference for space-borne CO₂ detection at 1572 nm [98, 99]. In this thesis, we address the application potential of telecom lasers in Rb vapor-cell atomic clocks and evaluate two frequency-doubled laser systems that are frequency-stabilized on Rb transitions (cf. section 2.1.2). One of these laser systems (FD-DFB) is based on a DFB laser diode emitting at 1560 nm [98] and the other laser system (FD-ECL) employs an external cavity laser based on planar waveguide technology [100]. The spectral properties of the home-built and well-established LH-CW (cf. Table 2.1) are accounted as reference. The presented analysis provides a comprehensive evaluation of the frequency-doubled lasers in view of their use in many high-precision applications.

4.2 Spectral characterization of FD laser systems

This section reports on the spectral characterization of the frequency-doubled laser systems. We first discuss the basic characteristics of the laser emission, followed by the intensity and frequency noise and the linewidth.

4.2.1 Basic spectral properties of FD laser systems

In this section, we focus on the basic properties of the laser emission. The dependence of the output power of the FD-ECL is measured as a function of the drive current at the LD output at 1560 nm and at the PPLN output at 780 nm (cf. section 2.1.2 and Figure 2.3) for different LD temperatures, as illustrated in Figure 4.1. The lower optical power at 780 nm agrees with the quadratic second harmonic generation process (cf. equation (2.1)) and no other significant power losses are noted. Mode jumps are observed with abrupt changes in the output power and exhibit hysteresis. As the planar ECL is implemented together with the gain medium in the packaging, the temperatures of the two parts are controlled simultaneously. The laser emission frequency can thus be tuned either via the drive current or the LD temperature, as reported in Figure 4.2.

The operational parameters of the FD-ECL allowing the highest output power at the Rb resonance frequency with a mode-hop free frequency tuning range up to 6 GHz and the output characteristics are gathered in Table 4.1 together with those of the FD-DFB and LH-CW. All three laser diodes operate using similar drive currents and LD temperatures. The relatively low optical powers at the 780-nm output of the FD laser systems (200 and 500 μ W) compared to that of the LH-CW (6 mW) are sufficient for their implementation in DR clocks in the CW scheme, but require amplification for the POP-DR scheme to guarantee an efficient optical pumping of the Rb atoms before the microwave interrogation. The current and temperature sensitivity coefficients of FD-ECL lasing frequency are

-0.05 GHz/mA and -3.2 GHz/K, respectively, corresponding to optical power changes of $3 \mu\text{W}/\text{mA}$ and $20 \mu\text{W}/\text{K}$ at the 780-nm output. The frequency tuning of the FD-ECL (where a planar ECL is integrated with the gain medium on the same temperature controller unit) is at least 10 times less sensitive to the drive current and temperature than the laser systems based on a DFB laser diode (FD-DFB and LH-CW). The side mode suppression ratios (cf. section 2.1.1.1) measured for all three laser systems using an optical spectrum analyzer (OSA) are also reported in Table 4.1 for 780-nm and 1560-nm lights. The SMSR of the LD emission is comparable for different laser chip technologies. At the 780-nm output of the FD laser systems, the SMSR is significantly improved by 20 dB via the quadratic power dependence of the SHG process.

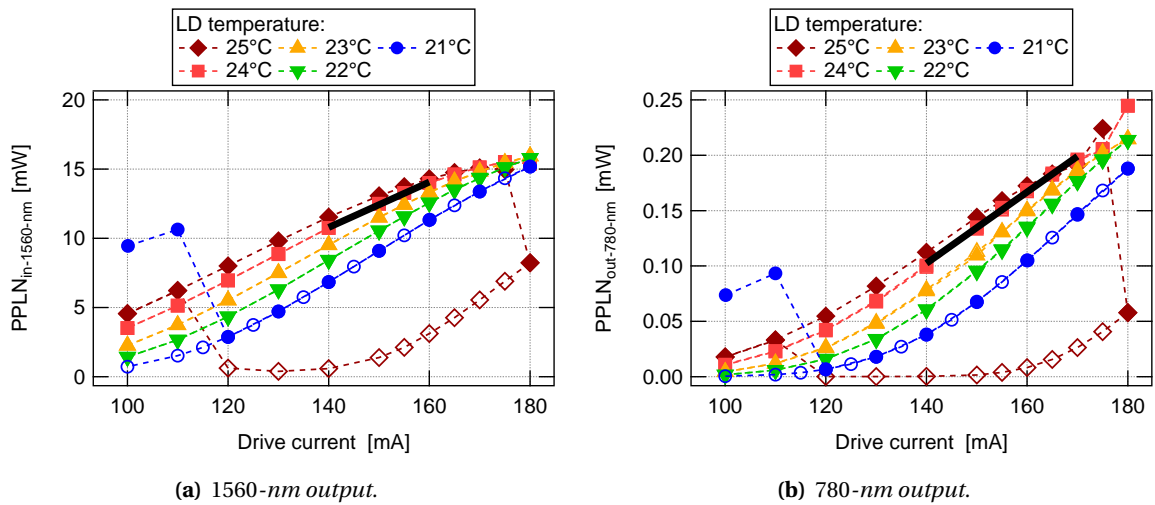
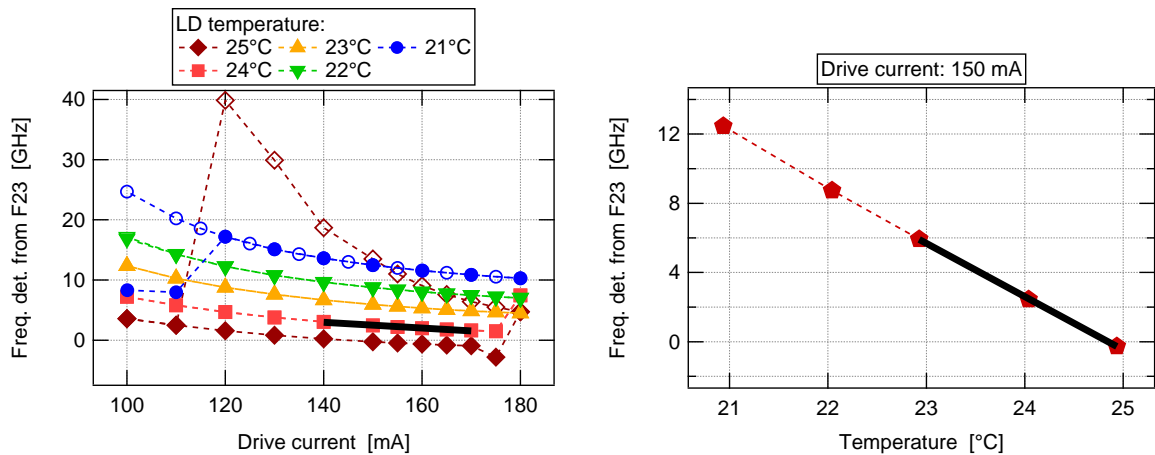


Figure 4.1 – Optical power at the 1560 and 780-nm of the FD-ECL versus the drive current for different LD temperatures. Filled markers: increased current. Empty markers: decreased current. Solid black line: linear fit at the typical operating conditions (24°C and 150 mA).



(a) Frequency tuning with laser drive current for varied chip temperatures. **(b)** Frequency tuning with laser temperature at constant drive current of 150 mA.

Figure 4.2 – Frequency tuning with laser drive current and temperature. The measurements are performed at the 780-nm output of the FD-ECL. Filled markers: increased current. Empty markers: decreased current. Solid black line: linear fit at the typical operating conditions (24°C and 150 mA).

4.2. Spectral characterization of FD laser systems

Table 4.1 – Spectral properties of the three laser systems. For the FD laser systems, the optical powers and the SMSRs are given for the 1560 and 780-nm outputs.

Parameter	Remark	Unit	FD-ECL	FD-DFB	LH-CW
Drive current		[mA]	150	184	121
LD temperature		[°C]	24.3	25.8	23.6
Optical power	at 1560 nm	[mW]	15	27	–
Optical power	at 780 nm	[μW]	200	500	6000
Current coeff. of frequency	at 780 nm	[$\frac{\text{GHz}}{\text{mA}}$]	–0.05	–0.6	–1
Temperature coeff. of frequency	at 780 nm	[$\frac{\text{GHz}}{\text{K}}$]	–3.2	–25	–25
SMSR	at 1560 nm	[dB]	> 54	> 44	–
SMSR	at 780 nm	[dB]	> 62	> 60	> 40

4.2.2 Relative intensity noise of FD laser systems

The laser intensity noise, often given by the RIN (cf. section 2.1.1.1), is measured using a photodetector that converts the incident optical power into an electrical current. Using an FFT spectrum analyzer, we measured the power spectral density of the associated electrical voltage fluctuations for Fourier frequencies up to 100-kHz. The RINs measured at the 1560 and 780-nm outputs of the FD-ECL system are depicted in Figure 4.3, as well as those of the 780-nm outputs of the FD-DFB and LH-CW. The specification for Rb vapor-cell clock applications to reach a short-term stability of $2 \cdot 10^{-13} \tau^{-1/2}$ given at all Fourier frequencies (dashed line) is particularly relevant around the modulation frequency of the clock detection, typically between 50 Hz and 500 Hz. The noise peaks (at 50 Hz and its harmonics and at high frequencies above 15 kHz) observed on the RIN of the LH-CW are due to the power source and intrinsic noise of the free-space photodetector¹.

Due to the quadratic process of the second harmonic generation (cf. equation (2.1)), the optical power fluctuations at the 1560-nm PPLN input are increased by a factor of 2 at the 780-nm output of the FD laser systems (i.e., $\delta P_{780nm} = 2 \eta P_{1560nm} \delta P_{1560nm}$). As for the RIN specifying the power noise normalized to the average power when described by a power spectral density as $\frac{\delta P_{780nm}^2}{P_{780nm}^2}$ (cf. section 2.1.1.1), the factor of 2 increase is squared and becomes 2^2 . The RIN of the 1560-nm output of the FD-ECL is in agreement with previously reported measurements using a similar ECL laser diode [100]. A ratio of 4.1 ± 1.3 is measured between the RINs of the 780-nm and 1560-nm outputs of the FD-ECL system, which indicates that no significant additional noise is introduced at this stage. The RIN of the 780-nm output of the FD-ECL at the Fourier frequencies of interest for Rb clock applications is below 10^{-12} Hz^{-1} , i.e., more than one order of magnitude lower than for the other two laser systems based on a DFB LD. All three laser systems satisfy the RIN

¹The RIN of the fiber-coupled laser systems are measured using battery-powered photodetectors.

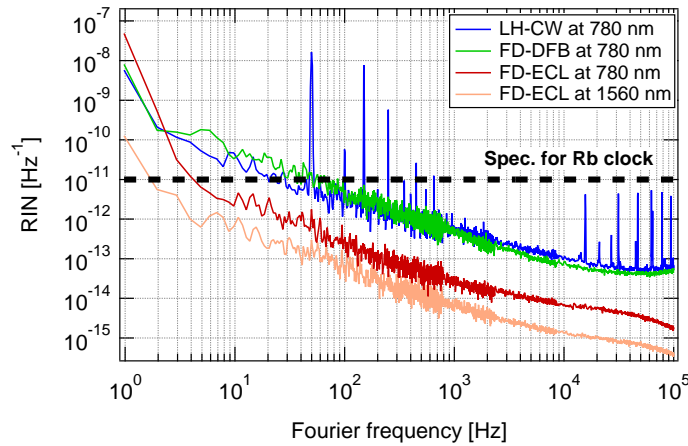


Figure 4.3 – Relative intensity noise spectrum for the three laser systems. Figure adapted from [122].

specification for excellent short-term stability in Rb vapor-cell clocks. Nevertheless, the low-noise FD-ECL represents a more attractive candidate compared to the DFB lasers emitting at 780 nm for high-precision spectroscopy applications.

4.2.3 Frequency noise of FD laser systems

To measure the frequency noise of the laser outputs, we make use of the absorption line of a reference Rb cell acting as a frequency discriminator to convert the FM noise into AM noise, which can be detected using a photodetector. The FM noise PSD is deduced from the AM noise PSD measured via the voltage fluctuations of the photodetector circuit using an FFT spectrum analyzer (cf. section 2.1.1.1). The FM noise spectra for the three laser systems measured at the 780-nm outputs with similar optical powers ($31.5 \pm 1.5 \mu\text{W}$) entering the reference Rb cell are presented in Figure 4.4. For the two laser systems based on a DFB LD, the FM noise is measured in the same order of magnitude; in contrast, for the FD-ECL, the FM noise of the 780-nm output is two to three orders of magnitude lower. The FM noise spectrum of the FD-ECL is limited by the laser current source and corresponds to the equivalent in FM noise of the laser current source noise ($1 \text{ nA}/\sqrt{\text{Hz}}$ drive current noise multiplied by the laser’s frequency-current tuning coefficient). Nevertheless, it agrees with the order of magnitude of the FM noise spectra reported for a similar ECL LD at 1560 nm [100] (which would degrade by a factor of 2^2 for the second harmonic at the 780-nm output of the PPLN).

We stabilize the laser frequency using the optical frequency references of a Rb vapor cell in order to reduce the FM noise at low Fourier frequencies corresponding to the modulation frequency of the clock detection, which is typically between 50 Hz and 500 Hz. We measure the FM noise for the frequency-stabilized lasers at 780 nm. In this case, for the two laser systems based on the DFB laser, the FM noise is reduced below $10^8 \text{ Hz}^2/\text{Hz}$ for Fourier frequencies up to the stabilization loop bandwidth of each system, which is between 2 to 5 kHz. Nevertheless, for the FD-ECL system, the FM noise in free-running mode (i.e., stabilization servo loop is open) being already limited by the employed current source noise, no substantial gain is acquired.

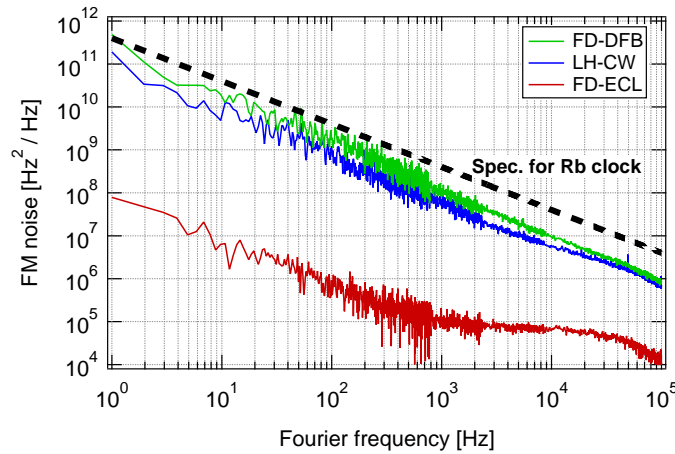


Figure 4.4 – FM noise spectra measured at the 780-nm outputs of the three laser systems in free running (not frequency stabilized). Figure adapted from [122].

4.2.4 Laser linewidth measurements

We determine the linewidth of the 780-nm outputs of the laser systems using two different methods and report the results in Table 4.2. The first method consists of measuring the linewidth of the beat note between two independent laser beams using a photodetector using an RF spectrum analyzer. We exploit the three laser systems to establish three simultaneous beat notes, as schematized in Figure 2.18. The individual laser LWs are deduced from the three-equation system and the error bars are determined by standard uncertainty propagation. In this case, the LW measurements for the FD-ECL are dominated by the larger LWs of the FD-DFB and LH-CW. To avoid modulation effects on the measured linewidths, the laser current modulation is switched off, leaving the lasers in free-running mode (open-loop conditions). The laser frequency fluctuations in this mode lead to the relatively large error bars (see Table 4.2), which present a limitation for this method. The LW measurement for the FD-ECL using the beat-note method can be improved if a more stable optical frequency reference with a narrower LW than that of the FD-ECL is employed instead of the free-running DFB laser.

In the second method, we exploit the beta-separation line [103] based on the measured FM noise spectra illustrated in Figure 4.4. The LW measurement of the FD-ECL in this case is characterized by lower uncertainty, but is limited by the FM noise measurement due to the current source noise. A linewidth of 2.6 kHz was reported for the 1560-nm output of a similar ECL in [142]. Assuming no additional noise in the frequency-doubling system, the LW of the 780-nm output of the PPLN would increase by a factor of two due to the SHG process. For the LH-CW and FD-DFB, the measured LWs are in good agreement with previously reported values in similar systems in [58] and [143], respectively. The error bars for the beta-line method are based on a statistical uncertainty where the errors arising from the FM noise spectra measurements are not included. The LWs measured using the two methods are essentially consistent within the error bars.

Table 4.2 – Linewidth of the three laser systems measured at 780-nm output. Method 1 estimates the laser linewidth from the beat-note signals and method 2 using the beta-line method. Table adapted from [122].

Laser system	Method 1 (Beat-note)	Method 2 (Beta-line)
FD-ECL	$0.57 + 1.1 / - 0.57$ MHz	0.15 ± 0.02 MHz
FD-DFB	1.95 ± 1.10 MHz	3.20 ± 0.32 MHz
LH-CW	2.10 ± 1.10 MHz	2.24 ± 0.22 MHz

4.3 Frequency instability measurements at two wavelengths

To evaluate the laser frequency instability, we measure the heterodyne beat signals realized with three laser systems in the configuration presented in Figure 2.18 using a fast photodetector and a frequency counter referenced to a H-maser (cf. section 2.5.2). Using a lock-in amplifier and a (PI) servo controller, each laser system is frequency stabilized to a different optical frequency reference corresponding to the Doppler-free features of the reference Rb cell (cf. Figure 2.10). The modulation and servo gain parameters of laser stabilization loops, which have a direct impact on the SNR limit of the laser frequency stability, are optimized for each laser system separately. The laser systems and the reference transitions used to stabilize their frequency for the three beat-note signals are summarized in Table 4.3. The beat-note frequency repeatability is assessed by five consecutive 900-s (≈ 15 -min) frequency measurements, for which the laser drive currents were switched off then on to their nominal value. The obtained beat-note frequency repeatability ranges between 10 and 100 kHz for different reference transitions used to stabilize the laser frequencies.

The fractional frequency fluctuations of the three beat-note signals are presented in Figure 4.5 with the reference LH-CW frequency instability measured separately by beating with a second identical LH-CW and the specification for high-performance Rb clock applications. The SNR limit of short-term laser frequency stability estimated from the associated lock-in error signal and detection noise are also presented for the FD-DFB ($2 \cdot 10^{-12} \tau^{-1/2}$) and LH-CW ($4 \cdot 10^{-12} \tau^{-1/2}$). The SNR limit of the FD-ECL frequency stability is estimated one order of magnitude lower $< 3 \cdot 10^{-13} \tau^{-1/2}$, which falls below the y-axis scale. The measured frequency instability at 1 s for Beat 1 (FD-ECL and LH-CW) and for Beat 2 (FD-DFB and LH-CW) is in reasonable agreement with the SNR limit of the LH-CW frequency stability. Meanwhile for Beat 3 (FD-ECL and FD-DFB), the measured frequency instability aligns with the SNR limit of the FD-DFB frequency stability. These results indicate that short-term frequency instability measurements for the FD-ECL using heterodyne beat are limited by the instability of the reference laser. This limitation can be tackled through employing a similarly or less noisy reference laser than the FD-ECL itself (e.g. beat between two identical FD-ECLs). The FD-DFB frequency stability of $2.5 \cdot 10^{-12}$ at $\tau = 1$ s measured with Beat 3 is improved by a factor of two due to the improved SNR of the detection signal, compared to the $5.2 \cdot 10^{-12}$ at $\tau = 1$ s instability previously measured at the 1560 nm against a stabilized commercial Er: fiber comb referenced to an H-maser [51].

4.3. Frequency instability measurements at two wavelengths

Table 4.3 – Three beat notes between the three laser systems (cf. Figure 2.18b). Each laser is frequency stabilized to a different optical frequency reference transition shown in Figure 2.10.

Beat label	Laser output wavelength	Laser system no 1:		Laser system no 2:	
		Name	Ref. transition	Name	Ref. transition
Beat 1	at 780 nm	FD-ECL	CO21-23	LH-CW	F23
Beat 2	at 780 nm	FD-DFB	CO22-23	LH-CW	F23
Beat 3	at 1560 nm	FD-ECL	CO21-23	FD-DFB	CO22-23

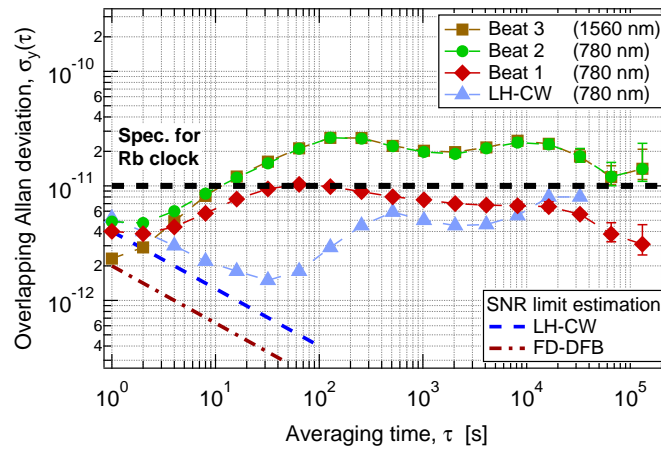


Figure 4.5 – Frequency instability of the beat-note signals between three laser systems (see Table 4.3). Frequency instability of the LH-CW (blue triangles) obtained from a separate beat-note measurement between two identical LHs is given as a reference. SNR ratio limit of laser frequency stability is estimated from the lock-in error signal and detection noise. For FD-ECL, the estimated SNR limit is below the y-axis scale ($< 3 \cdot 10^{-13} \tau^{-1/2}$). The specification for a high-performance CW-DR Rb vapor-cell clock is given with black dashed line. Figure adapted from [122].

For averaging times $\tau \geq 10$ s, fully overlapping Beat 2 and Beat 3 Allan deviations (see Figure 4.5) predominantly exhibit the frequency instability of the FD-DFB. The degraded medium-term frequency stability of the FD-DFB is attributed to the fluctuations of the residual reflections in the fiber-coupled system due to environmental temperature variations, which, by superimposing the absorption signal from the reference Rb cell, induce laser frequency fluctuations [51]. The first bump rising to $3 \cdot 10^{-11}$ at 100 s is mainly related to the cyclical temperature variations in the laboratory (period of $\sim 1.2 \cdot 10^2$ s), whereas the second bump on longer timescales at a similar level corresponds to the day-night temperature variations. Figure 4.6 presents the Beat 2 and Beat 3 frequency measurements, the simultaneously measured reference cell input and absorption signals, and the laboratory temperature. Both beat frequency fluctuations (Beat 2 and Beat 3) are strongly correlated with the FD-DFB reference cell input and absorption signals. The positive (or negative) correlation of the Beat 3 (or Beat 2) frequency with the reference cell signal of the FD-DFB can be explained by the positive (or negative) impact of the FD-DFB frequency shifts on the beat

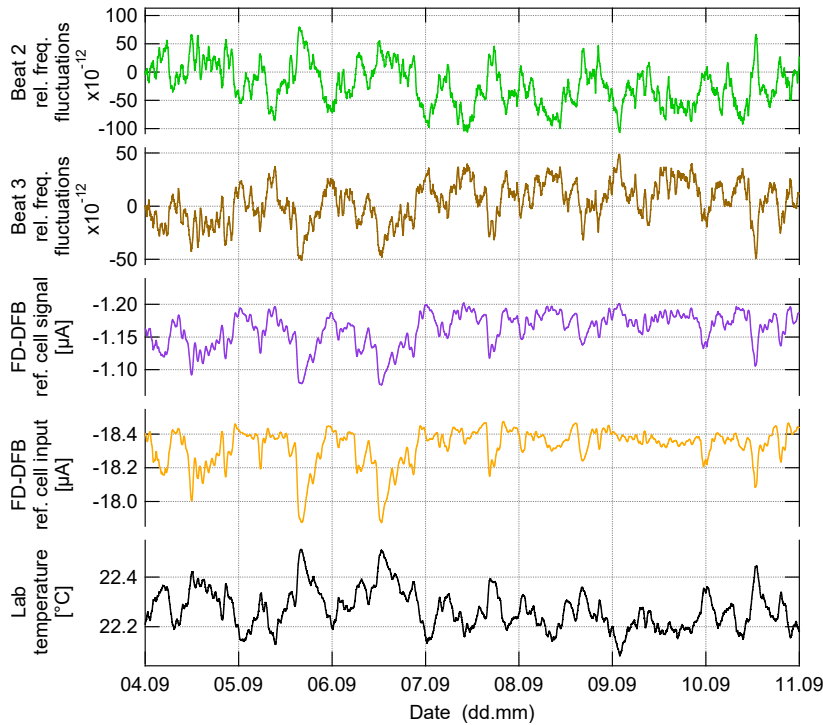


Figure 4.6 – Beat 2 and Beat 3 frequencies, reference Rb cell input and output signals of the FD-DFB laser system, and laboratory temperature.

frequency. The power fluctuations on the reference cell, originating from the fiber-coupled system due to the environmental temperature fluctuations, are transferred to the sub-Doppler absorption signal through the reference cell. As a result, the sub-Doppler features used as frequency references suffer a frequency shift due to the fluctuating Doppler background. A better thermal control of the fiber-coupled system, e.g., using a thermally stabilized baseplate, is necessary. Alternatively, the subtraction of the input power fluctuations from the sub-Doppler absorption signal would eliminate the instabilities originating before the reference cell.

The medium-term stability of Beat 1 frequency, which is dominated by the frequency instability of the fiber-coupled FD-ECL, remains below $1 \cdot 10^{-11}$ up to 1 day. The bump at 100 s is also attributed to the fluctuations of the optical power at the reference cell input of the FD laser system due to environmental temperature variations. On long-term timescales (up to 1 day), the Beat 1 frequency and reference cell signals of the FD-ECL or LH-CW do not present a consistent correlation, as depicted in Figure 4.7. We further evaluate Beat 1 frequency sensitivity to changes of the most relevant experimental parameters: the input optical power, the temperature of the reference Rb cell, and the C-field. Table 4.4 outlines the Beat 1 sensitivity coefficients and the instability of these parameters at the averaging time of 10^4 s that we use to estimate the contributions of variations of these parameters to the Beat 1 frequency instability. The C-field instability is deduced from the measured C-current instability via Ampere’s law. The measured sensitivity coefficients are in the same order of magnitude as those reported in [128] for an ECL formed by a LD chip and an external grating. The impact of the power fluctuations at the reference cell on the frequency stability has a lower impact for the FD-ECL system than for the FD-DFB system. The dominant contribution to FD-

4.3. Frequency instability measurements at two wavelengths

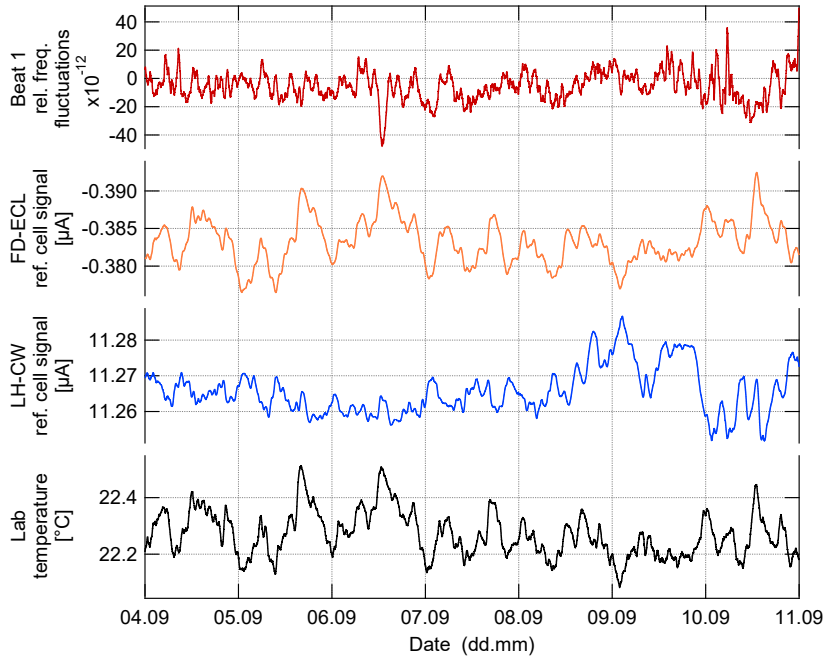


Figure 4.7 – Beat 1 frequency, reference Rb cell output signals of the two lasers systems forming the beat (FD-ECL and LH-CW), and laboratory temperature.

ECL frequency instability in the long term arises from the reference cell temperature fluctuations as outlined in Table 4.4. Both parameters primarily affect the Doppler background, where the sub-Doppler features used as frequency references are superimposed. The Doppler background may induce a frequency shift upon the sub-Doppler features with respect to their absolute frequencies [51], especially to the cross-over transitions located on the slope of the Doppler background (cf. Figure 2.10). Thus, the stabilized laser frequency is coupled to fluctuations of the reference Rb cell parameters via the Doppler background sensitivity. In addition to better thermal control of the fiber-coupled system, in this case, the subtraction of the Doppler background from the reference cell signal would reduce the impact of the parameter fluctuations on the laser frequency stability.

Table 4.4 – Measured Beat 1 frequency sensitivity coefficients due to variations of FD-ECL experimental parameter and estimated stability limitations at $\tau = 10^4$ s.

Parameter (FD-ECL)	Parameter fluctuations	Beat 1 sensitivity coeff.	Beat 1 rel. sensitivity coeff.	Estim. Beat 1 instab. contrib.
Optical power	0.53 %	$1.65 \cdot 10^3$ Hz/%	$4.3 \cdot 10^{-12}$ /%	$2.3 \cdot 10^{-12}$
Cell temp.	0.16 K	$-1.44 \cdot 10^4$ Hz/K	$-3.75 \cdot 10^{-11}$ /K	$5.9 \cdot 10^{-12}$
C-field	$1.64 \cdot 10^{-14}$ T	$6.0 \cdot 10^7$ Hz/T	$1.6 \cdot 10^{-7}$ /T	$2.6 \cdot 10^{-21}$
Estimated Beat 1 frequency instability ($\tau = 10^4$ s)				$6.3 \cdot 10^{-12}$
Measured Beat 1 frequency instability ($\tau = 10^4$ s)				$7.0 \cdot 10^{-12}$

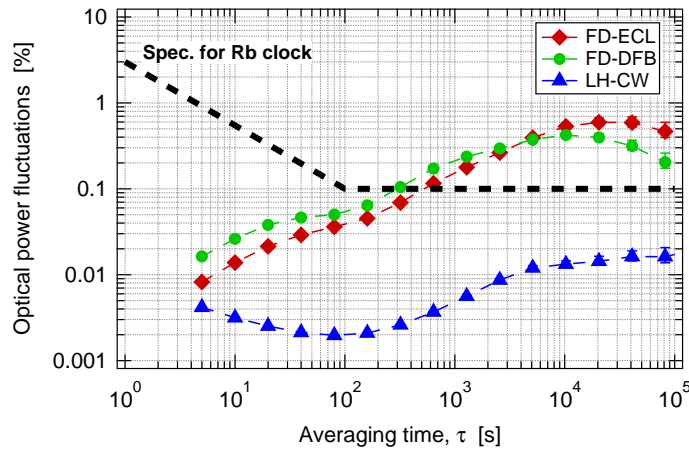


Figure 4.8 – Relative optical power fluctuations measured at the reference Rb cell input of the three laser systems. The measurement is carried out simultaneously with that of the frequency shown in Figure 4.5. The specification for a high-performance CW-DR Rb vapor-cell clock is given with black dashed line. Figure adapted from [122].

4.4 Evaluation of the optical power fluctuations

The relative intensity fluctuations at the 780-nm outputs of the laser systems are evaluated with optical power measurements at the input of reference Rb cells of FRU for FD laser systems and of LH-CW, see section 2.1. This configuration makes possible the simultaneous measurement of the optical power fluctuations with the beat-note frequency instability evaluation. Figure 4.8 presents the relative optical power instability of three laser systems in terms of the overlapping Allan deviation. The FD laser systems based on fiber-coupled components exhibit highly degraded power stability from the averaging time of $\tau = 5$ s compared to the LH-CW based on free-space optics. On long-term timescales, the optical power instability of FD laser systems reaches 0.5 % at the averaging time $\tau = 10^4$ s, while the LH-CW output power stability remains below 0.02 % up to $\tau = 10^5$ s, i.e., more than one order of magnitude better. The degraded optical power stability of the three laser systems at $\tau = 10^4$ s is attributed to the daily temperature variations of the laboratory, for which strong correlations were noted in Figures 4.6 and 4.7. The optical power instability of the FD laser systems is measured at the same level as the output power stability of the LH-POP with the integrated AOM (see Figure 3.12). The optical power instability of 0.5 % presents a serious limitation for the laser systems' use in high-performance vapor-cell clocks in the CW-DR scheme. In the POP-DR scheme, the AOM required for optical switching would further degrade the output power stability by about one order of magnitude (see Table 2.1). Therefore, an active optical power stabilization should be considered to restrain the limitations to clock stability, with a potential of several orders of magnitude improvement in power stability [115], thus the clock stability limit for unchanged intensity LS coefficient.

To identify the origin of the high power stability in the FD laser systems, we measure the optical power fluctuations at each stage of the FD-ECL system illustrated in Figure 2.3. The relative power fluctuations in terms of the overlapping Allan deviation are presented in Figure 4.9 for the 1560-nm and 780-nm outputs along with the FRU's reference cell input and absorption signals. According

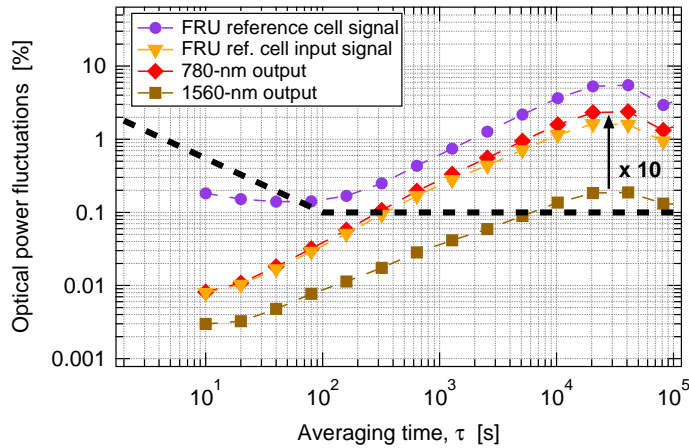


Figure 4.9 – Relative optical power fluctuations measured at different stages of the FD-ECL laser system. The specification for a high-performance CW-DR Rb vapor-cell clock is given with black dashed line. Figure adapted from [122].

to our results, the fiber-coupled beam splitter does not induce significant additional fluctuations. However, the degradation at the frequency-doubling process to the relative power stability is increased to a factor of 10 in particular in the long term instead of the expected factor of 2 due to the quadratic process (a factor of 2^2 degradation of RIN illustrated in Figure 4.3). The correlation between the variations of the laboratory temperature and the variations of the optical power at the FRU reference cell input, reflected in Figure 4.7, indicates that thermal effects are likely to be at the origin of the measured power instabilities.

4.5 Application to Rb vapor-cell clocks

In this section, we analyze the application potential of the frequency-doubled laser systems in Rb vapor-cell clocks. We estimate the clock SNR limit arising from laser AM and FM noise and the clock stability limitations due to the light-shift effects on medium-to-long-term timescales.

4.5.1 Impact on short-term clock stability

In Rb clocks based on optical detection, the clock detection noise comprises the transmitted laser AM noise and the FM noise converted into AM noise through the clock Rb cell [90, 91]. The impact of the FM-to-AM noise conversion depends on the atomic absorption through the cell (i.e., on the atomic density, laser frequency, cell temperature, buffer-gas pressure). In Table 4.5, we estimate the contributions of the measured laser AM and FM noise to the clock detection noise using the method presented in Appendix A. We then estimate the SNR limited short-term clock stability using the equation (1.56) and the error signal discriminator reported for a CW-DR clock in [80]. The RIN and FM noise of the stabilized laser systems are given at the Fourier frequency 70 ± 5 Hz, corresponding to a microwave modulation frequency for a CW-DR signal with a FWHM of 200 – 220 Hz. Two cases of FM-to-AM noise conversion through the clock Rb cell are investigated: low (0.3 nA/MHz) and high (3 nA/MHz) conversion rates. These noise conversion rates typically correspond to two

Chapter 4. Optical sources for Rb clocks based on frequency-doubled telecom lasers

Table 4.5 – Estimated SNR limit of short-term clock stability from laser intensity and frequency noise of the three laser systems. Two cases are investigated, a low and a high noise conversion rate.

Parameter	Unit	FD-ECL	FD-DFB	LH-CW
Laser RIN	/Hz	$3.5 \cdot 10^{-13}$	$8.2 \cdot 10^{-12}$	$3.3 \cdot 10^{-12}$
Laser FM noise	Hz ² /Hz	$1.2 \cdot 10^6$	$1.1 \cdot 10^7$	$2.3 \cdot 10^6$
<i>Low FM-to-AM noise conversion</i>				
Conversion rate	nA/MHz	0.3	0.3	0.3
AM noise contrib.	pA/Hz ^{1/2}	2.3	4.0	2.2
FM-to-AM noise contrib.	pA/Hz ^{1/2}	0.3	1.0	0.5
Tot. clock detection noise	pA/Hz ^{1/2}	2.3	4.1	2.2
Clock SNR limit	$\tau^{-1/2}$	$1.6 \cdot 10^{-13}$	$2.8 \cdot 10^{-13}$	$1.5 \cdot 10^{-13}$
<i>High FM-to-AM noise conversion</i>				
Conversion rate	nA/MHz	3.0	3.0	3.0
AM noise contrib.	pA/Hz ^{1/2}	2.3	4.0	2.2
FM-to-AM noise contrib.	pA/Hz ^{1/2}	3.3	9.8	4.5
Tot. clock detection noise	pA/Hz ^{1/2}	4.1	10.6	5.0
Clock SNR limit	$\tau^{-1/2}$	$2.8 \cdot 10^{-13}$	$7.2 \cdot 10^{-13}$	$3.4 \cdot 10^{-13}$

different laser frequencies for a given Rb vapor cell at a fixed temperature ($\approx 60^\circ\text{C}$).

The dominant laser noise contribution to the clock detection noise largely depends on the FM-to-AM noise conversion strength through the clock Rb cell. Under weak FM-to-AM noise conversion conditions, the laser AM noise contribution to the clock detection noise is the dominant factor. Meanwhile, under conditions yielding a high noise conversion, the noise contribution arising from the laser FM noise becomes the dominant limiting factor of the short-term clock stability. The FD-ECL exhibiting low AM and FM noise presents an advantage for its implementation in Rb vapor-cell clocks compared to DFB laser systems, particularly in terms of clock operational parameters that may yield a high FM-to-AM noise conversion rate. Excellent short-term clock stability at the level of $2 - 3 \cdot 10^{-13} \tau^{-1/2}$ that is weakly affected by noise conversion conditions is estimated for all considered laser reference frequencies, if the FD-ECL is used in the CW-DR Rb cell clock.

4.5.2 Impact on long-term clock stability

The long-term laser intensity and frequency fluctuations degrade the clock stability via light-induced shift effects (cf. section 1.5.5). In the CW-DR scheme, the main light-induced shift arises from the AC Stark shift effect, whose contribution is significantly reduced in the POP-DR scheme [144]. The impact of the laser intensity and frequency fluctuations on the clock stability via the LS effects is quantified by the associated LS coefficients (cf. section 1.5.5). We estimate the long-

term clock stability limits resulting from the intensity and frequency fluctuations of the three laser systems at $\tau = 10^4$ s, shown in Figures 4.5 and 4.8, for a CW-DR and a POP-DR clock. For the estimations presented in Table 4.6, we use the experimental LS coefficients of a CW-DR clock reported in [80] and for the POP-DR clock case, we use the coefficients reported in section 3.3.5.

For both interrogation schemes, the intensity instability of the FD laser systems is the dominant limiting factor of the clock stability: $> 10^{-13}$ in the CW-DR scheme and $> 10^{-14}$ in the POP-DR scheme. In the case of the LH-CW, the estimated clock stability limit of the intensity LS effect remains below $1 \cdot 10^{-13}$ in the two schemes. The estimated clock instability contribution of $0.4 \cdot 10^{-13}$ from frequency fluctuations of the FD-ECL and LH-CW in the CW-DR scheme presents an important instability source. Nevertheless, the reduced frequency LS coefficient in the POP-DR scheme results in a clock instability contribution at a negligible level $< 1 \cdot 10^{-15}$ for the FD-ECL and LH-CW. As the frequency fluctuations measured for the FD-DFB are 10 times higher, the frequency LS effect remains a significant clock instability source in both schemes. Thus, the frequency instability of the FD-DFB presents a serious limitation for its implementation in high-performance Rb vapor-cell clocks. The intensity instability is the dominant limiting factor for the FD laser systems as regards their application in high-performance Rb clocks. Meanwhile, for the LH-CW, laser intensity and frequency instability contribute equally to the long-term clock instability.

Table 4.6 – Estimated limitations of long-term clock stability from intensity and frequency fluctuations of the three laser systems via intensity LS (ILS) and frequency LS (FLS) effects, respectively. Laser relative intensity and frequency fluctuations are measured at $\tau = 10^4$ s (cf. Figures 4.5 and 4.8). ^(a) LS coefficients measured in CW-DR scheme are extracted from [80]. ^(b) measured LS coefficients for the POP-DR clock were presented in section 3.3.5.

Parameter ($\tau=10^4$ s)	Unit	FD-ECL	FD-DFB	LH-CW
Laser rel. intensity fluct.	%	0.5	0.5	0.02
Laser frequency fluct.	kHz	3	10	3
<i>CW-DR scheme</i>				
ILS coefficient, $ \alpha_{LS}^{CW} $ ^(a)	/%	$1.0 \cdot 10^{-12}$	$1.0 \cdot 10^{-12}$	$1.0 \cdot 10^{-12}$
ILS clock stability limit		$5.0 \cdot 10^{-13}$	$5.0 \cdot 10^{-13}$	$0.2 \cdot 10^{-13}$
FLS coefficient, $ \beta_{LS}^{CW} $ ^(a)	/kHz	$1.2 \cdot 10^{-14}$	$1.2 \cdot 10^{-14}$	$1.2 \cdot 10^{-14}$
FLS clock stability limit		$0.4 \cdot 10^{-13}$	$1.2 \cdot 10^{-13}$	$0.4 \cdot 10^{-13}$
Tot. LS clock stability limit		$5.0 \cdot 10^{-13}$	$5.1 \cdot 10^{-13}$	$0.4 \cdot 10^{-13}$
<i>POP-DR scheme</i>				
ILS coefficient, $ \alpha_{LS}^{POP} $ ^(b)	/%	$2.3 \cdot 10^{-14}$	$2.3 \cdot 10^{-14}$	$2.3 \cdot 10^{-14}$
ILS clock stability limit		$11.5 \cdot 10^{-15}$	$11.5 \cdot 10^{-15}$	$0.5 \cdot 10^{-15}$
FLS coefficient, $ \beta_{LS}^{POP} $ ^(b)	/kHz	$1.5 \cdot 10^{-16}$	$1.5 \cdot 10^{-16}$	$1.5 \cdot 10^{-16}$
FLS clock stability limit		$0.5 \cdot 10^{-15}$	$1.5 \cdot 10^{-15}$	$0.5 \cdot 10^{-15}$
Tot. LS clock stability limit		$11.5 \cdot 10^{-15}$	$11.6 \cdot 10^{-15}$	$0.6 \cdot 10^{-15}$

4.6 Conclusion

In this chapter we reported on the performance evaluation of two frequency-doubled and Rb-stabilized 1560-nm laser diodes based on different chip technologies as an alternative to 780-nm lasers. The RIN and FM noise of the FD-ECL, measured at 780 nm, is more than one order of magnitude lower than the reference laser (LH-CW) based on a LD emitting directly at 780 nm. These results make the FD-ECL a compelling candidate for implementation in high-performance Rb vapor-cell atomic clocks. Furthermore, the low frequency instability, better than 10^{-11} at all timescales, of the FD-ECL leads to a highly stable double-wavelength optical frequency source for many high-precision applications at both wavelengths (780 and 1560 nm). However, the frequency instability in the medium-to-long term of the FD-DFB is not suitable for high-performance Rb clock applications. The optical power instability for both frequency-doubled laser systems, transferred to the clock instability via the intensity light shift effect, currently presents a serious limitation for their use in Rb vapor-cell atomic clocks with 10^{-14} stability over one day. Nevertheless, particularly in the CW-DR scheme, the impact of the optical power fluctuations on the clock frequency via the intensity LS effect could be corrected through post processing of their simultaneous measurements and knowing the intensity LS coefficient under the specific clock operation conditions.

The heterodyne beat measurements of the linewidth and the short-term frequency instability for the FD-ECL are currently limited by the *worse* performance of the reference laser used to realize the beat note. To overcome this limitation, a reference laser with similar or lower noise should be employed. Moreover, the Grosslambert crossvariance analysis [145, 146] could, in principle, provide the individual laser system frequency instability from simultaneous measurements of more than two oscillators, such as in the configuration illustrated in Figure 2.18b. However, in our case, with one lower-noise laser (FD-ECL) compared to two similarly noisy lasers (FD-DFB and LH-CW), such analysis did not produce meaningful results, and should be considered in future studies with oscillators exhibiting similar noise levels.

The measured spectral properties and frequency instability for the FD-ECL system are very promising in view of high-performance Rb vapor-cell clocks. Nevertheless, given the long-term clock instability, the optical power fluctuations of the laser system must be reduced at least by one order of magnitude for both the CW and POP-DR schemes. The output power level at 780 nm is currently sufficient for CW-DR clock applications. In fact, the next chapter evaluates the realization of a CW-DR clock using the FD laser systems and experimentally compares this case to the use of the LH-CW emitting directly at 780 nm. However, the POP-DR scheme requires higher optical power at 780 nm of few tens of mW in order to guarantee an efficient optical pumping and an optical switching means, e.g. an AOM. To get a higher optical power at 780 nm from a FD telecom laser, one can use an optical amplifier. The optical amplifiers in the 780 nm spectral region are not as well developed as in the 1560 nm spectral region. Hence, by working in the telecom C-band (around 1560 nm) one can benefit from the high performance and reliability of erbium-doped fiber amplifiers (EDFA) operating at 1560 nm. Alternatively, a PPLN waveguide with a higher doubling efficiency or using a cascade of two PPLN waveguides such as demonstrated in [133] could increase the optical power at 780 nm.

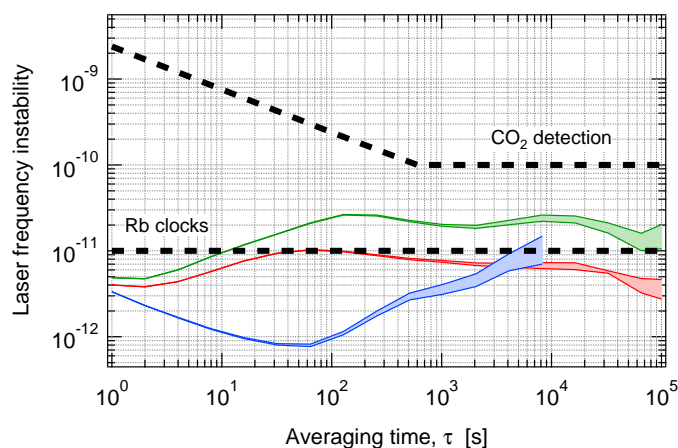


Figure 4.10 – Laser frequency instability and requirements for high-performance Rb-cell clock applications at 780 nm and for CO₂ detection at 1572 nm. The colored zones represent the fractional frequency instability of the three laser systems evaluated with beat-note frequency measurements; green: red: FD-ECL, FD-DFB, and blue: LH-CW.

Fiber-coupled lasers emitting at 1560 nm and benefiting from Rb atomic frequency references present many advantages towards compact and reliable optical sources with high-frequency stability for applications at both 1560 and 780 nm. The requirements for the frequency instability of optical sources in space-borne CO₂ detection applications at 1572 nm and Rb clock applications at 780 nm are presented in Figure 4.10 along with the frequency instability of the FD-ECL. Nevertheless, the sensitivity of the fibered systems to thermal and mechanical perturbations may represent an important drawback for applications requiring light with a highly stable frequency and intensity. The next chapter evaluates the potential of improving the short-term clock stability using a low-noise laser diode for optical detection. The requirements for other potential applications at both wavelengths are less stringent than those for Rb vapor-cell clocks, which makes frequency-doubled low-noise telecom lasers stabilized on Rb attractive candidates for implementation.

5 CW-DR Rb vapor-cell clock realization using telecom lasers

In the telecom C-band, laser diodes with better spectral properties (e.g. low noise, narrow linewidth) and higher reliability are more easily available than in the wavelength region corresponding to the Rb optical transitions (around 780 nm). Several high-precision applications dealing with Rb atoms have previously explored the potential of frequency-doubled telecom lasers stabilized using Rb frequency references [131, 134, 139] (see section 4.1 for more details). In this work, we employ frequency-doubled telecom lasers that are frequency stabilized using a Rb frequency reference in a CW-DR Rb vapor-cell clock for optical pumping and detection. The two FD laser systems (one based on an ECL, the other on a DFB LD) characterized in the chapter 4 as well as the LH-CW based on a DFB LD emitting directly at 780 nm are evaluated using the CW-DR clock described in section 2.3. In particular, the FD-ECL exhibiting low (AM and FM) noise has great potential for improving the short-term stability of Rb vapor-cell clocks by reducing the clock detection noise (cf. Table 4.5).

In the following sections, we evaluate the laser systems using two optical-pump frequencies leading to different FM-to-AM noise conversion rates through the clock Rb cell. First, the CW-DR signal is optimized for a high signal-to-noise ratio of clock detection as a function of the applied optical and microwave powers. Second, we quantitatively evaluate the independent contributions to the clock detection noise from the laser AM noise transmitted to the clock detection noise and the FM noise converted into AM noise through the clock Rb cell. In addition, we discuss the laser noise contributions via the light-shift effects and the LO-CW phase noise via the intermodulation effect. The comprehensive clock noise budgets are then established for the three laser systems. Finally, we present the measured short-term clock instabilities and discuss the impact of laser frequency and intensity fluctuations on the medium-to-long term clock stability. Sections 5.3 and 5.4 are essentially based on our article [147]. Nevertheless, these sections also include additional results on the evaluation of a third optical source (FD-DFB) and further discussion. The text and figures are adapted from [147].

5.1 FM-to-AM noise conversion via the atomic vapor cell

The optical detection noise in vapor-cell clocks includes the laser AM noise and the FM noise converted into AM noise via the Rb vapor cell acting as a frequency discriminator [43, 91]. The impact of this phenomenon is quantified by a FM-to-AM noise conversion rate, which is defined as the local slope of the vapor cell absorption line at the laser frequency. To analyze the impact of the laser FM noise on the short-term clock instability, we study the clock operation using the laser frequency stabilized on four reference transitions (labeled CO10-11, F12, F23, and CO21-23) obtained from the FRU or the reference module integrated in the LH-CW. The reference transitions demonstrate a substantial difference in their FM-to-AM noise conversion rates. The Doppler-free absorption signals denoting the reference transition frequencies and the linear absorption of the clock cell are illustrated in Figure 5.1, expressed in terms of photodetector current. The (direct or crossover) reference transitions with associated FM-to-AM conversion rates are outlined in Table 5.1. For the same experimental conditions (cell temperature, C-field, optical power, and microwave power), the change of the optical-pump frequency is expected to have a direct impact on the short-term clock instability due to the laser FM noise via the FM-to-AM conversion phenomenon [43, 91]. In the next sections, the analyses focus on the two optical frequencies CO10-11 and F12.

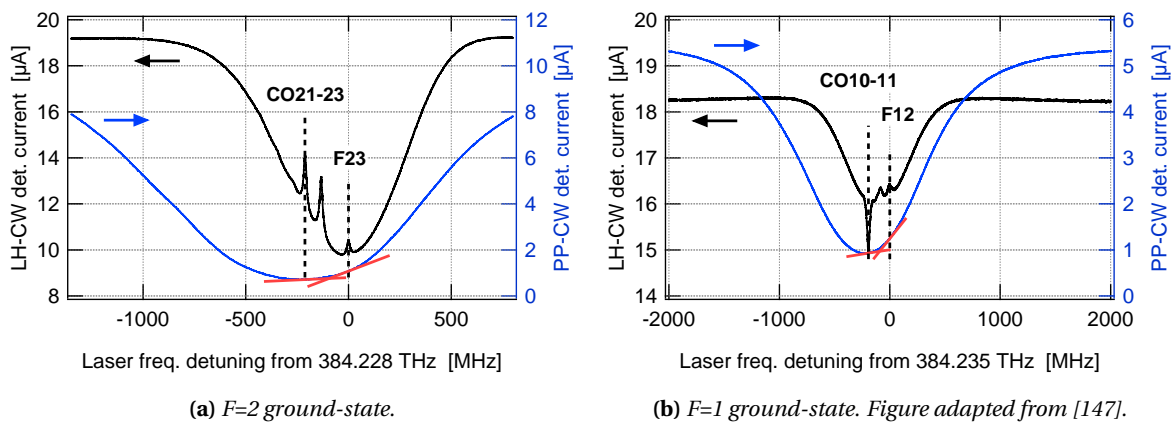


Figure 5.1 – Left axes: Doppler-free absorption signals of the reference Rb cell of LH-CW. Right axes: Linear absorption signals of the clock Rb cell of PP-CW. The signals are give in terms of the photodetector current. Red lines: local linear fit to deduce the local slopes corresponding to the FM-to-AM conversion rates.

5.2. Double-resonance clock signal optimization

Table 5.1 – Reference transition labels, frequency detunings from F12, and the corresponding frequency discriminators obtained via the clock Rb cell.

Label	Reference transition	Frequency detuning from F12 [MHz]	Conversion rate [nA/MHz]
F12	$ 5^2S_{1/2}, F = 1\rangle \leftrightarrow 5^2P_{3/2}, F = 2\rangle$	0	2.99 ± 0.06
CO10-11	$ 5^2S_{1/2}, F = 1\rangle \leftrightarrow 5^2P_{3/2}, F = 0, 1\rangle$	-193.054	0.38 ± 0.03
F23	$ 5^2S_{1/2}, F = 2\rangle \leftrightarrow 5^2P_{3/2}, F = 3\rangle$	-6'568.031	3.39 ± 0.05
CO21-23	$ 5^2S_{1/2}, F = 2\rangle \leftrightarrow 5^2P_{3/2}, F = 1, 3\rangle$	-6'779.825	0.42 ± 0.06

5.2 Double-resonance clock signal optimization

The experimental parameters that determine the clock operation conditions impact the clock frequency stability on all timescales. Moreover, the conditions for optimizing the short-term clock stability may differ from those for optimizing the long-term stability (e.g. section 3.2). To study the impact of the laser noise in this chapter, our main focus concerns the short-term clock instability, for which one of the main limitations arises from the signal-to-noise ratio of the detection (cf. section 1.6.2.1). In the CW-DR scheme, the signal-to-noise ratio limited clock stability is approximated by the equation (1.56) can be optimized via the clock signal parameters (amplitude, FWHM, background, contrast, and FoM, cf. section 1.3.2.1). The measured CW-DR signal parameters and estimated discriminator slopes for the optical-pump frequency on CO10-11 are illustrated in Figures 5.2 and 5.3 as a function of the optical and microwave powers applied to the clock cell, respectively. In addition, the LO-CW frequency modulation parameters (frequency and depth) are optimized (see Appendix B) in order to improve the SNR limited short-term clock stability via maximizing the discriminator slope D_s of the error signal (cf. equation (1.56)).

The optimized CW-DR signal parameters are obtained for an optical power within the interval of $68 - 72 \mu\text{W}$ (depending on the laser system) and a microwave power of -36.4 dBm ($0.23 \mu\text{W}$) at the cavity input. The CW-DR signals measured using the three laser systems tuned to CO10-11 and F12 are shown in Figure 5.4. Table 5.2 outlines the amplitude, FWHM, contrast, and discriminator slope deduced from the Lorentzian fits of the CW-DR signal, and the frequency shift of the resonance center from the unperturbed ^{87}Rb hyperfine splitting frequency is derived from the demodulated error signals depicted in Figure 5.5. As expected, the CW-DR signal parameters do not vary according to the employed laser. The amplitudes of the CW-DR signals fall within the error bars. The offsets in the background light are due to the discrete attenuation of the optical power at the PP-CW input using neutral density filters depending on the used laser system. The difference in the optical power with individual lasers leads to slight differences in the CW-DR signal line broadening (i.e., FWHM). For the optical-pump frequency on CO10-11, higher contrasts are reached thanks to the higher optical absorption compared to the absorption at F12. The central frequencies of the CW-DR clock signals (ν_{clock}) shift between the two optical-pump frequencies due to the frequency light-shift effect with the coefficient $4.9 \cdot 10^{-2} \text{ Hz/MHz}$ ($7.2 \cdot 10^{-12} / \text{MHz}$, see section 5.3.2).

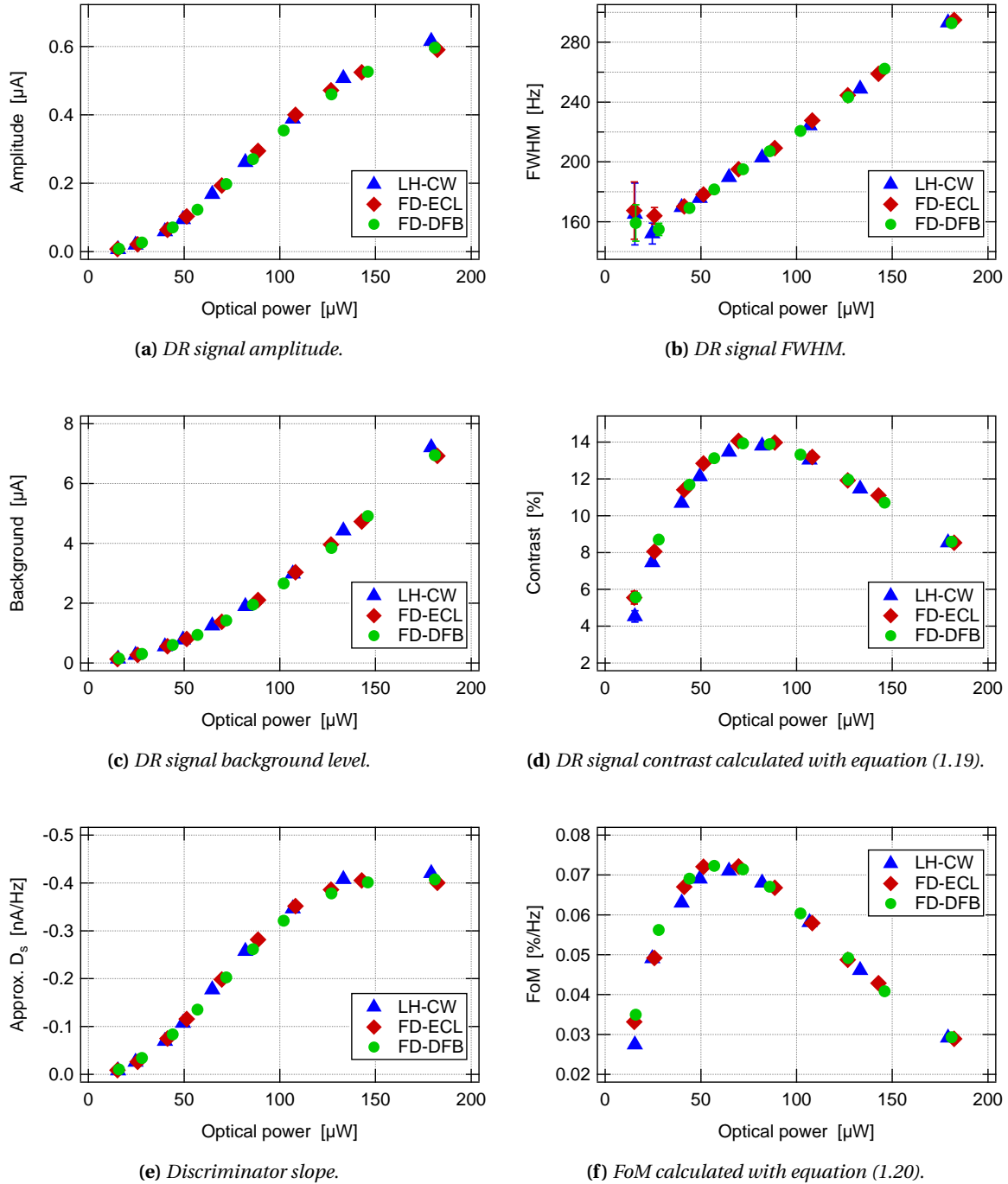


Figure 5.2 – CW-DR clock signal parameters as a function of the optical power at the PP-CW input. The laser frequency is stabilized on CO10-11 and the microwave power is -36.4 dBm (0.23 μ W) optimized as shown in Figure 5.3.

5.2. Double-resonance clock signal optimization

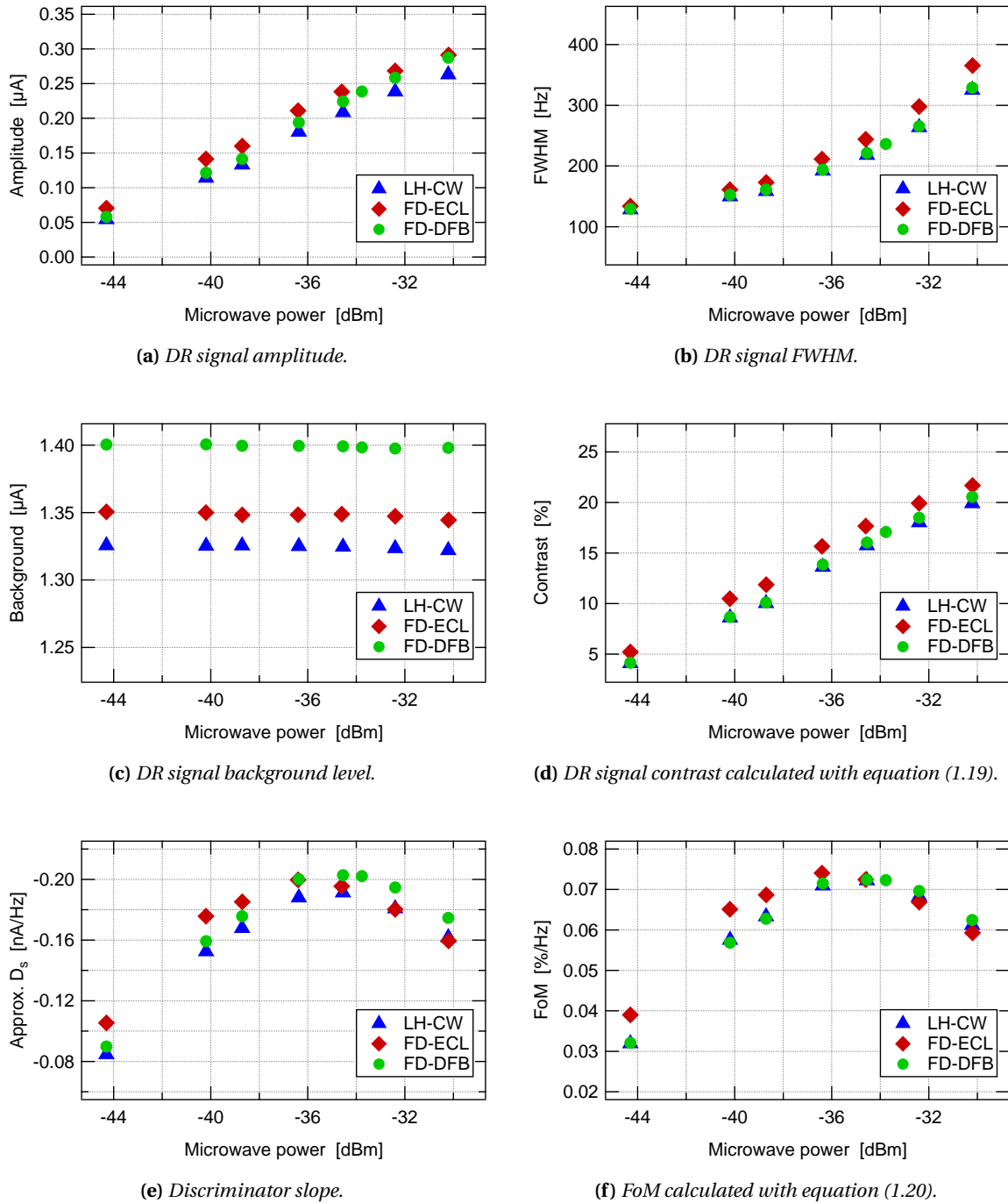


Figure 5.3 – CW-DR clock signal parameters as a function of the microwave power. The laser frequency is stabilized on CO10-11 and the optical power at the PP-CW input is $69 \pm 4 \mu\text{W}$, $68 \pm 4 \mu\text{W}$, $72 \pm 4 \mu\text{W}$ respectively for FD-ECL, FD-DFB, and LH-CW, optimized for each laser system as shown in Figure 5.2.

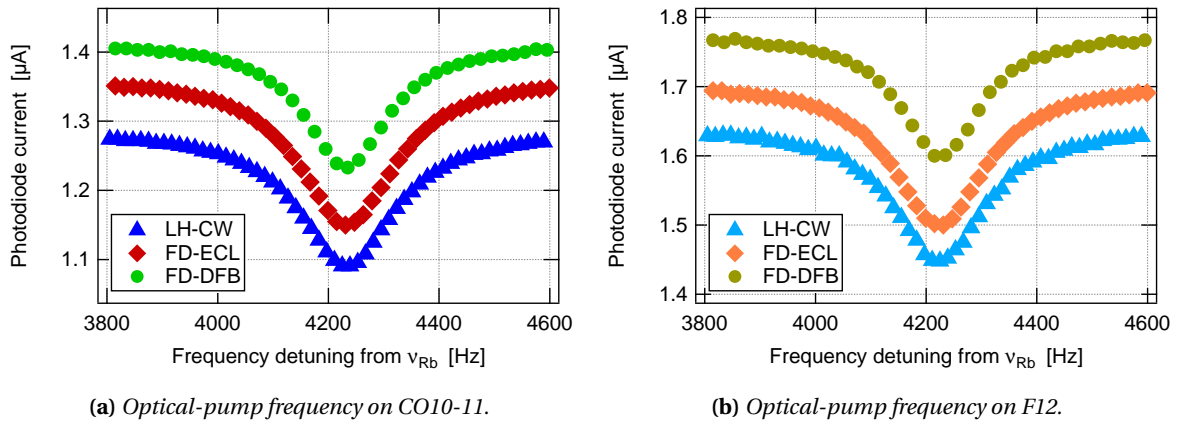


Figure 5.4 – CW-DR clock signals measured using the three laser systems for the two optical-pump frequencies. Figure adapted from [147] and includes additional data (FD-DFB).

Table 5.2 – Optimized CW-DR signal parameters measured using the three laser systems for two optical-pump frequencies. Amplitude, FWHM, contrast, and discriminator slope (D_s) deduced from the fitting of CW-DR signals and ($\Delta\nu_{clock} = \nu_{clock} - \nu_{Rb}$) central frequency detuning from the unperturbed hyperfine splitting frequency deduced from error signals. Table adapted from [147] and includes additional data (FD-DFB).

(a) Optical-pump frequency tuned to CO10-11.

Parameter	Unit	FD-ECL	FD-DFB	LH-CW
Amplitude	[μA]	0.21 ± 0.01	0.18 ± 0.01	0.20 ± 0.01
FWHM	[Hz]	212.2 ± 0.7	183.8 ± 1.0	210.2 ± 0.8
Contrast	[%]	15.7 ± 0.1	12.7 ± 0.1	15.1 ± 0.1
Approx. D_s	[nA/Hz]	-0.20 ± 0.01	-0.20 ± 0.01	-0.19 ± 0.01
$\Delta\nu_{clock}$	[Hz]	4233.5 ± 0.1	4232.6 ± 0.1	4233.3 ± 0.1

(b) Optical-pump frequency tuned to F12.

Parameter	Unit	FD-ECL	FD-DFB	LH-CW
Amplitude	[μA]	0.21 ± 0.01	0.18 ± 0.01	0.19 ± 0.01
FWHM	[Hz]	209.6 ± 0.8	172.0 ± 1.9	199.0 ± 1.9
Contrast	[%]	12.1 ± 0.1	9.9 ± 0.1	11.8 ± 0.1
Approx. D_s	[nA/Hz]	-0.20 ± 0.01	-0.21 ± 0.01	-0.19 ± 0.01
$\Delta\nu_{clock}$	[Hz]	4223.6 ± 0.1	4225.9 ± 0.1	4224.4 ± 0.1

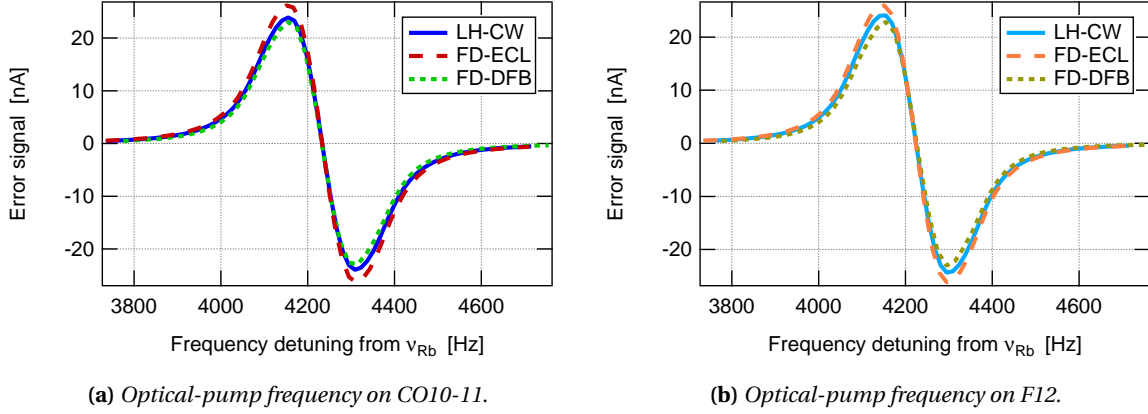


Figure 5.5 – Error signals measured using the three laser systems for the two optical-pump frequencies at the lock-in detector output. Figure adapted from [147] and includes additional data (FD-DFB).

5.3 Noise contributions to the short-term clock instability

In CW-DR Rb vapor-cell clocks, the main instability contributions on the short-term timescales generally arise from the optical detection noise, light-shift effects, and the LO-CW phase noise (cf. section 1.6.2). The laser AM and FM noises affect the clock stability through two independent and distinct processes: the detection signal-to-noise ratio and the light-shift effects. Meanwhile, the LO-CW phase noise contributes via the intermodulation effect. In this section, we first study the signal-to-noise limit of the clock stability and analyze various noise contributions to the optical detection signal for two optical-pump frequencies (on CO10-11 and F12). Secondly, we evaluate the short-term instability contributions of the laser intrinsic AM and FM noises via the intensity and frequency LS effects, respectively. Thirdly, we discuss the microwave phase noise contribution to the short-term clock instability. Finally, we establish the total short-term clock instability budget.

5.3.1 Signal-to-noise limit

In this section, we evaluate the different laser noise contributions to the SNR limit of the short-term clock stability for the three laser systems studied in this thesis. The instability contributions arising from the LS effects and the LO-CW phase noise are discussed in the next sections. The short-term frequency stability of a CW-DR clock limited by the detection signal-to-noise ratio is approximated by the equation (1.56) for the discriminator slope of the error signal (D_s) and the clock detection noise PSD (S_n) at the microwave modulation frequency. In order to evaluate the individual impacts of the laser AM noise and the FM-to-AM noise conversion through the clock cell, we measure the clock detection noise at the end of the clock Rb cell for two different laser frequencies corresponding to two known FM-to-AM noise conversion rates. We then calculate the independent clock detection noise PSDs arising from the two laser noise contribution mechanisms using the analysis presented in Appendix A. The clock detection noise PSDs measured at the end of the clock cell for laser frequencies stabilized on CO10-11 and F12 (FM-to-AM noise conversion rates in Table 5.1) are depicted in Figure 5.6. The peaks at the Fourier frequency of 70 Hz come from the microwave frequency modulation.

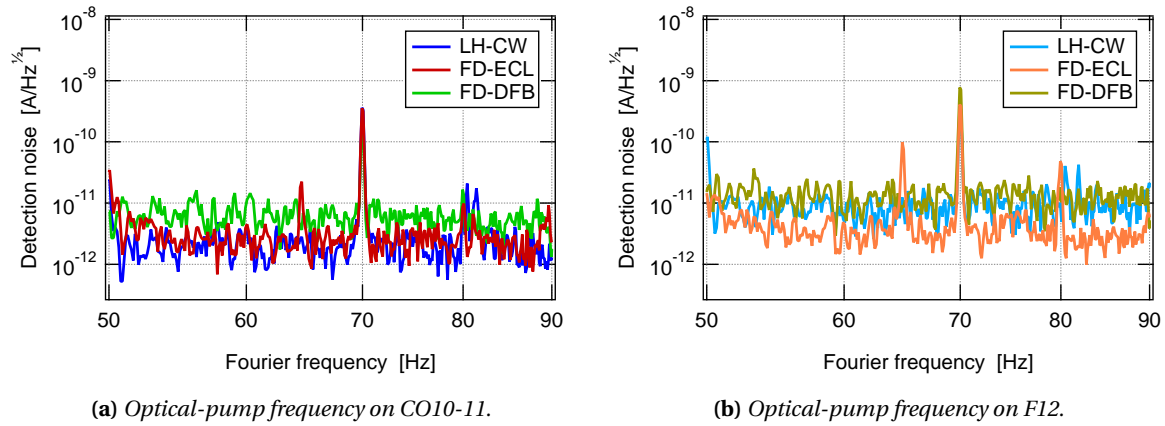


Figure 5.6 – Clock detection noise PSDs measured using the three laser systems for the two optical-pump frequencies. Figure adapted from [147] and includes additional data (FD-DFB).

Tables 5.3a and 5.3b outline the total SNR limits of the clock stability estimated using the measured error signals (cf. Figure 5.5) and clock detection noises (cf. Figure 5.6) and the limitations arising from the laser AM noise and the FM-to-AM noise conversion calculated using the measured clock detection noises (cf. Figure 5.6) and FM-to-AM noise conversion rates (cf. Table 5.1), as explained above. The detector intrinsic noise is measured in the absence of light and includes the thermal and dark current noises. The shot-noise limit of the clock stability is estimated using the equation (1.56) from the shot-noise PSD given by $N_{\text{shot-noise}} = \sqrt{2 \cdot e \cdot I_{\text{dc}}}$, where e is the electron charge and I_{dc} is the measured photocurrent at the FWHM of the CW-DR signal (cf. Figure 5.4). The calculated independent noise PSD contributions of the laser AM noise and the FM-to-AM noise conversion to clock detection noise are in good agreement with our predictions based on the laser AM and FM noise measured at the 780-nm output of the laser systems (cf. Table 4.5) and considering similar noise conversion rates to those studied in this section.

Using the FD-ECL and optical-pump frequency corresponding to a low FM-to-AM noise conversion rate, the estimated SNR limited clock stability of $1.3 \cdot 10^{-13}$ is at the state-of-the-art level reported for compact vapor-cell clocks (cf. Figure I3). Furthermore, under increased FM-to-AM noise conversion conditions, the SNR limit is weakly impacted and is increased to $2.3 \cdot 10^{-13}$. This result is highly promising for the use of the FD-ECL system in high-performance Rb vapor-cell clocks. In the case of weak FM-to-AM noise conversion (i.e., laser frequency tuned to CO10-11), laser AM noise is the dominant contribution to clock detection noise for all three laser systems. The noise contribution due to the FM-to-AM conversion through the clock Rb cell becomes the dominant clock detection noise for all three laser systems tuned to F12, i.e., conditions maximizing the FM-to-AM conversion. Thanks to the low FM noise of the FD-ECL, the estimated SNR limit of the clock stability is weakly impacted by the increased FM-to-AM noise conversion rate. Meanwhile, for laser systems based on DFB lasers (FD-DFB and LH-CW), the SNR limit of the short-term clock stability is increased by more than a factor of two due to their high FM noise. This aspect limits the clock operational parameters that govern the noise conversion phenomenon through the clock Rb cell, especially the laser frequency for a given vapor cell, for the use of the DFB laser systems in view of achieving excellent short-term clock stability.

5.3. Noise contributions to the short-term clock instability

Table 5.3 – Estimated SNR limit of the clock stability and the independent contributions of the laser AM noise and the FM-to-AM noise conversion via the clock Rb cell to the measured clock detection noise for three laser systems and two optical-pump frequencies tuned to CO10-11 and F12. Table adapted from [147] and includes additional data (FD-DFB).

(a) Optical-pump frequency tuned to CO10-11.

Noise source	FD-ECL		FD-DFB		LH-CW	
	Noise [pA/Hz ^{1/2}]	Est. clock instab.	Noise [pA/Hz ^{1/2}]	Est. clock instab.	Noise [pA/Hz ^{1/2}]	Est. clock instab.
Detector in dark	0.2	–	0.2	–	0.2	–
Shot-noise limit	0.6	$2.9 \cdot 10^{-14}$	0.6	$2.9 \cdot 10^{-14}$	0.6	$2.9 \cdot 10^{-14}$
Laser AM	2.9	$1.2 \cdot 10^{-13}$	6.1	$2.7 \cdot 10^{-13}$	2.1	$9.6 \cdot 10^{-14}$
Laser FM-to-AM	0.6	$2.5 \cdot 10^{-14}$	1.8	$7.7 \cdot 10^{-14}$	1.3	$5.8 \cdot 10^{-14}$
Total SNR limit	3.0	<u>$1.3 \cdot 10^{-13}$</u>	6.4	$2.8 \cdot 10^{-13}$	2.5	<u>$1.2 \cdot 10^{-13}$</u>

(b) Optical-pump frequency tuned to F12.

Noise source	FD-ECL		FD-DFB		LH-CW	
	Noise [pA/Hz ^{1/2}]	Est. clock instab.	Noise [pA/Hz ^{1/2}]	Est. clock instab.	Noise [pA/Hz ^{1/2}]	Est. clock instab.
Detector in dark	0.2	–	0.2	–	0.2	–
Shot-noise limit	0.7	$3.1 \cdot 10^{-14}$	0.7	$3.1 \cdot 10^{-14}$	0.7	$3.1 \cdot 10^{-14}$
Laser AM	2.9	$1.2 \cdot 10^{-13}$	6.1	$2.5 \cdot 10^{-13}$	2.1	$9.2 \cdot 10^{-14}$
Laser FM-to-AM	4.6	$2.0 \cdot 10^{-13}$	13.7	$5.6 \cdot 10^{-13}$	9.8	$4.3 \cdot 10^{-13}$
Total SNR limit	5.5	<u>$2.3 \cdot 10^{-13}$</u>	15.0	$6.2 \cdot 10^{-13}$	10.0	$4.4 \cdot 10^{-13}$

5.3.2 Light shift effects

Laser intensity and frequency noise at the clock Rb cell input degrade the clock frequency stability on the short-term timescales via the intensity and frequency light-shift effects (cf. section 1.6.2.2). The clock instability contributions of the LS effects are characterized by the sensitivity coefficients defined in section 1.5.5. We measure the clock frequency shift as a function of the applied optical power at the clock cell input for different optical-pump frequencies, using two reference transitions from each hyperfine component (cf. Table 5.1). The LS shifts measured using the three laser systems are presented in Figure 5.7. The intensity LS coefficient is deduced from the linear fit applied to the clock frequency shift for fixed laser frequency, while the frequency LS coefficient is deduced from the clock frequency shift as a function of the laser frequency for fixed optical power. The intensity and frequency LS coefficients measured for our CW-DR clock are gathered in Table 5.4 and 5.5. The frequency LS coefficients are determined for the input optical power (around $70 \mu\text{W}$) of the clock Rb cell while optimizing the short-term clock stability for optical-pump frequencies tuned to $F=1$ transitions. In the case of an optical-pump frequency tuned to $F=2$ transitions, the optical power (proportional to the optical Rabi frequency) required to optimize the CW-DR signal and the short-term clock stability is higher than $\sim 70 \mu\text{W}$ due to the higher optical absorption of the $F=2$ hyperfine component in comparison to the $F=1$. However, the frequency LS coefficient increases linearly for higher optical power, as predicted by the AC Stark shift effect, in the CW-DR scheme [79] and may become an important clock instability source in the case of optical-pump frequencies tuned to $F=2$ transitions.

We estimate the impact of the light-shift effects arising from laser noise using the equations (1.57) and (1.57) with the measured LS coefficients and laser RIN and FM noise measured at the clock cell input (equivalent to the measurements depicted in Figures 4.4 and 4.3). In contrast to the clock detection noises (see Figure 5.6), the laser RIN and FM noise are measured at the the clock Rb cell input for frequency-stabilized laser output lights. The estimated limitations arising from the intensity and frequency LS effects on the short-term clock stability ($\sigma_{\alpha_{\text{LS}}}$ and $\sigma_{\beta_{\text{LS}}}$) are described in Table 5.6 for two optical-pump frequencies. The clock instability contributions of the laser RIN and FM noise via the LS effects are well below $1 \cdot 10^{-13}$ at $\tau = 1$ s, which is lower than the SNR limits discussed in the previous section (cf. Table 5.3).

5.3.3 Microwave phase noise contribution

In addition to the instability contributions from the laser noise, via detection SNR and LS effects, the LO-CW phase noise can also be an important source of clock instability on short timescales via the intermodulation effect (cf. section 1.6.2.3). The clock stability limit due to the intermodulation effect is decreased for low modulation frequencies (cf. equation (1.61)). In contrast, the discriminator slope of the lock-in error signal is maximized for low modulation frequencies (see Appendix B). Optimized frequency modulation frequency of $f_{\text{mod}}^{\text{CW}} = 70$ Hz and depth of $f_{\Delta}^{\text{CW}} = 0.3 \cdot W^{\text{CW}} \approx 70$ Hz are used to operate the CW-DR clock. Under these conditions, the clock stability limit estimated using the LO-CW phase noise depicted in Figure 2.12 and equation (1.60) taking into account the even harmonics of $f_{\text{mod}}^{\text{CW}} = 70$ Hz up to 10 kHz is $\sigma_{\text{LO-CW}} = 1.6 \cdot 10^{-13} \tau^{-1/2}$.

5.3. Noise contributions to the short-term clock instability

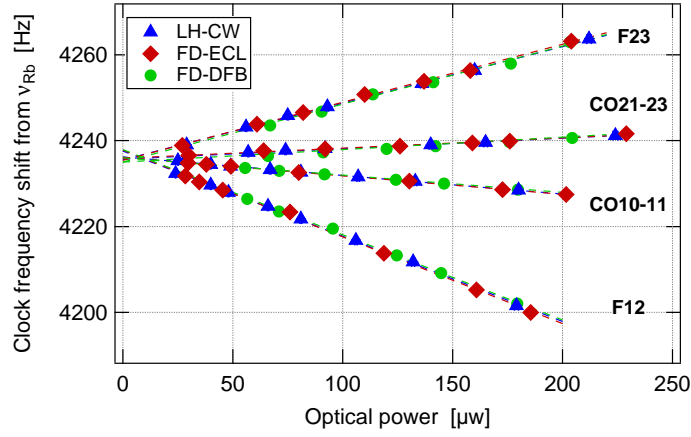


Figure 5.7 – Intensity light-shift measurements using the three laser systems for all the four optical-pump frequencies. Figure adapted from [147] and includes additional data (FD-DFB).

Table 5.4 – Intensity light-shift coefficients measured using the three laser systems and for the optical-pump frequencies tuned to the four reference transitions (cf. Figure 5.1).

Reference transition	FD-ECL [%]	FD-DFB [%]	LH-CW [%]
F12	$-2.1 \cdot 10^{-11}$	$-2.0 \cdot 10^{-11}$	$-2.0 \cdot 10^{-11}$
CO10-11	$-4.4 \cdot 10^{-12}$	$-4.1 \cdot 10^{-12}$	$-4.4 \cdot 10^{-12}$
F23	$3.3 \cdot 10^{-11}$	$3.5 \cdot 10^{-11}$	$3.3 \cdot 10^{-11}$
CO21-23	$5.8 \cdot 10^{-12}$	$7.1 \cdot 10^{-12}$	$5.9 \cdot 10^{-12}$

Table 5.5 – Frequency light-shift coefficients measured using the three laser systems for the laser frequency tuned to the reference transitions of the hyperfine components F=1 and F=2. The coefficients are determined from the fitted data in Figure 5.7 at a fixed optical power optimizing the CW-DR signal at the respective optical-pump frequency.

Reference transitions (hyperfine component)	Opt. pow. [μW]	FD-ECL [/MHz]	FD-DFB [/MHz]	LH-CW [/MHz]
F12, CO10-11 (F=1)	$72 \pm 6 \mu\text{W}$	$-7.0 \cdot 10^{-12}$	$-7.2 \cdot 10^{-12}$	$-6.5 \cdot 10^{-12}$
F23, CO21-23 (F=2)	$68 \pm 6 \mu\text{W}$	$4.3 \cdot 10^{-12}$	$4.9 \cdot 10^{-12}$	$5.6 \cdot 10^{-12}$

5.3.4 Total short-term instability budget

The limitations of the short-term clock stability evaluated in previous sections are summarized in Table 5.6 for the three laser systems under study and the optical-pump frequencies on CO10-11 and F12. For independent noise contribution processes, the resulting clock stability limit is the quadratic sum of individual contributions and is estimated using the equation (1.62). A short-term clock instability of $2.1 \cdot 10^{-13}$ is estimated for the FD-ECL frequency-stabilized on CO10-11 used for optical pumping. In this case (i.e., a weak FM-to-AM noise conversion rate through the clock Rb cell), the LO phase noise and the detection signal-to-noise ratio are the two dominant limiting factors on the clock stability. This is also the case for the LH-CW. However, for the FD-DFB, which exhibits higher AM and FM noise, the dominant limiting factor arises from the detection signal-to-noise ratio. The light-shift effect contributions to the short-term clock stability are negligible for all three laser systems.

Table 5.6 – Total short-term clock instability budget for the three laser systems and the two optical-pump frequencies. Table adapted from [147] and includes additional data (FD-DFB).

(a) Optical-pump frequency tuned to CO10-11.			
$(\tau = 1 \text{ s})$	FD-ECL	FD-DFB	LH-CW
$\sigma_{\text{SNR}}(\tau)$	$1.3 \cdot 10^{-13}$	$2.8 \cdot 10^{-13}$	$1.2 \cdot 10^{-13}$
$\sigma_{\alpha_{\text{LS}}}(\tau)$	$3.6 \cdot 10^{-15}$	$1.2 \cdot 10^{-14}$	$1.2 \cdot 10^{-15}$
$\sigma_{\beta_{\text{LS}}}(\tau)$	$2.3 \cdot 10^{-14}$	$7.2 \cdot 10^{-14}$	$7.2 \cdot 10^{-14}$
$\sigma_{\text{LO-CW}}(\tau)$	$1.6 \cdot 10^{-13}$	$1.6 \cdot 10^{-13}$	$1.6 \cdot 10^{-13}$
Estimated $\sigma_y(\tau)$	<u>$2.1 \cdot 10^{-13}$</u>	$3.3 \cdot 10^{-13}$	<u>$2.1 \cdot 10^{-13}$</u>
Measured $\sigma_y(\tau)$	<u>$2.4 \cdot 10^{-13}$</u>	$4.1 \cdot 10^{-13}$	<u>$2.3 \cdot 10^{-13}$</u>
(b) Optical-pump frequency tuned to F12.			
$(\tau = 1 \text{ s})$	FD-ECL	FD-DFB	LH-CW
$\sigma_{\text{SNR}}(\tau)$	$2.3 \cdot 10^{-13}$	$6.2 \cdot 10^{-13}$	$4.4 \cdot 10^{-13}$
$\sigma_{\alpha_{\text{LS}}}(\tau)$	$1.7 \cdot 10^{-14}$	$5.5 \cdot 10^{-14}$	$5.5 \cdot 10^{-15}$
$\sigma_{\beta_{\text{LS}}}(\tau)$	$2.3 \cdot 10^{-14}$	$7.2 \cdot 10^{-14}$	$7.2 \cdot 10^{-14}$
$\sigma_{\text{LO-CW}}(\tau)$	$1.6 \cdot 10^{-13}$	$1.6 \cdot 10^{-13}$	$1.6 \cdot 10^{-13}$
Estimated $\sigma_y(\tau)$	<u>$2.9 \cdot 10^{-13}$</u>	$6.4 \cdot 10^{-13}$	$4.8 \cdot 10^{-13}$
Measured $\sigma_y(\tau)$	<u>$3.1 \cdot 10^{-13}$</u>	$8.5 \cdot 10^{-13}$	$8.8 \cdot 10^{-13}$

In the case of strong FM-to-AM noise conversion through the cell (F12), while the LO-CW phase noise contribution remains important, the short-term clock stability is predominately limited by the detection SNR. The estimated SNR limit in this case is dominated by the FM-to-AM noise conversion phenomenon for all three laser systems and is analyzed in detail in section 5.3.1 (cf. Table 5.3). The reference transition F12 used as the optical-pump frequency increases not only the FM-to-AM noise conversion rate, but also the intensity LS coefficient (cf. Table 5.4). Nevertheless, the estimated clock stability limit due to the LS effects remain relatively negligible in each of the studied cases.

The short-term clock instability budget established for the FD-ECL used for optical pumping (tuned on CO10-11 or F12) estimates a slightly degraded clock stability by a factor of 2 – 2.5 compared to the budget presented in Table 1.5 [80] based on a similar CW-DR clock where a free-space DFB laser emitting at 780 nm is employed. The degradation is primarily due to the higher phase noise of the LO-CW used in this work compared to that of the LO used in [80].

5.4 Measured short-term clock instability

We measure the clock frequency instability through employing the FD laser systems and the LH-CW based on a LD emitting at 780 nm in the CW-DR clock, as presented in section 2.3. The short-term clock frequency instabilities measured using two optical-pump frequencies (CO10-11 and F12), which leads to different FM-to-AM noise conversion rates (by a factor of ten) through the clock cell, are shown in Figure 5.8. The short-term clock stability limits estimated in the previous section (cf. Table 5.6) are represented with dashed lines. In alignment with the predictions, the short-term clock instabilities measured using the FD-ECL and LH-CW stabilized on CO10-11 are at a similar level below $2.5 \cdot 10^{-13} \tau^{-1/2}$, which is comparable to the state-of-the-art performance reported for a CW-DR Rb-cell clock based on a laser diode emitting directly at 780 nm (cf. Figure I3). When using the optical-pump frequency on F12, which leads to an increased FM-to-AM noise conversion by a factor of 10, the measured short-term clock frequency stability with the FD-ECL is $3.1 \cdot 10^{-13} \tau^{-1/2}$. For the FD-ECL, the choice of the optical-pump frequency has little impact on the clock performance thanks to its low FM noise.

The clock instabilities measured using the FD laser systems degrade at an averaging time of only 10 s. Taking into account the laser frequency instabilities discussed in section 4.3 and the frequency LS coefficients measured for the CW-DR clock listed in Table 5.5, the clock frequency stability at 10 s is estimated to be below 10^{-13} , even in the case of high (AM and FM) noise FD-DFB. The (relative) optical power instabilities of 0.02 % at $\tau = 10$ s at the FD laser outputs (cf. Figure 4.8), however, yield the clock stability limit of $8.8 \cdot 10^{-14}$ for optical-pump frequency on CO10-11 and $4.2 \cdot 10^{-13}$ on F12, via the intensity LS effect (cf. Table 5.4). These estimated instability contributions from the optical power fluctuations in the fiber-coupled systems represent an important stability limitation of the measured clock instabilities as early as 10 s and are further discussed in the next section.

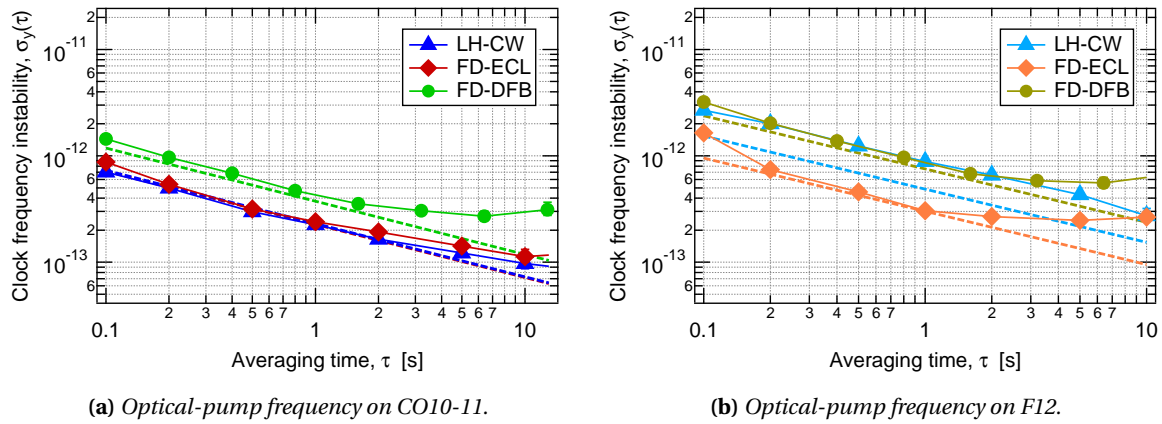


Figure 5.8 – Short-term clock instabilities measured using the three laser systems for the two optical-pump frequencies. Dashed lines show the SNR limited clock instability estimated in Tables 5.3a and 5.3b. Figure adapted from [147] and includes additional data (FD-DFB).

5.5 Discussion on the medium-long term clock instability

On medium-to-long term timescales, from 100 s up to 1 day averaging times, the fluctuations of the relevant parameters impact the clock frequency via the different processes reviewed in section 1.5. To evaluate the implementation of frequency-doubled telecom lasers, we first address the dominant stability limitation arising from optical power fluctuations. In the CW-DR Rb clock (presented in Figure 2.9), the 780-nm output lights of the three laser systems are transmitted to the clock PP-CW, where resides the clock Rb cell, via a (thermally isolated) PM optical fiber. The optical power instability is measured at the clock cell input (after the PM fiber) and depicted in Figure 5.9 for the optical-pump frequencies on CO10-11 and F12. The clock stability limits estimated using the intensity LS coefficients of Table 5.4 are found on the right axes. The left axes in Figure 5.9 are similarly scaled, but the right axes' scales differ by one order of magnitude due to the higher LS coefficient for F12.

The optical power instability measured at the clock cell input (after the PM fiber) using the fiber-coupled FD-ECL system is at a similar level as that measured at the 780-nm output of the FD-ECL (red diamonds in Figure 4.9) up to the averaging time of 500 s. In contrast for the LH-CW, which is based on free-space emitting laser diode and components, the PM fiber used to guide the laser light to the clock cell significantly deteriorates the optical power stability above 10 s of averaging time. Thermal or mechanical perturbations on the PM fiber result in power variations at the end of the fiber due to internal losses varying in time. The degraded optical power stability of the fiber-coupled systems correlated with temperature variations in the experimental environment was also discussed in the previous chapter (cf. section 4.4). Thus, the estimated clock stability limits arising from the intensity LS effect reaching $> 10^{-13}$ at 100 s represent a serious limitation to the use of the FD-ECL to achieve high performance on long timescales unless an active stabilization is employed. Alternatively, clock operation schemes such as pulsed-optical pumping [148], where the light is *switched off* during the microwave interrogation, could significantly reduce the impact of the LS effects. Indeed, the LS coefficients measured for the POP-DR clock (cf. section 3.3.5) are at least

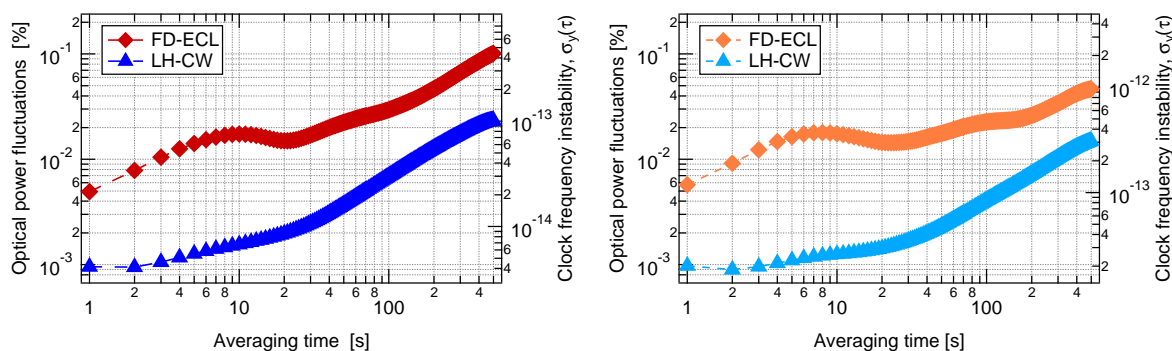
(a) *Optical-pump frequency on CO10-11.*(b) *Optical-pump frequency on F12.*

Figure 5.9 – *Optical power fluctuations measured at the clock PP-CW input for lasers stabilized to CO10-11 and F12. Left axes: Optical power fluctuations in terms of Allan deviation. Right axes: Clock frequency instability contribution estimated using the LS coefficient measured for CO10-11 and F12.*

one order of magnitude lower than those of the CW-DR clock. The long-term budget analyzed in chapter 3 represents a reasonable estimation for the CW-DR clock stability, as the PPs are nominally identical and the important effects perturbing the clock frequency stability are essentially the same as for the POP-DR clock, with the primary exception of the LS effects. The impact of the additional effects arising from pressure, temperature, microwave power, and magnetic field instabilities on the long-term clock stability are therefore expected to remain below the dominant limitation via the LS effects.

5.6 Conclusion

In this chapter, we demonstrated for the first time a Rb vapor-cell clock that employs frequency-doubled 1560-nm telecom lasers as the optical pump and detection light source and evaluated the limitations of the short-term clock frequency stability in the CW-DR scheme. We measured a short-term clock frequency stability better than $2.5 \cdot 10^{-13} \tau^{-1/2}$ using the FD-ECL exhibiting low AM and FM noise. This short-term clock stability is similar to those of state-of-the-art clock performance demonstrated using vapor-cell clocks based on laser diodes emitting directly at the Rb optical-pump wavelengths [44, 45, 48]. A second FD telecom laser based on a DFB LD, as well as the LH-CW based on a DFB laser emitting at 780 nm, lead to a degraded short-term clock frequency stability due to their relatively high laser AM and FM noises.

We analyzed in detail the independent contributions to the clock detection noise arising from laser AM and FM noise on short-term timescales. We demonstrated that, thanks to the low FM noise level of the FD-ECL, the short-term clock stability using this laser is only weakly impacted by the choice of the optical-pump frequency (i.e., by the FM-to-AM noise conversion rate through the clock Rb cell). This result indicates the advantage of the use of FD-ECL compared to DFB laser systems, which allows for setting the clock operation parameters more freely while avoiding deteriorating the short-term clock stability via the FM-to-AM noise conversion. As for optical-pump frequencies corresponding to a low FM-to-AM conversion rate, beyond the limitation due to the phase noise of

the LO-CW, the dominant contribution on short-term timescales is the laser AM noise for all three laser systems (based on ECL and DFB LDs).

For longer timescales, the estimated impact of the frequency LS effect remains well below 10^{-13} up to the 1 day timescale for the FD-ECL. The intensity LS effect currently represents the main limitation for high-performance clock applications. The high optical power fluctuations of the frequency-doubled laser systems (based on fiber-coupled components) are one of the main limiting factors of the clock frequency stability above 10^{-13} at averaging times above 10 s. The power fluctuations at the fiber-coupled laser system outputs are correlated with temperature fluctuations of the experimental environment (cf. chapter 4). One may reduce the intensity LS effect contribution to the medium-to-long-term clock instability by operating the clock in a pulsed-optical pumping scheme, such as the POP-DR clock studied in chapter 3. In the latter case, the AC Stark shift effect contribution is strongly reduced, leading to lower LS coefficients by more than a factor of 10. Such an interrogation scheme requires adding a supplementary component as an optical switch, such as an AOM, which also means introducing an additional noise source that could degrade the relative optical power stability by a factor of 10. However, the AOM, besides optical switching, can also serve to stabilize the light intensity at its output. A relative optical power instability of $2 \cdot 10^{-6}$ at 10^4 s is reported in [115] achieved by means of a temperature-stabilized AOM. In the case of our CW-DR clock based on the FD-ECL, such power stability would reduce the clock stability limit due to the intensity LS effect to below $6 \cdot 10^{-15}$, depending on the laser frequency.

Conclusions and perspectives

This thesis contributes to the development of compact and high-performance Rb vapor-cell atomic clocks and presents the metrological evaluation of their stability limitations. First, we studied and optimized the long-term frequency stability of a Rb vapor-cell clock where the pulsed-optical pumping (POP) scheme is applied using a laser source emitting at the ^{87}Rb D₂ line (780 nm). Secondly, we investigated laser systems based on a telecom laser diode (LD) emitting at 1560 nm, whose emission frequency is doubled and stabilized on Rb transitions, in view of high-precision applications at 1560 and 780 nm. We presented an in-depth analysis of the spectral properties of the frequency-doubled (FD) telecom lasers. We then evaluated their exploitation potential in a Rb vapor-cell clock where the continuous-wave double-resonance (CW-DR) scheme is applied.

C.1. High-performance POP-DR Rb clock

Rubidium vapor-cell clocks play a crucial role in GNSS applications thanks to their compact volume (< 3 L) and low power consumption (< 20 W) combined with excellent long-term stability performance $\leq 10^{-14}$ over one day. On these timescales, the clock frequency stability is mostly degraded due to the fluctuations of the sensitive parameters that perturb the Rb hyperfine splitting frequency via independent physical effects. We performed a systematic study of all the relevant physical effects perturbing the clock frequency to characterize their impact on the clock frequency stability. We established the exhaustive instability budget of our POP-DR Rb clock, which serves to assess the limitations of long-term clock frequency stability and to identify the dominant factor(s) to act on for further improvements. The measured long-term frequency stability of our POP-DR clock is $< 2 \cdot 10^{-14}$ for averaging times up to 1 day. The instability contribution from the second-order Zeeman effect, which was one of the dominant limitations, was reduced to $1.2 \cdot 10^{-15}$. Moreover, the instability contributions arising from the cell and stem temperature sensitivities were consolidated at $1.2 \cdot 10^{-15}$ and $6.0 \cdot 10^{-16}$, respectively, thanks to the simultaneous assessment of temperature fluctuations measured to be below 0.5 mK. While the estimated instability contributions are well below the 10^{-14} level for most of the effects in the budget, the measured long-term clock stability is predominantly limited by the laser intensity-induced effects' contribution of $1.6 \cdot 10^{-14}$. The microwave power shift effect and the spin-exchange effect present the next highest instability contributions at the level of $6 \cdot 10^{-15}$ and $3 \cdot 10^{-15}$, respectively, over one day.

According to the established budget, the principal limitation of the long-term stability arises from the laser intensity fluctuations, which perturb the clock frequency through different processes in the POP-DR interrogation scheme (e.g. the AC Stark shift effect and the residual coherence). To quantify the total impact on the clock stability, we measured the clock frequency sensitivity to the variation of the optical power ($\pm 2.3 \cdot 10^{-14}$ /%) and the fluctuations of the optical power at the clock cell input, which was at the level of 0.7 % over one day. Meanwhile, the results indicate that the optical power variations may be affected by the variations of environmental pressure and humidity. Further investigations are required to identify by which means these parameters degrade the light intensity fluctuations to effectively reduce their impact. Eventually, the laser system can be placed in a hermetic chamber, which would reduce environmental parameter fluctuations, but would compromise the size and power consumption.

To evaluate the clock stability limitations in a budget, the budget should be established taking into account the experimental parameters and the interrogation scheme that are applied to operate the clock; i.e., clock frequency sensitivity and parameter fluctuations should be evaluated under the closest possible conditions to the clock operation. For the presented clock instability budget, only the impact of the frequency light-shift effect of $6 \cdot 10^{-16}$ was estimated from the laser frequency fluctuations of 4 kHz that were measured in the CW scheme. The pulsed operation may however degrade the laser output frequency stability and thus increase the clock instability contribution of the frequency light-shift effect, which can be consolidated through a pulsed laser frequency instability measurement in future work. Nevertheless, we expect that the impact of the frequency light-shift effect on the long-term clock stability would still remain below 10^{-14} level up to a degradation by a factor of 20.

C.2. Optical frequency reference at two wavelengths (1560 and 780 nm)

The telecom C-band (1530 – 1565 nm) coincides with the twofold transition wavelengths of the optical resonances of ^{87}Rb D₂ line (780 nm). The laser diodes emitting at the telecom C-band through the frequency doubling of the laser emission provide an alternative to the LDs emitting directly at 780 nm for experiments manipulating ^{87}Rb atoms. We presented a thorough investigation of the spectral properties of the frequency-doubled telecom lasers in view of high-precision spectroscopy applications around 1560 or 780 nm. In particular, the FD laser system based on an external cavity LD emitting at 1560 nm, whose output frequency is first doubled then stabilized through a Rb vapor cell, exhibited excellent noise properties. The frequency noise measurement of the FD telecom laser was limited by the employed current source at $10^6 \text{ Hz}^2/\text{Hz}$ and should be improved by employing a lower noise current source. Table C1 compares the performance of the 780-nm output light of the FD telecom laser to that of two laser heads (LHs) based on a DFB LD emitting at 780 nm. One of the LHs incorporates an additional AOM that is used for the pulsed optical pumping in the POP-DR clock studied in chapter 3. In particular for Rb vapor-cell clock applications, the low (intensity and frequency) noise of the FD telecom laser represents a substantial advantage in view of improving the short-term stability with respect to the laser diodes emitting directly at 780 nm.

Table C1 – Performance of the frequency-doubled telecom laser compared to the laser heads based on a LD emitting at 780 nm.

Parameter	Unit	FD telecom laser	Laser head at 780 nm	Laser head at 780 nm with AOM
Frequency noise ($f = 100$ Hz)	Hz ² /Hz	$< 1 \cdot 10^6$	$< 1 \cdot 10^9$	$< 1 \cdot 10^9$
Rel. intensity noise ($f = 100$ Hz)	Hz ⁻¹	$< 5 \cdot 10^{-13}$	$< 5 \cdot 10^{-12}$	$< 2 \cdot 10^{-11}$
Frequency instability ($\tau = 1$ s)		$< 2 \cdot 10^{-12}$	$< 5 \cdot 10^{-12}$	$< 2 \cdot 10^{-11}$
Frequency instability ($\tau = 1$ day)		$< 1 \cdot 10^{-11}$	$< 1 \cdot 10^{-11}$	$< 1 \cdot 10^{-11}$
Opt. power instability ($\tau = 1$ s)	%	< 0.01	< 0.01	< 0.7
Opt. power instability ($\tau = 1$ day)	%	0.5	0.02	0.7

We demonstrated a laser fractional frequency instability of $2 \cdot 10^{-12}$ at 1 s of averaging time, which remained below 10^{-11} (equivalent to 4 kHz) on longer timescales up to 1 day. The optical power fluctuations of 0.01 % at 1 s measured for the FD telecom laser was strongly degraded on longer timescales reaching 0.5 % over one day. In fact, the FD system is based on fiber-coupled components whereas the LHs use free-space laser diode and optical components. Mechanical and thermal perturbations or residual back reflections along the fiber-coupled system degrade the output power stability in the medium-to-long term. High frequency stability performance makes the FD telecom laser an excellent candidate for high-performance Rb clock applications. In fact, as illustrated in Figure C1, many applications at both wavelengths (780 and 1560 nm) can benefit from the two-wavelength optical frequency references, which combine the telecom reliability with the Rb atomic frequency stability. Nevertheless, the long-term optical power fluctuations may present a serious limitation. An improved mechanical and thermal stabilization of the fiber-coupled system is essential for reliable and high-performance industrial developments (e.g. placing all the components on a compact and thermalized baseplate) or an active power stabilization.

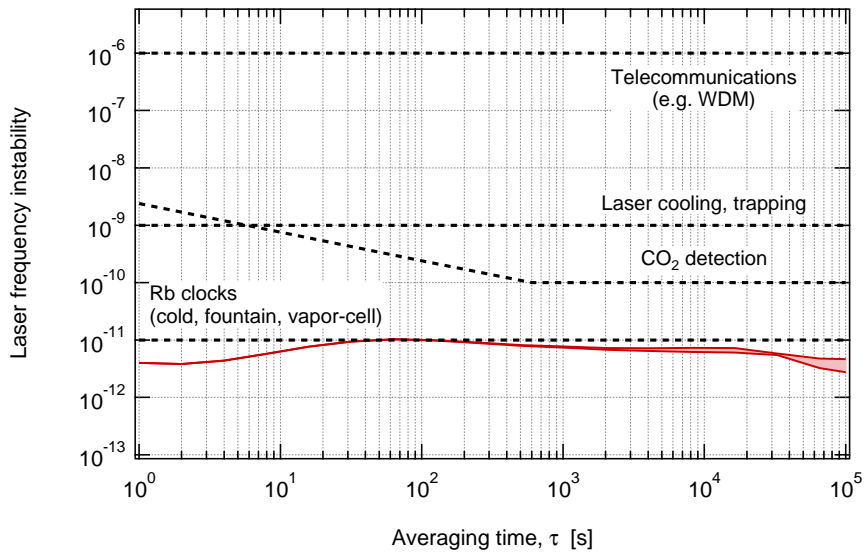


Figure C1 – Fractional frequency fluctuations of the optical frequency for the frequency-doubled telecom laser and typical instability requirements for applications around 780 nm and 1560 nm.

C.3. CW-DR Rb clock using a telecom laser

We presented for the first time the realization of a CW-DR Rb vapor-cell clock where a frequency-doubled telecom laser is used for optical pumping and detection. We demonstrated, regardless of the clock operation conditions, similar or better short-term clock stability than that of a clock using a laser emitting directly at 780 nm. The achieved short-term clock instability of $2.4 \cdot 10^{-13} \tau^{-1/2}$ is at the state-of-the-art level for vapor-cell frequency standards as depicted in Figure C2 (the red full line). Moreover, we studied the various contributions to the clock detection noise and established the detailed noise budgets in two particular cases: low and high rates of FM-to-AM noise conversion through the clock cell. We showed that if the FM-to-AM noise conversion is minimized, then the laser intensity noise constitute the dominant contribution to the clock detection noise. However, under the conditions yielding an increased rate of the noise conversion through the clock cell, the laser frequency noise becomes an important factor of the clock detection noise and limit the short-term clock stability. Nevertheless, thanks to the low frequency noise of the FD telecom laser, the short-term clock instability was weakly affected by the change in the FM-to-AM noise conversion rate and remained at $3 \cdot 10^{-13} \tau^{-1/2}$. This aspect of the FD telecom laser offers less stringent requirements to adjust the experimental parameters for optimizing the short-term clock performance and shows great prospect in high-performance Rb vapor-cell clock applications.

The intensity light-shift (LS) effect was identified as a limiting factor of the medium-to-long term stability of the CW-DR Rb clock, which employs the FD telecom laser relying on fiber-coupled components. The high optical power fluctuations of the FD telecom laser degrade the clock stability via the intensity LS effect already at 10 s of averaging time, which represent a serious limitation for the use of the FD telecom laser in high-performance vapor-cell clocks. To reduce the intensity LS limit, one solution would be to actively stabilize the optical power at the clock cell input to

compensate for the fluctuations occurring all along the fiber-coupled path, for instance by acting on the laser diode temperature. A reduction by a factor of 20 would improve the clock frequency stability to $< 5 \cdot 10^{-14}$ up to 500 s of averaging time. Alternatively, adopting the pulsed-optical pumping scheme, by decoupling the optical radiation from the microwave interrogation, would reduce the clock frequency sensitivity to the optical power fluctuations by two orders of magnitude yielding a clock stability limit $\leq 10^{-14}$ up to 500 s. In this case, it is however required to add an optical switch in the laser system, such as an AOM, to realize the pulsed light emission, which also means introducing an additional instability source and necessitates further characterization.

C.4. Perspectives

The detailed analysis of the long-term instability sources of our POP-DR Rb clock indicates that the principal limiting factor arises from the intensity light-shift effects ($2 \cdot 10^{-14}$). To reduce the impact of these effects, two possibilities exist: the clock frequency sensitivity to light intensity variations should be reduced, or the fluctuations of the light intensity should be decreased. In the POP-DR scheme, the light intensity fluctuations perturb the clock frequency stability via different processes such as the AC Stark shift or the residual coherence. Further numerical and experimental studies are required first to quantify the independent contributions, then to evaluate the clock frequency sensitivity to the light intensity fluctuations via the combination of these processes. These studies would eventually allow to reduce the clock frequency sensitivity to the light intensity fluctuations. Alternatively, we could directly act on the light intensity fluctuations by implementing an active stabilization loop through a feedback on the laser diode temperature or the RF power used to drive the AOM. For an efficient stabilization scheme, the light intensity should be detected as near as possible to the input of the clock cell to compensate for the perturbations occurring along the whole optical path. This implies splitting a part of the laser light before the clock cell, and therefore reducing the available optical power to the clock cell, which is necessary in the POP-DR scheme for an efficient optical pumping. In this case, an optical source with a high output power at 780 nm should be considered. For this purpose, frequency-doubled laser systems based on mature telecom components present an attractive solution. Laser diodes and optical components (such as amplifiers) with high reliability and excellent spectral properties are more easily available in the telecom wavelength region and can be applied to vapor-cell clocks when combined with the frequency-doubling technology. The results presented in this thesis show that frequency-doubled telecom lasers indeed present interesting alternatives to lasers emitting at 780 nm, especially in view of excellent short-term clock stability.

We demonstrated a fractional frequency instability $\leq 10^{-14}$ at 1 day for the compact Rb vapor-cell clock operated in the POP scheme and without placing any component in a vacuum environment. As shown in Figure C2, this stability performance positions among the state-of-the-art laboratory vapor-cell clock performance and better or similar compared to that of the GNSS-grade industrial RAFSs. For GNSS applications, besides an excellent frequency stability at 1-day timescale, the size, weight, and power consumption of the deployed clock are crucial parameters. We report in Figures C3a and C3b the frequency instability of the studied clocks as a function of the estimated SWaP (expressed in this thesis by the single number of the product of the three parameters) in

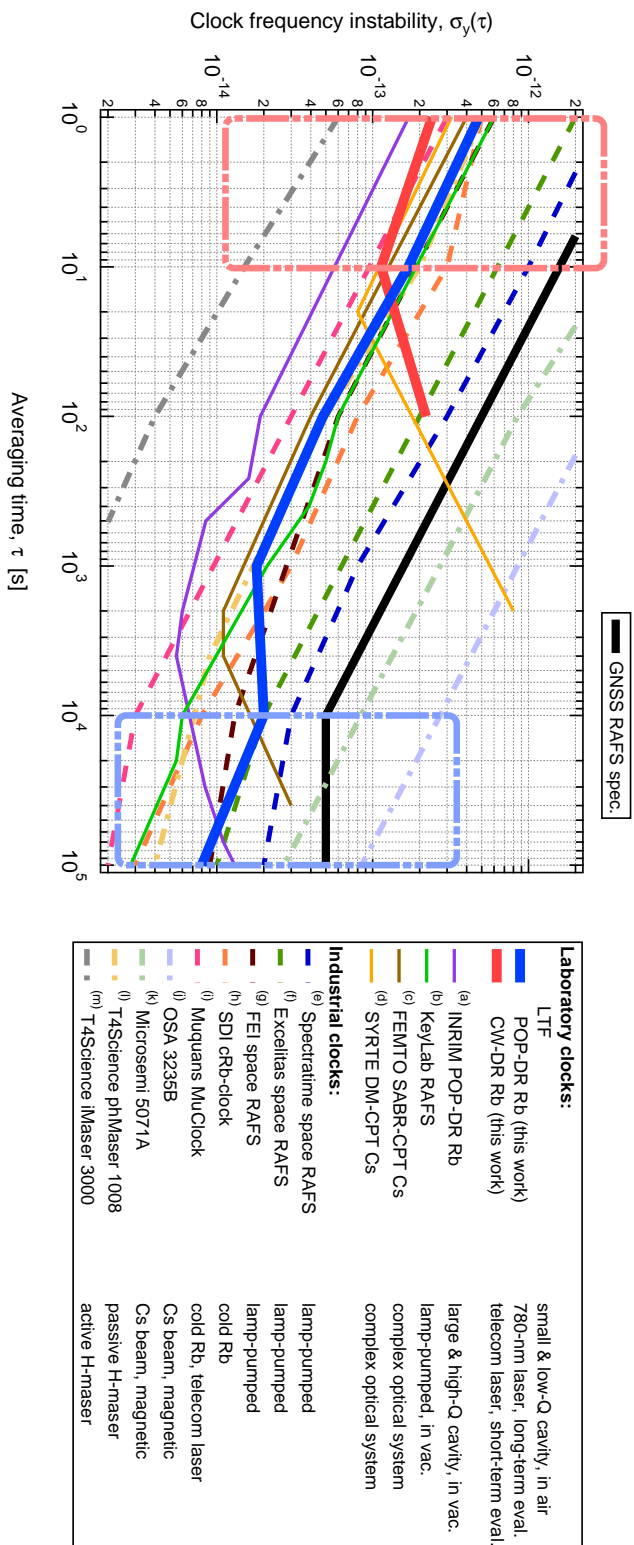


Figure C2 – State-of-the-art clock stability for laboratory and industrial clocks. This graph is an update of Figure I3 to highlight the results obtained in this work: Short-term instability (red) of the CW-DR Rb vapor-cell clock optically-pumped using a telecom laser (cf. chapter 5) and long-term instability (blue) of the POP-DR Rb vapor-cell clock optically-pumped using 780-nm laser diode (cf. chapter 3). State-of-the-art frequency instability demonstrated with compact atomic clocks. Data for other laboratory clocks are extracted from: ^(a) [44], ^(b) [28], ^(c) [52], ^(d) [53]. Data for industrial clocks are extracted from: ^(e) [34], ^(f) [35], ^(g) [36], ^(h) [149], ⁽ⁱ⁾ [150], ^(j) [37], ^(k) [38], ^(l) [39], ^(m) [40].

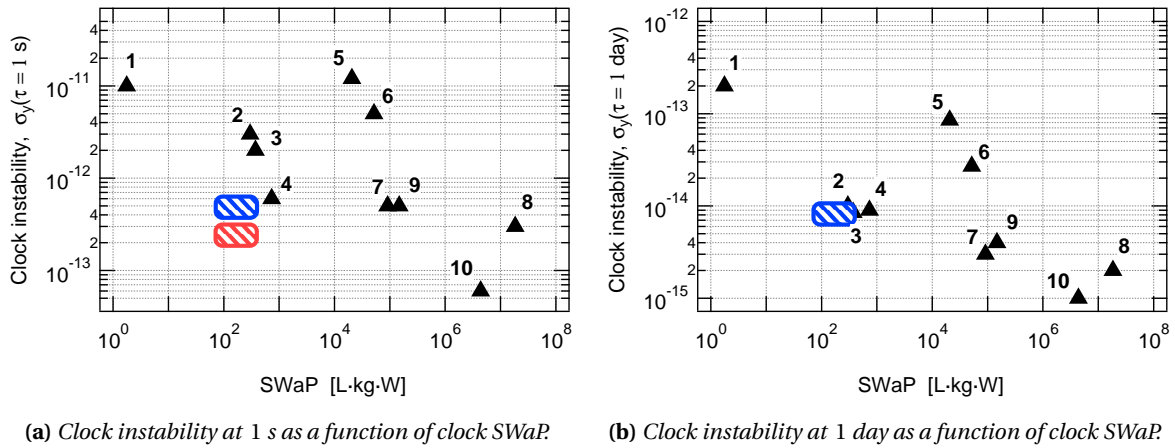


Figure C3 – Clock instability as a function of clock SWaP for industrial clocks and including the results of this work. Blue: POP-DR Rb vapor-cell clock (cf. chapter 3). Red: CW-DR Rb vapor-cell clock optically-pumped using a telecom laser (cf. chapter 5). 1: Spectratime space mini RAFS [33]. 2: Spectratime space RAFS [34]. 3: Excelitas space RAFS [35]. 4: FEI space RAFS [36]. 5: OSA Cs beam [37]. 6: Microsemi Cs beam [38]. 7: SDI cold Rb clock [149]. 8: Muquans cold Rb clock [150]. 9: T4Science PHM [39]. 10: T4Science AHM [40].

comparison with compact and high-performance industrial clocks. To estimate the SWaP of the studied clocks, we assume, based on the current industrial expertise, that the control electronics can be miniaturized and integrated within the volumes of the laser system and the physics package. Therefore, the SWaP of our clocks was estimated given the size and mass of the corresponding laser system and physics package. In the case of the POP-DR clock (LH-POP + PP-POP), the volume was $< 3.1 \text{ L}$ and the mass was $< 2.8 \text{ kg}$, whereas for the CW-DR clock (FD-ECL + PP-CW), the volume was $< 2.8 \text{ L}$ and the mass was $< 2.6 \text{ kg}$. The demonstrated short-term clock stability performance using the FD telecom laser was improved by a factor of 2 to 10 compared to the state-of-the-art industrial RAFSs. The long-term instability of our POP-DR clock consolidated in this thesis at the level of 10^{-14} is similar to that of the GNSS-grade RAFSs. Moreover, this long-term instability of our POP-DR clock is only a factor of 2 to 3 higher than those of the PHM and the SDI cold Rb clock while at a SWaP reduced by more than a factor of 100. These results show the high potential of the POP-DR clock based on a compact microwave cavity and the Rb-referenced laser diode (emitting at 780 nm or 1560 nm) for the development of the next generation of Rb frequency standards for space applications.

Appendix A

Optical detection noise

In this section, we discuss the various noise contributions to the clock detection noise. We make use of the following analysis to evaluate the laser AM and FM noise contributions to the experimental clock optical detection noise in chapter 5. The noise of the optically detected clock signal is composed of the detector intrinsic noise and the AM noise of the detected laser light. The intrinsic noise of the detector mainly includes its dark current noise and the thermal noise of the resistor, whereas the detected light noise is the result of two mechanisms: the laser AM noise contributes directly and the laser FM noise is converted into AM noise through the clock vapor cell. The optical detection noise is ultimately limited by the shot noise resulting from the discrete nature of the detected light, which is often dominated by the laser noise contributions to the optical detection noise. Assuming the different noise sources are independent and uncorrelated, the power spectral density of the optical detection noise is the quadratic sum of all of its contributions. Therefore, we can write the total optical detection noise power spectral density as

$$S_N = \sqrt{S_{\text{det}}^2 + S_{\text{laser}}^2}, \quad (\text{A.1})$$

where S_{det} is the total detector intrinsic noise PSD and S_{laser} is the total laser light noise PSD, expressed in the unit of $\text{A}/\text{Hz}^{1/2}$. The detector intrinsic noise is experimentally determined in the absence of light and becomes a negligible contribution in the presence of light. The total laser noise arises from the laser AM noise and the laser FM-to-AM noise conversion and can be written as

$$S_{\text{laser}} = \sqrt{S_{\text{AM}}^2 + S_{\text{FM-AM}}^2}, \quad (\text{A.2})$$

where S_{AM} and $S_{\text{FM-AM}}$ are the clock detection noise PSD contributions, in the unit of $\text{A}/\text{Hz}^{1/2}$, arising from the laser AM noise and the FM-to-AM noise conversion, respectively. The AM noise PSD (S_{AM}) is related to the laser RIN via the measured photocurrent (I_{DC}) through $S_{\text{AM}} = \sqrt{S_{\text{RIN}} \cdot I_{\text{DC}}^2}$. The FM-to-AM noise conversion is quantified with the conversion rate $D_{\text{FM-AM}}$ (in $[\text{A}/\text{Hz}]$) deduced from the local slope of the optical absorption line at the specific laser frequency (cf. Figure A.1). The noise PSD contribution of the FM-to-AM noise conversion process $S_{\text{FM-AM}}$ is given by

$$S_{\text{FM-AM}} = \sqrt{S_v D_{\text{FM-AM}}^2}, \quad (\text{A.3})$$

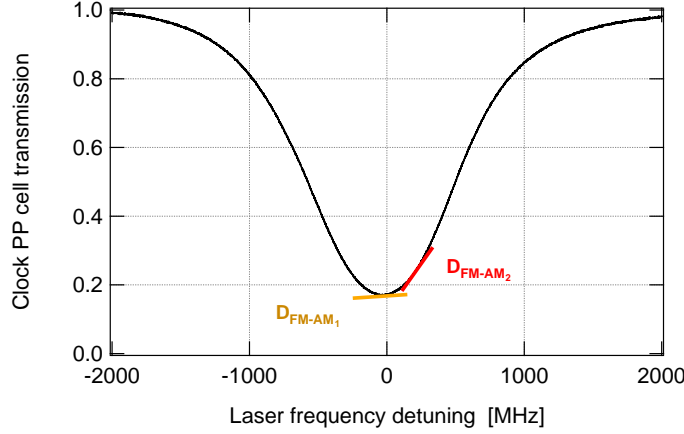


Figure A.1 – Typical transmission signal of the clock Rb vapor cell. Yellow and red lines: linear fits at two different laser frequencies whose slopes correspond to the FM-to-AM noise conversion rates D_{FM-AM_1} and D_{FM-AM_2} through the vapor cell.

where S_v is the laser FM noise at the clock cell input, expressed in the unit of Hz^2/Hz . Combining the equations (A.1) – (A.3), we write the total optical detection noise as

$$\begin{aligned} S_N &= \sqrt{S_{\text{det}}^2 + S_{\text{AM}}^2 + S_{\text{FM-AM}}^2} \\ &= \sqrt{S_{\text{det}}^2 + S_{\text{AM}}^2 + S_v D_{\text{FM-AM}_i}^2}, \end{aligned} \quad (\text{A.4})$$

where $D_{\text{FM-AM}_i}$ is the FM-to-AM noise conversion rate at the laser frequency ν_i .

In order to distinguish the individual contributions from laser AM and FM noise, one may take into account the total optical detection noise for two different laser frequencies while keeping all other parameters constant. The change of the laser frequency results in a different FM-to-AM noise conversion rate measured using the optical transmission signal of the clock Rb vapor cell, as depicted in Figure A.1. Knowing the associated FM-to-AM noise conversion rate, the total optical detection noise at each configuration is given by the equation (A.4). For two different conversion rates and assuming laser AM and FM noise at the clock cell input are constant in the two configurations, we get a two-equation system with two unknowns that correspond to the noise PSDs of the contributions arising from laser AM and FM noise (i.e., S_{AM} and $S_{\text{FM-AM}}$).

$S_{\text{FM-AM}}$ is given by the equation (A.3) for the laser frequency noise S_v calculated using

$$S_v = \frac{S_{N_2}^2 - S_{N_1}^2}{D_{\text{FM-AM}_2}^2 - D_{\text{FM-AM}_1}^2}, \quad (\text{A.5})$$

and S_{AM} is calculated with

$$S_{\text{AM}} = \sqrt{S_{N_1}^2 - S_{\text{det}}^2 - S_{\text{FM-AM}_1}^2} = \sqrt{S_{N_2}^2 - S_{\text{det}}^2 - S_{\text{FM-AM}_2}^2}. \quad (\text{A.6})$$

Furthermore, when the laser is operated well above the threshold, the clock detection noise is proportional to the optical power, as experimentally measured and reported in Figure A.2a. The noise measurements are performed in the absence of microwave radiation and correspond to the background level (i.e., the transmitted light in the absence of resonant microwave radiation). Nevertheless, the optical detection noise is weakly sensitive to the applied microwave power, as presented in Figure A.2b.

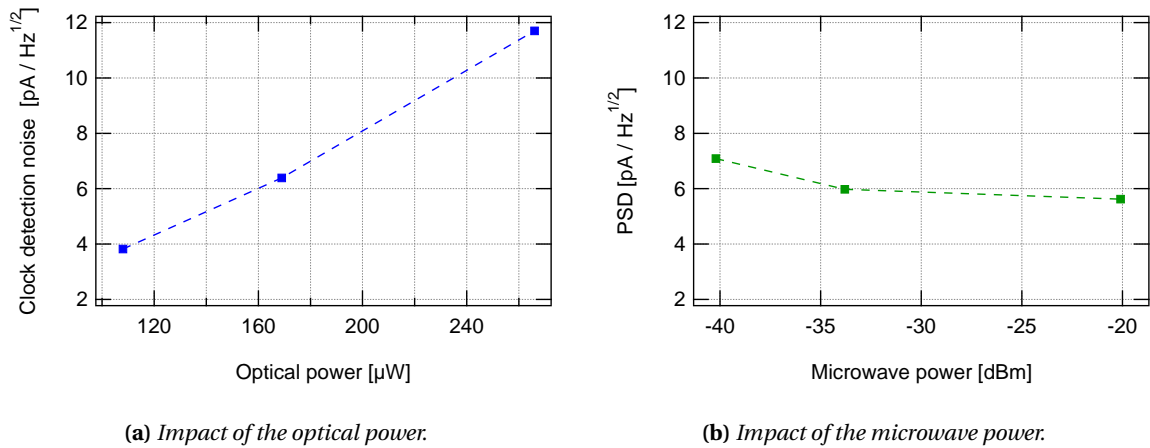


Figure A.2 – CW-DR clock detection noise PSD (S_N) as function of the optical and microwave powers. The noise PSDs are measured at Fourier frequency of 70 Hz (corresponding to the microwave modulation frequency of the studied CW-DR clock).

Appendix B

Error signal optimization for the clock

In this section, we present the optimization of the so-called error signal and the discriminator slope of interest. The results of the following are used to optimize the short-term stability of the CW-DR Rb vapor-cell clock presented in chapter 5.

Atomic clocks use an atomic resonance frequency to stabilize that of an external local oscillator [61]. To retrieve the precise location of the atomic resonance frequency, we modulate the frequency of the interrogation field (i.e. microwave field in microwave clocks) at a modulation frequency f_{mod} with a modulation depth f_{Δ} . We detect the response of the atoms to the modulated microwave frequency by synchronous detection using a lock-in amplifier to obtain the error signal that is used to maintain the local oscillator's frequency close to the atomic resonance frequency. We assume a slow modulation such that the atoms reach a steady state at each microwave interrogation frequency (i.e. a modulation frequency smaller than the atomic relaxation rates $\gamma_1 \approx 300 \text{ s}^{-1}$ and $\gamma_2 \approx 250 \text{ s}^{-1}$).

The clock signal in the CW-DR scheme that is detected through the transmitted light intensity at the end of the cell is given by the equation (1.16). The atomic response yielding the information on the reference transition frequency has a Lorentzian line shape with an amplitude A^{CW} and a FWHM W^{CW} given by the equations (1.17) and (1.18), respectively. When a modulation signal $h(t)$ is applied, the instantaneous angular frequency of the frequency-modulated microwave field is

$$\omega_M(t) = \omega_0 + \omega_{\Delta} h(t), \quad (\text{B.1})$$

where ω_0 is the mean angular frequency and $\omega_{\Delta} = 2\pi f_{\Delta}$ is the modulation depth. The function $h(t)$ describes the applied modulation signal and for a square-wave modulation and a modulation period of $T_{mod} = \frac{1}{f_{mod}}$ is given by

$$h(t) = \begin{cases} +1 & \text{for } 0 < t < \frac{T_M}{2}, \\ -1 & \text{for } \frac{T_M}{2} < t < T_M. \end{cases} \quad (\text{B.2})$$

Appendix B – Error signal optimization for the clock

For an easy derivation of the error signal, we first assume a normalized Lorentzian line shape such that the amplitude is 1 and the FWHM is 2. Then, we apply the results obtained for the normalized error signal to the case of the CW-DR Rb clock. The normalized Lorentzian line shape function is

$$f(x) = \frac{1}{1+x^2}, \quad (\text{B.3})$$

where x represents the normalized microwave frequency detuning. When a modulation described by the function $h(t)$ is applied, the normalized frequency detuning x is in the form of

$$x(t) = x_0 + x_\Delta \cdot h(t), \quad (\text{B.4})$$

where x_0 is the mean normalized frequency detuning and x_Δ is the normalized modulation depth. Considering the CW-DR clock signal given by the equation (1.16) and the above equations, the normalized quantities are written as

$$x_0 = \frac{2 \Omega_M}{W_\omega^{\text{CW}}}, \quad (\text{B.5})$$

$$x_\Delta = \frac{2 \omega_\Delta}{W_\omega^{\text{CW}}}, \quad (\text{B.6})$$

where $W_\omega^{\text{CW}} = 2 \pi W^{\text{CW}}$ is the linewidth of the CW-DR signal. For a better readability, the superscript ^{CW} is omitted for the rest of this section and we consider the CW-DR scheme unless it is indicated otherwise. The response to the frequency modulated input $x(t)$ is demodulated by synchronous detection, which consists in multiplying the response signal by the demodulation signal represented by the function $h(t)$. The resulting error signal corresponds to the mean value of the synchronous detector output over the modulation period and can be written as

$$d(x_0) = -\frac{2 x_0 x_\Delta}{(1+(x_0+x_\Delta)^2)(1+(x_0-x_\Delta)^2)}. \quad (\text{B.7})$$

The error signal is a dispersive curve and serves to accurately locate the atomic resonance frequency at the center of the Lorentzian signal, which corresponds to the zero crossing of the error signal. Therefore, we are interested in the region where $|x_0| \ll 1$ and more importantly in maximizing the slope in this region. In this case, the error signal can be approximated by

$$d(|x_0| \ll 1) \approx -\frac{2 x_0 x_\Delta}{(1+x_\Delta^2)^2}. \quad (\text{B.8})$$

The slope of the error signal close to the line center is obtained by the derivative of the equation (B.8) evaluated at the zero crossing ($|x_0| \ll 1$) as

$$s(|x_0| \ll 1) = -\frac{2 x_\Delta}{(1+x_\Delta^2)^2}. \quad (\text{B.9})$$

The slope given by the equation (B.9) is maximized for $x_\Delta = 1/\sqrt{3}$. Using the relation of the equation (B.6), we deduce the modulation depth maximizing the error signal slope at the line center is $\omega_\Delta = 0.29 W_\omega$ (or $f_\Delta = 0.29 W$).

In the case of the CW-DR Rb clock, the error signal at the synchronous detector output is generated from the clock signal given by the equation (1.16) with an amplitude A given by the equation (1.17). Using these two equations and (B.5), (B.6), and (B.8), the error signal for a small microwave detuning $\Omega_M \ll W_\omega$ is given by

$$d_{DR}(\Omega_M \ll W_\omega) = -8 A \frac{\Omega_M \omega_\Delta}{W_\omega^2} \frac{1}{\left(1 + \frac{4\omega_\Delta^2}{W_\omega^2}\right)^2}. \quad (\text{B.10})$$

The slope of the error signals measured at the synchronous detector output of the CW-DR Rb clock for different modulation depths and frequencies are reported in Figure B.1a. The slope of the error signal is maximized at a modulation depth corresponding to one third of the FWHM of the CW-DR signal, which is in this case $W \approx 220$ Hz. The optimal modulation depth is weakly affected by the change of the modulation frequency. Furthermore, the maximized error signal slope depends on the modulation frequency f_{mod} , as illustrated in Figure B.1b. The sharp drops observed in Figure B.1b around 50 and 100 Hz are due to the filtering of the lock-in amplifier around the power line frequency and its harmonics. For fast modulation frequency approaching the ground-state relaxation rates ($\gamma_1 \approx 300 \text{ s}^{-1}$ and $\gamma_2 \approx 250 \text{ s}^{-1}$), the signal is reduced significantly.

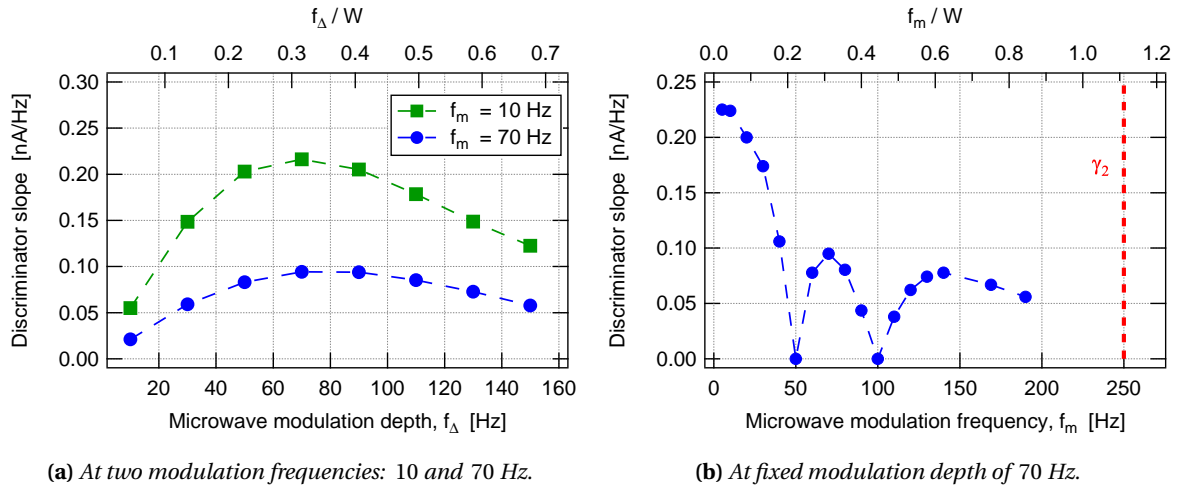


Figure B.1 – Discriminator slope of the error signal as function of microwave modulation depth f_Δ and frequency f_m . The FWHM of the CW-DR signal is $W \approx 220$ Hz.

Bibliography

- [1] 2018 CODATA adjustment: *Fundamental Physical Constants—Extensive Listing*, Available online at <http://physics.nist.gov/constants>.
- [2] D. A. Steck, *Rubidium 87 D Line Data*, Available online at <https://steck.us/alkalidata>, (revision 2.2.1, 21 November 2019).
- [3] M. A. Lombardi, T. P. Heavner, and S. R. Jefferts, “NIST Primary Frequency Standards and the Realization of the SI Second”, *NCSLI Measure*, vol. 2, no. 4, pp. 74–89, 2007. DOI: 10.1080/19315775.2007.11721402. eprint: <https://doi.org/10.1080/19315775.2007.11721402>.
- [4] CGPM, *Resolutions 1 of the 26 th CGPM*, <https://www.bipm.org/en/CGPM/db/26/1/>, 2018.
- [5] A. Bauch, “Caesium atomic clocks: function, performance and applications”, *Measurement Science and Technology*, vol. 14, no. 8, pp. 1159–1173, 2003. DOI: 10.1088/0957-0233/14/8/301.
- [6] R. Wynands and S. Weyers, “Atomic fountain clocks”, *Metrologia*, vol. 42, no. 3, S64–S79, 2005. DOI: 10.1088/0026-1394/42/3/s08.
- [7] N. F. Ramsey, “A molecular beam resonance method with separated oscillating fields”, *Phys. Rev.*, vol. 78, pp. 695–699, 6 1950. DOI: 10.1103/PhysRev.78.695.
- [8] T. P. Heavner, E. A. Donley, F. Levi, G. Costanzo, T. E. Parker, J. H. Shirley, N. Ashby, S. Barlow, and S. R. Jefferts, “First accuracy evaluation of NIST-F2”, *Metrologia*, vol. 51, no. 3, p. 174, 2014. DOI: 10.1088/0026-1394/51/3/174.
- [9] M. Abgrall, B. Chupin, L. De Sarlo, J. Guéna, P. Laurent, Y. Le Coq, R. Le Targat, J. Lodewyck, M. Lours, P. Rosenbusch, G. D. Rovera, and S. Bize, “Atomic fountains and optical clocks at SYRTE: Status and perspectives”, *Comptes Rendus Physique*, vol. 16, no. 5, pp. 461–470, 2015. DOI: 10.1016/j.crhy.2015.03.010.
- [10] A. Jallageas, L. Devenoges, M. Petersen, J. Morel, L. G. Bernier, D. Schenker, P. Thomann, and T. Södmeyer, “First uncertainty evaluation of the FoCS-2 primary frequency standard”, *Metrologia*, vol. 55, no. 3, p. 366, 2018. DOI: <https://doi.org/10.1088/1681-7575/aab3fa>.
- [11] B. J. Bloom, J. R. Nicholson, T. L. Williams, S. L. Campbell, M. Bishof, X. Zhang, W. Zhang, S. L. Bromley, and J. Ye, “An optical lattice clock with accuracy and stability at the 10^{-18} level”, *Nature*, vol. 506, pp. 71–75, 2014. DOI: 10.1038/nature12941.
- [12] A. D. Ludlow, M. M. Boyd, J. Ye, E. Peik, and P. O. Schmidt, “Optical atomic clocks”, *Rev. Mod. Phys.*, vol. 87, pp. 637–701, 2 2015. DOI: 10.1103/RevModPhys.87.637.

Bibliography

- [13] F. Riehle, P. Gill, F. Arias, and L. Robertsson, “The CIPM list of recommended frequency standard values: guidelines and procedures”, *Metrologia*, vol. 55, no. 2, pp. 188–200, 2018. DOI: 10.1088/1681-7575/aaa302.
- [14] P. Gill, “Is the time right for a redefinition of the second by optical atomic clocks?”, *Journal of Physics: Conference Series*, vol. 723, no. 1, p. 012 053, 2016. DOI: <https://doi.org/10.1088/1742-6596/723/1/012053>.
- [15] W. F. McGrew, X. Zhang, H. Leopardi, R. J. Fasano, D. Nicolodi, K. Beloy, J. Yao, J. A. Sherman, S. A. Schäffer, J. Savory, R. C. Brown, S. Römisch, C. W. Oates, T. E. Parker, T. M. Fortier, and A. D. Ludlow, “Towards the optical second: verifying optical clocks at the si limit”, *Optica*, vol. 6, no. 4, pp. 448–454, 2019. DOI: 10.1364/OPTICA.6.000448.
- [16] J. Camparo, “The rubidium atomic clock and basic research”, *Physics Today*, vol. 60, no. 11, pp. 33–39, 2007. DOI: 10.1063/1.2812121.
- [17] F. Riehle, *Frequency Standards: Basics and Applications*. Wiley-VCH Verlag GmbH & Co. KGaA, Weinheim, 2004, ISBN: 3-527-40230-6.
- [18] L. Maleki and J. Prestage, “Applications of clocks and frequency standards: from the routine to tests of fundamental models”, *Metrologia*, vol. 42, no. 3, S145–S153, 2005. DOI: 10.1088/0026-1394/42/3/s15.
- [19] S. Knappe, V. Shah, V. Gerginov, A. Brannon, L. Hollberg, and J. Kitching, “Long-term stability of nist chip-scale atomic clock physics packages”, in *38th Annual Precise Time and Time Interval (PTTI) Meeting*, 2006.
- [20] S. Lecomte, M. Haldimann, R. Ruffieux, P. Thomann, and P. Berthoud, “Performance demonstration of a single-frequency optically-pumped cesium beam frequency standard for space applications”, in *International Conference on Space Optics — ICSSO 2006*, E. Armandillo, J. Costeraste, and N. Karafolas, Eds., International Society for Optics and Photonics, vol. 10567, SPIE, 2017, pp. 925 –931. DOI: 10.1117/12.2308111.
- [21] F. Droz, P. Mosset, Q. Wang, P. Rochat, M. Belloni, M. Gioia, A. Resti, and P. Waller, “Space Passive Hydrogen Maser - Performances and lifetime data”, in *2009 IEEE International Frequency Control Symposium Joint with the 22nd European Frequency and Time forum*, 2009, pp. 393–398. DOI: 10.1109/FREQ.2009.5168208.
- [22] F. Droz, P. Rochat, and Q. Wang, “Performance overview of Space Rubidium standards”, in *24th European Frequency and Time Forum (EFTF)*, 2010, pp. 1–6.
- [23] L. A. Mallette, P. Rochat, and J. White, “Historical review of atomic frequency standards used in space systems – 10 year update”, in *38th Annual Precise Time and Time Interval (PTTI) Meeting*, 2006.
- [24] L. A. Mallette, “Atomic and quartz clock hardware for communication and navigation satellites”, in *Proc. of the 39th Annual Precise Time and Time Interval (PTTI) Meeting*, 2007.
- [25] L. Zhan, Y. Liu, W. Yao, J. Zhao, and Y. Liu, “Utilization of chip-scale atomic clock for synchrophasor measurements”, *IEEE Transactions on Power Delivery*, vol. 31, no. 5, pp. 2299–2300, 2016, ISSN: 0885-8977. DOI: 10.1109/TPWRD.2016.2521318.

- [26] F. Droz, P. Mosset, G. Barmaverain, P. Rochat, Qinghua Wang, M. Belloni, L. Mattioni, U. Schmidt, T. Pike, F. Emma, and P. Waller, “The on-board Galileo clocks: Rubidium standard and Passive Hydrogen Maser - current status and performance”, in *Proceedings of the 20th European Frequency and Time Forum*, 2006, pp. 420–426.
- [27] R. T. Dupuis, T. J. Lynch, and J. R. Vaccaro, “Rubidium frequency standard for the gps iif program and modifications for the rafsmo program”, in *2008 IEEE International Frequency Control Symposium*, 2008, pp. 655–660. DOI: 10.1109/FREQ.2008.4623081.
- [28] G. Mei, D. Zhong, S. An, F. Zhao, F. Qi, F. Wang, G. Ming, W. Li, and P. Wang, “Main features of space rubidium atomic frequency standard for beidou satellites”, in *2016 European Frequency and Time Forum (EFTF)*, 2016, pp. 1–4. DOI: 10.1109/EFTF.2016.7477803.
- [29] Microsemi, *Chip Scale Atomic Clock, SA.45s Space CSAC*, Specifications, 2019. [Online]. Available: https://www.microsemi.com/document-portal/doc_download/1243238-space-csac-datasheet [Accessed July 15, 2019].
- [30] Accubeat, *Rubidium frequency standard, NAC1 - nano atomic clock*, Specifications, 2019. [Online]. Available : <https://www.accubeat.com/wp-content/uploads/2018/10/456-1.pdf> [Accessed February 10, 2020].
- [31] Microsemi, *Miniature Atomic Clock, MAC-SA5x*, Specifications, 2019. [Online]. Available: https://www.microsemi.com/document-portal/doc_download/1244700-mac-sa5x-datasheet [Accessed February 10, 2020].
- [32] Accubeat, *Rubidium frequency standard, AR133A*, Specifications, 2019. [Online]. Available : <https://www.accubeat.com/wp-content/uploads/2018/05/AR133A-Specifications-13-05-2018.pdf> [Accessed February 10, 2020].
- [33] Spectratime, *iSpace+™ Space-Qualified miniRAFS*, Specifications, 2019. [Online]. Available : https://www.rolia.com/sites/default/files/document-files/iSpace_miniRAFS_Spec.pdf [Accessed February 10, 2020].
- [34] —, *iSpace+™ Space-Qualified RAFS*, Specifications, 2019. [Online]. Available : https://www.rolia.com/sites/default/files/document-files/iSpace_RAFS_Spec.pdf [Accessed February 10, 2020].
- [35] Excelitas, *High-Performance Space-Qualified Rubidium Atomic Frequency Standard*, Specifications, 2019. [Online]. Available : <https://www.excelitas.com/product/space-qualified-rubidium-atomic-frequency-standard-clocks> [Accessed February 10, 2020].
- [36] FrequencyElectronics, *Rubidium Atomic Frequency Standard, for Space Applications*, Specifications, 2019. [Online]. Available : <https://frelec.com/wp-content/uploads/2019/03/4-RAFS-Brochure.pdf> [Accessed February 10, 2020].
- [37] Oscilloquartz, *OSA 3235B Cesium Clock*, Specifications, 2019. [Online]. Available : <https://www.oscilloquartz.com/en/products-and-services/cesium-clocks/osa-3230-series> [Accessed February 10, 2020].
- [38] Microsemi, *5071A Primary Frequency Standard*, Specifications, 2019. [Online]. Available : https://www.microsemi.com/document-portal/doc_download/133269-5071a-datasheet [Accessed July 15, 2019].

Bibliography

- [39] T4Science, *pHMaser 1008 Passive Hydrogen Maser Clock*, Specifications, 2020. [Online]. Available : https://www.t4science.com/wp-content/uploads/2019/02/pH-Maser_Clock_Spec.pdf [Accessed February 10, 2020].
- [40] —, *iMaser 3000 Smart Active Hydrogen Maser Clock*, Specifications, 2019. [Online]. Available : https://www.t4science.com/wp-content/uploads/2019/07/iMaser_Clock_Spec-.pdf [Accessed July 30, 2019].
- [41] J. Guéna, F. Chapelet, P. Rosenbusch, P. Laurent, M. Abgrall, G. D. Rovera, G. Santarelli, S. Bize, A. Clairon, and M. E. Tobar, “New measurement of the rubidium hyperfine frequency using LNE-SYRTE fountain ensemble”, in *2008 IEEE International Frequency Control Symposium*, 2008, pp. 366–370. DOI: 10.1109/FREQ.2008.4623021.
- [42] A. Kastler, “Quelques suggestions concernant la production optique et la d’étection optique d’une inégalité de population des niveaux de quantification spatiale des atomes. Application à l’expérience de Stern et Gerlach et à la résonance magnétique”, *J. Phys. Radium*, vol. 11, no. 6, pp. 255–265, 1950. DOI: 10.1051/jphysrad:01950001106025500.
- [43] G. Mileti, “Etude du pompage optique par laser et par lampe spectrale dans les horloges à vapeur de rubidium”, PhD thesis, Université de Neuchâtel-Faculté des Sciences, 1995.
- [44] S. Micalizio, C. E. Calosso, A. Godone, and F. Levi, “Metrological characterization of the pulsed Rb clock with optical detection”, *Metrologia*, vol. 49, no. 4, p. 425, 2012. DOI: 10.1088/0026-1394/49/4/425.
- [45] T. Bandi, C. Affolderbach, C. Stefanucci, F. Merli, A. K. Skrivervik, and G. Mileti, “Compact, high-performance CW Double-Resonance rubidium Standard with $1.4 \times 10^{-13} \tau^{-1/2}$ Stability”, *IEEE Trans. Ultrason., Ferroelectr., Freq. Control*, vol. 61, pp. 1769–1778, 11 2014. DOI: <http://dx.doi.org/10.1109/TUFFC.2013.005955>.
- [46] G. Dong, J. Deng, J. Lin, S. Zhang, H. Lin, and Y. Wang, “Recent improvements on the pulsed optically pumped rubidium clock at SIOM”, *Chin. Opt. Lett.*, vol. 15, no. 4, p. 040 201, 2017. DOI: 10.3788/COL201715.040201.
- [47] W. J. Riley, “The Physics of the Environmental Sensitivity of Rubidium Gas Cell Atomic Frequency Standards”, *IEEE Transactions on Ultrasonics, Ferroelectrics, and Frequency Control*, vol. 39, no. 2, pp. 232–240, 1992. DOI: 10.1109/58.139119.
- [48] S. Kang, M. Gharavipour, C. Affolderbach, F. Gruet, and G. Mileti, “Demonstration of a high-performance pulsed optically pumped Rb clock based on a compact magnetron-type microwave cavity”, *J. Appl. Phys.*, vol. 117, no. 10, p. 104 510, 2015. DOI: 10.1063/1.4914493.
- [49] M. Arditi and T. R. Carver, “Atomic clock using microwave pulse-coherent techniques”, *IEEE Transactions on Instrumentation and Measurement*, vol. IM-13, no. 2 & 3, pp. 146–152, 1964, ISSN: 0018-9456. DOI: 10.1109/TIM.1964.4313389.
- [50] M. Gharavipour, C. Affolderbach, S. Kang, and G. Mileti, “Double-resonance spectroscopy in rubidium vapour-cells for high performance and miniature atomic clocks”, *Journal of Physics: IOP Conf. Series*, vol. 793, no. 1, p. 012 007, 2017. DOI: 10.1088/1742-6596/793/1/012007.

- [51] W. Moreno, "Rubidium vapour-cell frequency standards : metrology of optical and microwave frequency references", PhD thesis, Université de Neuchâtel, 2019.
- [52] M. Abdel Hafiz, G. Coget, M. Petersen, C. E. Calosso, S. Guérandel, E. de Clercq, and R. Boudot, "Symmetric autobalanced Ramsey interrogation for high-performance coherent-population-trapping vapor-cell atomic clock", *Applied Physics Letters*, vol. 112, no. 24, p. 244 102, 2018. DOI: 10.1063/1.5030009.
- [53] P. Yun, F. Tricot, C. E. Calosso, S. Micalizio, B. Francois, R. Boudot, S. Guérandel, and E. de Clercq, "High-Performance Coherent Population Trapping Clock with Polarization Modulation", *Phys. Rev. Applied*, vol. 7, p. 014 018, Jan. 2017. DOI: 10.1103/PhysRevApplied.7.014018.
- [54] J. Vanier, "Atomic clocks based on coherent population trapping: a review", *Appl. Phys. B*, vol. 81, pp. 421–442, 4 2005.
- [55] M. Abdel Hafiz, G. Coget, M. Petersen, C. Rocher, S. Guérandel, T. Zanon-Willette, E. de Clercq, and R. Boudot, "Toward a High-Stability Coherent Population Trapping Cs Vapor-Cell Atomic Clock Using Autobalanced Ramsey Spectroscopy", *Phys. Rev. Applied*, vol. 9, p. 064 002, 6 2018. DOI: 10.1103/PhysRevApplied.9.064002.
- [56] D. W. Allan, "Statistics of Atomic frequency Standards", in *Proc. of the IEEE*, vol. 54, 1966, pp. 221–230.
- [57] C. Stefanucci, T. Bandi, F. Merli, M. Pellaton, C. Affolderbach, G. Mileti, and A. K. Skrivervik, "Compact microwave cavity for high performance rubidium frequency standards", *Rev. Sci. Instrum.*, vol. 83, no. 10, 104706, p. 104 706, 2012.
- [58] F. Gruet, M. Pellaton, C. Affolderbach, T. Bandi, R. Matthey, and G. Mileti, "Compact and frequency stabilised laser heads for rubidium atomic clocks", in *Proc. ICSO*, Ajaccio, Corse, France, 2012. DOI: 10.1117/12.2309135.
- [59] W. Moreno, M. Pellaton, C. Affolderbach, N. Almat, M. Gharavipour, F. Gruet, and G. Mileti, "Impact of microwave-field inhomogeneity in an alkali vapour cell using Ramsey double-resonance spectroscopy", *Quantum Electronics*, vol. 49, no. 3, pp. 293–297, 2019. DOI: 10.1070/QEL16883.
- [60] W. Moreno, M. Pellaton, C. Affolderbach, and G. Mileti, "Barometric effect in vapor cell atomic clocks", *IEEE Transactions on Ultrasonics, Ferroelectrics, and Frequency Control*, vol. 65, no. 8, pp. 1500–1503, 2018, ISSN: 0885-3010. DOI: 10.1109/TUFFC.2018.2844020.
- [61] J. Vanier and C. Audoin, *The Quantum Physics of Atomic Frequency Standards*. Adam Hilger, 1989.
- [62] S. Micalizio, A. Godone, F. Levi, and C. Calosso, "Pulsed optically pumped ^{87}Rb vapor cell frequency standard: A multilevel approach", *Phys. Rev. A*, vol. 79, p. 013 403, 1 2009. DOI: 10.1103/PhysRevA.79.013403.
- [63] M. D. Rotondaro and G. P. Perram, "Collisional broadening and shift of the Rubidium D1 and D2 lines ($52S_{1/2} \rightarrow 52P_{1/2}$, $52P_{3/2}$) by rare gases, H₂, D₂, N₂, CH₄ and CF₄", *J. Quant. Spectrosc. Radiat. Transfer*, vol. 57, pp. 497–507, 1997.
- [64] D. W. Preston, "Doppler-free saturated absorption: laser spectroscopy", *Am. J. Phys.*, vol. 64, no. 11, pp. 1432–1436, 1996. DOI: 10.1119/1.18457.

Bibliography

- [65] W. Demtröder, *Laser Spectroscopy 1: Basic Principles*. Springer-Verlag Berlin Heidelberg, 2014. DOI: 10.1007/978-3-642-53859-9.
- [66] P. J. Oredo, Y.-Y. Jau, A. B. Post, N. N. Kuzma, and W. Happer, “Buffer-gas-induced shift and broadening of hyperfine resonances in alkali-metal vapors”, *Physical Review A*, vol. 69, p. 042 716, 2004.
- [67] J. Vanier and C. Mandache, “The passive optically pumped Rb frequency standard: the laser approach”, *Appl. Phys. B*, vol. 87, pp. 565–593, 2007.
- [68] A. Godone, F. Levi, and S. Micalizio, *Coherent Population Trapping Maser*. Torino, Italy: CLUT Editrice, 2002, p. 191, ISBN: 88-7992-166-5.
- [69] A. Godone, S. Micalizio, and F. Levi, “Pulsed optically pumped frequency standard”, *Phys. Rev. A*, vol. 70, p. 023 409, 2 2004. DOI: 10.1103/PhysRevA.70.023409.
- [70] S. Micalizio, C. E. Calosso, F. Levi, and A. Godone, “Ramsey-fringe shape in an alkali-metal vapor cell with buffer gas”, *Phys. Rev. A*, vol. 88, p. 033 401, 3 2013. DOI: 10.1103/PhysRevA.88.033401.
- [71] R. H. Dicke, ““The Effect of Collisions Upon the Doppler Width of Spectral Lines””, *Phy. Rev.*, vol. 89, pp. 472–473, 1953.
- [72] S. Micalizio, A. Godone, F. Levi, and J. Vanier, “Spin-exchange frequency shift in alkali-metal-vapor cell frequency standards”, *Phys. Rev. A*, vol. 73, p. 033 414, 3 2006. DOI: 10.1103/PhysRevA.73.033414.
- [73] M. Gharavipour, C. Affolderbach, F. Gruet, I. S. Radojčić, A. J. Krmpot, B. M. Jelenković, and G. Mileti, “Optically-detected spin-echo method for relaxation times measurements in a rb atomic vapor”, *New Journal of Physics*, vol. 19, no. 6, p. 063 027, 2017. DOI: 10.1088/1367-2630/aa73c2.
- [74] F. Levi, D. Calonico, C. E. Calosso, A. Godone, S. Micalizio, and G. A. Costanzo, “Accuracy evaluation of ITCsF2: a nitrogen cooled caesium fountain”, *Metrologia*, vol. 51, no. 3, p. 270, 2014. DOI: <https://doi.org/10.1088/0026-1394/51/3/270>.
- [75] M. Gharavipour, “Ramsey spectroscopy in a rubidium vapor cell and realization of an ultra-stable atomic clock”, PhD thesis, Laboratoire Temps-Fréquence (LTF), 2018.
- [76] J. Vanier, R. Kunski, N. Cyr, J. Y. Savard, and M. Têtu, “On hyperfine frequency shifts caused by buffer gases: Application to the optically pumped passive rubidium frequency standard”, *J. Appl. Phys.*, vol. 53, no. 8, pp. 5387–5391, 1982. DOI: 10.1063/1.331467.
- [77] C. E. Calosso, A. Godone, F. Levi, and S. Micalizio, “Enhanced temperature sensitivity in vapor-cell frequency standards”, *IEEE Transactions on Ultrasonics, Ferroelectrics and Frequency Control*, vol. 59, no. 12, pp. 2646 –2654, 2012, ISSN: 0885-3010. DOI: 10.1109/TUFFC.2012.2505.
- [78] S. Micalizio, A. Godone, F. Levi, and J. Vanier, “Erratum: Spin-exchange frequency shift in alkali-metal-vapor cell frequency standards [Phys. Rev. A 73, 033414 (2006)]”, *Phys. Rev. A*, vol. 74, p. 059 905, 5 2006. DOI: 10.1103/PhysRevA.74.059905.
- [79] B. S. Mathur, H. Tang, and W. Happer, “Light Shifts in the Alkali Atoms”, *Phys. Rev.*, vol. 171, pp. 11–19, 1 1968. DOI: 10.1103/PhysRev.171.11.

- [80] T. Bandi, “Double resonance studies on compact, high performance rubidium cell frequency standards”, PhD thesis, University of Neuchâtel, 2013.
- [81] A. Risley and G. Busca, “Effect of Line Inhomogeneity on the Frequency of Passive Rb 87 Frequency Standards”, in *32nd Annual Symposium on Frequency Control*, 1978, pp. 506–513. DOI: 10.1109/FREQ.1978.200282.
- [82] G. Mileti, I. Ruedi, and H. Schweda, “Line inhomogeneity effects and power shift in miniaturized rubidium frequency standard”, in *Proc. EFTF 1992*, 1992, pp. 515–519.
- [83] A. Risley, S. Jarvis, and J. Vanier, “The Dependence of Frequency Upon Microwave Power of Wall-coated and Buffer-gas-filled Gas Cell Rb⁸⁷ Frequency Standards”, *J. Appl. Phys.*, vol. 51, no. 9, pp. 4571–4576, 1980. DOI: 10.1063/1.328348.
- [84] C. Affolderbach, N. Almat, M. Gharavipour, F. Gruet, W. Moreno, M. Pellaton, and G. Mileti, “Selected Studies on High Performance Laser-Pumped Rubidium Atomic Clocks”, in *2018 IEEE International Frequency Control Symposium (IFCS)*, 2018, pp. 1–6. DOI: 10.1109/FCS.2018.8597452.
- [85] A. Godone, S. Micalizio, F. Levi, and C. Calosso, “Physics characterization and frequency stability of the pulsed rubidium maser”, *Phys. Rev. A*, vol. 74, p. 043 401, 4 Oct. 2006. DOI: 10.1103/PhysRevA.74.043401.
- [86] A. Godone, S. Micalizio, F. Levi, and C. Calosso, “Microwave cavities for vapor cell frequency standards”, *Rev. Sci. Instrum.*, vol. 82, no. 7, pp. 074 703–1–15, 2011, ISSN: 00346748. DOI: DOI:10.1063/1.3606641.
- [87] W. J. Riley and D. A. Howe, *Handbook of Frequency Stability Analysis*. NIST Spec. Pubs., 2008.
- [88] D. A. Howe, “ThêoH: a hybrid, high-confidence statistic that improves on the Allan deviation”, *Metrologia*, vol. 43, no. 4, S322–S331, 2006. DOI: 10.1088/0026-1394/43/4/s20.
- [89] J. A. Taylor and D. A. Howe, “Fast TheoBR: A method for long data set stability analysis”, *IEEE Transactions on Ultrasonics, Ferroelectrics, and Frequency Control*, vol. 57, no. 9, pp. 2091–2094, 2010, ISSN: 1525-8955. DOI: 10.1109/TUFFC.2010.1656.
- [90] G. Mileti and P. Thomann, “Study of the S/N performance of passive atomic clocks using a laser pumped vapour”, in *Proc. EFTF*, 1995, pp. 271–276.
- [91] J. C. Camparo, “Conversion of laser phase noise to amplitude noise in an optically thick vapor”, *J. Opt. Soc. Am. B*, vol. 15, no. 3, pp. 1177–1186, 1998. DOI: 10.1364/JOSAB.15.001177.
- [92] S. Kang, M. Gharavipour, C. Affolderbach, and G. Mileti, “Stability limitations from optical detection in ramsey-type vapour-cell atomic clocks”, *Electronics Letters*, vol. 51, no. 22, pp. 1767–1769, 2015, ISSN: 0013-5194. DOI: 10.1049/el.2015.1902.
- [93] J. Vanier and C. Tomescu, *The Quantum Physics of Atomic Frequency Standards: Recent Developments*. CRC Press, 2015.
- [94] C. Audoin, V. Candelier, and N. Dimarcq, “A limit to the frequency stability of passive frequency standards”, in *Conference on Precision Electromagnetic Measurements*, IEEE, 1990, p. 93.

Bibliography

- [95] G. Mileti, Jinquan Deng, F. L. Walls, D. A. Jennings, and R. E. Drullinger, “Laser-pumped rubidium frequency standards: new analysis and progress”, *IEEE Journal of Quantum Electronics*, vol. 34, no. 2, pp. 233–237, 1998, ISSN: 0018-9197. DOI: 10.1109/3.658700.
- [96] J. Q. Deng, G. Mileti, R. E. Drullinger, D. A. Jennings, and F. L. Walls, “Noise considerations for locking to the center of a Lorentzian line”, *Phys. Rev. A*, vol. 59, pp. 773–777, 1999. DOI: 10.1103/PhysRevA.59.773.
- [97] M. Pellaton, “High-resolution spectroscopic studies in glass-blown and micro-fabricated cells for miniature rubidium atomic clocks”, PhD thesis, Laboratoire Temps-Fréquence (LTF), 2014.
- [98] R. Matthey, F. Gruet, S. Schilt, and G. Mileti, “Compact rubidium-stabilized multi-frequency reference source in the 1.55- μm region”, *Opt. Lett.*, vol. 40, no. 11, pp. 2576–2579, 2015. DOI: 10.1364/OL.40.002576.
- [99] R. Matthey, W. Moreno, F. Gruet, P. Brochard, S. Schilt, and G. Mileti, “Rb-stabilized laser at 1572 nm for CO₂ monitoring”, *J. Phys. Conf. Ser.*, vol. 723, no. 1, p. 012 034, 2016. DOI: 10.1088/1742-6596/723/1/012034.
- [100] K. Numata, J. Camp, M. A. Krainak, and L. Stolpner, “Performance of planar-waveguide external cavity laser for precision measurements”, *Opt. Express*, vol. 18, no. 22, pp. 22 781–22 788, 2010. DOI: 10.1364/OE.18.022781.
- [101] C. E. Calosso, S. Micalizio, A. Godone, E. K. Bertacco, and F. Levi, “Electronics for the Pulsed Rubidium Clock: Design and Characterization”, *IEEE Transactions on Ultrasonics, Ferroelectrics, and Frequency Control*, vol. 54, no. 9, pp. 1731–1740, 2007, ISSN: 0885-3010. DOI: 10.1109/TUFFC.2007.458.
- [102] S. Kang, M. Gharavipour, F. Gruet, C. Affolderbach, and G. Mileti, “Compact and high-performance rb clock based on pulsed optical pumping for industrial application”, in *2015 Joint Conference of the IEEE International Frequency Control Symposium the European Frequency and Time Forum*, 2015, pp. 800–803. DOI: 10.1109/FCS.2015.7138962.
- [103] G. D. Domenico, S. Schilt, and P. Thomann, “Simple approach to the relation between laser frequency noise and laser line shape”, *Applied Optics*, vol. 49, no. 25, pp. 4801–4807, 2010.
- [104] F. Gruet, R. Matthey, C. Affolderbach, N. Almat, and G. Mileti, *Methods and setup for spectral characterization of laser diodes for atomic clocks*, 2017. DOI: 10.1117/12.2296126.
- [105] F. Gruet and C. Affolderbach, “Report on production and testing of the compact laser system for the POP clock”, Laboratoire Temps-Fréquence (LTF), Tech. Rep., 2014, EMRP IND55-REG1 Mclocks, technical report REG D2.11.
- [106] M. Ohtsu and E. Ikegami, “Frequency stabilisation of 1.5 μm DFB laser using internal second harmonic generation and atomic ⁸⁷Rb line”, *Electronics Letters*, vol. 25, no. 1, pp. 22–23, 1989, ISSN: 0013-5194. DOI: 10.1049/el:19890016.
- [107] S. Peil, S. Crane, and C. R. Ekstrom, “High-efficiency frequency doubling for the production of 780 nm light”, in *IEEE International Frequency Control Symposium and PDA Exhibition Jointly with the 17th European Frequency and Time Forum, 2003. Proceedings of the 2003*, 2003, pp. 159–161. DOI: <https://ieeexplore.ieee.org/document/1275080/>.

- [108] H. S. Schweda, G. Busca, and P. Rochat, “Atomic frequency standard”, pat. 5 387 881, 1995.
- [109] W. Froncisz and J. S. Hyde, “The Loop-Gap Resonator: A New Microwave Lumped Circuit ESR Sample Structure”, *Journal of magnetic resonance*, vol. 47, pp. 515–521, 1982. DOI: 10.1016/0022-2364(82)90221-9.
- [110] M. Pellaton, C. Affolderbach, A. Skrivervik, A. Ivanov, T. Debogovic, E. de Rijk, and G. Mileti, “3D printed microwave cavity for atomic clock applications: proof of concept”, English, *Electron. Lett.*, vol. 54, pp. 691–693, 11 2018, ISSN: 0013-5194. DOI: 10.1049/el.2017.4176.
- [111] SpectraDynamics, *Rb-1, 6.834 GHz Frequency Synthesizer*, Specifications, 2019. [Online]. Available : <https://spectradynamics.com/products/rb-1-frequency-synthesizer/> [Accessed February 10, 2020].
- [112] J. E. Gray and D. W. Allan, “A Method for Estimating the Frequency Stability of an Individual Oscillator”, in *28th Annual Symposium on Frequency Control*, 1974, pp. 243–246. DOI: 10.1109/FREQ.1974.200027.
- [113] N. Almat, M. Gharavipour, W. Moreno, F. Gruet, C. Affolderbach, and G. Mileti, “Long-Term Stability Analysis Towards $<10^{-14}$ Level for a Highly Compact POP Rb Cell Atomic Clock”, *IEEE Transactions on Ultrasonics, Ferroelectrics, and Frequency Control*, vol. 67, no. 1, pp. 207–216, 2020, ISSN: 1525-8955. DOI: 10.1109/TUFFC.2019.2940903.
- [114] M. Abdel Hafiz, G. Coget, P. Yun, S. Guérandel, E. de Clercq, and R. Boudot, “A high-performance Raman-Ramsey Cs vapor cell atomic clock”, *Journal of Applied Physics*, vol. 121, no. 10, p. 104 903, 2017. DOI: 10.1063/1.4977955.
- [115] F. Tricot, D. H. Phung, M. Lours, S. Guérandel, and E. de Clercq, “Power stabilization of a diode laser with an acousto-optic modulator”, *Review of Scientific Instruments*, vol. 89, no. 11, p. 113 112, 2018. DOI: 10.1063/1.5046852. eprint: <https://doi.org/10.1063/1.5046852>.
- [116] M. Shuker, J. W. Pollock, R. Boudot, V. I. Yudin, A. V. Taichenachev, J. Kitching, and E. A. Donley, “Ramsey spectroscopy with displaced frequency jumps”, *Phys. Rev. Lett.*, vol. 122, p. 113 601, 11 2019. DOI: 10.1103/PhysRevLett.122.113601.
- [117] M. Gozzelino, S. Micalizio, F. Levi, A. Godone, and C. E. Calosso, “Reducing cavity-pulling shift in Ramsey-operated compact clocks”, *IEEE Transactions on Ultrasonics, Ferroelectrics, and Frequency Control*, pp. 1–1, Jun. 14, 2018, ISSN: 0885-3010. DOI: 10.1109/TUFFC.2018.2828987.
- [118] S. Micalizio, A. Godone, F. Levi, E. K. Bertacco, C. Calosso, F. Gruet, M. Pellaton, T. Bandi, C. Affolderbach, and G. Mileti, “Pulsed Optically Pumped Rb Clock with Optical detection: First Results”, in *24th European Frequency and Time Forum*, 2010.
- [119] E. J. Angstmann, V. A. Dzuba, and V. V. Flambaum, “Frequency shift of hyperfine transitions due to blackbody radiation”, *Phys. Rev. A*, vol. 74, p. 023 405, 2 2006. DOI: 10.1103/PhysRevA.74.023405.
- [120] J. R. Mowat, “Stark effect in alkali-metal ground-state hyperfine structure”, *Phys. Rev. A*, vol. 5, pp. 1059–1062, 3 1972. DOI: 10.1103/PhysRevA.5.1059.

Bibliography

- [121] J. Deng, “Light shift compensation in a rb gas cell frequency standard with two-laser pumping”, *IEEE Trans. Ultrason., Ferroelectr., Freq. Control*, vol. 48, no. 6, pp. 1657–1661, 2001, ISSN: 0885-3010.
- [122] N. Almat, W. Moreno, M. Pellaton, F. Gruet, C. Affolderbach, and G. Mileti, “Characterization of Frequency-Doubled 1.5- μm Lasers for High-Performance Rb Clocks”, *IEEE Transactions on Ultrasonics, Ferroelectrics, and Frequency Control*, vol. 65, no. 6, pp. 919–926, 2018, ISSN: 0885-3010. DOI: 10.1109/TUFFC.2018.2793419.
- [123] C. E. Wieman and L. Hollberg, “Using diode lasers for atomic physics”, *Rev. Sci. Instrum.*, vol. 62, no. 1, pp. 1–20, 1991.
- [124] K. Numata, J. R. Chen, S. T. Wu, J. B. Abshire, and M. A. Krainak, “Frequency stabilization of distributed-feedback laser diodes at 1572 nm for lidar measurements of atmospheric carbon dioxide”, *Appl. Opt.*, vol. 50, no. 7, pp. 1047–1056, 2011. DOI: 10.1364/AO.50.001047.
- [125] M. Nakazawa, “Recent progress on ultrafast/ultrashort/frequency-stabilized erbium-doped fiber lasers and their applications”, *Frontiers of Optoelectronics in China*, vol. 3, no. 1, pp. 38–44, 2010, ISSN: 1674-4594. DOI: 10.1007/s12200-009-0085-x.
- [126] M. Têtu, B. Villeneuve, N. Cyr, P. Tremblay, S. Thériault, and M. Breton, “Multiwavelength source using laser diodes frequency-locked to atomic resonances”, *J. Lightwave Technol.*, vol. 7, pp. 1540–1548, 1989.
- [127] O. Schmidt, K.-M. Knaak, R. Wynands, and D. Meschede, “Cesium saturation spectroscopy revisited: How to reverse peaks and observe narrow resonances”, *Applied Physics B*, vol. 59, no. 2, pp. 167–178, 1994.
- [128] C. Affolderbach and G. Mileti, “Tuneable, stabilised diode lasers for compact atomic frequency standards and precision wavelength references”, *Optics and Lasers in Engin.*, vol. 43, pp. 291–302, 2004. DOI: 10.1016/j.optlaseng.2004.02.009.
- [129] M. Poulin, N. Cyr, C. Latrasse, and M. Tetu, “Progress in the realization of a frequency standard at 192.1 THZ (1560.5 nm) using ^{87}Rb D₂-line and second harmonic generation”, *IEEE Transactions on Instrumentation and Measurement*, vol. 46, no. 2, pp. 157–161, 1997. DOI: 10.1109/19.571801.
- [130] Y. Han, S. Guo, J. Wang, H. Liu, J. He, and J. Wang, “Efficient frequency doubling of a telecom 1560 nm laser in a waveguide and frequency stabilization to Rb D₂ line”, *Chinese Optics Letters*, vol. 12, no. 12, p. 121401, 2014.
- [131] S. Peil, S. Crane, T. Swanson, and C. R. Ekstrom, “The USNO rubidium fountain”, in *2006 IEEE IFCS*, 2006, pp. 304–306.
- [132] K. W. Martin, G. Phelps, N. D. Lemke, M. S. Bigelow, B. Stuhl, M. Wojcik, M. Holt, I. Coddington, M. W. Bishop, and J. H. Burke, “Compact optical atomic clock based on a two-photon transition in rubidium”, *Phys. Rev. Applied*, vol. 9, p. 014019, 1 2018. DOI: 10.1103/PhysRevApplied.9.014019.

- [133] R. J. Thompson, M. Tu, D. C. Aveline, N. Lundblad, and L. Maleki, “High power single frequency 780 nm laser source generated from frequency doubling of a seeded fiber amplifier in a cascade of PPLN crystals”, *Opt. Express*, vol. 11, no. 14, pp. 1709–1713, 2003. DOI: 10.1364/OE.11.001709.
- [134] F. Theron, Y. Bidel, E. Dieu, N. Zahzam, M. Cadoret, and A. Bresson, “Frequency-doubled telecom fiber laser for a cold atom interferometer using optical lattices”, *Optics Communications*, vol. 393, no. Supplement C, pp. 152–155, 2017. DOI: 10.1007/s00340-014-5975-y.
- [135] V. Ménolet, P. Vermeulen, N. Le Moigne, S. Bonvalot, P. Bouyer, A. Landragin, and B. Desruelle, “Gravity measurements below 10^{-9} g with a transportable absolute quantum gravimeter”, *Nature*, vol. 8, pp. 926–929, 2018, ISSN: 2045-2322. DOI: 10.1038/s41598-018-30608-1.
- [136] R. Caldani, S. Merlet, F. Pereira Dos Santos, G. Stern, A.-S. Martin, B. Desruelle, and V. Ménolet, “A prototype industrial laser system for cold atom inertial sensing in space”, *The European Physical Journal D*, vol. 73, no. 12, p. 248, 2019, ISSN: 1434-6079. DOI: 10.1140/epjd/e2019-100360-2.
- [137] F. Lienhart, S. Boussem, O. Carraz, N. Zahzam, Y. Bidel, and A. Bresson, “Compact and robust laser system for rubidium laser cooling based on the frequency doubling of a fiber bench at 1560 nm”, English, *Applied Physics B*, vol. 89, no. 2-3, pp. 177–180, 2007, ISSN: 0946-2171. DOI: <https://link.springer.com/article/10.1007/s00340-007-2775-7>.
- [138] O. Carraz, F. Lienhart, R. Charrière, M. Cadoret, N. Zahzam, Y. Bidel, and A. Bresson, “Compact and robust laser system for onboard atom interferometry”, *Appl. Phys. B*, vol. 97, no. 2, p. 405, 2009. DOI: <https://doi.org/10.1007/s00340-009-3675-9>.
- [139] T. Lévêque, L. Antoni-Micollier, B. Faure, and J. Berthon, “A laser setup for rubidium cooling dedicated to space applications”, *Appl. Phys. B*, vol. 116, no. 4, pp. 997–1004, 2014. DOI: 10.1007/s00340-014-5788-z.
- [140] Q. Wang, Z. Wang, Z. Fu, W. Liu, and Q. Lin, “A compact laser system for the cold atom gravimeter”, *Opt. Commun.*, vol. 358, pp. 82–87, 2016. DOI: 10.1016/j.optcom.2015.09.001.
- [141] J. Dingjan, B. Darquié, J. Beugnon, M. Jones, S. Bergamini, G. Messin, A. Browaeys, and P. Grangier, “A frequency-doubled laser system producing ns pulses for rubidium manipulation”, *Appl. Phys. B*, vol. 82, no. 1, pp. 47–51, 2006.
- [142] M. Alalusi, P. Brasil, S. Lee, P. Mols, L. Stolpner, A. Mehnert, and S. Li, “Low noise planar external cavity laser for interferometric fiber optic sensors”, in *Fiber Optic Sensors and Applications VI*, E. Udd, H. H. Du, and A. Wang, Eds., International Society for Optics and Photonics, vol. 7316, SPIE, 2009, pp. 235–247. DOI: 10.1117/12.828849.
- [143] W. Moreno, R. Matthey, F. Gruet, P. Brochard, S. Schilt, and G. Miletì, “Rb-stabilized optical frequency reference at 1572 nm”, in *2016 European Frequency and Time Forum (EFTF)*, 2016, pp. 1–4. DOI: 10.1109/EFTE2016.7477785.
- [144] M. Gharavipour, C. Affolderbach, S. Kang, T. Bandi, F. Gruet, M. Pellaton, and G. Miletì, “High performance vapour-cell frequency standards”, *J. Phys. Conf. Ser.*, vol. 723, no. 1, p. 012 006, 2016. DOI: 10.1088/1742-6596/723/1/012006.

Bibliography

- [145] J. Gros Lambert, D. Fest, M. Olivier, and J. J. Gagnepain, “Characterization of Frequency Fluctuations by Crosscorrelations and by Using Three or More Oscillators”, in *Thirty Fifth Annual Frequency Control Symposium*, May 1981, pp. 458–463. DOI: 10.1109/FREQ.1981.200512.
- [146] F. Vernotte, C. E. Calosso, and E. Rubiola, “Three-cornered hat versus allan covariance”, in *2016 IEEE International Frequency Control Symposium (IFCS)*, 2016, pp. 1–6. DOI: 10.1109/FCS.2016.7546784.
- [147] N. Almat, M. Pellaton, W. Moreno, F. Gruet, C. Affolderbach, and G. Mileti, “Rb vapor-cell clock demonstration with a frequency-doubled telecom laser”, *Appl. Opt.*, vol. 57, no. 16, pp. 4707–4713, 2018. DOI: 10.1364/AO.57.004707.
- [148] S. Micalizio, A. Godone, C. Calosso, F. Levi, C. Affolderbach, and F. Gruet, “Pulsed optically pumped rubidium clock with high frequency-stability performance”, *IEEE Trans. Ultrason., Ferroelect., Freq. Control*, vol. 59, no. 3, pp. 457–462, 2012, ISSN: 0885-3010. DOI: 10.1109/TUFFC.2012.2215.
- [149] SpectraDynamics, *cRb-Clock*, Specifications, 2019. [Online]. Available : <https://spectradynamics.com/product-sheets/cRb-Clock-2019.pdf> [Accessed February 10, 2020].
- [150] Muquans, *MuClock*, Specifications, 2019. [Online]. Available : https://www.muquans.com/wp-content/uploads/2019/03/muquans_muclock.pdf [Accessed February 10, 2020].

Nil Almat

nil.almat@alumni.epfl.ch

ORCID 0000-0002-8619-8702



Work Experience

- Since 02/2016** **PhD student**, *Laboratoire Temps-Fréquence, Institut de Physique, Université de Neuchâtel, Neuchâtel, Switzerland*
- Metrological characterization of the instability sources in high-performance double-resonance rubidium vapor-cell clocks
 - Experimental demonstration and study of a continuous-wave double-resonance rubidium vapor-cell clock using a frequency-doubled telecom laser
 - Evaluation of the clock frequency stability through the establishment of the exhaustive budget at short and medium-to-long term timescales
 - Spectral characterization and evaluation of various laser sources for high-performance (rubidium and cesium) clocks
 - Laser, double-resonance, and Ramsey spectroscopy in alkali-metal vapor cells
 - Numerical simulation on resonant microwave cavities
 - Teaching laboratories in Physics for 1st-year medicine, biology, and pharmacy students
 - Supervision of undergraduate student internships
 - Scientific expertise for general-public science festivals
- 05/2015 - 12/2015** **R&D Engineer**, *Alpes Lasers SA, Neuchâtel, Switzerland*
- Design, realization, and optimization of various workbenches for spectral characterization of medium to large number of laser chips or diodes
 - Laser process analysis on wafer-sized developments
 - Project reporting and contribution to weekly follow-ups with clients
 - Literature and market review on novel techniques for laser diode integration on silicon
- 09/2013 - 02/2014** **“Boron and Gallium Doping of Amorphous Silicon for Solar Cells”** (Master thesis), *PV-Lab, EPFL, Neuchâtel, Switzerland*
- Realization of thin film solar cells using a novel p-doping agent (Gallium)
 - Experimental comparison of Gallium and Boron as p-doping agent in thin film solar cells
 - Optimization of p-layer for p-i-n thin film solar cells
 - Fabrication of solar cells by layer deposition techniques and their optical and electrical characterization
- 02/2012 - 06/2012** **“Optical Characterization of Microsphere Arrays: A Solar Energy Concentrator”** (Semester Project II), *OPT Lab, EPFL, Neuchâtel, Switzerland*
- Achievement of depositing dielectric microsphere monolayers on glass substrates
 - Optical characterization of the realized dielectric monolayers
 - Incorporation of optimized dielectric monolayers with p-i-n thin film solar cells
- 09/2010 - 02/2011** **“Silver Nanoparticles for Light Scattering in Amorphous n-i-p Thin Film Silicon Solar Cells”** (Semester Project I), *PV-Lab, EPFL, Neuchâtel, Switzerland*
- Enhancement of photo-generated current in n-i-p thin film solar cells using silver nanoparticle layers for light-trapping
 - Deposition and optimization of the layer structure
 - Optical and electrical characterization of fabricated solar cells
- 05/2008 - 06/2008** Engineering internship, *Elsim Elektrotechnik AS, Istanbul, Turkey*
- Machining and assembling, automation programming, and update of management tools

Education

Since 02/2016	PhD in Physics, Laboratoire Temps-Fréquence, Université de Neuchâtel, Neuchâtel, Switzerland
2011 – 2014	MSc in Micro Engineering, EPFL, Lausanne, Switzerland Specialization in Production Techniques
2008 – 2011	BSc in Micro Engineering, EPFL, Lausanne, Switzerland

Skills

Computational	Programming and data analysis: IGOR, Python, Matlab, C Numerical simulation: COMSOL Organizational and graphical: GanttProject, Inkscape, Adobe Illustrator Office and OS: LATEX, MS Office, Windows, Linux, Mac OS X
Technical and laboratory	Time and frequency metrology, atomic spectroscopy (optical, microwave, and double-resonance), frequency-stabilized laser systems, noise measurements, laser spectral characterization, lock-in and servo electronics, RF electronics Clean room fabrication methods (PECVD, sputtering, spin-coating, annealing, etching) Optical and electrical characterization (Photo-spectrometry, Ellipsometry, SEM, Sigma dark)
Languages	Turkish (mother tongue), French (fluent), English (fluent), Spanish (intermediate), German (beginner)